University of Modena and Reggio Emilia
Department of Engineering "Enzo Ferrari"

PhD in Industrial and Environmental Engineering
(XXXIV cycle)

ICAR/09 - Structural Engineering

Model updating and soft computing techniques for structural and damage identification

Federico Ponsi

Supervisor
Prof. Loris Vincenzi

School Director
Prof. Alberto Muscio

May 2022

Abstract

A multitude of structures or infrastructures is damaged or degraded due to, for example, a seismic event or the protracted exposure to adverse environmental and atmospheric conditions. This situation may prevent the construction serviceability and, in even more serious cases, may determine their collapse. In this context, vibration-based structural health monitoring became very diffused for the strict relationship existing between dynamic properties and stiffness of the structure, that depends on its health state. Damage detection methods based on data registered by a monitoring system are often supported by the definition of numerical models. They allow, if properly calibrated, a better knowledge of the structure, to obtain more reliable results about the structure safety and to identify possible anomalies through the comparison with the expected behavior. In case of damage, they further enable localization and quantification of damage itself.
In the present work, several aspects related to damage detection techniques with the support of numerical models are studied and deepened.
Multi objective approach for model updating, typically necessary in problems of structural safety, provides a set of optimal solutions, called Pareto front. The preferred solution has to be selected within this front. In this framework, the author proposes a procedure for the direct computation of the preferred solution, without the need to determine the whole front, by means of the minimization of a single objective function defined according to the criterion of the minimum distance from the equilibrium point. This procedure is validated on several case studies, including the case of the San Felice sul Panaro fortress, an historical structure strongly damaged by the Emilia-Romagna seism occurred in 2012.
Bayesian model updating involves the stochastic modelling of model parameters and errors so that the updating result can be expressed also in terms of uncertainty. About the case of the San Felice sul Panaro fortress, results in terms of both parameters and weights attributed to frequencies and mode shapes, are compared with those obtained through bi-objective optimization, analyzing the associated uncertainties. Variants of the classical methodology are presented with the aim of reducing the computational effort, especially for the computation of the updated parameter uncertainties.
Model updating methods for damage detection are usually time-consuming and do not enable the real-time identification of a damaged condition. Instead, artificial neural networks ensure a quick identification if they are appropriately calibrated before their use by means of numerical models able to simulate ordinary conditions and damage scenarios. To investigate the performance of neural networks for damage identification purposes, two models of a concrete/steel mixed railway bridge are developed, which differ in detail level. They simulate the "real" structural behavior and that of "the model", defined starting from the identified modal properties. The last model, i.e. the simpler one, is employed for

the generation of the dataset finalized to the training phase. With the first model, defined in more detail, the experimental data adopted for the network test are simulated. They unavoidably differ from those of the simplified model, despite it was calibrated. Results show how, in order to have accurate network predictions in the test phase, the residual errors obtained at the end of the calibration must be used to correct the data given in input to the network.

Abstract

Numerose strutture e infrastrutture si trovano in uno stato di degrado o danneggiamento causato, per esempio, da un evento sismico o dall'esposizione prolungata a condizioni ambientali sfavorevoli. Questa situazione può compromettere la funzionalità dell'opera o, in casi più gravi, portare al collasso della stessa. In questo contesto, il monitoraggio dello stato di salute delle strutture mediante prove dinamiche rappresenta un'attività in crescente diffusione. Le metodologie per l'identificazione del danno basate sui dati acquisti dal sistema di monitoraggio sono spesso supportate dalla definizione di modelli numerici che, opportunamente calibrati, permettono una migliore conoscenza della struttura, di ottenere risultati più affidabili in merito alla valutazione della sicurezza delle strutture e di rilevare possibili condizioni anomale dal confronto con il comportamento atteso. In caso di danno, permettono inoltre la localizzazione e la quantificazione del danno stesso.
Nel presente lavoro sono stati studiati e approfonditi diversi aspetti riguardanti tecniche per l'identificazione del danno con l'ausilio di modelli numerici.
L'approccio multi-obiettivo alla calibrazione di modelli numerici, tipicamente necessario in problemi di sicurezza strutturale, fornisce un insieme di soluzioni ottimali, chiamato frontiera di Pareto, all'interno della quale deve essere scelta la soluzione preferita. In questo contesto, l'autore propone una procedura che consente il calcolo diretto della soluzione preferita, senza la necessità di determinare la frontiera, attraverso l'ottimizzazione di un'unica funzione obiettivo definita sulla base del criterio della minima distanza dal punto di equilibrio. Tale procedura è stata validata su una serie di casi studio, compreso quello della Rocca di San Felice sul Panaro, una struttura storica severamente danneggiata dal sisma dell'Emilia del 2012.
L'approccio Bayesiano consente la modellazione stocastica dei parametri e degli errori in modo tale che il risultato della calibrazione possa essere espresso anche in termini di incertezza. Sul caso della Rocca di San Felice, i risultati, sia in termini di parametri che di pesi attribuiti a frequenze e forme modali, sono stati confrontati con quelli ottenuti tramite l'ottimizzazione bi-obiettivo e analizzando le incertezze associate. Sono inoltre presentate varianti alla metodologia, per cercare di ridurne l'onere computazionale, soprattutto per la valutazione delle incertezze dei parametri identificati.
Le metodologie di model updating applicate all'identificazione del danno risultano spesso computazionalmente onerose e non permettono l'identificazione in tempo reale del possibile stato di danneggiamento. Le reti neurali, invece, permettono una rapida identificazione del possibile danno, se vengono opportunamente calibrate prima dell'utilizzo tramite modelli numerici capaci di simulare condizioni ordinarie e scenari di danno. Con riferimento al caso di un ponte ferroviario in struttura mista acciaio-calcestruzzo, sono stati sviluppati due modelli che differiscono per grado di dettaglio e permettono di simulare il compor-

tamento “reale” della struttura e quello “del modello”, definito a partire dai parametri modali identificati. Quest’ultimo modello, più semplice, viene usato per la generazione dei dati destinati all’addestramento della rete. Con il primo modello, più dettagliato, si simulano i dati sperimentali impiegati per il test della rete, i quali inevitabilmente si discostano da quelli del modello semplificato, nonostante sia esso calibrato. I risultati ottenuti evidenziano come, per avere previsioni accurate nella fase di test, gli errori residui ottenuti al termine della calibrazione devono essere utilizzati per correggere i dati forniti in input alla rete.

Contents

List of Figures

List of Tables

Chapter 1

Introduction

Numerous structures and infrastructures are in a state of damage or degradation caused by several factors, like seismic events, inappropriate human actions or the protracted exposure to adverse environmental conditions. The lack of knowledge about a damaged state, or its underestimation, may bring to a dangerous evolution of the situation, that may prevent the structure serviceability or determine a partial or the complete collapse of the structure. The implications of these events may involve economical aspects but, in more serious cases, also physical injuries and loss of human lives. The experimental monitoring of a structure allows to control its health state and to point out critical situations. In this way, the possibility of carrying out effective countermeasures before the occurrence of a disaster is surely enhanced. Structural Health Monitoring (SHM) is the general term indicating the research field that aims at developing different solutions, in terms of sensor equipment and procedures, for the detection of changes and anomalies in the integrity of a structural system [156, 173]. The monitoring of the dynamic behaviour of a structure represents a very diffused solution since its behaviour depends on the stiffness, that is directly related to its health state. The monitoring system is composed of a series of accelerometric sensors disposed over the structure that are able to record its acceleration response due to different sources of excitation. This system is minimally invasive, so the structure can remain in operational condition. Modal properties are often used as representative features of the health state, since they provide information about both the global (natural frequencies) and the local (mode shapes) behaviour of the structure. Moreover, output-only techniques of modal extraction can be employed. They exploit environmental sources of excitation and do not require the knowledge of the input force [27, 138].

Damage detection methods are commonly divided in two main groups: model-based and data-driven methods. Methods of the first group directly use numerical models describing the structure for damage identification, localization and quantification. The stiffness reduction of an element, or a group of elements, can be detected through the updating of the model repeated in different measurement epochs [65]. The stiffness reduction represents the severity of the damage occurred. Model updating allows to reduce as much as possible the discrepancy between the experimental observations and the same quantity predicted by the numerical model by adjusting suitable parameters of the model [117]. The discrepancy is expressed by means of specific functions that, in the case of modal properties, are the frequency and mode shape residuals. The efficiency of the detection procedure strongly

depends on several aspects characterizing model updating, that affect the accuracy of its results. Among them, there are the quality and the quantity of experimental observations available, the parametrization of the model, the definition of the optimization problem and the algorithm employed for its resolution.

In this last context, two different approaches are generally distinguished: the single or the multi objective approach. In the first, a single objective function is defined as the weighted sum of frequency and mode shape residuals. Despite the rapidity of the approach, very unbalanced results can be obtained if the weighting factor of the residuals is not properly selected. The weighting factor measures the relative importance between the residuals. Indeed, model updating is part of the family of inverse problems, whose characteristic is ill-conditioning [165]. Therefore, in some cases the modification of the weighting factor may produce significant variation of the updated parameters. In the multi-objective approach, each residual, that represents an objective, is separately minimized and a set of optimal solutions can be obtained, each one having the value of one objective better than that of others [32]. This set is named Pareto front. The solution that represents the optimal trade-off between the objectives is selected once the front is computed through a criterion based on additional features [7, 52, 92, 113, 49]. As concerns the optimization algorithm, classical solutions are represented by gradient-based [154] or evolutionary algorithms [159]. Both families, despite positive peculiarities, are characterized by drawbacks. Gradient based algorithms have efficient convergence rates but may reach local minima depending on the starting vector. Conversely, evolutionary or genetic algorithms are very robust and the starting point has a low influence on the optimization results. The main disadvantage is related to the high number of objective function evaluations required to reach convergence. For this reason, recent interesting developments in this field involve the implementation of surrogate models for evolutionary algorithms [142, 119, 169] or the use of hybrid solutions [109, 134], where the search is initially performed with a non-gradient based method and after a given number of iterations the best point evaluated is chosen as the starting point for the gradient-based algorithm.

Uncertainties and errors unavoidably affect model updating problems. They are associated both to measurement acquisition and elaboration [132, 155, 143] and to modeling assumptions [117, 98, 172]. Taking into account also the ill-conditioned nature of model updating, the reliability of its results may be compromised by these factors. For this reason, treating the problem in probabilistic terms, reasoning about parameter distributions could be more appropriate than considering a single optimal parameter vector in deterministic terms. One of the most diffused method that allows uncertainty quantification is founded on the Bayes theorem. Reference works about Bayesian model updating in the context of structural engineering was produced by Beck and Katafygiotis [18, 96], Beck [15], Katafygiotis et al. [95] and Jaynes [88]. An important application of this method occurred in the field of structural health monitoring (SHM): the first works about probabilistic damage assessment based on observed modal properties are those of Sohn and Law [157] and Vanik et al. [166]. Later, different authors improved the method by introducing the concept of system mode shape [40], system frequencies [178] or by incorporating temperature as a variable affecting modal properties [11]. Despite the efficiency of the methods, the computation of the parameter posterior distribution represents a challenging task, since the exact solution cannot be calculated when the number of updating parameters is sufficiently large. To this aim, several approximated methods was developed: a distinction can be made between

analytical method based on asymptotic approximations [18] and numerical methods based on Markov Chain Monte Carlo (MCMC) algorithms [74, 71, 41].

Model based damage detection methods are usually time-consuming and do not enable the real-time identification of a damaged condition. On the other hand, data-driven methods are characterized by a considerable rapidity since they are able to detect a damage state according to the variation of damage sensitive features extracted directly from the acquired data. In this regard, the choice of appropriate features plays a fundamental role.

Early data-driven methods were analyzed and summarized by Doebling et al. [54]. In the following, the main physical parameters used to construct damage indices are discussed. Natural frequencies and mode shapes were surely the first properties used to create damage indices thanks to the development of modal analysis technology. Zak et al. [180], for example, examined the changes in resonant frequencies produced by closing delamination in a composite plate. Salawu [148] realized a comprehensive review of damage detection techniques founded on frequency modification. Zhang et al. [184] and Feng and Feng [58] directly employed mode shapes to determine damage location. Ahmadian et al. [2] used changes in mode shapes and participation factors for SHM purposes.

Judging benefits and drawbacks, frequencies can be measured with a minimal instrumentation, but they suffer variations caused by environmental conditions, that are usually larger or comparable to those caused by damage. Furthermore, they exhibit a low sensitivity to local damage, allowing only detection and not localization in real structures. On the other hand, mode shapes enable localization of damage and are less affected by environmental variation. However, they are identified with more uncertainty compared to frequencies and need a more dense sensor equipment in order to provide spatial information about damage.

Mode shape curvature [128], modal strain energy [160] and modal flexibility [127] are indices very sensitive to stiffness variation, more than mode shapes. Several works are founded on this kind of indices: strain energy methods were developed by Hu et al. [79] and Seyedpoor [151]. Bernagozzi et al. [22] and Zare Hosseinzadeh [181] focused their attention on modal flexibility matrix. Radzienski performed a comparative study of damage detection methods using modal parameter indices [137]. These indices are calculated starting from mode shapes and, similarly, require a sufficiently high number of sensors acquiring information. Moreover, their computation through mode shape numerical differentiation magnifies the effect of noise and errors.

In contrast to modal data, frequency response functions (FRFs) and operational deflection shapes (ODSs) [150] provide information about a whole frequency range. Limongelli proposed a damage identification method based on interpolation error of FRFs or ODSs [107, 108, 51], Zhang et al. introduced a detection algorithm for bridges that is founded on operating deflection shape curvature extracted from dynamic response of a passing vehicle [183]. The main drawbacks related to FRF application involve the choice of the optimum frequency range and the need to measure excitation force and structural response simultaneously.

Conversely, transmissibility, defined as the ratio between two sets of responses [146], is independent from input excitation and it can be also defined in random processes [61]. As local quantity, it is highly sensitive to damage. Maia et al. [112] proposed a method for damage detection and quantification based on the correlations of acceleration response

transmissibilities . Kong et al. utilized the transmissibility of vehicle responses to identify damage in a bridge [104].

Results presented in literature, some of which are summed up in a review realized by Sohn et al. [156], additionally highlight the necessity to develop statistical models for feature discrimination, since the effect of noise or other external factors over the selected features may be comparable to that of damage. Machine Learning (ML) techniques are a widespread solution to this problem since they are capable of working with uncertain and noise-corrupted data [99]. The application of these techniques to the field of damage detection is quite recent, but a vast amount of works have been produced. Review works that aim also at the classification of ML-based damage detection techniques are those of Avci et al. [6] and Hou and Xia [78]. Numerical models are not directly involved in the actual identification of a damaged state with data-driven methods, but they may be employed in previous phases, as the creation of data related to damaged scenarios that cannot be reproduced in a real situation. Several methods, indeed, have been developed starting from information generated by models, like the integrated use of spatial Fourier analysis and artificial neural networks of Pawar et al. [131] or the two-phase detection method of Yuen and Lam [179].

1.1 Objectives of the thesis

Structural health monitoring is a research field arose some decades ago and a large variety of solutions have been proposed in function of the type of problem. The same can be stated focusing only on vibration-based monitoring, that is one of the most diffused approaches in SHM. In the last decades, the development of soft computing techniques contributed to a further improvement in this field, enabling the implementation of more complex and elaborated methods from the computational point of view.

The objective of the thesis is to implement and analyze different methods for structural and damage identification, most of them based on soft computing techniques, and to improve some aspects of these procedures. Model-based techniques have been first considered. The author focuses on the calibration of a single state of the model, related to a single measurement epoch, that is the central operation to repeat several times in order to monitor the evolution of the model parameters. Adopting a deterministic approach, uncertainties affecting the problem are usually accounted for by assigning a different weight to modal residuals. The choice of the optimal weight is still a discussed theme, subject to several insights. The multi-objective approach is surely the most general approach, since it enables to evaluate multiple solutions of the problem and to select the preferred one a posteriori, according to additional criteria. After the evaluation of some criteria found in literature, the author proposes a direct procedure for the computation of the preferred solution with the aim to maintain the accuracy of the classical approach and to considerably reduce the computational time. Moreover, the weight associated to the preferred solution is estimated a posteriori giving the opportunity to compare it with the one selected with the classical approach.

Another family of model-based techniques concerns stochastic modelling of errors and parameter, enabling uncertainty quantification and damage detection in probabilistic terms.

Bayesian model updating has been implemented and applied for the calibration of structural models in some case studies. The influence of the prior distribution and the likelihood function has to be evaluated. Furthermore, the Bayesian framework enables the selection of the optimal likelihood coefficients, which can be related to the weights defined in the deterministic approach. The implemented solution needs to be validated through the comparison with the results of the deterministic approach for the same case studies. The exact computation of the posterior distribution implies a significant computational effort, hence a Gaussian surrogate is introduced in order to solve this issue.

Model-based methods can be rarely applied for a real time monitoring because they require a high number of modal analysis to obtain the solution, so data-driven methods represent more adequate solutions in this perspective. The first objective in this context is to delineate a complete procedure for damage detection. Considering the case study of a railway bridge, a procedure using artificial neural network is developed. The procedure employs only simulated data, but includes a series of expedients to approach a real situation, like the stochastic modelling of measurement errors and the use of two different models to account for the residual discrepancy between model and reality that exists even at the end of the calibration (model error). Moreover, different data and feature extraction techniques are considered, each of one is taken in input by a specific network. The performances of the networks are analyzed with respect to datasets generated by the two different models, assessing their effective applicability.

1.2 Outline of the thesis

The thesis is organized as follows. Chapter 2 provides an introduction to the problem of model updating based on experimental modal properties, treating the main aspects that characterize the theme, such as the definition of the functions expressing the discrepancy between experimental data and numerical predictions, the ill-conditioning of the problem and the need to adopt an adequate parametrization. As concerns the problem resolution, the single objective approach consisting of the weighted sum of modal residuals is described as well as the optimization algorithm specifically developed for that aim, which is an improved surrogate-assisted evolutionary algorithm. At the end of the chapter, the theory previously presented is applied to the calibration of the 3D FE model of the San Prospero Bell tower. First, the results of the experimental campaign conducted to characterize the dynamical behaviour of the structure are showed. Then, the updated model is presented and validated through a sensitivity analysis.

Chapter 3 addresses the topic of the weight selection in model updating, summarizing the main approaches proposed in literature, where the selection can be made before the resolution of the problem or subsequently in a multi-objective optimization context. For the latter, a multitude of optimal solutions is computed and the preferred solution is then selected on the basis of specific criteria, based on additional or experience-driven information. The robustness of four selection criteria found in literature is assessed by means of the calibration of three numerical case studies. Finally, the author proposes a direct procedure for the determination of the preferred solution without the need to compute all the optimal solutions of the problem, enabling a significant reduction in the

computational effort. The procedure is based on the criterion of the minimum distance from the equilibrium point, that showed the best performances in the previous analysis. The validation of the procedure is performed considering the FE model of the San Felice sul Panaro fortress, an historical masonry structure that suffered serious damage due to the seismic events occurred in Emilia-Romagna in 2012.

Chapter 4 focuses on Bayesian model updating, motivating the necessity of uncertainty quantification in the calibration of structural models. The mathematical framework of this approach is presented along with the principal works on the argument. In particular, attention is paid to the construction of the prior distribution, of the likelihood function and to the methods developed for the computation of the posterior distribution. The approach is implemented and applied to a simple numerical case study and to the FE model of the San Felice sul Panaro fortress, showing the variation of the results by changing prior distribution and parameters of the likelihood function.

Chapter 5 treats more specifically the influence of the frequency and mode shape coefficients of variation constituting the corresponding prediction errors. It is shown the relationship between these coefficients and the weights of the modal residuals defined in the deterministic approach of chapter 3. The selection of the optimal coefficients of variation is performed at an additional level of model updating, called Bayesian Model Class Selection. This is characterized by a high computational complexity, which the author seeks to alleviate by introducing a surrogate model. The effectiveness of the proposal is tested with two real case studies, the already presented San Felice sul Panaro fortress and the Ficarolo bell tower. In addition, a comparison with the deterministic approach is performed in terms of weights and computational burden.

In chapter 6 a vibration-based damage detection procedure for railway bridges using artificial neural networks is delineated. A literature review of the main works about damage identification is first presented, then the feature extraction and pattern recognition techniques used are outlined. The detection of damage is accomplished thanks to a multi-layer perceptron with the aim to classify the structure condition according to the damage features provided in input. Different data are employed, such as modal properties, displacement and acceleration responses caused by the passage of a train over the bridge, and their applicability as damage feature is tested. In the chapter all the other aspects characterizing the procure are described in detail, as the the use of two numerical models to simulate the unavoidable discrepancy between model and reality, the modelling of different sources of uncertainty affecting measurements, the creation of the network datasets composed by different damage scenarios and the optimization of the network architecture. Results of network predictions, related to the datasets generated by the two different models, are illustrated at the end of the chapter.

Finally, a summary of the main conclusions of the research work as well as recommendations for future research are presented in chapter 7.

Chapter 2

Model updating: motivations and single objective approach

Models are fundamental tools for the comprehension and reproduction of a physical phenomenon. For this reason, they are very diffused in all the branches of science and engineering. In the field of structural engineering, the wide diffusion of FE models is due to the different aims for which they are employed, varying from design to research purposes. Very common applications are the analysis of a structural condition or the prediction of the response of a structure due to different type of loading. It is obvious to say that the reliability of the model results strongly depends on how accurate the model is. Uncertainty or lack of knowledge about different aspects of modeling, such as boundary conditions, geometry, material property and load conditions, implies that assumptions and simplification are necessary for the development of a model. Consequently, the subjective judgment of an analyst, which cannot be deleted for the previous reasons, affects model results.

Model updating or calibration is a practice finalized to increase the accuracy of a model employing experimental observations. These methods are also referred as inverse modeling since a set of uncertain model parameter is calibrated in order that the predicted quantities match as close as possible the experimental measurements. An optimization problem is based on the minimization of an objective function defining the discrepancy between experimental observations and numerical predictions.

The chapter is organized in this way: in section 2.1 the principal contributes to structural model updating using dynamic data are summed up; the mathematical framework of model updating as single objective optimization problem is discussed in section 2.2. The specific optimization algorithm employed for all the applications of the thesis is described in section 2.3. Finally, section 2.4 presents the results of the calibration of the FE model of a real case study, the San Prospero bell tower.

2.1 Model updating in structural dynamics

Model updating allows to reduce the uncertainties related to a model, and at the same time to increase the reliability of its predictions, by means of the calibration of a pre-determined

set of model parameters. They are adjusted in such a way that the model predictions are as similar as possible to the experimental observations used for the updating. This procedure is carried out applying optimization techniques aimed at the minimization of a function expressing the discrepancy between experimental observations and numerical predictions.

Focusing the discussion on structural context, dynamic properties obtained by vibration tests, such as natural frequencies, mode shapes, modal strains or curvatures, are the most employed data for updating, since they offer information about both global and local behavior of the structure. Moreover, vibration tests can be performed in operational condition of the structure and can exploit ambient excitation like wind or traffic [138].

Traditional reference works on model updating in structural dynamics are those of Ibrahim [81], Imregun and Visser [84] and Mottershead and Friswell [117, 66]. A more recent work comparing deterministic and probabilistic approaches to model updating was realized by Simoen et al. [152].

Applications of structural FE model updating are numerous. These include damage detection [163], health monitoring and structural assessment [34, 60, 30], structural control [94], validation of innovative structural designs [68, 124, 135] and evaluation of earthquake or strong-winds effects [140].

One of the most significant and diffused area of application of model updating is without doubt that of structural health monitoring (SHM) and damage detection. The motivation can be attributed to the fact that structural damage causes a local reduction of stiffness and, consequently, the modification of the dynamic properties of the structure. Reference works on SHM were realized by Sohn et al. [156] and Worden et al. [173]. Vibration-based SHM was extensively analyzed by Rytter [147], Doebling et al. [54, 53] and Carden and Fanning [33]. Rytter proposed a classification in four level of the damage assessment approach: (i) damage identification, (ii) damage localization, (iii) damage quantification and (iv) prognosis of the actual safety of the structure. Model-based damage assessment can fulfill the procedure until the third level: it is able to detect, localize and quantify damage by means of the calibration of the stiffness parameters of a structure performed with reference to different measurements epochs regarding the structure. This classification was resumed by different authors and it was extended to a fifth level of healing for self-healing smart structures by Park et al. [130]. A recent review on model-based damage assessment method, in particular concerning the use of evolutionary algorithm, has been realized by Alkayem et al. [4].

2.2 Single objective approach for model updating

The following section focuses on FE model updating based on modal data, that are surely the most diffused type of dynamic data in this field. Accelerations time series are not often used directly, as the input excitation should be precisely known. This rarely happens for this kind of applications, especially if ambient excitation is considered. Moreover, the response in time domain predicted by a model is affected by a large number of factors such as, for example, the degree of detail that characterizes the modeling of the structure and of the loads. The matching between predicted and measured responses in time domain can be a very difficult operation. From this point of view, difficulties in matching modal

properties are surely more limited.

2.2.1 Statement of the optimization problem

As introduced in section 2.1, model updating is performed by minimizing an objective function expressing the discrepancy between experimental data and numerical predictions. When dealing with natural frequencies, the objective function corresponds to the frequency residual error defined in a least squares sense:

$$e_F(\mathbf{x}) = \sum_{m=1}^{M} \left(\frac{f_{num,m}(\mathbf{x}) - f_{exp,m}}{f_{exp,m}} \right)^2 \tag{2.1}$$

where $\mathbf{x}$ is the vector collecting the updating parameters, M is the number of modes selected for the calibration, $f_{exp,m}$ and $f_{num,m}$ are the m-th experimental and numerical frequencies, respectively. Although some works rely on frequency-based model updating [86, 126, 82], it was proved how information about the local behaviour of the structure are fundamental in order to obtain accurate results [62]. In damage detection problems, furthermore, the localization of damage is improved only if local information are available [102, 141]. Hence, mode shapes or derived properties like modal curvatures, strains or flexibilities are included in the updating scheme [86]. In the following, only mode shapes are discussed, but the same considerations can be made for the other properties. Mode shape residual error can be expressed with different formulations, some of the more diffused are:

$$e_M(\mathbf{x}) = \sum_{i=1}^{N} \left(\frac{1 - \mathrm{MAC}(\boldsymbol{\phi}_{num,m}, \boldsymbol{\phi}_{exp,m})}{\mathrm{MAC}(\boldsymbol{\phi}_{num,m}, \boldsymbol{\phi}_{exp,m})} \right)^{\gamma} \tag{2.2}$$

$$e_M(\mathbf{x}) = \sum_{m=1}^{M} \frac{1}{\left\|\boldsymbol{\phi}_{exp,m}\right\|_2^2} \left\| \frac{\boldsymbol{\phi}_{exp,m}}{\left\|\boldsymbol{\phi}_{exp,m}\right\|_2} - l_m \frac{\boldsymbol{\phi}_{num,m}(\mathbf{x})}{\left\|\boldsymbol{\phi}_{num,m}(\mathbf{x})\right\|_2} \right\|_2^2 \tag{2.3}$$

where $\boldsymbol{\phi}_{exp,m}$ and $\boldsymbol{\phi}_{num,m}$ are the m-th experimental and numerical mode shapes, respectively. Common values employed for the exponent γ in Eq. (2.2) are 0.5, 1 and 2. Experimental mode shapes are defined with very low components compared to numerical mode shapes, so it is necessary to retain only the components of $\boldsymbol{\phi}_{num,i}$ corresponding to the DOFs (degrees of freedom) of $\boldsymbol{\phi}_{exp,i}$. MAC is the Modal Assurance Criterion [5] and l_m is a scaling factor computed as:

$$l_m = \frac{\boldsymbol{\phi}_{exp,m}^T \boldsymbol{\phi}_{num,m}(\mathbf{x})}{\left\|\boldsymbol{\phi}_{exp,m}\right\|_2 \left\|\boldsymbol{\phi}_{num,m}(\mathbf{x})\right\|_2} \tag{2.4}$$

The symbol $\|\cdot\|_2$ denotes the Euclidean norm.

When different kinds of residuals are used for the updating, the most common procedure, at least in the structural engineering field, involves their combination in one single objective

function through the weighted sum method [101]. The single objective function H is defined as:

$$H(\mathbf{x}) = \alpha e_F(\mathbf{x}) + (1 - \alpha) e_M(\mathbf{x}) \tag{2.5}$$

where $\alpha \in [0, 1]$ is the weighting factor that measures the relative importance between the residuals. The weighting factor represents a measure of the accuracy of the measured data at hand. It is usually chosen on the basis of engineering judgment or trial and error strategy. A review of the main approaches finalized at the weight selection will be presented in chapter 3, while in chapter 5 a Bayesian approach for weight selection will be described in detail.

2.2.2 Resolution of the single objective optimization problem

The relationship between modal properties and any kind of mechanical parameter is non-linear and usually not explicit, so an iterative optimization process must be defined. This problem can be solved with gradient-based or not gradient-based methods. Gradient-based methods require the computation of the first and the second order sensitivities of the model predictions with respect to the model parameters, collected in the Jacobian and Hessian matrix, respectively.

In this context, sensitivities can be numerically computed with the finite difference method. This approach is computationally expensive, because the number of modal analysis required to numerically compute the sensitivities grows exponentially with the number of updating parameters, and it is only locally accurate. The alternative is to express the sensitivities with exact or approximated analytical expressions. Modal sensitivities can be computed analytically through the formulas of Fox and Kapoor [64] or Nelson [121]. Difficulties, or inability in some cases, may arise when the mass and stiffness matrix are extremely large or when the FE software does not make them available to be exported. Conventional gradient-based methods have an efficient convergence rate but they may reach local minima, depending on the starting vector adopted [170]. Moreover, they may fail or obtain low accuracy when the objective function has low sensitivities to parameter variation close to the solution point [66].

On the other hand, non gradient-based methods, like genetic or evolutionary algorithms, that carry out a global search, are very robust and the starting point has a low influence on the optimization results. The main disadvantage is related to the high number of objective function evaluations required to reach convergence. Indeed, they perform a probabilistic search without information about the shape of the optimization function. When complex and large FE models are adopted, the effort requested for the model creation and the analysis at each iteration may practically make the operation unfeasible. In order to reduce the computational effort, several strategies involves the approximation of the objective function with efficient models, such as Response Surface (RS) [142], high polynomial functions [119] or Kriging models [29, 57, 63].

In this work, an improved surrogate-assisted evolutionary algorithm called DE-S [169] is employed. It combines the robustness of the differential evolution (DE) algorithm with RS methodology and a proper infill sampling strategy. The architecture of the DE-S algorithm is described in section 2.3.

2.2.3 Ill-posedness, parametrization and regularization

Model updating is an inverse problem, whose characteristic is ill-posedness. A problem is well posed if its solution exist, is unique and continuously depends on the errors present in the problem formulation [165]. As concerns sensitivity-based FE model updating, the uniqueness and the stability of the solution depends on the conditioning of the Jacobian matrix. Near-rank-deficiency of the Jacobian matrix is extremely common, causing the instability of the solution with respect to small change in the data. The same drawback occurs using non gradient-based method despite it is not necessary to invert a coefficient matrix, since the global minimum of the objective function may vary significantly with small perturbations in the data. In this context, updated parameters are rarely physically meaningful.

The main cause of ill-conditioning in model updating, in fact, is the low compatibility between parametrization of the model and experimental data. For example, the modification of the same parameter in two neighboring elements of a model may have approximately the same effects on the modal properties [161]. This effect is more pronounced the finer is the discretization. In general terms, a good parametrization involves the selection of physically meaningful parameters that affect the structure response. In some model updating applications, for example finalized at the realization of reliable predictions, the number of parameters can be limited by a smart choice on the basis of the previous recommendation.

For damage detection purposes, however, the necessity to have local information with the aim to localize damage implies a more refined parametrization. The so-called over-parametrization may be avoided adopting proper strategies. The most common is based on the definition of substructures, groups of finite elements characterized by the same values of the updating parameters. The parametrization of the stiffness matrix is the following:

$$\mathbf{K}(\mathbf{x}) = \mathbf{K}_0 + \sum_{i=1}^{N_S} x_i \mathbf{K}_i \tag{2.6}$$

where N_S is the number of substructures used. The whole stiffness matrix $\mathbf{K}(\mathbf{x})$ is obtained by the sum of a matrix $\mathbf{K}_0$, independent from the updating parameter vector $\mathbf{x}$, and the matrices $\mathbf{K}_i$, representing the contributes of the substructures, scaled by the updating parameter x_i. In this case, the updating parameter has the role of multiplication factor of a specific property that is the same for all the elements of the substructure.

Other more advanced approaches involve the definition of functions describing the variation of a parameter inside a substructure [163], defined damage functions by the authors, or a two stage procedure where the parametrization is initially coarse and in the second stage it is refined in the damaged region identified in the first stage [133].

Another pure mathematical approach relies on the introduction of regularization techniques. The main concept is to modify the objective function adding a term, commonly named regularization term, that depends on the parameter variation with respect to a given value, determined on the basis of engineering assumptions, but does not depend on the experimental data involved in the calibration. This term is weighted in the objective function by a regularization parameter. This parameter has a large influence on the updating results and its selection must be made with accuracy: if the regularization parameter

is too small the problem will be still prone to ill-posedness, while if the parameter is too large the solution will have no connection with the original physical problem.

A wide literature exists about the regularization of ill-posed problems, among which the works of Tikhonov [164] and Hansen [75] are milestones. The theme of regularization in model updating has been addressed by Titurus and Friswell [165] and Ahmadian et al. [3]. They have analyzed several methods for the selection of the regularization parameter, such as the L-curve method, the generalized cross validation and the generalized singular value decomposition.

2.3 DE-S algorithm

In section 2.2.2 it has been treated the resolution of an updating problem as a single objective optimization, highlighting benefits and drawbacks associated to gradient-based or not gradient-based methods. The main disadvantage of this last class of methods, namely the high number of objective function evaluations required to find the solution, motivated the development of strategies aimed at approximating the objective function with efficient models. In this section, it will be described the optimization algorithm, named DE-S algorithm, employed for the resolution of the case studies presented in this thesis. The DE-S algorithm is an improved surrogate-assisted evolutionary algorithm, which adopts a smart strategy of sampling. It is an enhancement of the original DE algorithm [159] in terms of speed performance without neglecting the accuracy in the search of the solution. The main stages of the algorithm are briefly described in the following.

It simultaneously evaluates N_P vectors denoted as $\mathbf{x}_{i,G}$ for i=1,2,...,N_P, where G indicates the G-th generation of parameters, called population. Each vector $\mathbf{x}_{i,G}$ has dimension D and contains the parameters to be optimized during the process. The number of vectors N_P is maintained constant during the process. The layout of the algorithm is shown in the flow chart of Fig.2.1.

First, the initial population is randomly selected starting from an uniform distribution defined over the parameter space and the objective function associated to each vector is computed. Then, and at each new iteration, a subset of N_S vector is chosen in order to calibrate a quadratic response surface. If the surface is convex, the new vector, called mutant vector ($\mathbf{v}_{i,G}$) is defined as the one who minimizes the response surface. Otherwise, if the surface is concave, the classical operation of mutation is carried out, generating the mutant vectors $\mathbf{v}_{i,G}$ as linear combination of vectors of the same population. During the following operation of crossover, vector components are shuffled with the aim to obtain a grater variability, forming the so-called trial vector. The introduction of the response surface is the distinctive feature of the first enhancement of the DE algorithm, called DE-Q algorithm [170].

The peculiarity of the latest version (DE-S), that distinguishes it from the DE-Q, is the introduction of a new sampling strategy focused on the assignment of a weight w at each candidate vector. Only a limited number N_H of candidates is selected for new evaluations according to the assigned score. The resulting vector will be included in the subsequent generation only if the related objective function value is lower than the value associated to the vector of the previous generation (selection operation). The iterative procedure

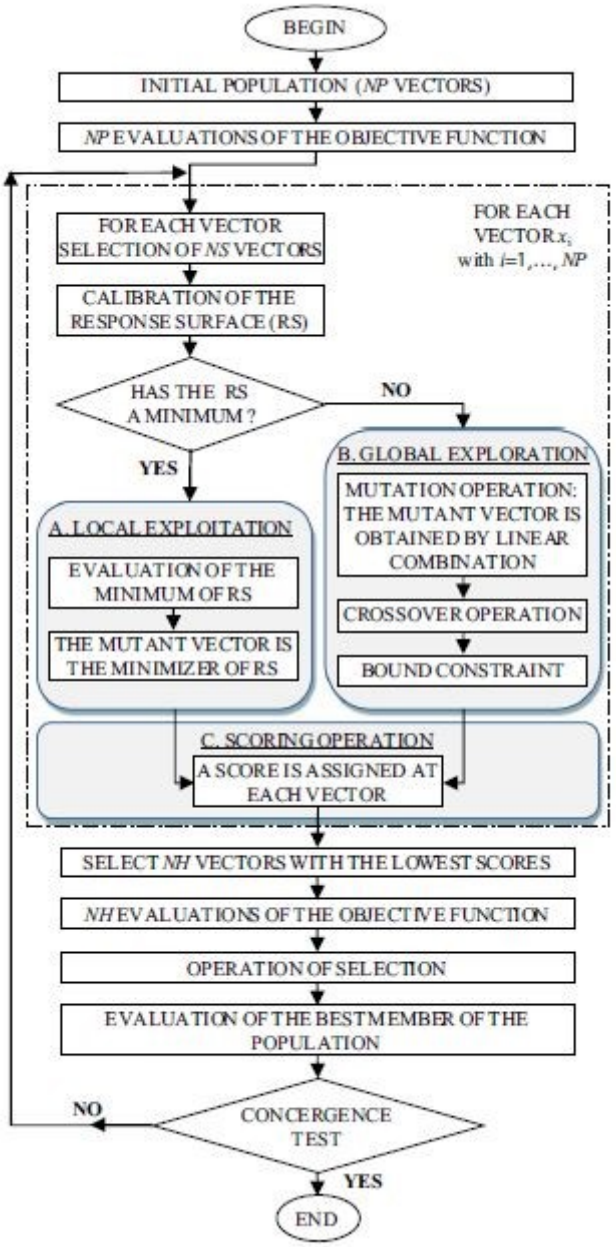

Figure 2.1: Flow chart of the DE-S algorithm [169].

ends when convergence, defined on the basis of specific criteria, is reached. The extensive description of each stage of the algorithm is addressed hereinafter.

2.3.1 Response surface (RS) method

The core concept of the RS method is the approximation of the objective function H with explicit and simpler interpolation functions. When dealing with engineering problem which involves the execution of complex codes, this method enables to alleviate the computational

effort. The objective function H is approximated with an analytic function $\hat{H}$

$$\hat{H} = g(\mathbf{x}) \tag{2.7}$$

where $\mathbf{x}$ is the vector of dimension D that contains the unknown parameters to be determined and $g(\mathbf{x})$ is the response function. The latter can be defined in different ways: commonly it is obtained combining polynomials of first and second order approximating the objective function in a set of sampling point. Second order approximations are commonly used in structural engineering problems as they provide computational efficiency together with a reasonable accuracy. Polynomials of higher order are rarely employed because the number of coefficients to be determined strongly grows with the polynomial order. Adopting a second order approximation Eq.(2.7) can be rewritten as:

$$\hat{H} = \frac{1}{2}\mathbf{x}^T\mathbf{Q}\mathbf{x} + \mathbf{L}^T\mathbf{x} + \beta_0 \tag{2.8}$$

where $\mathbf{Q}$ is a $D \times D$ matrix containing the quadratic terms, L is a $D \times 1$ vector of linear terms and β_0 a constant. According to the procedure proposed by Khuri and Cornell [100], a limited number of numerical simulations, called experiments, is used to determine an analytical relationship between the parameters to be identified and the approximated objective function. Without loss of generality, but only for reasons of simplicity, we can consider only two unknown parameters $\mathbf{x}$=$\{x_1, x_2\}$. Eq. (2.8) can be formulated as:

$$\hat{H} = \beta_0 + \beta_1 x_1 + \beta_2 x_2 + \beta_3 x_1^2 + \beta_4 x_2^2 + \beta_5 x_1 x_2 \tag{2.9}$$

where the coefficients β_i are unknown. If N_S observations, namely N_S evaluations of the approximated function starting from N_S different vectors, are available, Eq.(2.9) gives:

$$\hat{\mathbf{H}} = \mathbf{Z}\boldsymbol{\beta} \tag{2.10}$$

The vector $\boldsymbol{\beta} = \{\beta_0, \beta_1, ..., \beta_5\}$ contains the RS unknown coefficients, $\mathbf{Z}$ is the matrix of components $\mathbf{Z}_i(\mathbf{x}_i)$ which collects polynomials with constant, linear, quadratic and cross terms, and $\hat{\mathbf{H}}$ is a vector containing the objective function values computed for the vectors $\mathbf{x}_1, ..., \mathbf{x}_{N_S}$.

The number N_S of observations is generally larger than the dimension of vector $\boldsymbol{\beta}$. For this reason, the latter is obtained by applying the least square estimate method:

$$\boldsymbol{\beta} = \left(\mathbf{Z}^T\mathbf{Z}\right)^{-1}\mathbf{Z}^T\hat{\mathbf{H}} \tag{2.11}$$

Eq.(2.11) refers to the case of equal weight for all observations. A more accurate RS can be computed by increasing the weight of points close to the solution point, so having:

$$\boldsymbol{\beta} = \left(\mathbf{Z}^T\mathbf{W}\mathbf{Z}\right)^{-1}\mathbf{Z}^T\mathbf{W}\hat{\mathbf{H}} \tag{2.12}$$

where $\mathbf{W}$ is a $N_S \times N_S$ diagonal matrix of weight coefficients. Once the vector $\boldsymbol{\beta}$ is calculated, the optimal vector that minimize $\hat{H}$ is easily found as:

$$\mathbf{x}^* = -\mathbf{Q}^{-1}\mathbf{L} \tag{2.13}$$

A detailed description of sampling strategies for the RS method, necessary in order to obtain a response function representing the objective function to minimize as well as possible,

is provided by Khuri e Cornell [100]. A quadratic RS can identify a single minimum even when the objective function presents multiple local minima. Hence, in the DE-S algorithm RS method is employed as surrogate model in the mutation operation. Once the RS coefficients β_i are calculated (Eq. (2.11) or Eq. (2.12)), the shape of the RS function is checked, and two possibilities may occur. If the function is convex, the new parameter vector is defined as the one minimizing the RS surface through Eq. (2.13). Otherwise, the classical mutation operation is performed.

2.3.2 Mutation operation

For each vector $\mathbf{x}_{i,G}$ of the G-th population, the mutant vector is obtained by summing to $\mathbf{x}_{i,G}$ the weighted difference between other two vectors of the same population. Three different strategies, called "random", "best" and "best-to-rand", can be chosen. The random strategy generates the mutant vector based on the following expression:

$$\mathbf{v}_{i,G+1} = \mathbf{x}_{q_1,G} + F(\mathbf{x}_{q_2,G} - \mathbf{x}_{q_3,G}) \tag{2.14}$$

where indexes $q_1, q_2, q_3 \in \{1, 2, ..., N_P\}$ are selected in a random way provided that there they is not the repetition of the same index and F is a positive constant, defined scale parameter, controlling the amplitude of the mutation. In all the applications presented F takes the value of 0.6.

In the "best" strategy the mutant vector is always generated starting from the best member of the previous population, called $\mathbf{x}_{best,G}$, on the basis of the expression:

$$\mathbf{v}_{i,G+1} = \mathbf{x}_{best,G} + F(\mathbf{x}_{q_1,G} - \mathbf{x}_{q_2,G}) \tag{2.15}$$

Finally, in the "best-to-rand" strategy the mutant vector is generated as:

$$\mathbf{v}_{i,G+1} = \mathbf{x}_{i,G} + F(\mathbf{x}_{q_1,G} - \mathbf{x}_{q_2,G}) + F(\mathbf{x}_{best,G} - \mathbf{x}_{i,G}) \tag{2.16}$$

combining both randomly selected vectors and vectors selected according to the best member of the G-th population.

The efficiency of a strategy depends on the type of problem, specifically on the regularity of the objective function. For regular functions, characterized by the presence of a single minimum, the "best" strategy converges more quickly than the others, since the subsequent populations are completely generated from the point having the minimum value of the objective function. When the objective function has local minima or it has a low sensitivity with respect to the parameters, "random" and "best-to-rand" strategies are recommended because they avoid the convergence towards local minima.

2.3.3 Crossover operation

The crossover operation is introduced in order to increase the variability of vectors composing a population. The trial vector $\mathbf{u}_{i,G+1}$ is obtained by shuffling in a random way the components of the mutant vector $\mathbf{v}_{i,G+1}$ with those of the original vector, according to the rule:

$$\mathbf{u}_{i,G+1} = \{u_{1i,G+1}, u_{2i,G+1}, ..., u_{Di,G+1}\} \tag{2.17}$$

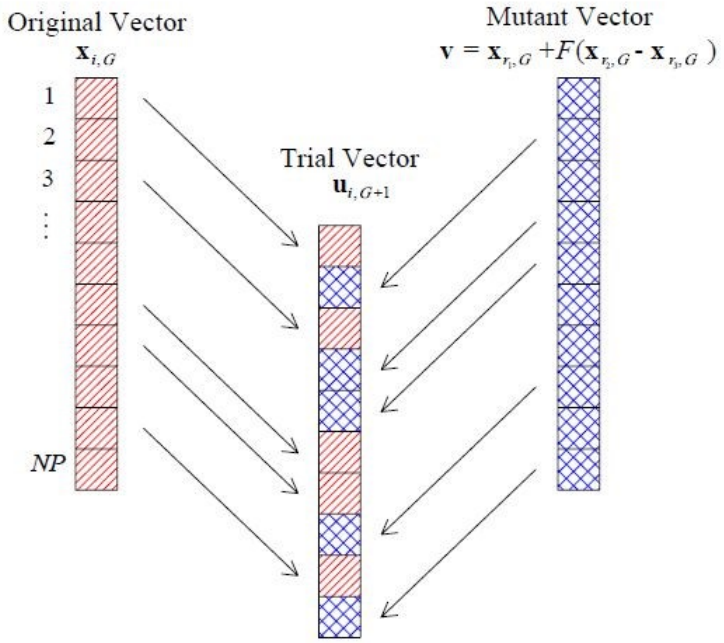

Figure 2.2: Crossover operation [167].

$$u_{ji,G+1} = \begin{cases} v_{ji,G+1} & \text{if} \quad \text{rand}(j) \leq CR \\ x_{ji,G} & \text{if} \quad \text{rand}(j) > CR \end{cases} \tag{2.18}$$

Crossover operation is schematically represented in Fig.2.2. In Eq. (2.18) u_{ji} is the $j-th$ component of the vector $\mathbf{u}_i$, with $j = 1, 2, ..., D$. rand(j) is a random number extracted from a uniform distribution defined in the interval [0; 1] and CR, called crossover constant, indicates the percentage of mutations considered in the trial vector. In all the applications presented we set CR equal to 0.5.

2.3.4 Bound constraint

In engineering problems, the search of the parameters to be optimized is commonly significant inside a specific interval of values which can be defined with physical considerations

$$x_j \in [x_{j,\min};\, x_{j,\max}] \tag{2.19}$$

Different method can be used to introduce constraint over parameters. In this algorithm, vectors that are located outside the parameter domain due to the mutation operation are projected onto the bound of this domain (see Fig. 2.3).

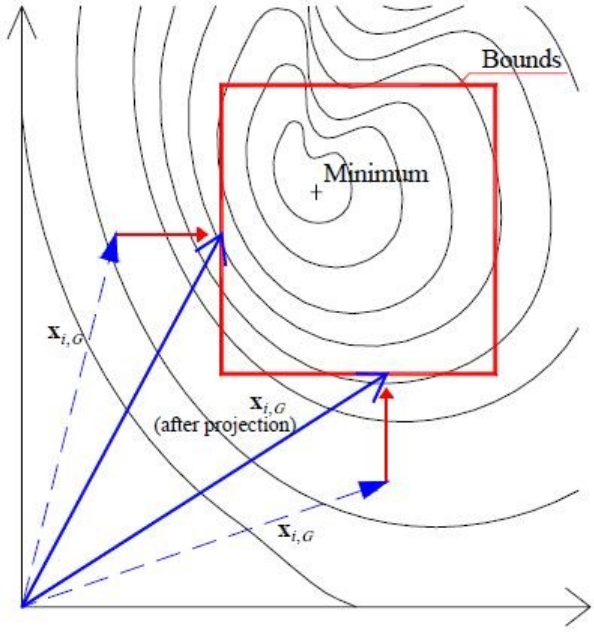

Figure 2.3: Projection of vectors onto the bound of the parameter domain [167].

2.3.5 Sampling strategy

The improvement that characterizes the DE-S algorithm relies on a proper sampling strategy finalized to create an efficient set of sampling points and to evaluate only a given subset of it. In this way, the number of objective function evaluations is reduced but, at the same time, the accuracy of the solution is preserved. This strategy involves the introduction of scoring criteria that allow to select a limited number N_H of candidates to evaluate at each iteration. N_H is set at the beginning of the process and maintained constant during the optimization.

For each candidate $\mathbf{v}_{i,G}$ the score is defined as the weighted sum of two criteria. The first depends on the value of the objective function predicted by the surrogate, while the second depends on the distances of candidates from the points already evaluated, for which the objective function value is known. Criteria are combined in this way:

$$W(\mathbf{v}_{i,G}) = w_R V_R(\mathbf{v}_{i,G}) + w_D V_D(\mathbf{v}_{i,G}) \tag{2.20}$$

where $V_R(\mathbf{v}_{i,G})$ and $V_D(\mathbf{v}_{i,G})$ are the scores, while w_R and w_D are the weights. Candidate points with low values of W are preferred. V_R is computed on the basis of the objective function value provided by the surrogate. For the i-th candidate point $\mathbf{v}_{i,G}$, V_R is defined as:

$$V_R(\mathbf{v}_{i,G}) = 1 - \exp\left(\frac{s_f^2}{H_{\text{best}} H_{\min,s}}\right) \tag{2.21}$$

where s_f is the minimum of the quadratic approximation $\hat{H}$, H_{best} is the best value of the objective function at the current iteration and $H_{\min,s}$ is the minimum value of the function

considering only the N_S points selected for the calibration of the response surface. The lower is the predicted value s_f compared to the global or local optimum, the lower is the score V_R and the whole score W, hence the candidate will be preferred.

The score V_D derives from distances of candidate points from the n points for which the objective function has been already evaluated, starting from the beginning of the optimization until the previous generation $G-1$. For this reason, a database of all the considered points, including both coordinates and the associated objective function value, is created. For the i-th candidate $\mathbf{v}_{i,G}$, first the Euclidean distance $d(\mathbf{v}_{i,G}, \mathbf{x}_{p,G})$ from a generic point $\mathbf{x}_{p,G}$ is computed. The score V_D is defined as:

$$V_D(\mathbf{v}_{i,G}) = 1 - \frac{\Delta_{\min}}{\Delta_{\max}} \tag{2.22}$$

where $\Delta_{\min}$ and $\Delta_{\max}$ are the minimum and maximum weighted distance $D(\mathbf{v}_{i,G}, \mathbf{x}_{p,G})$, respectively, whose expression is:

$$\Delta_{\min} = \min_{p=1,\dots,n} D(\mathbf{v}_{i,G}, \mathbf{x}_{p,G}) \tag{2.23}$$

$$\Delta_{\max} = \max_{p=1,\dots,n} D(\mathbf{v}_{i,G}, \mathbf{x}_{p,G}) \tag{2.24}$$

Two different formulations for the weighted distance have been proposed. The first one defines it equal to the Euclidean distance:

$$D(\mathbf{v}_{i,G}, \mathbf{x}_{p,G}) = d(\mathbf{v}_{i,G}, \mathbf{x}_{p,G}) \tag{2.25}$$

Alternatively, it can be defined also considering the objective function value:

$$D(\mathbf{v}_{i,G}, \mathbf{x}_{p,G}) = d(\mathbf{v}_{i,G}, \mathbf{x}_{p,G}) \sqrt{\frac{H_{\text{best}}}{H(\mathbf{x}_{p,G})}} \tag{2.26}$$

H_{best} has already been defined in Eq. (2.21) and $H(\mathbf{x}_{p,G})$ is the evaluation for the p-th vector $\mathbf{x}_{p,G}$. Preferred candidates are located far from the points already evaluated or in an intermediate location. Consequently, it may be correct to select a point situated in an unexplored region of the domain. Furthermore, if the formulation (2.26) is adopted, the score V_D increase if the candidate is close to a point with high value of the objective function. On the other hand, if the point is far from points with a high objective function value, the score V_D as well as the whole score W decreases.

The weights w_R and w_D are chosen in the range [0; 1] provided that $w_R + w_D$=1. If w_D approaches 1, the global search has more influence than the local one, so candidates located in an unexplored region of the parameter domain are preferred. Conversely, if the value of w_R is high, the local search is emphasized and preferred points have a low estimated value of the objective function.

In this algorithm two different sets of weights are employed based on the convexity of the response function. In case A (surrogate has a minimum and the minimizer of the response function is the candidate for the subsequent generation) could be appropriate to investigate

the region close to the optimal value predicted by the surrogate, so performing a local search. A large value has to be assigned to the criterion based on the value predicted by the surrogate ($w_{R,A} \geq w_{D,A}$). The author set the weight value as $w_{R,A}$=2/3 and $w_{D,A}$=1/3 on the basis of the study conducted by Vincenzi and Gambarelli [169]. In case B (search performed by the surrogate fails) global exploration of the domain is preferred and only the distance criterion is maintained. Weights are fixed as $w_{R,B}$=0 and $w_{D,B}$=1.

2.3.6 Selection operation

Each vector $\mathbf{u}_i$ of the G+1-th generation is compared to the vector $\mathbf{x}_{i,G}$ of the previous generation. $\mathbf{u}_{i,G+1}$ will be part of the new population if the associated objective function value is lower than the value of H associated to $\mathbf{x}_{i,G}$. In this case, $\mathbf{u}_{i,G+1}$ substitutes $\mathbf{x}_{i,G}$, otherwise $\mathbf{x}_{i,G}$ remains member of the subsequent population. The selection operation is analytically defined by the rule:

$$\mathbf{x}_{i,G+1} = \begin{cases} \mathbf{u}_{i,G+1} & \text{if} \quad H(\mathbf{u}_{i,G+1}) < H(\mathbf{x}_{i,G}) \\ \mathbf{x}_{i,G} & \text{if} \quad H(\mathbf{u}_{i,G+1}) \geq H(\mathbf{x}_{i,G}) \end{cases} \tag{2.27}$$

with i=1,2,...,N_P.

2.3.7 Convergence criteria

The first operation needed to evaluate if convergence is reached involves the ordering of the vectors belonging to the G+1-th population on the basis of their objective function value, following the relationship:

$$\tilde{\mathbf{x}}_{1,G+1} \prec \tilde{\mathbf{x}}_{2,G+1} \prec ... \prec \tilde{\mathbf{x}}_{NP,G+1} \tag{2.28}$$

such that

$$H\left(\tilde{\mathbf{x}}_{1,G+1}\right) < H\left(\tilde{\mathbf{x}}_{2,G+1}\right) < ... < H\left(\tilde{\mathbf{x}}_{NP,G+1}\right) \tag{2.29}$$

Convergence is reached when two conditions for the first N_C vectors are simultaneously satisfied:

- the relative difference among the objective function values associated to the first N_C vectors is lower than a predefined constant (VTR_1);
- the relative distance among the same N_C vectors is lower than a second constant (VTR_2).

These conditions are analytically expressed as:

$$\Delta_i^H = \frac{\left|H\left(\tilde{\mathbf{x}}_{i,G+1}\right) - H\left(\tilde{\mathbf{x}}_{i+1,G+1}\right)\right|}{\left|H\left(\tilde{\mathbf{x}}_{i,G+1}\right)\right|} < VTR_1 \tag{2.30}$$

$$\Delta_{ij}^x = \frac{\left\|\tilde{\mathbf{x}}_{i,G+1} - \tilde{\mathbf{x}}_{i+1,G+1}\right\|}{\left\|\tilde{\mathbf{x}}_{i,G+1}\right\|} < VTR_2 \tag{2.31}$$

The only check of the objective function value is not always sufficient, like in the case where the objective function has small values of the gradient in the vicinity of the solution. For this reason, convergence is deemed to be reached when also the distances among the first N_C vectors are sufficiently small. Constants VTR_1 and VTR_2 values are chosen according to the complexity of the problem under consideration, namely the number of updating parameters and the extension of the FE model. The number N_C of vectors considered is set to 4 for all the applications.

2.4 The San Prospero bell tower

In this section an example of FE model calibration is provided in order to show the whole procedure of updating, to test the DE-S algorithm introduced in section 2.3 and to validate its results by means of hand-operated computations. The structure under consideration is the San Prospero bell tower. The updating of its FE model is based on the weighted sum of frequency and mode shape residuals (Eq. (2.5)) for a given value of the weighting factor, determined according to engineering judgment.

2.4.1 Description of the case study

The case study is represented by a bell tower located in Saint Prospero Square (Reggio Emilia, Italy) next to the Basilica of Saint Prospero, an architectural evidence of baroque style. The tower, characterized by an octagonal plan, dates back to the 1571 and lies on the right side of the church façade (see Fig.2.4(a)).

The tower of Saint Prospero shows some constructive peculiarities. The masonry is composed of two layers: the inner part, made up of brick and mortar with maximum thickness of about 1.30 m, and a stone coating that encases the brick inner part and varies in thickness between 0.08 m and 0.24 m. Problems were reported by historians about marble covering and stones supplied from the nearby central Apennines and the combined use of bricks and living stones for the structural walls. Moreover, the use of inhomogeneous recycled material was also discovered in the lower part of the structure. Finally, some concentrations of vertical load on the relatively thin stone coating and the discontinuity of materials could be critical in the event of earthquakes with possible detaching phenomena or breaks. Internally, two octagonal vaulted rooms are found (see Fig.2.4(b)). At the top of the tower, the third room constitutes the bell cell, where five bronze bells are mounted on a contemporary wooden castle, of the same age as the bells (Fig.2.4(c)). The five bells, characterized by a weight ranging from 2.4 tons to 0.2 tons and major diameter between 1.5 m and 0.6 m, were established in 1796. Atmospheric and seismic events have caused damage to the masonry tower across the centuries. Due to this damage, the sound of bells was interrupted in 1822 to avoid further failures. Two main restorations were carried out in 1840 and later in 1977. The latter constitutes a complete restoration works, involving both the structures and the stone façades. Despite this, in the recent years some detachments from the sandstone coating have been reported and, following such events, a technical committee for the restoration has been nominated.

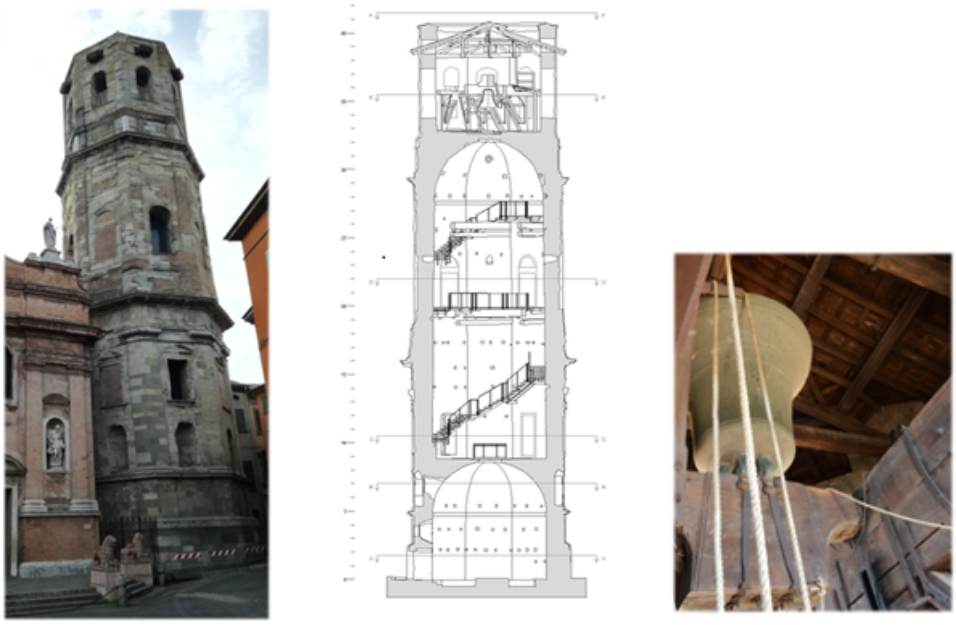

(a) (b) (c)

Figure 2.4: The Tower of Saint Prospero in Reggio Emilia (Northern Italy): (a) picture of the tower from the adjacent square, (b) internal geometry of the bell tower and (c) picture of the major bell in its upside-down position during the traditional "suonata distesa".

2.4.2 Ambient vibration test

The ambient vibration testing was carried out in July 2018 by measuring the structural response of the tower in operational conditions, from which the modal properties of the tower are estimated. Dynamic tests were performed adopting two types of accelerometer-based acquisition systems: one relied on piezoelectric accelerometers and the other one built on micro electro-mechanical systems (MEMS) technology. The first dynamic acquisition system is composed of 12 uniaxial piezoelectric accelerometers PCB/393B12 with a dynamic range of ± 0.5 g (where g denotes the gravity acceleration), a bandwidth ranging from 0.15 to 1000 Hz and a resolution of 8 μg. The accelerometers are connected to a National Instruments acquisition system for data storage and management. The main feature of this system is the high signal-to-noise ratio, which allows for a clear acquisition of the structural response in operational conditions even when the excitation is low. On the other hand, the analogic data transmission is very sensitive to external disturbance. The MEMS-based acquisition system (SHM602, Teleco SpA manufacturing) is composed a control and storage unit and six digital bus-connected sensing units, assuring a high degree of reliability and prevention against electromagnetic interferences. Each sensing unit can record the accelerations along two orthogonal axes as well as the temperature while the sampling frequency can be chosen in the range 20-80 Hz. Thanks to local digital filtering techniques and oversampling rates implemented, these units relied on MEMS sensors can exhibit a noise floor of about 0.3-0.5 mg [73, 12]. Moreover, the possibility of performing some system analyses directly on-board of the sensors allows transmitting only the processed synthetic data to the main computer. The main drawback of this system lies in the

limited frequency range, not suitable for very stiff structures. The higher dynamic range associated to the low noise floor value makes the MEMS-based system a suitable tool for the monitoring of tower accelerations during the bell concert. On the contrary, due to the high signal-to-noise ratio of the piezoelectric accelerometers, the dynamic identification in operational conditions is performed with reference to the accelerations measured from the piezoelectric system.

The dynamic response of the tower is recorded simultaneously in seven points belonging to five levels (L1-L5 in Fig. 2.5). In each measuring point (except for those at levels L1 and L5), two uniaxial piezoelectric sensors and a biaxial MEMS accelerometer are placed in order to compare the accelerations acquired from the two measuring systems and to measure valuable information in the measurement conditions. Level L1 is monitored using only piezoelectric accelerometers (Fig. 2.6(a)), while the accelerometer M6 is placed on a beam of the wooden frame that supports the bells (Fig. 2.6(e)). A total of 12 piezoelectric accelerometers (A1-A12 in Fig. 2.6) and 6 MEMS accelerometers (M1-M6 in Fig. 2.6) are employed. Except for the accelerometer M6, the others are installed on the inner walls by means of metal plates and screws, as shown in Fig. 2.7. The layout of the accelerometers has not been designed only to identify the main natural modes, but also to compare the performances of the MEMS-based and the piezoelectric accelerometers and to measure the structural response during a traditional concert of bells. Results of the comparison between MEMS and piezoelectric accelerometers, which are not of interest for this thesis, can be found in [35]. As far as the modal identification is concerned, the first two bending (both in X and Y directions) and torsional modes could be identified thanks to the sensors placed at levels L2 and L4 only. Sensors at levels L1 and L3 allow for a more accurate definition of the tower deformation during the bell concert while the sensor M6 is placed at level L5 to evaluate the displacements of the wooden frame supporting the bells. The sampling frequency is set to 200 Hz and 80 Hz for the piezoelectric and the MEMS accelerometers, respectively. Starting from the acquired accelerations, the modal identification is performed through the enhanced frequency domain decomposition (EFDD) method [139, 28]. The EFDD method is based on a singular value decomposition (SVD) of the power spectral density (PSD) matrix of the acquired accelerations. The j-th natural frequency is identified from the peak of the PSD graph while the singular vector of the PSD matrix and the corresponding singular value represent, respectively, the j-th mode shape and the amplification factor.

The identification procedure allows for a clear identification of the six natural modes listed in Table 2.1, characterized by natural frequencies ranging from 1.38 Hz to 9.80 Hz. Fig. 2.8 shows a 3D representation of the corresponding mode shapes. The first bending modes in Y (Fig. 2.8(a)) and X (Fig. 2.8(b)) direction are both identified at frequencies of about 1.4 Hz, due to the symmetry of stiffness in the two directions. However, because of the walkway connecting the tower to the adjacent church, the structure is slightly stiffer in X direction than in Y direction. The third natural mode (Fig. 2.8(c)) mainly involves torsion of the tower while the fourth and fifth modes (Fig. 2.8(d) and 2.8(e)) are second bending modes in X and Y direction, respectively. Finally, the sixth mode (Fig. 2.8(f)) exhibits deformation of the horizontal cross section at the tower mid-height. In Table 2.1, this mode is referred to as "cylindrical", meaning that the cross-section gets tight in one direction and extends in the other one. This kind of deformation can be better observed from the corresponding numerical mode (Fig. 2.8(f)). A full representation of the mode

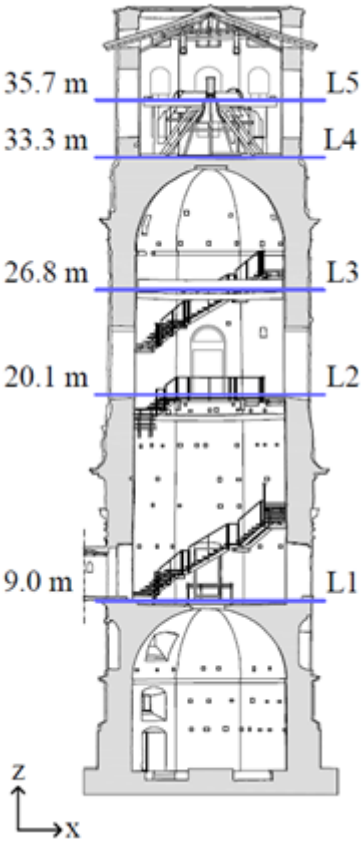

Figure 2.5: San Prospero bell tower: instrumented levels L1-L5..

Table 2.1: San Prospero bell tower: description of the experimental modes.

Mode number	Mode type	Experimental Frequency [Hz]
1	First bending - Y dir.	1.38
2	First bending - X dir.	1.44
3	Torsional	4.27
4	Second bending - X dir.	5.30
5	Second bending - Y dir.	5.36
6	Cylindrical	9.80

shapes can be found in Fig. 2.8, where the numerical mode shapes are presented.

2.4.3 FE model and calibration

A detailed FE model of the Saint Prospero bell tower (Fig. 2.9) is developed starting from a 3D geometrical model created by the Geomatics research group of the University of Modena and Reggio Emilia. Details about the creation procedure, that begins with an integrated survey combining terrestrial laser scanning (TLS) and photogrammetry by

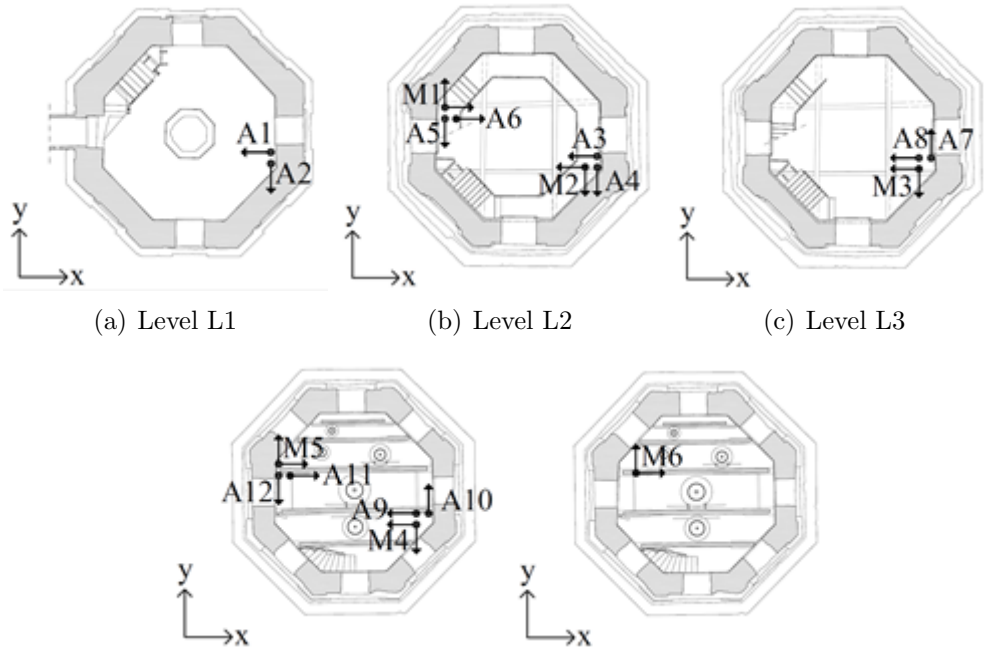

(a) Level L1 (b) Level L2 (c) Level L3

(d) Level L4 (e) Level L5

Figure 2.6: San Prospero bell tower: layout of the piezoelectric (A1-A12) and MEMS-based (M1-M6) accelerometers.

Figure 2.7: San Prospero bell tower: typical installation of piezoelectric and MEMS accelerometers.

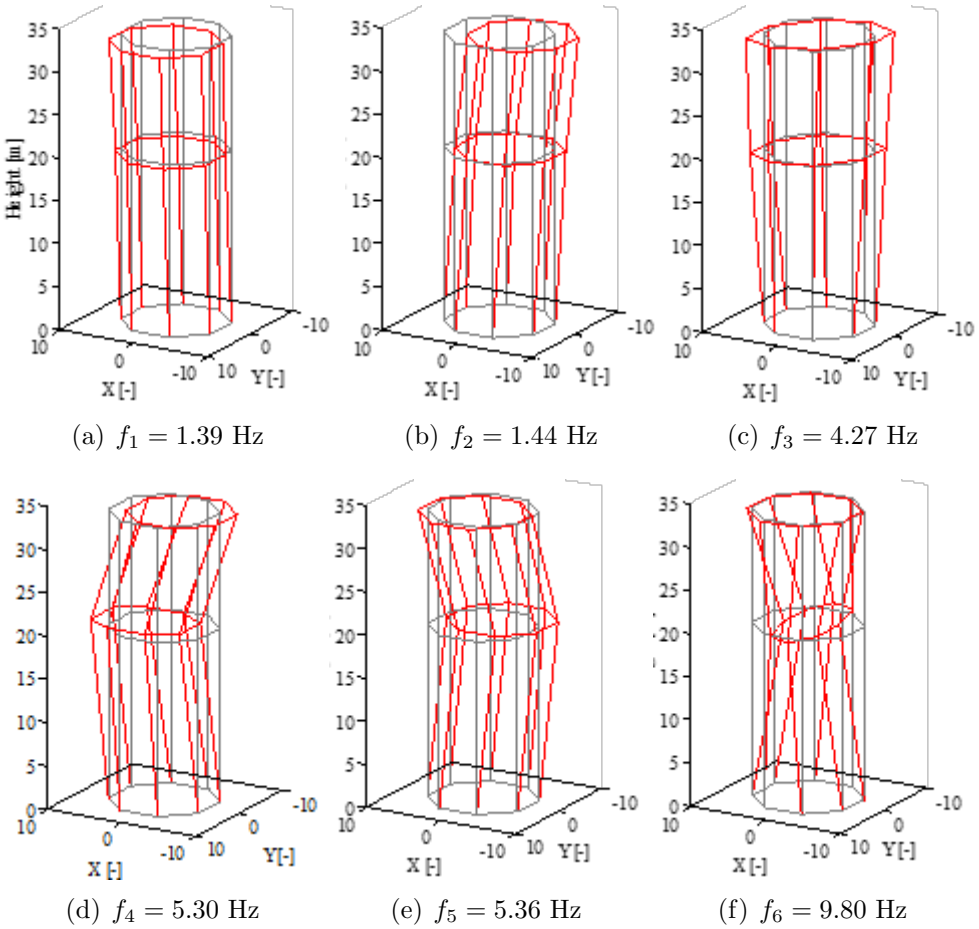

(a) $f_1 = 1.39$ Hz (b) $f_2 = 1.44$ Hz (c) $f_3 = 4.27$ Hz

(d) $f_4 = 5.30$ Hz (e) $f_5 = 5.36$ Hz (f) $f_6 = 9.80$ Hz

Figure 2.8: San Prospero bell tower: experimental mode shapes.

means of an unmanned aerial vehicle (UAV), are found in [168].

As concerns the FE model, a simplified geometrical model is first built considering forty sections of the detailed 3D model with a step size of 1 m and assuming a linear variation of the geometry between following sections. After that, openings are modeled thanks to the results of the geometrical survey. The simplified geometrical model is considered rather than the detailed model developed starting from the integrated survey, as the latter includes many architectural details which do not affect the structural behaviour but would only increase the complexity of the meshing process as well as the computational cost. The solid model is then imported in ABAQUS software and meshed using 10-node quadratic tetrahedron to properly represent the wall and the vault thickness while the wooden roof is modeled through an equivalent diaphragm highly deformable in its plane. Being the mesh generated from a solid model, it presents the same accuracy over the whole thickness of the structure. On the contrary, the mean size of the mesh changes where significant modifications in the geometry occur. The masonry walkway connecting the tower to the church is modeled in order to account for the interaction with the adjacent structures.

The tower is fixed at the ground level and at the end of the walkway. Although the walkway is fixed at the end, the effects of the interaction between the tower and the adjacent church

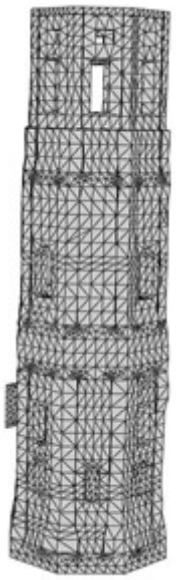

Figure 2.9: San Prospero bell tower: FE model of the structure.

are accounted for by assigning an equivalent elastic modulus to the walkway as shown in the following. For the masonry elements, a linear elastic material with density equal to 1800 kg/m^3 is adopted, while the Young's modulus and Poisson's ratio are identified through the tuning procedure described in the following. Finally, the bells are considered as concentrated mass on the tower top elements.

Thanks to the geometric survey, physical dimensions of masonry elements and floors are modeled with significant accuracy while the mechanical properties of the structural elements are affected by higher uncertainties. The FE model is calibrated so that the numerical frequencies and mode shapes of the tower agree as close as possible with the experimental ones. To this aim, a set of unknown structural parameters is evaluated from the minimization of an objective function representing the difference between numerical and experimental modal properties. The objective function is defined by Eq. (2.5), where the frequency e_F and mode shape e_M residuals are defined by Eqs. (2.1) and (2.2) with γ=1, respectively. The same weight is adopted for the two residuals.

A sensitivity analysis showed that the structural parameters mainly influencing the dynamic behaviour of the tower are the Young's modulus of the masonry walls E_M and of the walkway E_W, the Poisson's ratio of the masonry walls ν and the effective deep of the base constraint L. As concerns this last parameter, it is highlighted that although the model has been built considering the tower fixed at the ground level, the foundation of the tower consists of the tower walls that continue below the ground level. Moreover, the simplified assumption of ideal constraint at the base of a structure is rarely verified in real cases, due to a complex interaction between the structure and the surrounding elements (in this case the masonry foundation, several layers of the road stone paving placed during the centuries, the effect of the soil below the tower, etc.). The effective deep of the base constraint L represents an ideal height where the deformation and rotation of the tower can be assumed negligible. For this reason, it may be also deeper than the effective base of the tower and

Table 2.2: San Prospero bell tower: Identified structural parameters: Young's modulus of the masonry walls E_M and of the walkway E_W, Poisson's ratio ν and effective deep L.

E_M [10^6Pa]	E_W [10^6Pa]	ν [-]	L [m]
2430	255	0.43	1.55

it may not belong to the tower itself. The sensitivity of the first three numerical modes to the structural parameter L is evaluated by repeating the modal analysis considering different models characterized by a different deep of the base constraint, and, consequently, a different total height of the tower. From the results presented in Fig.2.10, it can be observed that the minimum differences between experimental and numerical frequencies are obtained for a deep L of about 1.5 m, while the mode shapes are barely affected from this parameter. The Young's modulus of the walkway E_W is chosen to represent the effects of the connection between the church and the tower. Fig. 2.11 shows that this parameter mainly influences the natural frequency of mode no.2 and the mode shape of mode no.1 and 2 when E_W is lower than about 200 MPa. The relative error of the second natural frequency is minimum when E_W is about 250 MPa. Finally, the Poisson's ratio ν is adjusted to evaluate the correct shear modulus of the masonry walls. Figure 2.12 shows that the natural frequencies of the first two modes are almost unaffected by the value of the Poisson's ratio ν while the third natural frequency is closer to the experimental one when ν is equal to about 0.4.

The first three experimentally identified modes (modes 1-3 in Table 2.1) are considered in the calibration procedure, adopting the same weights for frequency and mode shape residuals (i.e., $\alpha = 0.5$), whereas modes 4-6 are adopted for the purpose of validation of the updated FE model. Indeed, as the higher modes are often identified with less accuracy than the lower ones, minimizing the difference between experimental and numerical properties for higher modes may prevent matching the lower vibration modes. The optimization procedure is performed with the DE-S algorithm, described in section 2.3.

The identified structural parameters are listed in Table 2.2, while numerical and experimental modes are compared in Table 2.3, and the numerical mode shapes are shown in Fig. 2.13. The optimal value of the masonry elastic modulus E_M is higher than the one proposed by the Italian Codes [1] for masonry elements made of solid bricks and lime mortar, which is expected to lie in the range [1200; 1800] MPa. Indeed, the tower walls are composed of masonry elements covered by a stone layer and E_M represents the elastic modulus of an equivalent material with properties between the masonry and the stone. As far as the calibrated modes (1-3) are concerned, a large agreement between numerical and experimental modes can be observed, with frequency errors lower than 0.25%. A pretty good match can be observed also for modes 4-6, stating the goodness of fit of the calibrated model.

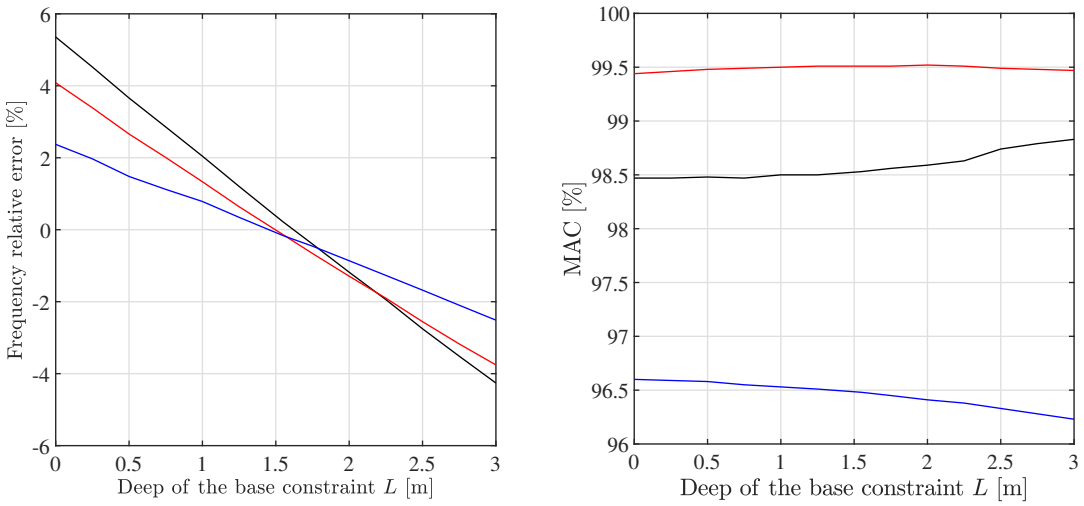

(a) (b)

Figure 2.10: San Prospero bell tower: variation of (a) the frequency relative error and (b) the MAC value with the parameter L.

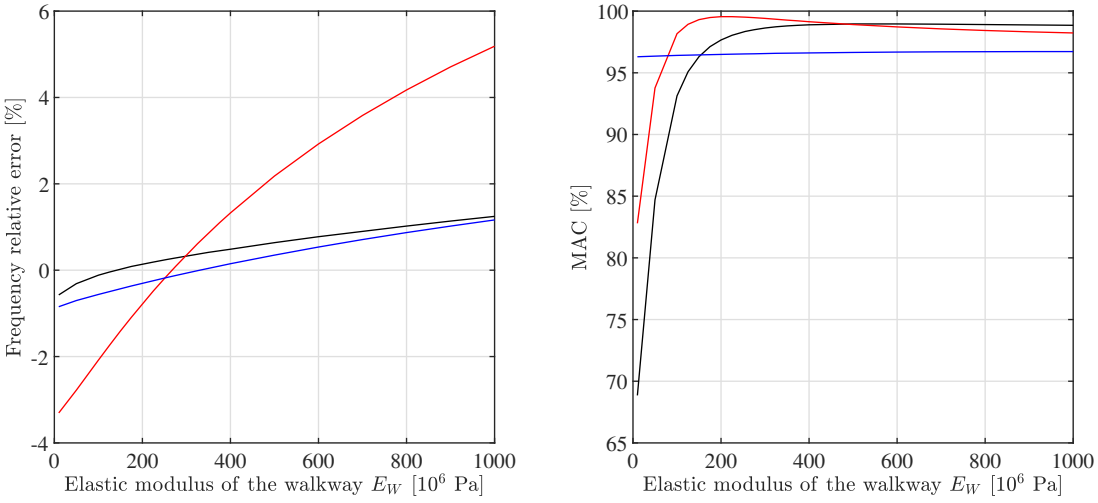

(a) (b)

Figure 2.11: San Prospero bell tower: variation of (a) the frequency relative error and (b) the MAC value with the parameter E_W.

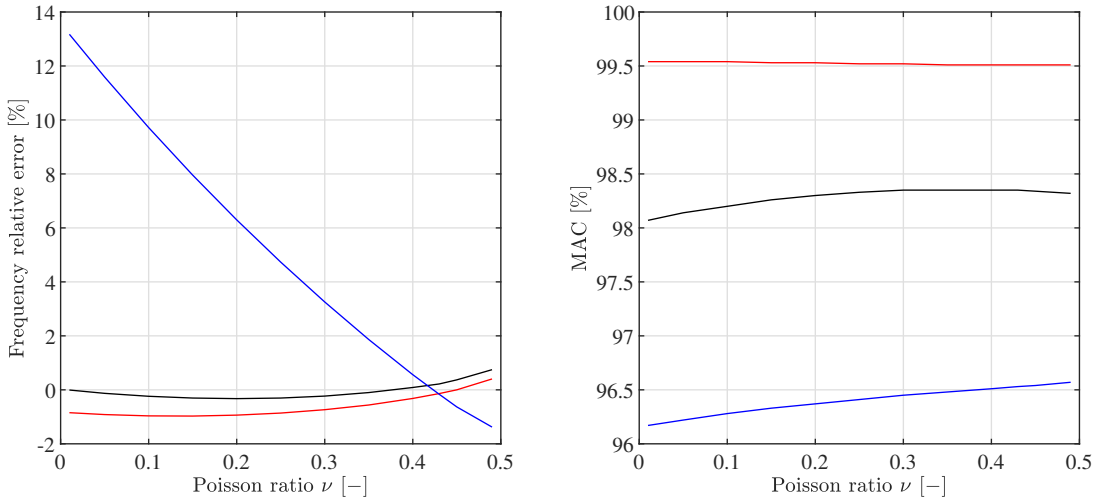

(a) (b)

Figure 2.12: San Prospero bell tower: variation of (a) the frequency relative error and (b) the MAC value with the parameter ν.

Table 2.3: San Prospero bell tower: comparison between experimental and numerical modes

Mode number	Exp. Freq. [Hz]	Num. Freq. [Hz]	Freq. Error [%]	MAC [%]
1	1.38	1.383	0.25	98
2	1.44	1.438	-0.14	100
3	4.27	4.263	-0.17	97
4	5.30	5.790	9.24	77
5	5.36	5.668	5.74	97
6	9.80	9.852	0.53	84

2.5 Concluding remarks

In this chapter, some of the main aspects related to model updating have been presented. The theme has been assessed both from the physical and the numerical point of view. About the latter, section 2.3 has been dedicated to the description of an optimization algorithm specifically developed for the calibration of FE models, named DE-S. It combines the robustness of the evolutionary algorithms with the RS methodology and a proper infill sampling strategy, that allow an improvement of the speed performance without neglecting the accuracy in the search of the solution.

An example of model updating has been provided in section 2.4, where the model of the San Felice sul Panaro bell tower is calibrated with respect to the experimental modal properties determined thanks to an ambient vibration test. In the author's opinion, the example is particularly interesting for the extension and the complexity of the FE model. Indeed,

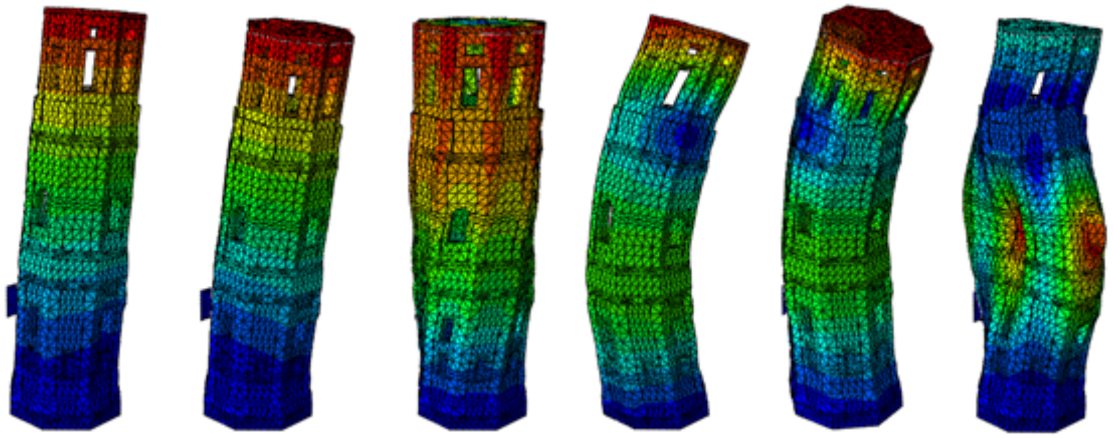

(a) Mode no.1 (b) Mode no.2 (c) Mode no.3 (d) Mode no.4 (e) Mode no.5 (f) Mode no.6

Figure 2.13: San Prospero bell tower: numerical mode shapes.

the detailed three-dimensional model has been built starting from an integrated survey combining terrestrial laser scanning and photogrammetry by means of an unmanned aerial vehicle. The calibration of the model has been performed with the DE-S algorithm and its results have been then validated by a sensitivity analysis showing the variation of the frequency error and of the MAC value with the updating parameters.

Chapter 3

Multi-objective optimization approach for model updating

The single-objective approach described in chapter 2 is traditionally the most diffused in the structural engineering context since it is easily understandable and it can be promptly solved. Furthermore, the weighting factor represents a quantitative measure of the importance of the modal properties in the optimization process. The choice of the weighting factor is a challenging problem: if it is not carried out in a proper way, unbalanced results in terms of frequency and mode shape residuals can be obtained at the end of the updating process. This is especially true when the updated parameters may vary significantly according to the chosen weighting factor.

The main approaches to the weight selection found in literature are discussed in section 3.1. The more general approach, based on the resolution of a multi-objective optimization problem and the selection of the preferred solution with specific criteria, is described in section 3.2. The robustness of the selection criteria previously introduced is assessed with specific tests, whose description is found in section 3.3. In the same section, the case studies considered for the execution of the tests are illustrated.

A direct procedure for the selection of the preferred solution is presented in section 3.4. This is developed in order to alleviate the computational effort of the classical procedure, consisting of the resolution of a multi-objective optimization problem. Finally, the direct and the classical procedure are compared in section 3.5 considering the calibration of the FE model of the San Felice sul Panaro fortress, an historical masonry structure that was severely damaged by the seismic event that occurred in 2012 in the Emilia-Romagna region.

3.1 Weight selection approaches

Different approaches to the weight selection have been proposed and a possible classification can be founded on whether the selection is carried out before the updating (a priori approach) or if it is part of the optimization process or a subsequent operation (a posteriori approach).

The possibility to fix a priori the weight value implies an obvious rapidity in the problem

resolution. The first approach of this kind involves engineering judgement for the weight selection according to the specific problem under examination. For example, the calibration of the FE model of the San Prospero bell tower, presented in section 2.4, has been performed with the same weights for both frequency and mode shape residuals. This approach may conduct to very unbalanced results if insufficient attention is paid to relative magnitude between residuals or if the variability of residuals is not well known, though. Teughels and De Roeck [162] set the mode shape weight as one tenth of the frequency weight because of the high number of mode shape residuals compared to the frequency residuals. Vincenzi and Savoia [170] set the mode shape weight equal to one hundredth of the frequency weight due to the high variability of the mode shape residuals. In this regard, the appropriate balance can be obtained with a trial-and-error approach modifying iteratively the weighting factor. Numerous runs could be needed to reach the aim and the rapidity of the method would be compromised.

The weighting factor denotes the confidence degree attributed to the measured data available. For this reason, when information about the measurement accuracy is available, weights can be taken inversely proportional to modal property standard deviation, which yields to the optimal estimate at least for linear prediction models following the Gauss-Markov theorem [14]. In practice, statistical characterization of identified modal properties is complex to compute [144] and not always available [162].

Following the interpretation of weight as a confidence measure, another rational choice is to select the weights to be inversely proportional to the values of the corresponding residual, so that a modal property with small residuals has a larger weight compared to another property with higher residuals. Since the residuals are not known before the calibration for a given weighting factor, the selection must be carried out simultaneously with the updating in a nested optimization problem, like in the procedure proposed by Christodolou et al. [42]. Finally, the more general approach involves the application of a multi-objective optimization scheme, that allows to minimize more objectives at the same time, frequency and mode shape residuals in the cases examined in this thesis. The weight selection is performed a posteriori among the multiple solutions of the multi-objective optimization problem, constituting the so-called Pareto front, which have been computed. In the following section, the relationship between weights and solutions of the front will be explored and criteria for the selection of the preferred solution introduced.

3.2 Bi-objective optimization for model updating

The framework of multi-objective optimization is described with reference to two objectives. The discussion does not loss generality and, in addition, results can be easily represented in two-dimensional plots. However, the same considerations can be drawn considering more than two objectives. The bi-objective optimization problem reads:

$$\begin{cases} \min\{e_1(\mathbf{x}), e_2(\mathbf{x})\} \\ \mathbf{x} \in \mathbf{S} \end{cases} \tag{3.1}$$

where $\mathbf{x}$ is the $n \times 1$ vector containing the calibration parameters, $\mathbf{S} \subset \mathbf{R}^n$ denotes the set of feasible solutions in the decision space and e_i is the i-th objective defined as:

$$e_i : \mathbf{S} \mapsto \mathbf{R}, i = 1, 2 \tag{3.2}$$

In problems involving experimental data the objectives are conflicting, meaning it is not possible to improve one objective without worsening the other, because of the presence of measurements and modelling errors influencing the problem resolution. Then, the resolution of the optimization problem gives rise to a set of optimal solutions forming the Pareto front, i.e., the set of feasible non-inferior solutions that are not dominated by other solutions. A generic solution $\mathbf{x}_A$ is said to dominate the solution $\mathbf{x}_B$ if the following conditions are observed:

$$\begin{cases} e_i(\mathbf{x}_A) \leq e_i(\mathbf{x}_B), & \text{for } i = 1, 2 \\ e_i(\mathbf{x}_A) < e_i(\mathbf{x}_B), & \text{for at least one index } i \end{cases} \tag{3.3}$$

Hence, a parameter vector $\mathbf{x}^*$ is a Pareto-optimal solution if there does not exist another vector that dominates $\mathbf{x}^*$ according to Eq.(3.3). A Pareto-optimal solution is a global optimum because Eq.(3.3) applies over the whole feasible set of the problem. In the case of vibration-based modal updating, the objectives e_1 and e_2 can be defined as the frequency e_F and mode shape e_M residuals. Their expression has been introduced in chapter 2 with Eq. (2.1) for e_F and Eqs. (2.2) and (2.3) as possible alternatives for e_M.

Resolution procedures for multi-objective optimization are numerous and diversified on the basis of the function and the method used to promote solution diversity. A review of the principal genetic algorithms developed for this aim is found in [103]. In this work, the weighted sum method already presented is employed to solve the multi-objective optimization problem. Defining the single objective function H as the weighted sum of frequency and mode shape residuals (Eq. (2.5)) the problem reads:

$$\begin{cases} \min H(\mathbf{x}) \\ \mathbf{x} \in \mathbf{S} \end{cases} \tag{3.4}$$

Depending on the value of the weighting factor, the optimization procedure can lead to different results because of the uncertainties affecting the measurements and the numerical model. The set of Pareto-optimal solutions can be generated solving the optimization problem for different values of the weighting factor. Although the well-known drawback related to the difficulty in the determination of a set of weights able to generate a uniform distribution of Pareto solutions, the author has decided to implement this method for its strict connection with the subject of the chapter.

Regardless of the resolution procedure, once the Pareto front is generated, a decision is still needed to find the preferred solution among the optimal solutions of the front. At the same time the weight selection is performed, given the relationship between weights and solutions. The importance of the decision is very meaningful when values of the parameters contained in the parameter vector $\mathbf{x}$ are different among the solutions that form the Pareto front. The preferred solution is selected on the basis of additional, qualitative, experience-driven and sometimes subjective, requirements. Indeed, the preferred solution cannot be

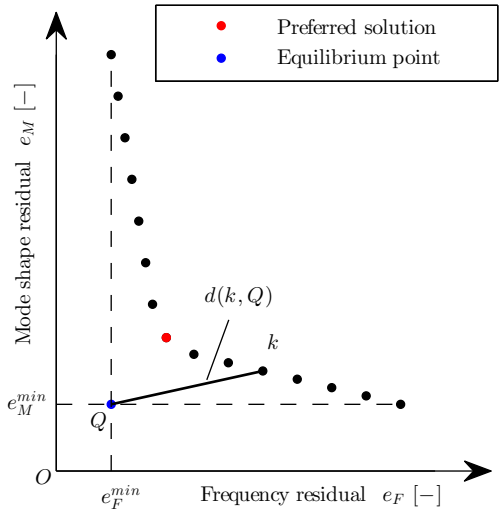

Figure 3.1: Criterion A: minimum distance from the equilibrium point.

identified as the one corresponding to the minimum value of H because different objective functions H (defined with different values of α) cannot be compared.

In the following, some criteria proposed in literature to define the preferred solution among those forming the Pareto front are described. These are the minimum distance from the equilibrium point [7, 52], the maximum bend angle [92], the fuzzy satisfying approach [113] and the maximum distance from the boundary line [49].

3.2.1 Criterion A: minimum distance from the equilibrium point

The best solution is identified as the point of the Pareto front characterized by the minimum distance from the equilibrium point Q of the objective function space (see Fig. 3.1). In this point, both objectives exhibit their optimal values independently on the other one, so its coordinates are (e_F^{min}, e_M^{min}). It is a hypothetical point that does not belong to the Pareto front. Hence, the point of the front closer to the equilibrium point ensures the best compromise between frequency and mode shape errors. The distance of a generic solution k from the equilibrium point is expressed as:

$$d(k,Q) = \sqrt{[e_F(k) - e_F^{min}]^2 + [e_M(k) - e_M^{min}]^2} \tag{3.5}$$

3.2.2 Criterion B: maximum bend angle

The best solution is identified as the point of the Pareto front characterized by the maximum bend angle. For this solution, a large sacrifice S is needed to make a small gain G moving to any other solution. The bend angle β of a generic solution k of the Pareto front depends on the slopes of the two lines connecting k with its adjacent left and right

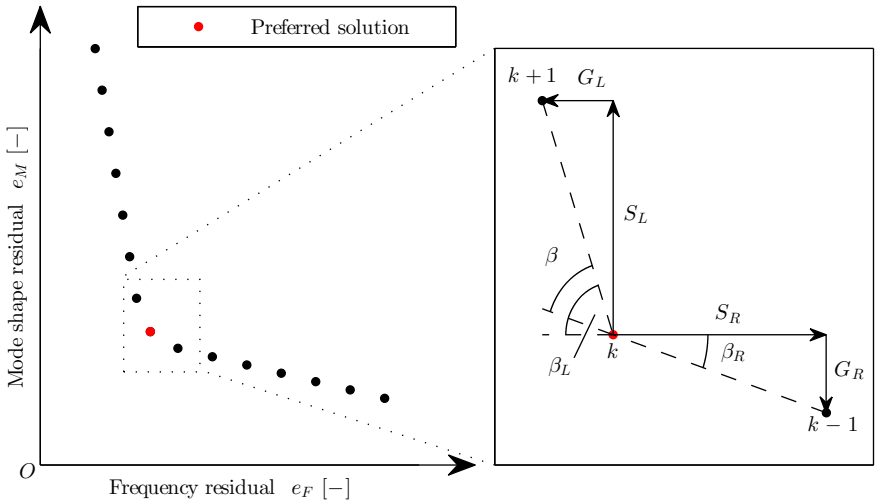

Figure 3.2: Criterion B: maximum bend angle.

neighbours (Fig. 3.2). The bend angle of the k-th solution is computed as:

$$\beta(k) = \beta_L - \beta_R \tag{3.6}$$

where:

$$\beta_L = \arctan \frac{e_M(k+1) - e_M(k)}{e_F(k) - e_F(k+1)} \tag{3.7}$$

$$\beta_R = \arctan \frac{e_M(k) - e_M(k-1)}{e_F(k-1) - e_F(k)} \tag{3.8}$$

$k+1$ and $k-1$ are respectively the left and right solution of the considered point k.

3.2.3 Criterion C: fuzzy satisfying approach

The best possible solution is the one that can provide a win-win strategy between the conflicting objective functions. First, the fuzzy membership of each objective function, that maps it to the interval [0,1], is determined. The linear membership function of e_F and e_M for the k-th solution is expressed as:

$$\Phi_{k,e_F} = \begin{cases} 1 & \text{if } e_F(k) \leq e_F^{min} \\ \frac{e_F(k) - e_F^{max}}{e_F^{min} - e_F^{max}} & \text{if } e_F^{min} \leq e_F(k) \leq e_F^{max} \\ 0 & \text{if } e_F(k) \geq e_F^{max} \end{cases} \tag{3.9}$$

$$\Phi_{k,e_M} = \begin{cases} 1 & \text{if } e_M(k) \leq e_M^{min} \\ \frac{e_M(k) - e_M^{max}}{e_M^{min} - e_M^{max}} & \text{if } e_M^{min} \leq e_M(k) \leq e_M^{max} \\ 0 & \text{if } e_M(k) \geq e_M^{max} \end{cases} \tag{3.10}$$

In Eqs.(3.9) and (3.10), e_F^{min} and e_M^{min} are the minimum values of the objective functions, while e_F^{max} and e_M^{max} are the maximum ones. Φ_{k,e_F} and Φ_{k,e_M} express how optimal the k-th solution would be for the objectives e_F and e_M, respectively. The membership function of the k-th solution is:

$$\Phi_k = \min(\Phi_{k,e_F}, \Phi_{k,e_M}) \tag{3.11}$$

The best possible solution of multi-objective optimization model is the solution with the weakest membership function.

$$\Phi^{max} = \max(\Phi_1, ..., \Phi_k, ..., \Phi_z) \tag{3.12}$$

where z is the number of points that form the Pareto front.

3.2.4 Criterion D: maximum distance from the boundary line

Given a Pareto front, the two extreme points P_1 and P_2 (Fig. 3.3) are used to construct the boundary line $L(P_1, P_2)$:

$$e_M = me_F + q \tag{3.13}$$

where:

$$m = \frac{e_M(P_2) - e_M(P_1)}{e_F(P_2) - e_F(P_1)} \tag{3.14}$$

is the slope of the boundary line, and:

$$q = e_M(P_1) - me_F(P_1) \tag{3.15}$$

is the intercept for $e_F = 0$. The best solution is identified as the point with the maximum distance from the boundary line (Fig. 3.3). The distance of the solution k from the boundary line is expressed as:

$$d(k, L) = \frac{|e_M(k) - [me_F(k) + q]|}{\sqrt{1 + m^2}} \tag{3.16}$$

3.3 Assessment of the selection criteria robustness

Three different tests are designed to evaluate the robustness of the selection criteria with respect to the variability of the optimization algorithm (test I), the choice of the weighting factor range (test II) and the definition of the objective function (test III). The optimization process is carried out adopting the DE-S algorithm (section 2.3).

This section first presents three numerical case studies specifically designed to assess the robustness of the four selection criteria described in 3.2.1, 3.2.2, 3.2.3 and 3.2.4. For each case study, a set of geometrical and mechanical parameters is defined and the modal

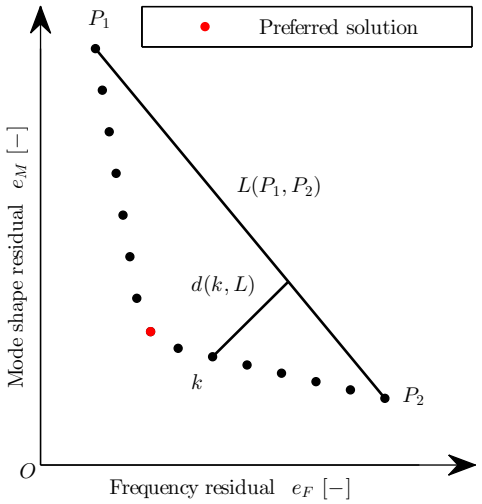

Figure 3.3: Criterion D: maximum distance from the boundary line.

Selection criterion	Description
A	Minimum distance from the equilibrium point
B	Maximum bend angle
C	Fuzzy satisfying approach
D	Maximum distance from the boundary line
Case study	**Description**
1	Plane frame with three floors and one bay
2	Simply supported beam with damage at a given location
3	3-D scale-model frame with a damaged pair of braces
Test	**Description**
I	Variability of the optimization algorithm
II	Choice of the weighting factor range
III	Different definitions of the mode shape residuals e_M

Table 3.1: Summary of selection criteria, case studies and tests.

analysis of the structure is performed to obtain the exact values of natural frequencies and mode shapes. In real applications, the optimization process is performed with reference to the experimentally identified modal properties, which unavoidably differ from the exact ones. Hence, pseudo-experimental modal properties are defined and assumed as reference values in the optimization process. These are obtained by varying up to 3.8% and 16% the exact values of natural frequencies and mode shape components, respectively.

Next, results of the three tests are illustrated. Test I and II are performed for all the case studies, while test III is performed only for case study 1 and 2. Table 3.1 presents a summary and a brief description of the different selection criteria, case studies and tests.

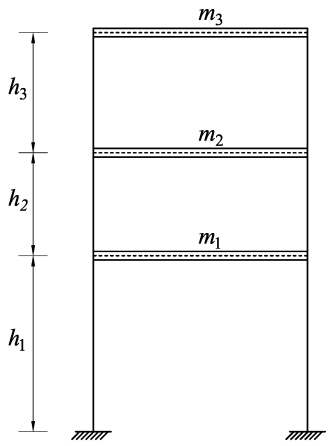

Figure 3.4: Case study 1: layout of the structure.

Floor N.	1	2	3
Height of columns h [m]	4.1	2.4	2.8
Section of columns [m^2]	0.3 x 0.45	0.3 x 0.45	0.3 x 0.45
Young's modulus E [GPa]	30	30	30
Mass m [1×10^3kg]	41.0	16.0	16.0

Table 3.2: Case study 1: geometrical and mechanical parameters.

3.3.1 Case study 1

The first case study is a shear-type plane frame composed of three floors and one bay (Fig. 3.4). The structure has three degrees of freedom (DOFs) in total, which are the horizontal displacements of the three floors. The columns are modelled as Euler-Bernoulli elements. The distributed masses of the structure are represented as concentrated masses at floor levels.

In Table 3.2, the geometrical and mechanical parameters of the structure are listed. The corresponding modal properties and the pseudo-experimental values, assumed as reference values in the optimization process, are reported in Table 3.3.

Mechanical parameters to be identified with reference to pseudo-experimental values are the mass concentrated at the first floor level m_1 and the height of the first floor h_1. The unknown parameters are searched imposing the following constraints:

$$m_1 + m_2 = 57 \cdot 10^3 \text{kg} \tag{3.17}$$

$$h_1 + h_2 = 6.5 \text{m} \tag{3.18}$$

while values of m_3 and h_3 are known values. The parameter m_1 is searched in the interval [5; 55] 10^3kg while h_1 in the interval [1.3; 4.8] m.

		Exact			Pseudo-experimental		
Mode N.		1	2	3	1	2	3
Frequency [Hz]		2.794	10.231	19.999	2.797	10.590	20.059
Mode shape component [−]	ϕ_1	0.8537	-0.5063	-0.2350	0.8023	-0.5131	-0.2102
	ϕ_2	0.9340	0.1151	1.0000	0.9639	0.1040	1.0000
	ϕ_3	1.0000	1.0000	-0.4200	1.0000	1.0000	-0.3519

Table 3.3: Case study 1: exact and pseudo-experimental modal properties. Mode shapes are normalized to their maximum entry.

Fig. 3.5 shows that the first two natural frequencies are very sensitive to variations of the structural parameters m_1 and h_1. The same goes for the third natural frequency, not presented here for the sake of brevity. The optimal values of m_1 and h_1 obtained from the minimization of the objective function H (defined in Eq.(2.5)) for different values of the weighting factor α are presented in Fig. 3.6. The identified parameters show small variations with the weighting factor α. Indeed, variations of m_1 and h_1 produce significant variations in the natural frequencies and consequently increasing values of the frequency residuals e_F, while the mode shape residuals e_M remain almost the same (not presented here). This causes increasing values of the objective function H, implying that the optimal values of m_1 and h_1 are almost the same independently on the weighting factor α.

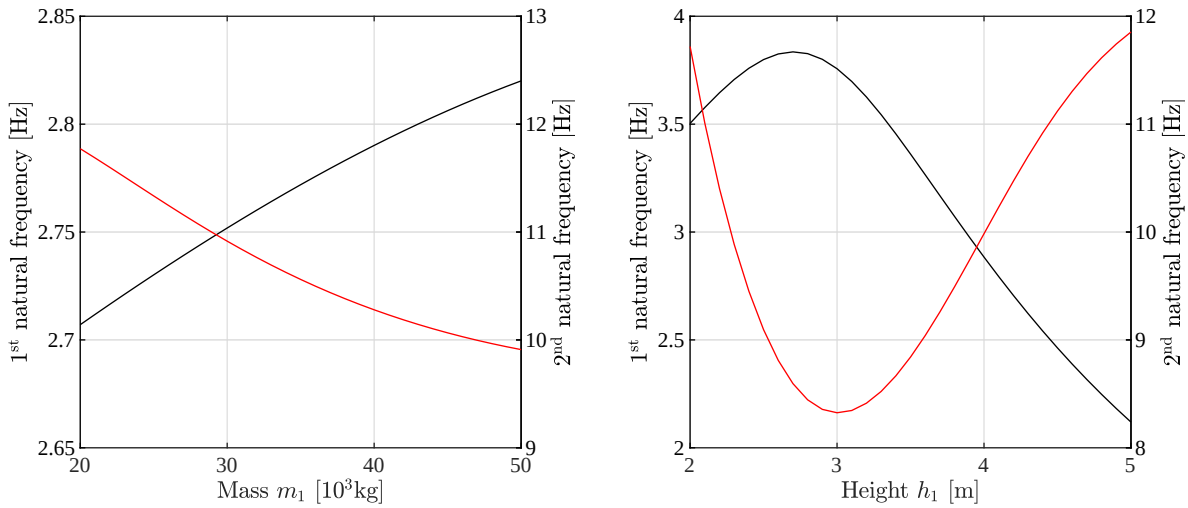

(a) (b)

Figure 3.5: Case study 1: trend of the first (black line) and second (red line) natural frequency with the structural parameter (a) m_1 and (b) h_1.

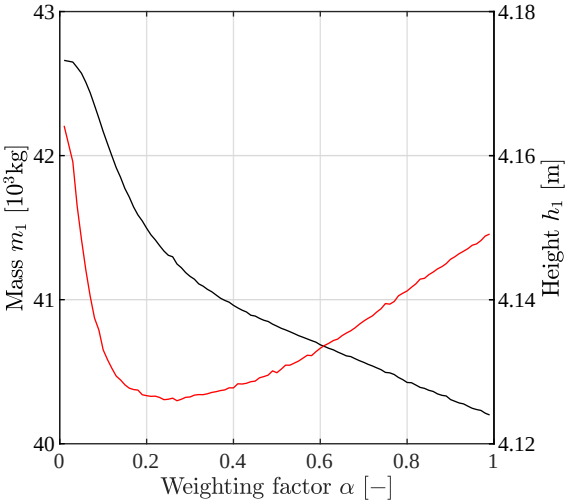

Figure 3.6: Case study 1: trend of the structural parameter m_1 (black line) and h_1 (red line) with the weighting factor α.

3.3.2 Case study 2

The second case study is a simply supported beam that presents damage at a given location. The beam is discretized in an high number of elements that are 0.1 m length and the damage is located at a distance y_d from the left end, as highlighted in Fig. 3.7. The elements are Eulero-Bernoulli 2-node plane beams where each node has vertical displacement and in-plane rotation as DOFs. Mass is concentrated at nodes obtaining a lumped mass matrix.

The presence of cracks in a structural member introduces local flexibilities, so modifying its dynamic behaviour. The changes of dynamic characteristics (frequencies and mode shapes) can be measured and subsequently used for damage detection. With the assumption that the crack in a structural element is open and remains open during the vibrations, the damage can be simulated by the reduction of the elastic modulus of the damaged element. The linear elastic cracked beam model is a very simplified theoretical case-study, the dynamic behaviour of a cracked beam being usually heavy non-linear, varying also in positive and negative bending oscillations. Nevertheless, even if simpler than real cases, this benchmark is of interest because it shows the impact of the weighting factor on the results and proves the importance of expressively accounting for mode shapes in the objective function. Therefore, and differently from the first example, a multi-objective optimization is required to identify the damage in the beam.

Table 3.4 sums up the values of the geometrical and mechanical parameters of the structure. The corresponding modal properties and the pseudo-experimental properties, assumed as reference values in the optimization process, are reported in Table 3.5. As regards mode shapes, only displacements of nodes located every 0.5 meters from the left support are considered in the updating process, hence only these one are reported in Table 3.5. In Table 3.5, ϕ_1,...ϕ_8 indicate the mode shape components measured in point $1-8$ of Fig. 3.7.

The mechanical parameters to be identified are the reduction factor r_d and the position of

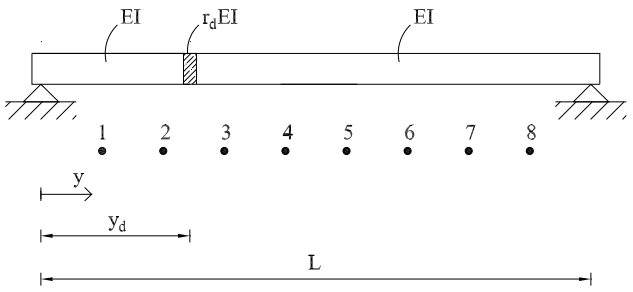

Figure 3.7: Case study 2: layout of the structure.

Total length L [m]	4.5
Dimension of the cross section [m^2]	0.3 x 0.4
Undamaged elastic modulus E_{und} [GPa]	30
Reduction factor r_d [-]	0.2
Position of the damage y_d [m]	1.25
Mass density ρ [kg/m^3]	2500

Table 3.4: Case study 2: geometrical and mechanical parameters.

		Exact		Pseudo-experimental	
Mode N.		1	2	1	2
Frequency [Hz]		29.5075	115.3368	30.6412	118.9535
Mode shape comp. [−]	ϕ_1	0.3649	0.6219	0.3368	0.5923
	ϕ_2	0.6914	1.0000	0.6401	0.9205
	ϕ_3	0.9114	0.8583	0.8766	0.8436
	ϕ_4	1.0000	0.2614	1.0000	0.3641
	ϕ_5	0.9795	-0.4138	0.9666	-0.3538
	ϕ_6	0.8504	-0.8902	0.8329	-0.8846
	ϕ_7	0.6263	-0.9692	0.6093	-1.0000
	ϕ_8	0.3318	-0.6210	0.3213	-0.6487

Table 3.5: Case study 2: exact and pseudo-experimental modal properties. Mode shapes are normalized to their maximum entry.

the damaged element y_d. r_d is searched in the interval [0.01; 1.50] while y_d in the interval [0.05; 4.45] m.

The trend of the first two natural frequencies with the calibration parameters r_d and y_d is shown in Fig. 3.8. In this case, natural frequencies are very sensitive to values of the reduction factor r_d in the range [0; 0.25], while for values larger than 0.25 the variation is less pronounced. Also the position of the damaged element y_d affects the first two frequencies. It is possible to observe that values of both frequencies are the same for symmetrical positions of the damaged element with respect to mid-span (in this example the first for y_d and the second for $L-y_d$). As a matter of fact, in the perfect (exact) identification problem, if only the natural frequencies are selected in the definition of the objective function H (for instance after paired the correct experimental and numerical natural frequencies by the Modal Assurance Criterion), two minima with the same objective function value would be found. Therefore, the identification of the correct damage location is not possible. In the case of experimental data, one of the two optima is slighting preferred, depending on the errors between the experimental and numerical natural frequencies. As depicted in Fig. 3.9, this case study shows a large variation of the optimal position y_d with the weighting factor α, while the optimal value of the reduction factor r_d is less sensitive to α. In particular, when α is larger than 0.58, the identified value of y_d is very different from the exact (expected) value. This is due to the negligible contribution of the mode shapes to the objective function H. On the other hand, when α is lower than 0.58, the predominant contribution of mode shapes ensure that the optimal parameter is close to the expected value.

In Fig 3.10 contour plots of the objective function H for 3 values of the weighting factor α are shown. For $\alpha = 0.15$ the global minimum is easily recognizable (see Fig. 3.10(a)). When α moves toward 0.58 the values of H corresponding the two minima are very close, as reported in Fig. 3.10(b) for $\alpha = 0.55$, but the global minimum is still in the same area of the case with $\alpha = 0.15$. For values of α larger than 0.58, the global minimum moves close to the right end (Fig. 3.10(c)) and the identification of the correct damage position fails.

3.3.3 Case study 3

The third case study is a steel braced frame, employed as benchmark problem for Structural Health Monitoring (SHM) purposes by the IASC-ASCE SHM Task Group in the early 2000s [56, 55]. The structure has four stories with an overall height of 3.6 m and a 2-bay by 2-bay plan of dimension 2.5 m $\times$ 2.5 m. The structural elements are composed of columns, floor beams and braces, while each floor is composed of four slabs, one for each bay. Fig.3.11 shows the schematic front view of a generic structure side. It remains the same for all the four sides except for the column orientation. The latter is presented in the schematic plan view of the first floor (Fig.3.12), where it is also highlighted the numeration of the braces. Further details about the properties of the structural element sections, that are unusual because they have been designed for a scale model, and the values of the floor masses can be found in [93].

The modal properties of the frame are generated by using a FE model with 12 DOFs in total. Each floor moves as rigid body with three DOFs, the translations u and v along

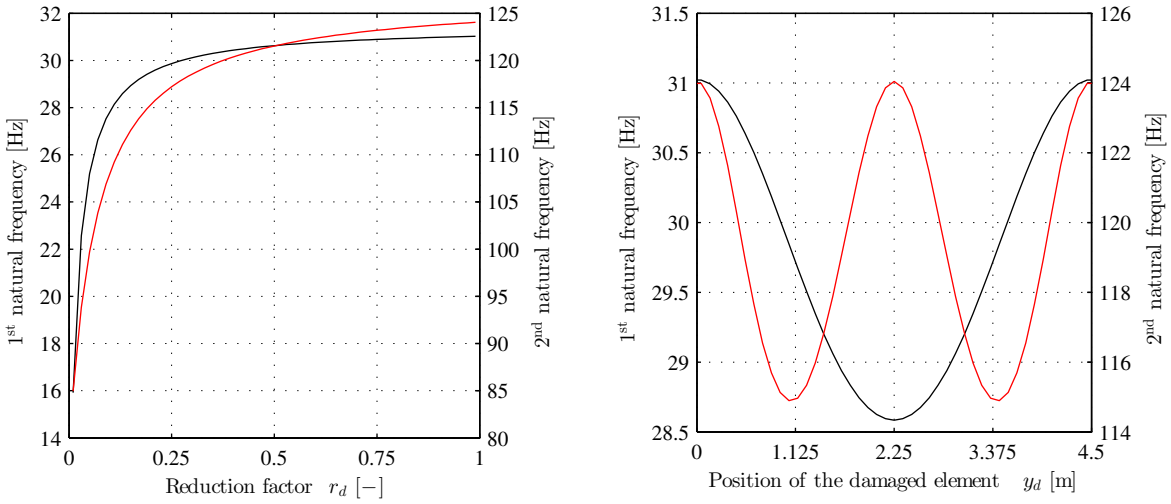

Figure 3.8: Case study 2: trend of the first (black line) and second (red line) natural frequency with the structural parameter (a) r_d and (b) y_d.

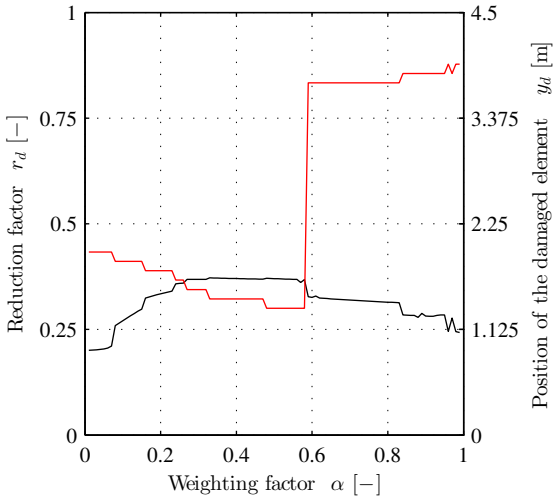

Figure 3.9: Case study 2: trend of the structural parameter r_d (black line) and y_d (red line) with the weighting factor α.

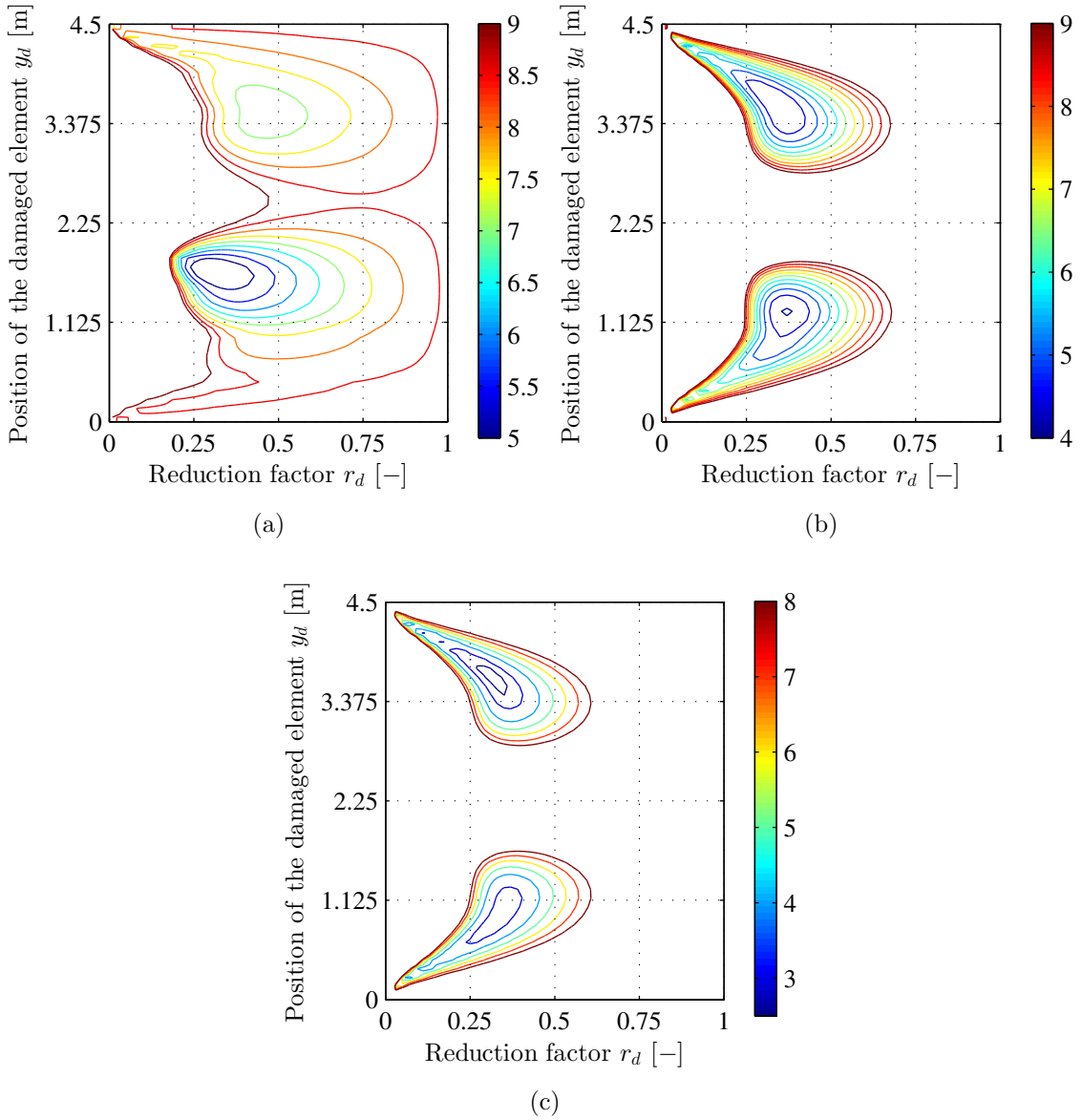

Figure 3.10: Case study 2: Contour plot multiplied by a factor 10^4 of the objective function H for (a) α =0.15, (b) α =0.55 and (c) α =0.75.

the x and y directions, respectively, and the rotation θ around the vertical axis. The columns are modelled as Euler-Bernoulli elements and the braces as truss elements. The connections among columns and floor beams are able to transfer the bending moment. The authors used a MATLAB based FE code, released by the IASC-ASCE SHM Task Group and available at the web site `http://datacenterhub.org/`, in order to compute mass and stiffness matrices. The code provides the implementation of a lumped mass matrix.

The model updating involves the identification of the stiffnesses of the first floor braces with reference to a damaged state of the structure. Indeed, the axial stiffness of the pair of braces N.3-N.4, located at the first floor on the East side, is reduced of the 25 %. The exact and pseudo-experimental values of the modal properties are presented in Table 3.6.

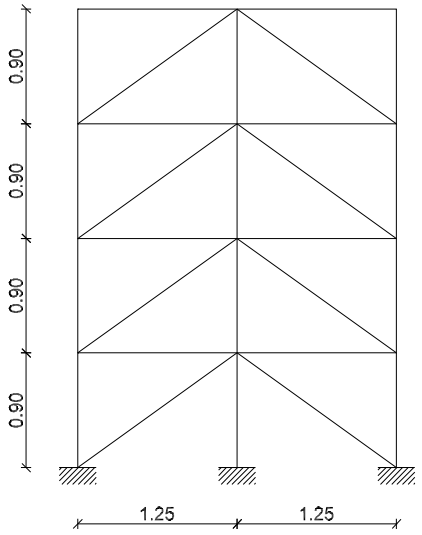

Figure 3.11: Case study 3: schematic front view of the structure. Dimensions expressed in meters.

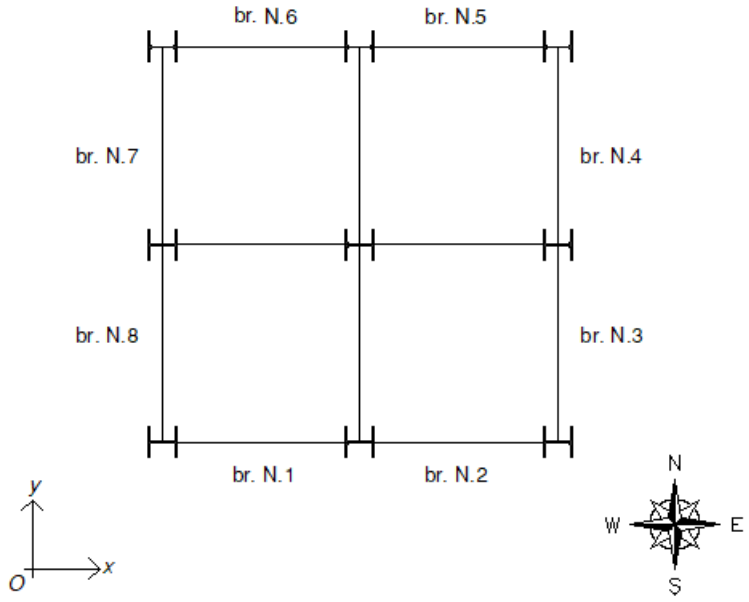

Figure 3.12: Case study 3: schematic plan view of the first floor.

The parameters to update are the four stiffness multipliers r_i $(i = S, E, N, W)$ for the pairs of braces located at the first floor on the South, East, North and West side, respectively. Reference is made to Fig.3.12 for the disposition of the braces with respect to the coordinate system Oxy. All the parameters are searched in the interval [0.50; 1.50].

Fig.3.13 shows the trend of the updated parameters r_E and r_W with the weighting factor α. For very low values of α the solution of the optimization problem does not represent the

		Exact			Pseudo-experimental		
Mode N.		1	2	3	1	2	3
Frequency [Hz]		9.1829	11.7913	16.2092	9.2019	11.7610	16.2145
Mode shape comp. [−]	$\phi_{u,1}$	0	0.3785	0	0	0.3854	0
	$\phi_{v,1}$	0.4053	0	0.0253	0.3670	0	0.0239
	$\phi_{\theta,1}$	0.0172	0	0.3890	0.0151	0	0.3602
	$\phi_{u,2}$	0	0.6898	0	0	0.6820	0
	$\phi_{v,2}$	0.7040	0	-0.0081	0.6612	0	-0.0051
	$\phi_{\theta,2}$	0.0196	0	0.6949	0.0168	0	0.6899
	$\phi_{u,3}$	0	0.9068	0	0	0.8954	0
	$\phi_{v,3}$	0.9113	0	-0.0383	0.9040	0	-0.0349
	$\phi_{\theta,3}$	0.0211	0	0.9080	0.0184	0	0.9032
	$\phi_{u,4}$	0	1.0000	0	0	1.000	0
	$\phi_{v,4}$	1.0000	0	-0.0529	1.0000	0	-0.0475
	$\phi_{\theta,4}$	0.0218	0	1.0000	0.0189	0	1.0000

Table 3.6: Case study 3: exact and pseudo-experimental modal properties. Mode shapes are normalized to their maximum entry. Subscript numbers denote the floor number.

reference damaged state. Indeed, for this solution, the braces on the East side (N.3-N.4) are identified as undamaged and those on the West side (N.7-N.8) are characterized by a stiffness increment. Mode shapes of this state of the structure are very similar to those of the reference damaged state considered for the generation of the pseudo-experimental data. For this reason, when the contribution of mode shape residuals in the optimization process is predominant, the previous solution can be obtained. On the contrary, there is a discrepancy among the natural frequencies of these two states. Consequently, for larger values of α, when the contribution of frequency residuals becomes significant, a solution close to the reference damaged one is found.

3.3.4 Test I

Test I consists in the resolution for 100 times of the same optimization problem to assess the robustness of the selection criteria to the variability of the optimization algorithm. The algorithm is based on a stochastic research, so it can produce small differences in the definition of the Pareto front at each repetition. The aim of the test is to evaluate if these differences affect the choice of the preferred solution among those forming the Pareto front. This is assessed through the statistics of the results obtained from the 100 resolutions in terms of weighting factor and structural parameters corresponding to the preferred solution. For each quantity, the mean value and the coefficient of variation (CV) are reported. Table 3.7, 3.8 and 3.9 present the results of case study 1, 2 and 3, respectively.

Results show that, for all the case studies, the optimal weighting factor α estimated from the criterion B is highly influenced by the variability of the optimization algorithm, being it characterized by coefficients of variation higher than 20%. This is because results of

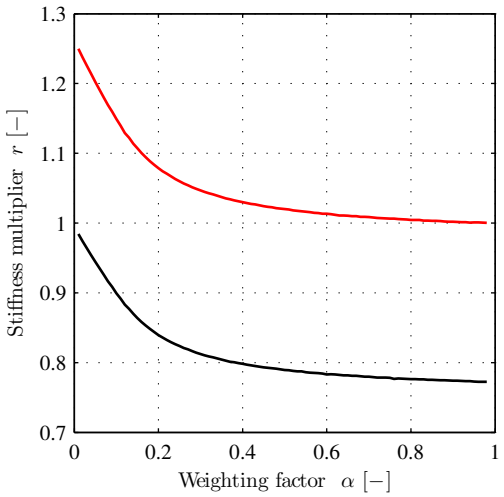

Figure 3.13: Case study 3: trend of the structural parameter r_E (black line) and r_W (red line) with the weighting factor α.

Criterion	α		m_1		h_1	
	Mean [-]	CV [%]	Mean [10^3kg]	CV [%]	Mean [m]	CV [%]
A	0.386	1.3	41.0	0.02	4.13	0.004
B	0.610	26.4	40.7	0.53	4.13	0.131
B*	0.260	12.3	41.3	0.23	4.13	0.005
C	0.220	0.6	41.4	0.02	4.13	0.004
D	0.286	2.1	41.2	0.03	4.13	0.003

Table 3.7: Case study 1: results of test I.

Criterion	α		r_d		y_d	
	Mean [-]	CV [%]	Mean [-]	CV [%]	Mean [m]	CV [%]
A	0.370	10.4	0.373	0.2	1.450	0.0
B	0.452	32.3	0.359	4.5	2.076	49.0
B*	0.571	15.9	0.364	2.2	2.486	47.8
C	0.159	4.3	0.323	1.7	1.765	1.4
D	0.199	6.1	0.334	0.8	1.750	0.0

Table 3.8: Case study 2: results of test I.

Criterion	α		r_S		r_E		r_N		r_W	
	Mean [-]	CV [%]	Mean [-]	CV [%]	Mean [-]	CV [%]	Mean [-]	CV [%]	Mean [-]	CV [%]
A	0.300	0.0	0.98	0.0	0.81	0.0	0.98	0.0	1.05	0.0
B	0.696	20.7	0.98	0.0	0.78	0.8	0.98	0.0	1.00	0.7
B*	0.477	13.7	0.98	0.0	0.79	0.6	0.98	0.0	1.02	0.6
C	0.126	15.3	0.99	0.1	0.88	1.2	0.99	0.1	1.13	1.1
D	0.141	46.4	0.99	0.1	0.88	2.5	0.99	0.1	1.12	2.3

Table 3.9: Case study 3: results of test I.

criterion B are significantly affected by inaccuracies of the optimization algorithm in the definition of the Pareto front, that may cause sharp changes of slope, and consequently of the bend angle β, between following points. In addition, due to these inaccuracies, a point of the front can be found above the line connecting the previous and following point, as shown in Fig. 3.14, causing a negative bend angle β.

For this reason, a curve fitting of the Pareto front is introduced in the criterion B. For all the case studies, the curve that fits the discrete points of the Pareto front is defined as a power model of equation:

$$y(x) = ax^b + c \tag{3.19}$$

where a, b and c are the model coefficients. The curve fitting allows avoiding the sharp changes of slope of the Pareto front, although the fitted curve does not exactly represent the Pareto front but its average trend. The goodness of the fit is guaranteed by the analysis of the coefficient of determination (R^2) and of the sum of squares of residuals (SSR) for every fitting model. Considering the 100 repetitions of the optimization problem, mean value and coefficient of variation can be computed for each indicator. The mean values of R^2 are equal to 0.96, 0.98 and 0.99 for case study 1,2 and 3, respectively. In the same order, the mean values of SSR are $2.3{\cdot}10^{-7}$, $9.5{\cdot}10^{-8}$ and $1.12{\cdot}10^{-8}$, that are low if it is considered that the order of magnitude of the fitted function is 10^{-3} for case study 1 and 10^{-4} for case study 2 and 3. Coefficients of variation for both indicators are small in all the case studies.

The application of the maximum bend angle criterion to the fitting of the Pareto font is denoted as criterion B*. Figs. 3.15(a) and 3.15(b) show the values of β corresponding to the points of the Pareto front shown in Fig. 3.14 obtained from the criterion B and B*, respectively. The adoption of the criterion B* allows smoothing the trend of β with α and avoiding negative values of β, although some sharp changes of slope can still be found. These are due to the non-uniform spacing of e_F, and, consequently, to a non-uniform spacing for the computation of β. Indeed, the fitting of Pareto front is built by calculating the fitted values of e_M, according to Eq.(3.19), from the values of e_F of the points forming the Pareto front, which are not equally spaced.

Tables 3.7, 3.8 and 3.9 show that the coefficient of variation of α obtained from criterion B* is lower than the one obtained from criterion B, although it is still a large value compared

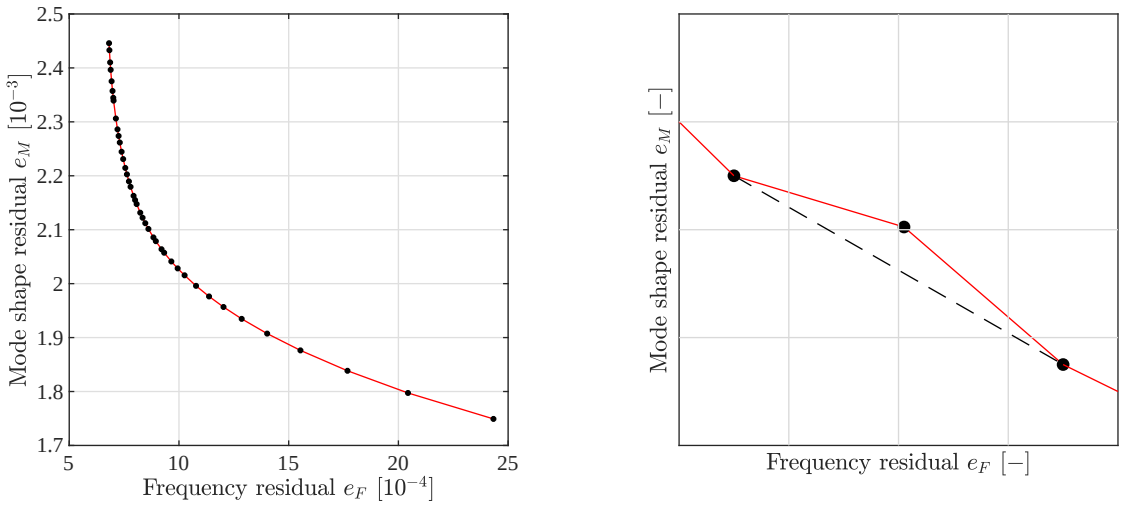

(a) (b)

Figure 3.14: Case study 1: (a) Pareto front obtained from one of the 100 iterations with α step size 0.02 and (b) detail of the point characterized by a negative value of β. Black dots: points of the Pareto front. Red line: line connecting neighbouring points. Dashed black line: expected Pareto front.

to most of results related to criteria A, C and D. As far as case study 1 is concerned, the variability of α does not affect the values of the identified parameters, which are almost insensitive to the weighing factor values (see Fig. 3.6). On the contrary, the identified position of the damaged element y_d in the case study 2 strongly depends on the weighting factor α (see Fig. 3.9). The position spans from 1.450 m for criterion A to 2.486 m for criterion B*. Criterion A provides the value of y_d closer to its exact value, namely 1.250 m. However, as the optimization is performed with reference to the pseudo-experimental modal properties, the identified structural parameters are not necessarily as close as possible to their exact values. Hence, a direct comparison between the estimated structural parameter and its exact value is not an indication of the quality of the identified optimal solution. To evaluate the quality of the optimization in terms of identified structural parameters, the analysis should be repeated considering different pseudo-experimental modal properties and evaluating the mean value of the estimated parameter.

As concerns case study 3, where the variation of parameters is less pronounced compared to case study 2 but not negligible (see Fig. 3.13), also results of criteria C and D are characterized by an high variation, especially the weighting factor. On the contrary, criterion A is very stable also for this case study.

In summary, test I shows that results of the criterion A are almost unaffected by the variability of the optimization algorithm, while criteria B and B* are highly sensitive to this variability for all the cases examined. Criteria C and D are stable in the first two case studies but show drawbacks in the last one.

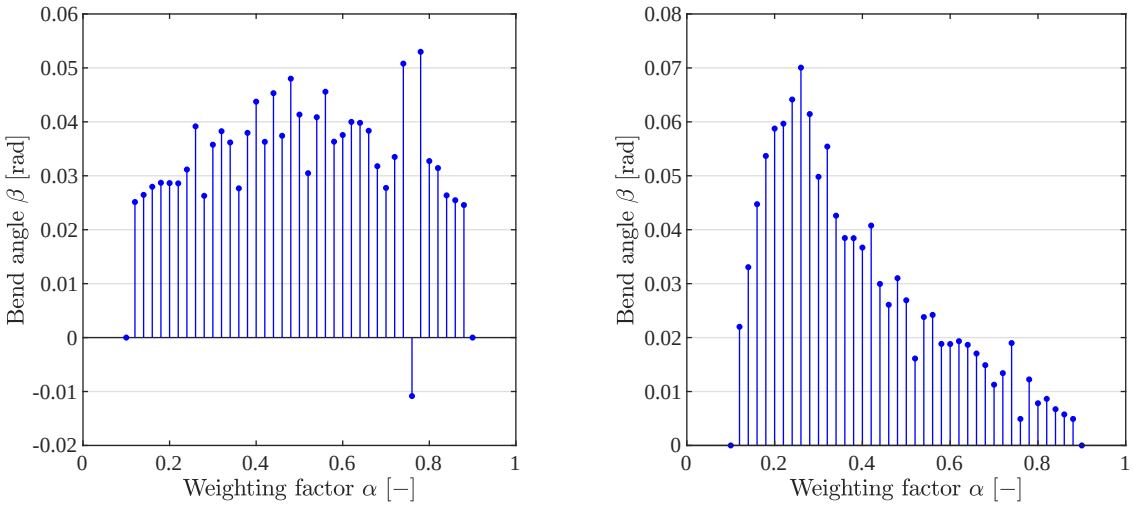

Figure 3.15: Case study 1: values of the bend angle β obtained from (a) criterion B and (b) criterion B* performing the optimization with α step size 0.02.

Selection criterion	Case study 1		
	Preferred α[−]	m_1 [10^3kg]	h_1 [m]
A	0.35-0.39	41.0-41.1	4.13-4.13
B	0.50, 0.92	40.8, 40.3	4.13, 4.15
B*	0.18	41.6	4.13
C	0.14-0.23	41.4-41.8	4.13 -4.13
D	0.17-0.31	41.1-41.6	4.13 -4.13

Table 3.10: Case study 1: results of test II.

3.3.5 Test II

Test II aims at evaluating how the choice of the weighting factor range for the definition of the Pareto front affects the selection of the preferred solution. For each case study, nine Pareto fronts are defined starting from a reference front generated adopting weighting factors in the range 0.01-0.99, with step size 0.01. Each front differs from the others in at least one extremity of the weighting factor range. Possible values for the inferior extremity are 0.01, 0.05 and 0.10, while for the superior extremity are 0.90, 0.95 and 0.99. These nine fronts are subsets of the reference front obtained disregarding some extremity points when the corresponding weighting factor α is not included in that range. In this way, the variability of the optimization algorithm treated in section 3.3.4 does not affect the results of the test.

The different selection criteria are applied to the nine Pareto fronts obtaining, for each criterion, nine preferred solutions and corresponding weighting factors α. Tables 3.10,

Selection criterion	Case study 2		
	Preferred $\alpha[-]$	$r_d[-]$	$y_d[m]$
A	0.33-0.39	0.37	1.37
B	0.56	0.37	1.26
B*	0.59	0.33	3.64
C	0.15-0.26	0.30-0.36	1.53-1.76
D	0.18-0.31	0.33-0.37	1.42-1.65

Table 3.11: Case study 2: results of test II.

Selection criterion	Case study 3				
	Preferred $\alpha[-]$	r_S [-]	r_E [-]	r_N [-]	r_W [-]
A	0.30-0.33	0.98-0.99	0.81	0.98-0.99	1.04-1.06
B	0.61	0.98	0.78	0.98	1.01
B*	0.59	0.98	0.78	0.98	1.01
C	0.12-0.22	0.99	0.83-0.88	0.99	1.07-1.13
D	0.12-0.35	0.98-0.99	0.80-0.88	0.99	1.04-1.13

Table 3.12: Case study 3: results of test II.

3.11 and 3.11 provide the range of variation of the preferred weighting factors and the corresponding structural parameters obtained from the nine fronts for case study 1, 2 and 3, respectively. Selection performed by criteria B and B* does not depend on the choice of the weighting factor range unless the preferred point of the front is in the extreme region, as with case study 1 considering the criterion B. In this case, in fact, α=0.92 is the preferred solution as long as it is included in the weighting factor range, otherwise the preferred solution corresponds to α=0.50. On the contrary, results obtained from criteria A, C e D depend on the definition of the weighting factor range. As stated before, the variation of the weighting factor does not affect the values of the identified parameters for the case study 1. Hence, the following considerations focus on the case study 2, characterized by a wide variability of the parameter y_d with the weighting factor.

Fig. 3.16 illustrates the values of the membership function Φ that rules the selection of the preferred solution according to criterion C. It can be observed that, when the range 0.01-0.99 is considered, the maximum value of Φ is obtained for α=0.16, corresponding to y_d =1.63 m, while the maximum corresponds to α=0.26 and y_d =1.55 m when the range 0.10-0.99 is considered. The same happens for criterion D, as shown in Fig. 3.17. In this case, depending on the weighting factor range, the preferred solution changes from $\alpha = 0.18$ to $\alpha = 0.31$, corresponding to a position y_d from 1.65 m to 1.47 m. Criterion A shows to be less sensitive to the weighting factor range, with values of α varying from 0.33 to 0.39, corresponding to a position y_d equal to 1.37 m that remains almost constant. The variability is mainly due to the uncertainty in the equilibrium point definition, which produces slight changes in the computed distance and thus in the selected optimal point.

The same considerations can be formulated also for the case study 3, even if the variation

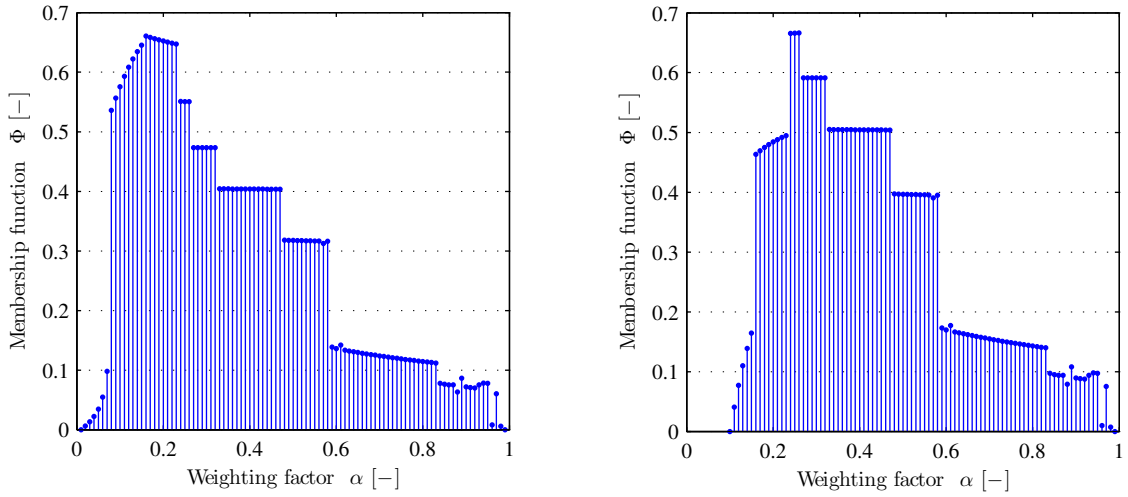

(a) (b)

Figure 3.16: Case study 2: values of the membership function Φ obtained from the criterion C considering different weighing factor ranges: (a) 0.01-0.99 and (b) 0.10-0.99.

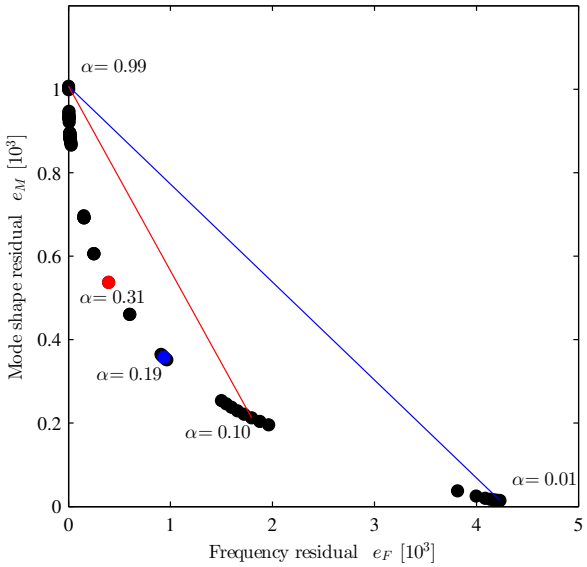

Figure 3.17: Case study 2: preferred solutions obtained from the criterion D considering different weighting factor ranges. Blue line and dot: boundary line and preferred solution for the range 0.01-0.99. Red line and dot: boundary line and preferred solution for the range 0.10-0.99.

of the updated parameters is less marked compared to case study 2. However, it is observed from Table 3.12 that the stiffness parameter r_E identified by criterion D from the same set of measurements shows a variation of 8 %. In the context of damage detection, this can lead to different conclusions about the damage extension. This does not occur, or it occurs in a very limited way, for criteria A, B and B*.

Criterion	e_M	α Mean [-]	α CV [%]	m_1 Mean [10^3kg]	m_1 CV [%]	h_1 Mean [m]	h_1 CV [%]
A	Eq. (2.2); γ=0.5	0.386	1.3	41.0	0.02	4.13	0.004
	Eq. (2.2); γ=1	0.498	0.9	41.3	0.02	4.13	0.004
	Eq. (2.3)	0.499	0.9	41.2	0.01	4.13	0.003
B	Eq. (2.2); γ=0.5	0.610	26.4	40.7	0.53	4.13	0.131
	Eq. (2.2); γ=1	0.547	33.9	41.2	0.93	4.13	0.108
	Eq. (2.3)	0.538	33.4	41.2	0.51	4.13	0.055
B*	Eq. (2.2); γ=0.5	0.260	12.3	41.3	0.23	4.13	0.005
	Eq. (2.2); γ=1	0.463	12.2	41.4	0.27	4.13	0.026
	Eq. (2.3)	0.403	15.9	41.3	0.18	4.13	0.028
C	Eq. (2.2); γ=0.5	0.220	0.6	41.4	0.02	4.13	0.004
	Eq. (2.2); γ=1	0.490	1.1	41.4	0.02	4.13	0.005
	Eq. (2.3)	0.513	1.9	41.2	0.01	4.13	0.004
D	Eq. (2.2); γ=0.5	0.286	2.1	41.2	0.03	4.13	0.003
	Eq. (2.2); γ=1	0.491	1.3	41.4	0.03	4.13	0.005
	Eq. (2.3)	0.527	1.1	41.2	0.01	4.13	0.002

Table 3.13: Case study 1: results of test III.

3.3.6 Test III

Test III aims at evaluating the influence of the definition of the objective function on the preferred solution. In particular, three possible expressions for the mode shape residuals e_M are considered, which are those reported in Eqs. (2.2) with the exponent γ equal to 0.5 and 1, and (2.3). The optimization process is performed three times, each time adopting a different expression for e_M in the definition of the objective function H (Eq. (2.5)). For each definition of e_M, the optimization algorithm is solved 100 times to account for the variability of the optimization process. The influence of e_M on the choice of the preferred solution is shown in Table 3.13 and 3.14 for case study 1 and 2, respectively. For each definition of the mode shape residuals e_M, the statistics of the results from the 100 iterations in terms of weighting factor and structural parameters corresponding to the preferred solution are presented.

The three different expressions of the mode shape residuals e_M, and consequently of the objective function H, imply three different Pareto fronts. Hence, three preferred solutions are obtained for each selection criterion. The robustness of a selection criterion depends on coherence in the selection of the preferred set of parameters despite the modification of e_M.

As reported before, the only structural parameter that significantly changes and depends on the selected weighting factor is the position of the damaged element y_d for the case study 2. Indeed, Table 3.13 shows that, although the optimal weighting factors α change with

Criterion	e_M	α		r_d		y_d	
		Mean [-]	CV [%]	Mean [−]	CV [%]	Mean [m]	CV [%]
A	Eq. (2.2); γ=0.5	0.370	10.4	0.373	0.2	1.450	0.0
	Eq. (2.2); γ=1	0.550	0.3	0.344	0.1	1.75	0.0
	Eq. (2.3)	0.553	7.4	0.375	2.2	1.95	0.0
B	Eq. (2.2); γ=0.5	0.452	32.3	0.359	4.5	2.076	49.0
	Eq. (2.2); γ=1	0.791	10.9	0.374	4.1	1.95	45.0
	Eq. (2.3)	0.684	13.7	0.342	7.6	1.81	30.0
B*	Eq. (2.2); γ=0.5	0.571	15.9	0.364	2.2	2.486	47.8
	Eq. (2.2); γ=1	0.643	13.5	0.363	3.6	1.67	16.9
	Eq. (2.3)	0.620	7.6	0.485	0.2	1.75	0.0
C	Eq. (2.2); γ=0.5	0.159	4.3	0.323	1.7	1.765	1.4
	Eq. (2.2); γ=1	0.612	2.3	0.355	2.3	1.72	1.3
	Eq. (2.3)	0.661	8.5	0.340	7.5	1.65	1.0
D	Eq. (2.2); γ=0.5	0.199	6.1	0.334	0.8	1.750	0.0
	Eq. (2.2); γ=1	0.554	8.5	0.347	2.9	1.72	2.6
	Eq. (2.3)	0.662	8.3	0.335	0.3	1.65	0.0

Table 3.14: Case study 2: results of test III.

the definition of the mode shape residuals e_M, the optimal parameters of case study 1 are almost insensitive to α. On the contrary, the optimal value of the position of the damaged element y_d depends on the value of α (Table 3.14). As shown in section 3.3.4, results of criteria B and B* are highly affected by the variability of the optimization algorithm, leading to unreliable results in terms of estimated values of y_d. In these cases, except for the results obtained with the criterion B* and Eq. (2.3), the estimated values of y_d show coefficient of variations from 16.9% to 50.1%. On the contrary, results of criteria A, C and D are unaffected by the variability of the optimization algorithm and can be employed to assess the influence of e_M. It can be observed that optimal parameters selected by criteria C and D are very similar despite the modification of the objective e_M while there is a slightly higher difference between the optimal values of y_d selected by criterion A.

3.3.7 Discussion

The previous tests showed that the choice of the criterion for the selection of the preferred solution among those forming the Pareto front is especially important when the estimated structural parameters change depending on the considered solution. Indeed, when dealing with simple cases, as case study 1, results are basically independent on the choice of the preferred solution and, consequently, on the selection criterion. On the contrary, when more complex cases are considered, different optimal solutions can be obtained depending on the selection criterion, as with case studies 2 and 3. First, it is observed that the results

of the maximum bend angle criterion (criterion B) are strongly affected by the variability of the optimization algorithm even for the case study 1. Even with the introduction of a curve fitting of the Pareto front (criterion B*), results remain highly unstable. Results of criteria C (fuzzy satisfying approach) and D (maximum distance from the boundary line) are almost unaffected by the variability of the optimization algorithm for the first two case study, but the opposite behaviour occurs for the case study 3. Moreover, they depend on the choice of weighting factor range for the definition of the Pareto front. On the contrary, results are fairly stable with respect to the definition of the mode shape residuals e_M. Criterion A (minimum distance from the equilibrium point) is stable with respect to the variability of the optimization algorithm and the definition of the weighting factor range, but it shows a lower coherence in the test III compared with criteria C and D.

3.4 Proposed updating procedure

Being the computation of the Pareto-optimal solutions a very time-consuming task, methods that directly evaluate the optimal solution should be preferred in real applications. Analyses presented in section 3.3 have shown that the criterion of the minimum distance from the equilibrium point (criterion A, section 3.2.1), the fuzzy satisfying approach (criterion C, section 3.2.3) and the criterion of the maximum distance from the boundary line (criterion D, section 3.2.4) provided good results with respect to the tests carried out, even if they exhibited some weaknesses. In particular, criteria C and D show a certain sensitivity towards the definition of the weighting factor range, or in general towards extreme values of objectives involved in the selection of the preferred solution. This may limit the applicability of a method based on a evolutionary algorithm for the direct evaluation of the optimal solution, as the stochastic search involved in the algorithm produces a certain variability of the extreme values of the objectives.

This section presents a new procedure for the direct evaluation of the optimal solution in multi-objective optimization problems based on the criterion of the minimum distance from the equilibrium point. In the following, results of this direct procedure are referred to as DP(A) results. To evaluate the efficiency and robustness of the DP(A) procedure, results are compared to those obtained through the computation of the whole Pareto front and the following selection of the preferred solution with the criterion of the minimum distance from the equilibrium point, indicated as AP results. The proposed approach for the direct evaluation of the preferred solution is based on the DE-S algorithm (section 2.3) to solve the optimization problem. The adoption of an evolutionary algorithm is essential for this approach as it allows to simultaneously handle and compare a population of candidate vectors. This would not be possible with gradient-based methods that consider one point at a time [123, 154].

The objective function δ to minimize is defined as the distance from the equilibrium point, whose coordinates are (e_F^{min}, e_M^{min}):

$$\delta = \sqrt{(e_F - e_F^{min})^2 + (e_M - e_M^{min})^2} \tag{3.20}$$

At each iteration, the values of e_F^{min} and e_M^{min} are searched from all the vectors of the current population as well as from the previously considered vectors. Therefore, the values

of e_F^{min} and e_M^{min}, and consequently of δ, may change, and a database containing the values of the objectives for each vector is created. When for the generic i-th vector at least one of the following conditions occurs:

$$\begin{aligned} e_F^i &< e_F^{min} \\ e_M^i &< e_M^{min} \end{aligned} \tag{3.21}$$

the values of the objective function δ are recalculated for all the vectors existing in the database considering the new value of e_F^{min} and/or e_M^{min}. The need to recalculate the values of δ for all the vectors in the database is due to two reasons. First, a point belonging to a previous generation can exhibit a lower value of the objective function δ if the equilibrium point changes during the optimization procedure and, thus, it could be a good candidate for the next generation even if it was previously discarded. On the contrary, points that had low values of the objective function can be replaced by others due to their updated relative distance with respect to the equilibrium point. Second, the DE-S algorithm chooses the vectors of the subsequent population based both on a combination of vectors of the current population and on the values of the objective function for all the vectors considered until then. This means that when a parameter vector $\mathbf{x}_A$ is close to another vector $\mathbf{x}_B$ that has been previously discarded owing to a high value of the corresponding objective function, the vector $\mathbf{x}_A$ can be ruled out with no need to perform a modal analysis, improving the speed performances of the algorithm. Indeed, the re-evaluation of δ for a large number of vectors implies a computational effort which is negligible compared to the effort needed to perform a large number of modal analyses of complex FE models. Finally, it is highlighted that for the initial population the objective function δ is computed as the distance from the origin of the objective function space, because no objective has been evaluated yet.

The objective function δ expressed in Eq.(3.20) does not explicitly includes the weighting factor α. Once the minimum of Eq.(3.20) is evaluated, the relative importance between frequency and mode shape residuals for the optimal solution, represented by the weighting factor α, can be estimated as follows. Let's consider the generic Pareto front defined in the objective function space and reported in Fig. 3.18. The point of the Pareto front with the minimum distance from the equilibrium point Q is indicated as P. According to the Taylor's theorem, the Pareto front around the point P can be approximated by a first order Taylor polynomial. Denoting with γ the quantity $[e_F(P) - e_F^{min}]/[e_M(P) - e_M^{min}]$, the slope of the segment QP is $1/\gamma$. The tangent line to the Pareto front at the point P (blue line in Fig. 3.18) is perpendicular to the segment QP and is formulated as:

$$e_M = e_M(P) - \gamma(e_F - e_F(P)) \tag{3.22}$$

Hence, the coordinates of a point T on the tangent line (Eq.(3.22)) close to P are given by:

$$e_F(T) = e_F(P) + \varepsilon, \quad e_M(T) = e_M(P) - \gamma\ \varepsilon \tag{3.23}$$

where it is assumed that $e_F(T) - e_F(P) = \varepsilon$, with ε a very small number. According to the weighted sum method (Eq. (2.5)), the objective functions H evaluated in P and T are written:

$$\begin{cases} H(P) = \alpha_P\ e_F(P) + (1 - \alpha_P)\ e_M(P) \\ H(T) = \alpha_T\ e_F(T) + (1 - \alpha_T)\ e_M(T) \end{cases} \tag{3.24}$$

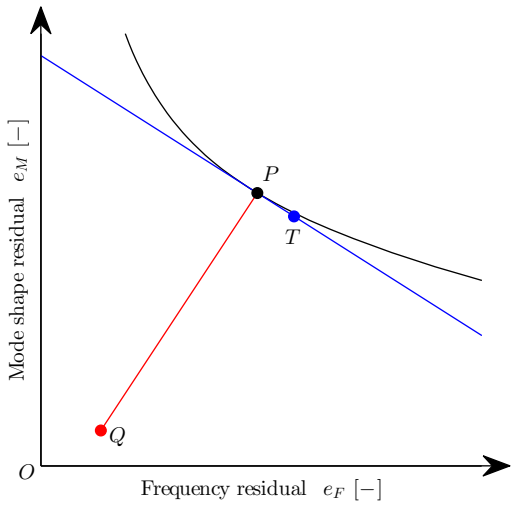

Figure 3.18: Estimate of α for the DP(A) procedure: segment QP (red) and tangent line (blue) to the Pareto front (black) at point P.

Being ε a very small number, it is assumed that the points P and T have almost the same values of weighting factor α and objective function H:

$$\begin{cases} H(P) \approx H(T) \\ \alpha(P) \approx \alpha(T) \end{cases} \tag{3.25}$$

Finally, substituting Eqs.(3.23) and (3.25) into Eq.(3.24), an estimate α^* of the weighting factor α related to the optimal solution is obtained:

$$\alpha^* = \frac{\gamma}{1+\gamma} \tag{3.26}$$

The main stages of the proposed direct procedure can be summarized as follows:

1. Sampling of the initial population (N_P vectors).
2. Evaluation of the residuals e_F-e_M and of the objective function δ (Eq. (3.20)) assuming e_F^{min} and e_M^{min} equal to zero.
3. Definition of e_F^{min} and e_M^{min} on the basis of the minimum values of e_F and e_M previously computed.
4. Selection of N_S vectors and calibration of a response surface (section 2.3.1).
5. If the calibrated RS is convex, computation of the vector that minimize the RS. Otherwise, execution of the classical operations of an evolutionary algorithm: mutation (section 2.3.2), crossover (section 2.3.3) and bound constraint (section 2.3.4).
6. Scoring operation according to the indications of section 2.3.5.

Procedure	α		m_1		h_1		Nr. of eval.	
	Mean [-]	CV [%]	Mean 10^3kg]	CV [%]	Mean [m]	CV [%]	Mean [-]	CV [%]
AP	0.386	1.3	41.0	0.02	4.13	0.004	11961	1.1
DP(A)	0.381	5.8	41.0	0.10	4.13	0.009	136	8.5

Table 3.15: Case study 1: comparison between DP(A) and AP results.

Procedure	α		r_d		y_d		Nr. of eval.	
	Mean [-]	CV [%]	Mean [-]	CV [%]	Mean [m]	CV [%]	Mean [-]	CV [%]
AP	0.370	10.4	0.373	0.2	1.450	0.0	25711	4.5
DP(A)	0.330	25.8	0.385	6.4	1.759	47.0	200	62.9

Table 3.16: Case study 2: comparison between DP(A) and AP results.

7. Evaluation of the residuals e_F-e_M and of the objective function δ (Eq. (3.20)) for the N_H vectors with the lowest scores.

8. Updating of e_F^{min} and e_M^{min} on the basis of the new vectors evaluated. Computation of the objective function δ again for all the vectors considered until now if at least one of the values of e_F^{min} and e_M^{min} changes.

9. Execution of the selection operation (section 2.3.6).

10. Assessment of the algorithm convergence following the criteria of section 2.3.7.

11. Repetition of stages 4-10 until convergence is reached.

3.4.1 Comparison between DP(A) and AP procedure

In this section, the proposed direct procedure based on the selection criterion A - DP(A) procedure - is applied to the case studies presented in section 3.3. To evaluate its robustness and efficiency, results are compared to those obtained from the AP procedure, namely with the criterion A applied to the whole Pareto front. By analogy with test I (section 3.3.4), the optimization of case study 1, 2 and 3 is performed 100 times to evaluate the effects of the variability of the optimization algorithm on the optimal updated model. In Tables 3.15, 3.16 and 3.17 statistics of results are compared in terms of mean values and coefficients of variation (CV) of the weighting factor α, of the identified structural parameters and of the number of modal analyses performed (Nr. of evaluations). The last is accounted for because the modal analysis execution is the most time-consuming task of the optimization process when dealing with complex FE models.

At first, it is observed that for all the case studies the mean values of the weighting factor and of the structural parameters identified from the two approaches are very similar. On

Procedure	α		r_S		r_E		r_N		r_W		Nr. of eval.	
	Mean [-]	CV [%]	Mean [-]	CV [%]	Mean [-]	CV [%]	Mean [-]	CV [%]	Mean [-]	CV [%]	Mean [-]	CV [%]
AP	0.300	0.0	0.98	0.0	0.81	0.0	0.98	0.0	1.05	0.0	13497	3.6
DP(A)	0.390	11.1	0.98	0.0	0.80	0.6	0.98	0.0	1.03	0.5	118	9.8

Table 3.17: Case study 3: comparison between DP(A) and AP results.

the contrary, the variability of the results obtained from the DP(A) procedure is slightly increased. The highest variability is observed for the position of the damaged element y_d of case study 2, which goes from 0.0 % for the AP procedure to 47.0 % for the DP(A) procedure. The higher variability obtained with the proposed method is mainly due to the uncertainty in the definition of the equilibrium point. In summary, it can be stated that the DP(A) procedure is slightly affected by the variability of the optimization algorithm in the choice of the optimal set of structural parameters.

The main difference between the two approaches is in the requested computational effort: for case study 1 (Table 3.15), the AP procedure needs a mean number of evaluations that is about 100 times higher than the number of evaluations for the DP(A) method. It is worth noting that in the first case (AP), the optimization process is repeated for each value of α, namely 99 times with α ranging from 0.01 to 0.99 with step size 0.01. The mean number of evaluations for a single optimization can be calculated dividing the total number of evaluations (11961) by the number of weighting factors considered (99). In this case, a single optimization with the AP method requires almost the same number of evaluations as the DP(A) method, namely 121 and 136, respectively. However, with the DP(A) procedure, the optimal solution is evaluated from a single optimization, while the optimization has to be repeated for different values of α to evaluate the whole Pareto front according to the AP procedure. Similar considerations can be drawn for case studies 2 and 3 (Tables 3.16 and 3.17). In these cases, the total number of evaluations required by the AP method is respectively about 130 and 115 times higher than the number of evaluations required by the DP(A) method, confirming that the direct estimation of the optimal solution is less time consuming than the evaluation of the Pareto-optimal solutions.

3.5 The San Felice sul Panaro fortress

In this section, the proposed DP(A) procedure is applied to case study of the San Felice sul Panaro fortress. The fortress is an historical masonry structure located in the town of San Felice sul Panaro (Modena, Italy). The fortress was built in the XIV century, but over the centuries it underwent several modifications. Now the fortress presents a quadrilateral plan with an inner yard and five towers (Fig. 3.19(a)). The main tower, located in the south-east corner, is called the "Mastio" due to its prevailing dimensions compared to the rest of the building. The seismic events that affected the Emilia-Romagna region in 2012 have caused several damages to the structure: the roofs of the four minor towers collapsed and many cracks of different size occurred [39]. Relevant shear cracks arose in the Mastio

(a) (b) (c)

Figure 3.19: (a) The San Felice sul Panaro fortress before the 2012 earthquake and the damaged Mastio: view from the (b) south and (c) north side.

and some vertical cracks were observed between the Mastio and the perimeter walls (Fig. 3.19(b) and Fig. 3.19(c)). Finally, also the merlons and the vaults inside the Mastio exhibited important damaging. After the earthquake, the municipality of San Felice sul Panaro planned the realization of some reinforcement operations in order to avoid further collapses. In particular, the diagonal cracks of the Mastio were filled with mortar and steel strands were introduced into the walls.

3.5.1 Ambient vibration testing and modal identification

Ambient vibration testing was performed on the Mastio of the San Felice sul Panaro fortress in 2016. Tests were designed to identify the Mastio modal properties starting from its dynamic response measured in operational conditions. Since the fortress has been strongly damaged by the earthquake that affected the Emilia Romagna region in 2012, the modal identification presented in the following refers to the dynamic behaviour of the Mastio in damaged conditions.

The dynamic acquisition system consisted of 10 uniaxial piezoelectric accelerometers (seven PCB/393B12 and three PCB/393B31), with a dynamic range of ± 0.5 g, a bandwidth ranging from 0.15 to 1000 Hz and a resolution of 8 μg (PCB/393B12) and 1 μg (PCB/393B31). A National Instruments acquisition system was connected to the accelerometers for data storage and system management purposes, while the sampling frequency was set to 200 Hz. The response of the tower was simultaneously recorded in seven points belonging to four levels along the height of the Mastio (see Fig.3.20). In each measuring position, one or two accelerometers were placed, for a total of 10 measurement channels (A1–A10 in Fig.3.20). Fig.3.21 shows an example of the typical installation of accelerometers, made with metal plates and screws.

An illustrative acceleration time series measured at the upper instrumented level (L4) is presented in Fig. 3.22(a). The recorded acceleration ranges between ± 15 mg (corresponding to $\pm 0.15 \mathrm{m/s^2}$). The corresponding power spectral density (PSD) function is presented in Fig. 3.22(b). Acquired accelerations are post-processed through the Enhanced Fre-

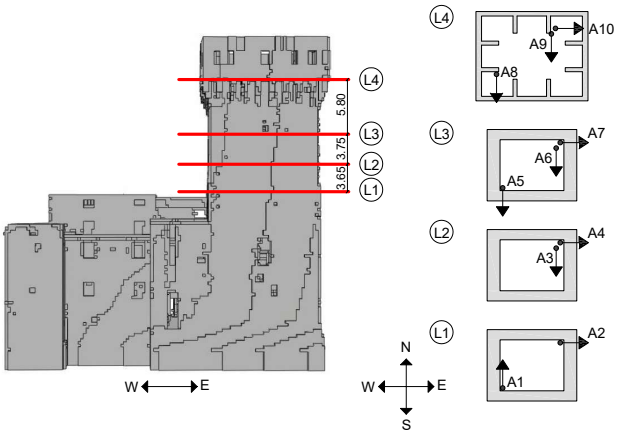

Figure 3.20: Fortress: instrumented levels (L1-L4) and piezoelectric accelerometer positioning.

(a) (b)

Figure 3.21: Fortress: typical installation of piezoelectric accelerometers.

quency Domain Decomposition method to identify the modal parameters, namely natural frequencies and mode shapes [27].

The first five identified mode shapes are presented in Fig. 3.23 where the corresponding natural frequencies are indicated. Two closely spaced modes are identified around 1.7 Hz, which are dominant bending modes and involve flexure in W-E direction (Fig. 3.23(a)) and N-S direction (Fig. 3.23(b)). The third mode mainly involves torsion of the main tower (Fig. 3.23(c)). The fourth (Fig. 3.23(d)) and the fifth (Fig. 3.23(e)) mode are second bending modes characterized by dominant flexure in N-S and E-W direction, respectively.

3.5.2 FE model of the fortress

An accurate FE model of the San Felice sul Panaro fortress (Fig. 3.24) has been developed by Castellazzi et al. [36, 37] through an innovative numerical modelling strategy called CLOUD2FEM. This strategy is based on the semi-automatic transformation of a three-dimensional points cloud of a structure into three-dimensional FE meshes. The resulting mesh is composed by eight-node hexahedral elements with resolution 25 cm × 25 cm × 25 cm, for a total amount of 409,300 FEs and 1,512,444 DOFs. A jagged 3D representation of the original geometry of floors and vaults has been used in order to automatically generate their meshes. Conversely, the roof structure has been introduced in the model as

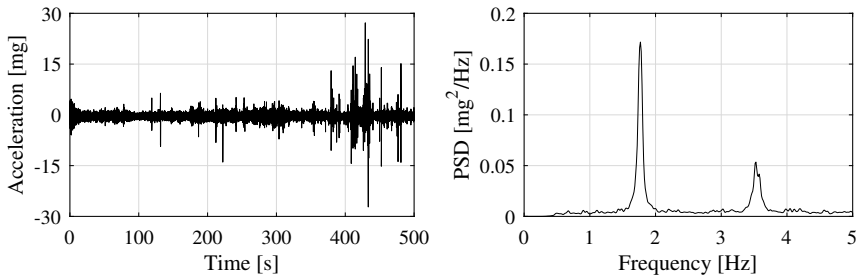

(a) (b)

Figure 3.22: Fortress: (a) typical acceleration time history recorded at the upper instrumented level and (b) corresponding power spectral density (PSD) function.

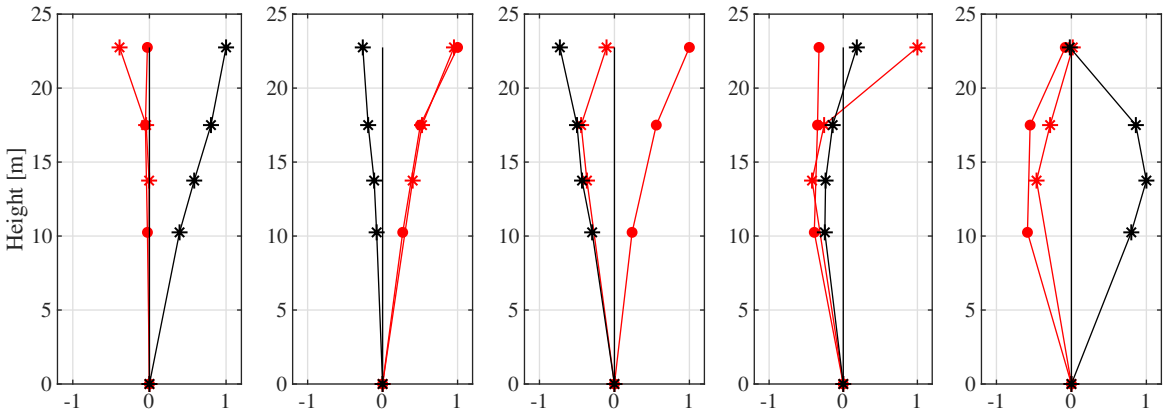

(a) $f_1 = 1.72$ Hz (b) $f_2 = 1.75$ Hz (c) $f_3 = 3.55$ Hz (d) $f_4 = 4.83$ Hz (e) $f_5 = 5.08$ Hz

Figure 3.23: Natural frequencies and mode shapes of the (a, b, d, e) bending and (c) torsional modes normalized to their maximum entry. Black asterisks: modal displacements of the measuring points in the N-E corner of the cross-section in E-W direction; Red asterisks: modal displacement of the N-E corner in N-S direction; Red dots: modal displacement of the W-S corner in N-S direction.

concentrated mass disposed on the top elements of the Mastio. The mass matrix of the overall structure is lumped. Finally, the restraint condition of the structure is affected by the presence of a moat surrounding the fortress. Clamped boundary conditions have been imposed to all the nodes at the moat level, while the elements located within the courtyard have been modelled through an elastic continuum to coarsely take into account the presence of terrain. The three-dimensional points cloud of the fortress was obtained from a laser scanning survey performed after the 2012 earthquake, which allowed the reconstruction of all the internal and external surfaces. Therefore, the FE model represents the post-earthquake condition of the structure.

The study presented in [13] showed that to fully describe the actual behaviour of the Mastio in operational conditions, the effect of the severe crack pattern has to be accurately accounted for. To this aim, mesh elements corresponding to the damaged masonry have been identified in the FE model and a different elastic modulus has been assigned to them, as shown in Fig. 3.24. This allows accounting for the effect of damage and cracks in

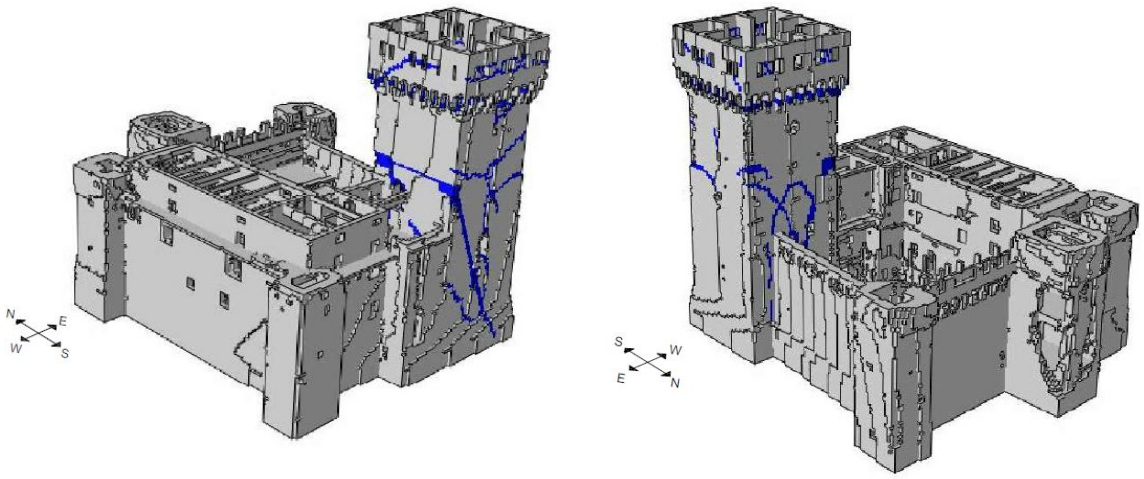

(a) (b)

Figure 3.24: FE model of the fortress with highlighting of the damaged elements (blue).

operational conditions, i.e. when the external actions are not such as to involve non-linear behaviour and damage and cracks only imply a local stiffness reduction. As the calibration is performed with reference to the modal properties of the Mastio, only the cracks of the Mastio are introduced in the FE model. Hence, the structural parameters to be identified with reference to the experimental modal properties are the elastic modulus of the masonry E_M and of the damaged elements E_D. Other stiffness parameters related to floors, vaults and terrain do not significantly affect the modal properties of the structure as a consequence of the predominant contribution of the main walls, which have a thickness of the order of meters. No mass parameter is considered for the calibration due to the presence of only structural masses and the high accuracy achieved in the representation of the structure geometry.

3.5.3 Evaluation of the optimal updated FE model

The optimal updated model is identified applying the DP(A) procedure presented in section 3.4, and results are compared with those obtained from the AP procedure. According to the AP approach, the whole Pareto front shown in Fig. 3.25(a) is firstly evaluated and the optimal solution is estimated through the criterion of the minimum distance from the equilibrium point. The objectives e_F and e_M are expressed by Eqs. (2.1) and (2.2) with γ=0.5, respectively. On the contrary, the direct procedure for estimating the optimal solution is based on the subsequent evaluation of many candidate vectors, indicated with black dots in Fig. 3.25(b). It can be observed how the candidate vectors are concentrated in the proximity of the optimal solution, except for a few points spread out in the objective function space. Fig. 3.26 presents a detail of the front where the equilibrium points obtained from the AP (point Q) and the DP(A) (point Q*) approach can be observed, together with the optimal solution of the DP(A) procedure (point P*). Fig. 3.25(b) shows that the candidate vectors corresponding to the minimum values of e_F and e_M can be

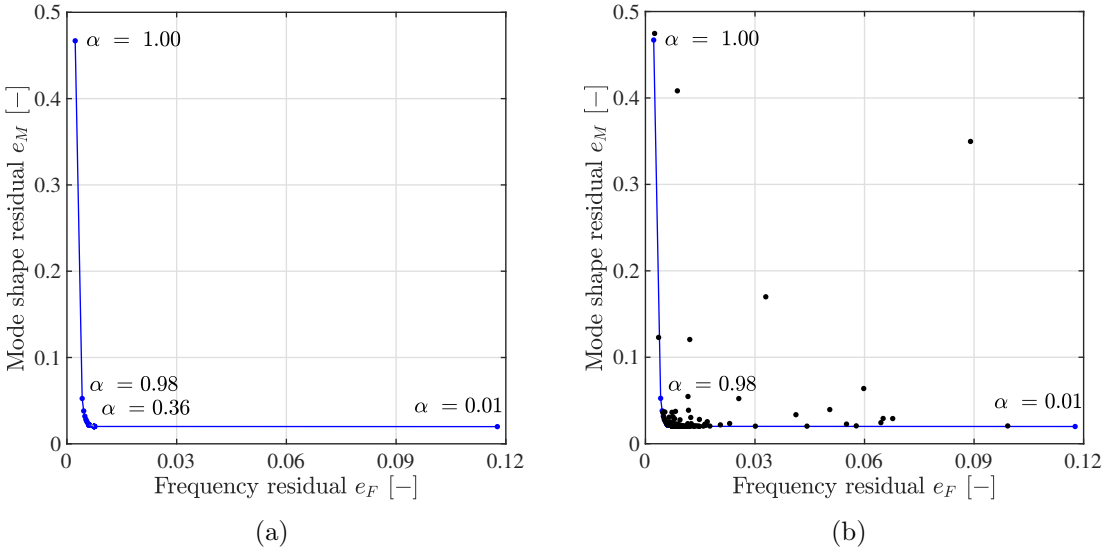

Figure 3.25: (a) Pareto front and (b) comparison between the front and the candidate vectors evaluated in the subsequent iterations of the optimization algorithm (black dots).

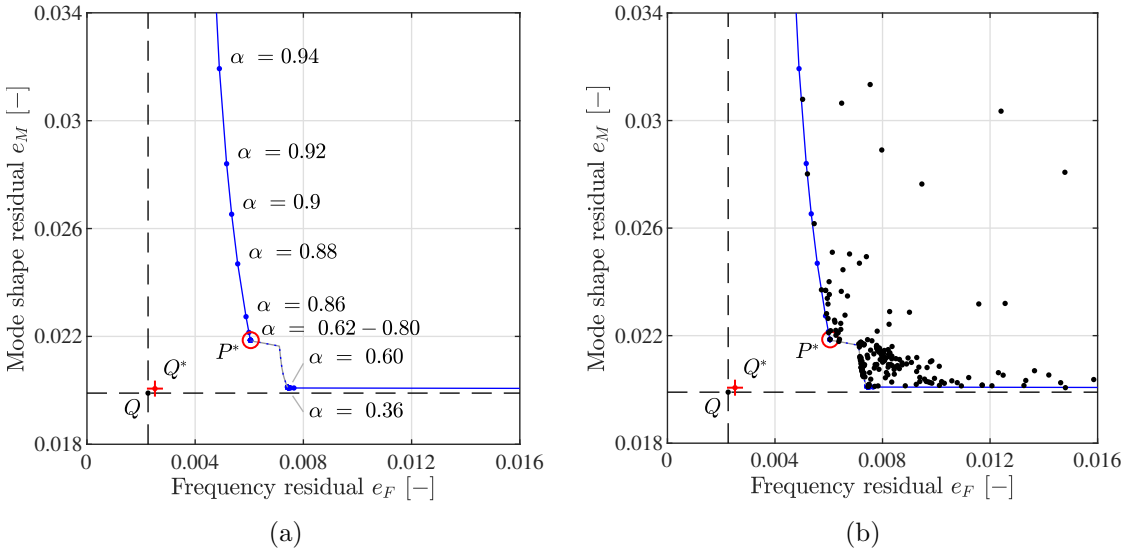

Figure 3.26: (a) Detail of the Pareto front and (b) comparison between the front and the candidate vectors evaluated in the subsequent iterations of the optimization algorithm (black dots). Point Q: equilibrium point obtained from the AP procedure. Point Q*: equilibrium point obtained from the DP(A) procedure. Point P*: preferred solution of the DP(A) procedure.

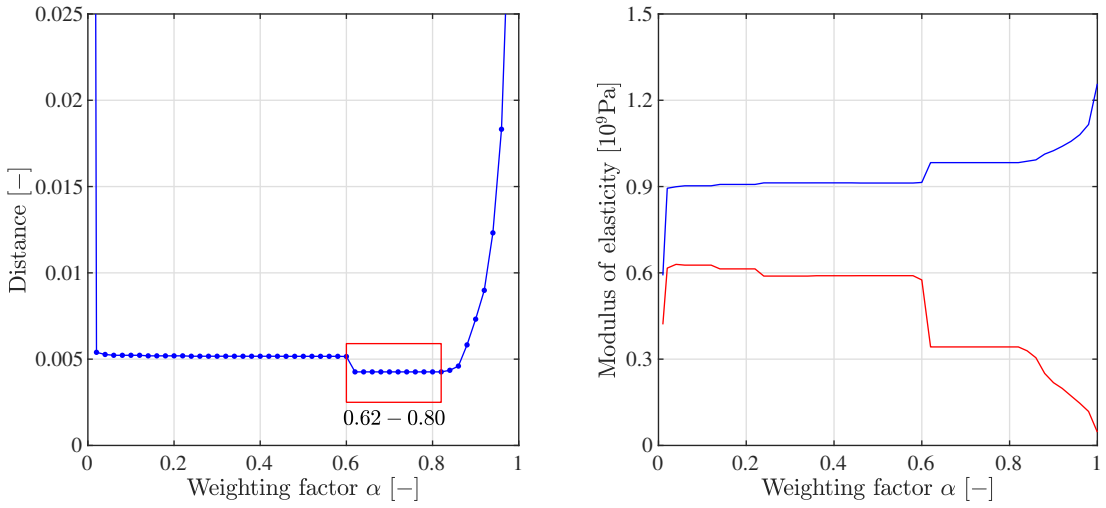

Figure 3.27: (a) Distance from the equilibrium point Q and (b) values of the structural parameters for the points of the Pareto front. Blue line: masonry elastic modulus E_M. Red line: elastic modulus of the damaged elements E_D.

found close to the extreme points of the Pareto front, causing the proximity, but not perfect correspondence, of the equilibrium points Q* and Q. Moreover, between $\alpha = 0.60$ and $\alpha = 0.62$ the Pareto front presents a non-convex shape, which is clearly recognized with the direct procedure (see Fig. 3.26(b)). To define the non-convex part of the Pareto front, the dominant solutions are evaluated according to Eq.(3.3).

The weighting factor corresponding to the optimal solution obtained from the direct procedure (P*) is estimated through Eq.(3.26) and is equal to 0.66. The distances of the points forming the Pareto front from the equilibrium point Q are shown in Fig. 3.27(a) while the values of the identified structural parameters with α are reported in Fig. 3.27(b). As the points of the front between $\alpha = 0.62$ and $\alpha = 0.80$ coincide with each others (see Fig. 3.26(a)), they are all characterized by the same distance from the equilibrium point, which corresponds to the minimum one. The optimal structural parameters identified from the two approaches and the corresponding α values are listed in Table 3.18, while the modal properties of the calibrated modes are reported in Table 3.19. The optimal structural parameters identified from the two approaches are very close to each other and therefore also the modal properties of the optimal updated models, proving the good match between results. Finally, the number of modal analyses performed by the DP(A) procedure is equal to 173, while the mean number of modal analyses performed by the AP procedure for each point of the Pareto front is 157. Having regard to the need to evaluate several points of the Pareto front, the DP(A) procedure is confirmed to be significantly less time consuming than the AP procedure.

Approach	E_M [MPa]	E_D [MPa]	α [-]
AP	983	342	0.62-0.80
DP(A)	986	346	0.66

Table 3.18: Identified structural parameters and α values.

Mode Shape	Exp. Freq. [Hz]	Num. Freq. [Hz]	Rel. Error [%]	MAC [%]
1^{st} Bending E-W	1.72	1.82	5.81	95
1^{st} Bending N-S	1.75	1.66	−5.14	90
1^{st} Torsional	3.55	3.70	4.23	93

Table 3.19: Experimental and numerical modes - DP(A) procedure.

3.6 Concluding remarks

In this chapter, a new procedure for the direct evaluation of the optimal updated solution in multi-objective optimization problems has been presented. The multi-objective optimization problem is solved through a single-objective approach, namely by defining the objective function to minimize as the combination of different objectives. In particular, the objective function is defined as the distance from the equilibrium point and the optimization procedure is performed through an evolutionary algorithm. Compared to methods based on the evaluation of the whole Pareto front and the subsequent selection of the preferred solution, the proposed procedure has proven to be computationally efficient and able to provide reliable results. Moreover, the proposed approach is able to directly estimate the best weighting factor α with a good accuracy, without the need to defined it a priori, allowing to evaluate the relative importance between the selected objectives. A preliminary study has been carried out to assess the performances of different criteria for the selection of the preferred solution among those forming the Pareto front. It has allowed to identify the criterion of the minimum distance from the equilibrium point as the most robust with respect to the variability of the optimization algorithm, the weighting factor range and the shape of the Pareto front. Results of this preliminary study performed considering three numerical case studies have led to the choice of the criterion of the minimum distance from the equilibrium point for the definition of the objective function.

The proposed procedure for the direct evaluation of the preferred solution is adopted to calibrate the FE model of the San Felice sul Panaro fortress, an historical masonry structure that was severely damaged by the seismic events that affected the Emilia Romagna region (Italy) in 2012. The FE model represents the structure in its damaged condition and the effect of the crack pattern on the structural behaviour is accounted for. Results of the proposed direct procedure are compared to those obtained from evaluation of the whole Pareto front and the subsequent selection of the preferred solution. This problem presents a non-convex part of the Pareto front that can be recognized with the direct procedure, investigating all the vectors evaluated by the algorithm. The optimal updated models

identified from the two procedures are very consistent, while the computational cost of the direct procedure is significantly lower.

Chapter 4

Bayesian model updating

Uncertainties and errors unavoidably affect model updating problems. Taking into account the ill-posed nature of model updating when it is treated deterministically, in particular the stability of the solution with respect to small perturbations of the data, there is the concrete possibility to obtain unreliable results and predictions. An example is provided by the large variation of the updated parameters of the FE model of the San Felice sul Panaro fortress according to the selected objective weights (see Fig. 3.27(b)).

Treating the problem of model updating in probabilistic terms, the adoption of parameter distributions could be more appropriate than considering a single optimal parameter vector in deterministic terms. One of the most diffused approach for uncertainty quantification in model updating is surely the Bayesian one, that will be the subject of this chapter.

In section 4.1 the main sources of uncertainty affecting model updating in structural dynamics are highlighted. At the same time, the most important reference works about Bayesian model updating are cited. The mathematical framework of Bayesian model updating is treated in section 4.2. Finally, the Bayesian approach is applied to the calibration of two case studies, a simple numerical benchmark and the FE model of the San Felice sul Panaro fortress. Results of the updating and a comparison with the already presented deterministic approach based on bi-objective optimization are showed in section 4.3 and 4.4, respectively.

4.1 Uncertainty sources and literature review

The response predicted by a model unavoidably differs from the same quantity measured thanks to an experimental test. This discrepancy is denoted as prediction error. Both measurement and modeling errors contribute to prediction error. Measurement error is mathematically defined as the difference between the observed system behaviour and the real system response while model error is the difference between the model predicted behaviour and the real system response. Combining the two definitions, the total prediction error is given by the sum of measurement and model errors.

As regards measurement error, the uncertainty of experimental data may depend on sensor noise or bias caused by imperfections in the measurements equipment. The common limited

number of adopted sensors implies a not detailed spatial information about the structure. Other challenges derive from the approximation introduced by the system identification methods for modal extraction [143] or errors due to signal processing. Furthermore, modal properties suffer variation induced by environmental conditions [132, 155, 45, 140].

Uncertainties depending on the prediction model are no less important. A model is, by definition, not able to reproduce perfectly the behavior of a real system. Lack of knowledge or understanding about the real system leads to make assumptions or simplifications when developing a model. Detailed analysis about model uncertainty, including the classification of several types of uncertainty, can be found in works of Mottershead and Friswell [117], Kennedy and O'Hagan [98], Walker et al. [172]. In summary, uncertainties may arise from incorrect boundary conditions and governing equations, from insufficient accuracy in the characterization of material and geometric properties or load conditions and from the mathematical algorithms that produce the model output.

In this context, one of the most diffused approach for uncertainty quantification in model updating is based on Bayesian inference, since a large amount of scientific publications have been realized on the argument. Reference works about Bayesian model updating in structural engineering was produced by Beck and Katafygiotis [18, 96], Beck [15], Katafygiotis et al. [95] and Jaynes [88]. An important application of this method occurred in the field of structural health monitoring (SHM): the first works about probabilistic damage assessment based on observed modal properties are those of Sohn and Law [157] and Vanik et al. [166]. Later, Ching and Beck [40] employed the concept of system mode shape to improve damage detection, while Yuen et al. [178] introduced system frequencies for the same reason. Bao et al. [11] incorporates temperature as variable affecting modal properties. More recent works have been realized by Behmanesh and Moaveni [20], Behmanesh et al.[21], Yin et al. [175] and Ierimonti et al. [82]. In-depth reviews of Bayesian model updating for damage assessment can be found in Simoen et al. [152] and Huang et al. [80].

4.2 Bayesian model updating

Bayesian model updating provides a stochastic framework for parameter updating by considering the model parameters $\mathbf{x}$ and prediction error as random variables. In this way, different sources of uncertainties can be included in the method. The general principle, founded on the Bayes' theorem, involves the updating through a set of measured data $\mathbf{d}$ of the prior probability distribution of the model parameters $p(\mathbf{x}|\mathcal{M})$ into the posterior distribution $p(\mathbf{x}|\mathbf{d},\mathcal{M})$:

$$p(\mathbf{x}|\mathbf{d},\mathcal{M}) = c^{-1}p(\mathbf{d}|\mathbf{x},\mathcal{M})p(\mathbf{x}|\mathcal{M}) \tag{4.1}$$

where c is the Bayesian evidence, a constant ensuring that the posterior distribution of parameters integrates to one, and it is computed as:

$$c = \int_{\mathbf{I}} p(\mathbf{d}|\mathbf{x},\mathcal{M})p(\mathbf{x}|\mathcal{M})\mathrm{d}\mathbf{x} \tag{4.2}$$

$\mathbf{I} \subset \mathbf{R}^n$ is the integration domain where the product $p(\mathbf{d}|\mathbf{x},\mathcal{M})p(\mathbf{x}|\mathcal{M})$ has a significant value of probability density.

$p(\mathbf{d}|\mathbf{x}, \mathcal{M})$ is the likelihood function representing the plausibility that model $\mathcal{M}$ parametrised by $\mathbf{x}$ provides the measured data $\mathbf{d}$. It reflects the contribution of data in the determination of the updated posterior distribution of parameters.

4.2.1 Prior distribution

The prior distribution $p(\mathbf{x}|\mathcal{M})$ denotes the plausibility of model parameter $\mathbf{x}$ when experimental data are not available. It can be proven that the prior distribution represents a soft constraint in case of ill-conditioned problem providing regularization [25]. Its choice is very significant when the data set is small: in this case, the posterior PDF is highly affected by the prior distribution. On the other hand, when the calibration is performed using a wide amount of data, results of the Bayesian procedure are very similar even starting from different smooth prior distributions.

In the past, some methods have been developed in order to build consistent prior distributions. The most diffused approaches are probably those of conjugate priors [50] and the one based on the principle of maximum entropy [89, 158]. The property of conjugate priors is that the related posterior PDF belongs to the same family of the prior. The choice of the prior family must be in accordance with the likelihood function formulation. This approach enables the exact computation of distributions but, in the context of vibration-based model updating, often implies the need to approximate the likelihood function with a known distribution.

The principle of maximum entropy states that best prior distribution according to the present level of knowledge about the parameter vector $\mathbf{x}$ is the one who enables to obtain the greater information entropy $h(p)$, defined for a continuous random variables with probability density function (PDF) $p(x)$ as:

$$h(p) = E\left[-\ln(p(x))\right] = -\int_{\mathbf{X}} p(x) \ln\left[p(x)\right] \, dx \tag{4.3}$$

where E denotes the expected value and $\mathbf{X}$ is the support of $p(x)$. As reported in Simoen et al. [152], when it is known that a parameter is defined in a given interval, the application of the principle of maximum entropy entails the adoption of a uniform distribution for the parameter. Conversely, if the information about the parameter consist of a finite mean and standard deviation this principle leads to a normal distribution. As concerns multivariate variables, the ME principle implies to use independent prior variables, building the joint distribution $p(\mathbf{x})$ through the product among the marginal PDFs $p(x_i)$ of the single parameters x_i.

4.2.2 Likelihood function

The formulation of the likelihood function depends on the definition of the prediction error. As previously mentioned in section 4.1, it represents the discrepancy between the experimentally measured and predicted features, in this case frequencies and mode shapes. The total prediction error is given by the sum of measurement and model errors. When no information about the individual errors is available, as happens in most cases, the likelihood

function is usually built using the total prediction error. The probabilistic model used for prediction error can be assumed and/or determined in different ways. The usual practice is to assume a known probabilistic model with fixed parameter. In vibration-based model updating, the frequency and mode shape prediction error for a mode m is selected as a zero-mean Gaussian distribution [15, 152]:

$$e_{f_m} = f_{exp,m} - f_{num,m}(\mathbf{x}) \sim N(0, \sigma_{f_m}^2) \tag{4.4}$$

$$\boldsymbol{e}_{\boldsymbol{\phi}_m} = \frac{\boldsymbol{\phi}_{exp,m}}{\left\|\boldsymbol{\phi}_{exp,m}\right\|_2} - l_m \frac{\boldsymbol{\phi}_{num,m}(\mathbf{x})}{\left\|\boldsymbol{\phi}_{num,m}(\mathbf{x})\right\|_2} \sim N(\mathbf{0}, \boldsymbol{\Sigma}_{\boldsymbol{\phi}_m}) \tag{4.5}$$

with the scaling factor l_m already defined in Eq.(2.4). Under the assumption of statistical independence of identified modal properties, the likelihood function can be written as:

$$p(\mathbf{d}|\mathbf{x}, \mathcal{M}) = \prod_{m=1}^{M} N(f_{exp,m}, \sigma_{f_m}^2) N(\boldsymbol{\phi}_{exp,m}, \boldsymbol{\Sigma}_{\boldsymbol{\phi}_m}) \tag{4.6}$$

where $N(f_{exp,m}, \sigma_{f_m}^2)$ is the Gaussian distribution with mean $f_{exp,m}$ and standard deviation σ_{f_m} and $N(\boldsymbol{\phi}_{exp,m}, \boldsymbol{\Sigma}_{\boldsymbol{\phi}_m})$ is a multi-dimensional Gaussian distribution with mean vector $\boldsymbol{\phi}_{exp,m}$ and covariance matrix $\boldsymbol{\Sigma}_{\boldsymbol{\phi}_m}$. $\boldsymbol{\Sigma}_{\boldsymbol{\phi}_m}$ is usually assumed to be diagonal which means that no correlation is considered between different mode shape components.

The variance of the frequency prediction error is expressed as $\sigma_{f_m}^2 = \epsilon_f^2 f_{exp,m}^2$, while the covariance matrix of the mode shape prediction error is expressed as $\boldsymbol{\Sigma}_{\boldsymbol{\phi}_m} = \epsilon_{\boldsymbol{\phi}}^2 \left\|\boldsymbol{\phi}_{exp,m}\right\|_2^2 \mathbf{I}$, where $\mathbf{I}$ is the identity matrix. The coefficients of variation ϵ_f and $\epsilon_{\boldsymbol{\phi}}$ are assumed to be the same for all the frequencies and mode shapes, respectively.

On the basis of the previous assumptions, the likelihood function of Eq.(4.6) can be written as:

$$p(\mathbf{d}|\mathbf{x}, \mathcal{M}) = c_1 \exp\left[-\frac{1}{2} J(\mathbf{x})\right] \tag{4.7}$$

where c_1, that is a function of the coefficients of variation ϵ_f and $\epsilon_{\boldsymbol{\phi}}$, is a normalizing factor [17]. $J(\mathbf{x})$ is a discrepancy function defined as:

$$\begin{aligned} J(\mathbf{x}) = & \frac{1}{\epsilon_f^2} \sum_{m=1}^{M} \left(\frac{f_{num,m}(\mathbf{x}) - f_{exp,m}}{f_{exp,m}} \right)^2 + \\ & + \frac{1}{\epsilon_{\boldsymbol{\phi}}^2} \sum_{m=1}^{M} \frac{1}{\left\|\boldsymbol{\phi}_{exp,m}\right\|_2^2} \left\| \frac{\boldsymbol{\phi}_{exp,m}}{\left\|\boldsymbol{\phi}_{exp,m}\right\|_2} - l_m \frac{\boldsymbol{\phi}_{num,m}(\mathbf{x})}{\left\|\boldsymbol{\phi}_{num,m}(\mathbf{x})\right\|_2} \right\|_2^2 \end{aligned} \tag{4.8}$$

If the coefficients of variation ϵ_f and $\epsilon_{\boldsymbol{\phi}}$ are considered equal, denoted as $\bar{\epsilon}$ in this case, the

expression of the discrepancy function is simplified:

$$J(\mathbf{x}) = \frac{1}{\bar{\epsilon}^2} \sum_{m=1}^{M} \left[\left(\frac{f_{num,m}(\mathbf{x}) - f_{exp,m}}{f_{exp,m}} \right)^2 + \right. \\ \left. + \frac{1}{\left\| \boldsymbol{\phi}_{exp,m} \right\|_2^2} \left\| \frac{\boldsymbol{\phi}_{exp,m}}{\left\| \boldsymbol{\phi}_{exp,m} \right\|_2} - l_m \frac{\boldsymbol{\phi}_{num,m}(\mathbf{x})}{\left\| \boldsymbol{\phi}_{num,m}(\mathbf{x}) \right\|_2} \right\|_2^2 \right] \tag{4.9}$$

In general, no or little information is available about the coefficients of variation of the prediction error, hence a common practice is to fix these parameters in order to simplify the updating procedure. A critical analysis of this practice, along with a more rigorous method to asses the coefficient of variation, is discussed in chapter 5.

4.2.3 Computation of the posterior distribution

In accordance with Eq. (4.1), for the determination of the posterior distribution of parameters $p(\mathbf{x}|\mathbf{d}, \mathcal{M})$ the evaluation of the Bayesian evidence is needed, other than the prior distribution $p(\mathbf{x}|\mathcal{M})$ and the likelihood function $p(\mathbf{d}|\mathbf{x}, \mathcal{M})$. In practice, direct application of Eq. (4.2) for the computation of the Bayesian evidence involves numerical integration of the product between prior distribution and likelihood function over the parameter domain discretized through a grid. This operation becomes unfeasible when the number of updating parameters is high since the number of evaluations of the likelihood functions grows exponentially with the number of parameters. Furthermore, it would be necessary to know a priori in which region of the parameter domain the integrand function (i.e. the product between prior distribution and likelihood function) has a significant value, in order to reduce the extension of the grid as much as possible. For this reason, several approximated methods were developed for the determination of the updated distribution of parameters and the evidence. Among these, a distinction can be made between an analytical method based on asymptotic approximation and numerical methods based on Markov Chain Monte Carlo (MCMC) algorithms.

As concerns the first method, Beck and Katafygiotis [18], under the assumption of globally identifiable model class and that many observed data of the same quantities are available, expanded the logarithm of the likelihood function in Taylor's series around the point $\hat{\mathbf{x}}$ that maximizes the likelihood and employed the Laplace's method to approximate the evidence integral of Eq. (4.2). Consequently, the posterior distribution can be approximated as Gaussian with mean vector equal to the parameter vector $\hat{\mathbf{x}}$ and covariance matrix equal to the inverse of the Hessian matrix calculated at $\hat{\mathbf{x}}$. Laplace asymptotic approximations have been subsequently applied also to the locally identifiable case [18] and to the unidentifiable case [97].

The hypothesis of large amount of data cannot be always satisfied, hence numerical methods like the MCMC samplers can be used. These algorithms generate samples that are consistent with any probability distribution by constructing a Markov chain that has the desired distribution, in this case the posterior distribution, as its equilibrium distribution [80]. Among several MCMC methods proposed, most of them are based on Metropolis-Hastings (MH) algorithm [115, 76] because it enables to sample a random distribution

Table 4.1: Two floor frame: mechanical parameters of the structure

Floor N.	1	2
Mass m [10^3kg]	60.0	60.0
Stiffness multiplier r [-]	2.0	1.5
Stiffness k [kN/m]	16000	12000

defined as the ratio between a function of the same random variable and a normalization constant whose value is unknown. Known methods based on the MH algorithm have been proposed by Haario et al. [74] (adaptive MH MCMC) and Green and Mira [71] (delayed rejection MH MCMC). Beck and Au [16] underlined some difficulties in applying the original Metropolis-Hastings algorithm, related to the influence of the proposal distribution and to the limited region of probability concentration of the posterior PDF. They proposed an adaptive simulation method that was later improved by Ching and Chen [41]. The latter takes the name of Transitional MCMC method. Finally, another class of MCMC methods which has been developed but still not applied in the context of structural engineering is based on evolutionary algorithms [26, 171].

4.3 Case study: two floor frame

A simple case study is first considered in order to asses the influence of prior distribution and likelihood function in given conditions. Moreover, results of the Bayesian model updating are compared with those of the deterministic bi-objective optimization.

4.3.1 Description of the case study

The case study is a shear-type frame composed of two floors and one bay (Fig.4.1). Axial deformation of all the elements is neglected, moreover beams are infinitely rigid in flexure. Distributed masses of the structure are represented as concentrated masses at the floor levels. In table 4.1, masses and stiffness, expressed as multiples of a reference stiffness k_0=8000 kN/m, of each floor are listed. The floor stiffness k_1 and k_2 are thus obtained as:

$$\begin{aligned} k_1 &= r_1 k_0 \\ k_2 &= r_2 k_0 \end{aligned} \tag{4.10}$$

where r_1 and r_2 are the multiplication factors. The subscript is related to the floor number. The corresponding modal properties and the pseudo-experimental values, assumed as reference values in the optimization process, are reported in table 4.2. Pseudo-experimental properties are generated to account for errors that unavoidably affect real measurements. Parameters to identify are the multiplication factors r_1 and r_2 of the base stiffness k_0. Both parameters are searched within the range [0.5; 4].

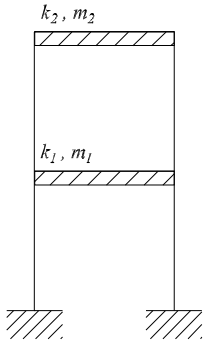

Figure 4.1: Two floor frame: layout of the structure.

Table 4.2: Two floor frame: exact and pseudo-experimental modal properties. The first subscript of the mode shape component indicates the floor number while the second one is the mode number.

Modal properties	Mode N.1			Mode N.2		
	f_1 [Hz]	ϕ_{11} [−]	ϕ_{21} [−]	f_2 [Hz]	ϕ_{12} [−]	ϕ_{22} [−]
Exact	1.535	0.535	1.000	3.812	1.000	-0.535
Pseudo-experimental	1.517	0.769	1.000	3.846	1.000	-0.633

4.3.2 Deterministic model updating

The deterministic approach is based on the solution of a bi-objective optimization problem using the weighted-sum method, as described in section 3.2. The objectives e_F and e_M are expressed by Eqs. (2.1) and (2.2) with γ=1, respectively. The Pareto front obtained is reported in Fig.4.2 where the preferred solution, selected with the criterion of minimum distance from the equilibrium point, is shown in red. This solution represents a compromise between objectives e_F and e_M, since it is located in the central part of the front. The weighting factor, calibration parameters and modal properties associated to the preferred solution are summed up in Table 4.3.

The variation of the updated parameter r_1 and r_2 with the weighting factor α is reported in Fig.4.3(a) and Fig.4.3(b), respectively. Both parameters exhibit variations in the range [1.5; 2], but associated to different trends: updated values of r_1 increase with α, while r_2 shows a decreasing trend.

4.3.3 Bayesian model updating

Bayesian model updating has been performed according to the inference process presented in section 4.2. Six tests have been carried out using two different definitions of the likelihood function and three different prior distributions for parameters. The first definition of the

Table 4.3: Two floor frame: weighting factor α, calibration parameters r_1, r_2 and modal properties of the preferred solution.

α	r_1	r_2	Mode N.1			Mode N.2		
			f_1	ϕ_{11}	ϕ_{21}	f_2	ϕ_{12}	ϕ_{22}
[–]	[–]	[–]	[Hz]	[–]	[–]	[Hz]	[–]	[–]
0.56	1.605	1.847	1.465	0.657	1.000	3.969	-1.000	0.657

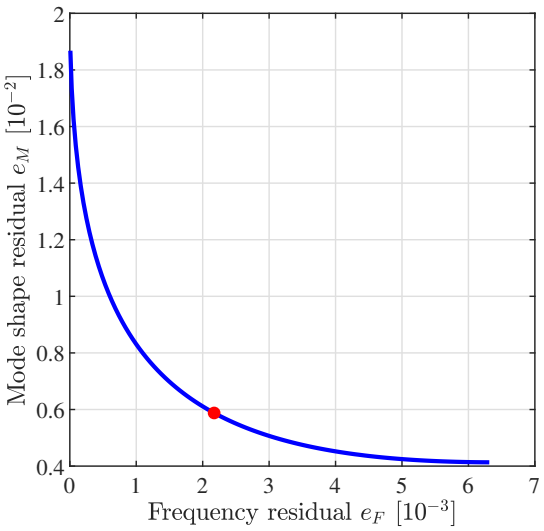

Figure 4.2: Two floor frame: Pareto front. Red dot: preferred solution.

likelihood function is that of Eqs. (4.7) and (4.8) with different coefficients of variation for frequencies (ϵ_f) and mode shapes ($\epsilon_{\boldsymbol{\phi}}$). The second considers a unique value $\bar{\epsilon}$ for the coefficients of variation ((4.8)). The coefficients of variation selected for Eq. (4.8) are ϵ_f=1 % and $\epsilon_{\boldsymbol{\phi}}$=10 %, while that of Eq. (4.9) is $\bar{\epsilon}$=5%. The prior distributions are a non informative uniform distribution and two Gaussian distributions with different values of mean and standard deviation. Table 4.4 illustrates likelihood equation and parameters of the prior distribution used for each test. In the Table, a and b indicate the upper and lower bound of the uniform distribution, respectively, while μ and σ are the mean value and the standard deviation of the Gaussian distribution. In all the tests, calibration parameters are considered as uncorrelated, hence the conjunct prior distribution can be expressed as the product of the marginal distributions. Due to the simplicity of the model and the limited number of the calibration parameters, Bayesian evidence (Eq.(4.2)) has been numerically evaluated on a very dense square grid (step size 0.005 for both r_1 and r_2) built on the domain. Posterior distribution is then obtained according to Eq.(4.1).

Results of updating procedure are listed in Table 4.5. Maximum a posteriori (MAP) values of test N.1, N.2 and N.3 are very similar, showing how in this case the contribution of the likelihood function is predominant with respect to the prior distribution. The same consideration is valid for MAP values of test N.4 and N.5, while those of test N.6 are

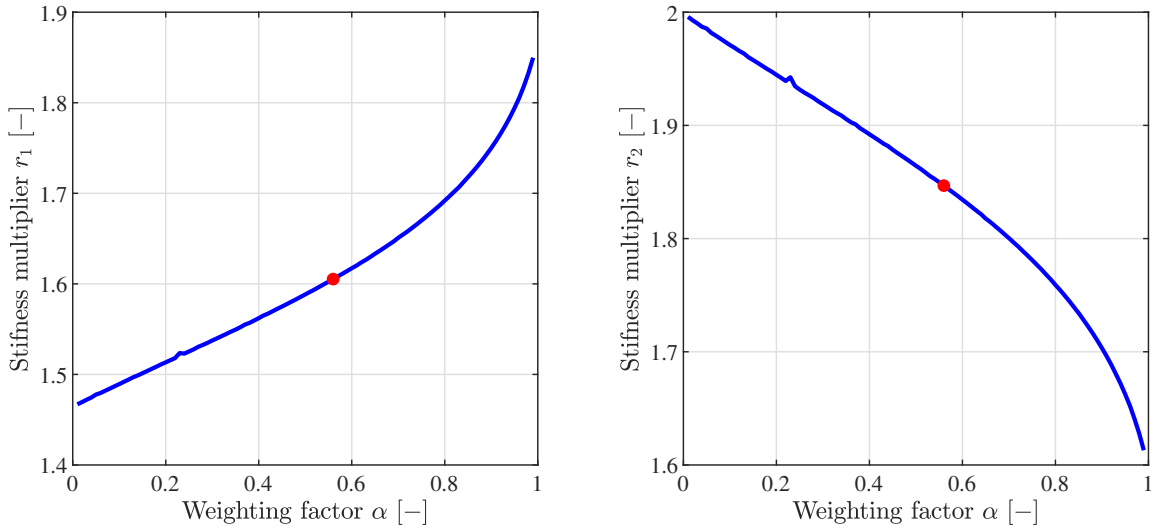

(a) (b)

Figure 4.3: Two floor frame: variation of the parameter (a) r_1 and (b) r_2 with the weighting factor α. Red dot: value of the parameter for the preferred solution.

Table 4.4: Two floor frame: description of the tests for Bayesian model updating.

Test N.	Likelihood equation	Prior distribution	Parameters for r_1	Parameters for r_2
1	(4.8)	Uniform	a=0.5 ; b=4.0	a=0.5 ; b=4.0
2	(4.8)	Gaussian	μ=2.0 ; σ=0.4	μ=1.5 ; σ=0.3
3	(4.8)	Gaussian	μ=3.0 ; σ=0.6	μ=1.0 ; σ=0.2
4	(4.9)	Uniform	a=0.5 ; b=4.0	a=0.5 ; b=4.0
5	(4.9)	Gaussian	μ=2.0 ; σ=0.4	μ=1.5 ; σ=0.3
6	(4.9)	Gaussian	μ=3.0 ; σ=0.6	μ=1.0 ; σ=0.2

different from the previous, especially r_2. As concerns standard deviations, we can compare tests characterized by the same prior distribution and different likelihood function, namely pairs N.1-N.4, N.2-N.5 and N.3-N.6, observing how the lower uncertainty is obtained using Eq.(4.8). Indeed, the comparison between contour plot of the two likelihood functions used, performed in Fig.4.4, shows how in the case of Eq.(4.8) the area of the domain with probability density different from zero is smaller than in the case of Eq.(4.9).

4.3.4 Comparison of results

Table 4.6 presents results obtained by different approaches in terms of calibrated parameters, relative error ϵ for frequencies and MAC value for mode shapes. Relative error for

the m-th frequency is computed as:

$$\epsilon = \frac{f_{num,m} - f_{exp,m}}{f_{exp,m}} \cdot 100 \tag{4.11}$$

Results of the Bayesian model updating for tests N.1, N.2 and N.3 are characterized by smaller relative errors for frequencies compared to the preferred solution of the bi-objective optimization and MAP values of test N.4, N.5 and N.6. On the contrary, a slightly higher correlation with the first pseudo-experimental mode shapes is obtained with the latter.

Fig.4.5 shows solutions obtained with Bayesian model updating in the objective space e_F-e_M, where objectives are defined by Eq.(2.1) and Eq.(2.2) with γ=1: the solutions of tests N.1, N.2 and N.3 (black dot, asterisk and square, respectively) are located in the part of the front characterized by values of α close to one. This highlights the predominant

Table 4.5: Two floor frame: results of the Bayesian model updating.

Test N.	r_1		r_2	
	MAP [−]	σ [−]	MAP [−]	σ [−]
1	1.825	0.069	1.635	0.060
2	1.835	0.068	1.625	0.059
3	1.885	0.078	1.570	0.061
4	1.545	0.143	1.910	0.169
5	1.575	0.135	1.830	0.139
6	1.525	0.135	1.605	0.111

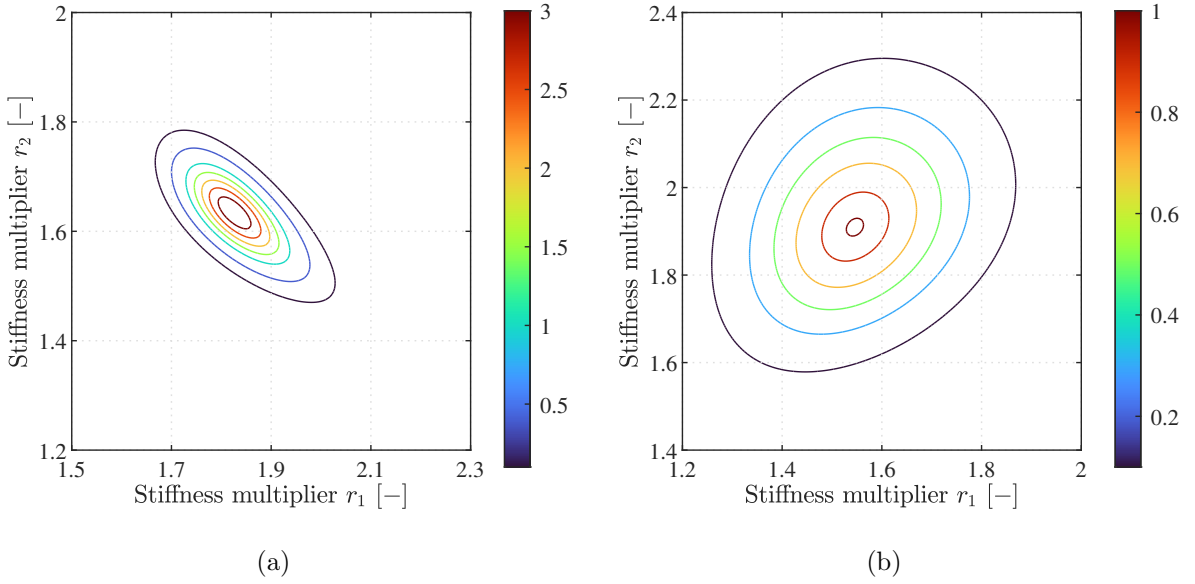

(a) (b)

Figure 4.4: Two floor frame: likelihood function employed for (a) test N.1-N.2-N.3 and (b) test N.4-N.5-N.6 both scaled by a factor 10^{-4}.

Table 4.6: Two floor frame: comparison among the results of the different methods.

Method	r_1 [−]	r_2 [−]	Mode N.1 ϵ [%]	Mode N.1 MAC [%]	Mode N.2 ϵ [%]	Mode N.2 MAC [%]
Deterministic	1.605	1.847	-3.40	99.44	3.19	99.97
Bayesian Test N.1	1.825	1.635	-0.46	98.46	0.46	99.89
Bayesian Test N.2	1.835	1.625	-0.36	98.40	0.33	99.87
Bayesian Test N.3	1.885	1.570	0.00	98.05	-0.41	99.76
Bayesian Test N.4	1.545	1.910	4.06	99.92	-4.44	99.62
Bayesian Test N.5	1.575	1.830	2.59	99.97	-4.20	99.47
Bayesian Test N.6	1.525	1.605	-2.72	100	-6.89	99.16

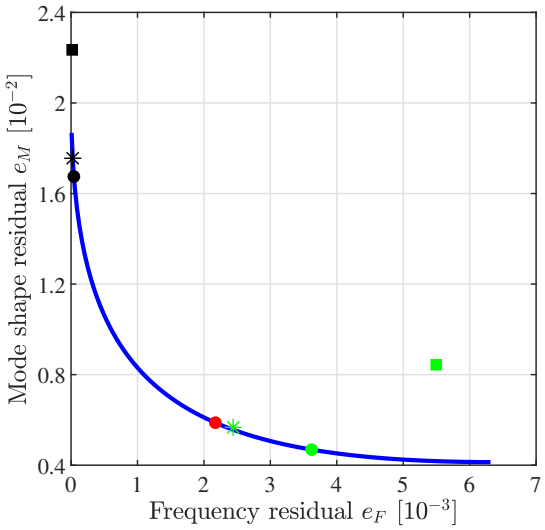

Figure 4.5: Two floor frame: solutions of Bayesian model updating in the objective space e_F-e_M. Red dot: preferred solution of bi-objective optimization. Black dot, asterisk and square: solutions of test N.1., N.2. and N.3. Green dot,asterisk and square: solution of test N.4., N.5. and N.6.

contribution of frequency residuals in the calibration procedure. In particular, solutions of test N.1 and N.2 are non-dominated by other solutions, hence they represent points of the Pareto front. The same for solutions of test N.4 and N.5 (green dot and asterisk, respectively), that are located in another region of the front, closer to the preferred solution of bi-objective optimization (red dot). Instead, solution of test N.6 (green square) is dominated by the Pareto front.

4.4 The San Felice sul Panaro fortress

In this section, the focus is the calibration of the FE model of the San Felice sul Panaro fortress. For the description of the structure, the ambient vibration test and the FE model the reader is referred to section 3.5. In both the approaches considered, namely the deterministic bi-objective optimization and the Bayesian updating, the calibration has been perfermed on the basis of the first three identified modes.

4.4.1 Deterministic model updating

The bi-objective optimization has been conducted considering the objectives defined by Eqs. (2.1) and (2.2) with γ=0.5, the same functions employed in section 3.5.3. Hence, results have been already presented in that section. Refer in particular to the Pareto front of Fig. 3.25(a) and to the table 3.18 where the updated parameters and the weighting factor associated to the preferred solution are listed.

4.4.2 Bayesian model updating

Bayesian model updating has been performed considering a uniform distribution for the prior and the two different expressions for the likelihood function previously defined by Eq.(4.8) and Eq.(4.9). The coefficients of variation selected for Eq. (4.8) are ϵ_f=5 % and ϵ_ϕ=1 %, while that of Eq. (4.9) is $\bar{\epsilon}$=2.5 %. The choice of a very small value for ϵ_ϕ is unusual but has been made in order to obtain a particular solutions, whose properties will be discussed later. The corresponding contour plots, that have been realized on a regular grid with a step size of 25 MPa for both parameters, are reported in Fig.4.6. The global identifiability of the problem is assured considering the first three mode experimentally identified. Indeed, both contour plots show that the likelihood functions have a single peak [177].

Once the MAP value has been identified through the Matlab function "fminsearch", Bayesian evidence (Eq.(4.2)) has been numerically estimated on the grid previously described and the conjunct posterior distribution has been computed according to Eq.(4.1). In table 4.7 the MAP values of E_D and E_U and the corresponding standard deviations, obtained using the different definitions of likelihood function, are summed up. MAP values are similar, almost identical for E_U and with a difference of about 7 % for E_D. Focusing on the uncertainties of parameters, the standard deviation of E_U computed in the second case is lower than in the first one, but the standard deviation of E_D is extremely larger, more than twice. It depends on the coefficient of variation used for the likelihood function (Eq.(4.9)), where the use of a value of 2.5 % determines a distribution very elongated in the E_D direction (see Fig. 4.6(b)). Fig.4.7 enables the comparison between posterior distributions obtained. Despite these differences, standard deviation of E_D is still high in both cases. For this reason, the state of the structure defined on the basis of the modal property identified is uncertain. More data are needed to reduce dispersion. Table 4.8 and 4.9 present the comparison between numerical and experimental modal properties for both situations, where numerical properties are computed considering MAP values of table 4.7.

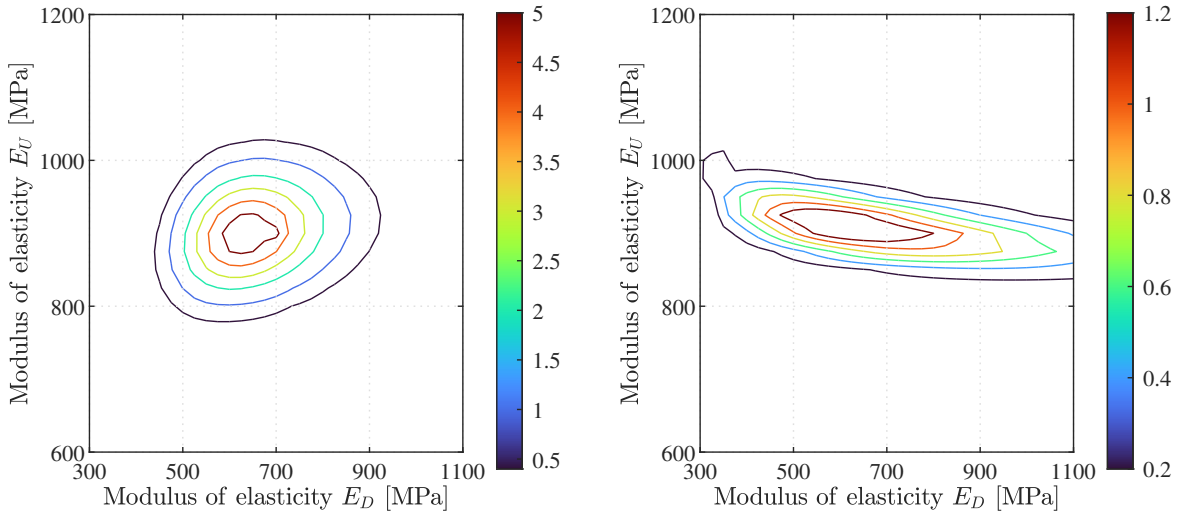

(a) (b)

Figure 4.6: Fortress: likelihood function defined by (a) Eq.(4.8) scaled by a factor 10^{137} and (b) Eq.(4.9) scaled by a factor 10^{-1}.

Table 4.7: Fortress: results of Bayesian model updating.

Likelihood Eq.	E_D		E_U	
	MAP [MPa]	σ [MPa]	MAP [MPa]	σ [MPa]
(4.8)	632	107	904	53
(4.9)	585	234	912	36

Table 4.8: Fortress: experimental and numerical modes - Bayesian approach (Eq.(4.8)).

Mode Shape	Exp. Freq. [Hz]	Num. Freq. [Hz]	ϵ [%]	MAC [%]
1st Bending E-W	1.72	1.79	3.81	94.52
1st Bending N-S	1.75	1.63	−7.43	90.12
1st Torsional	3.55	3.62	2.22	93.58

4.4.3 Comparison of results

Tables 3.18 and 4.7 show that values of parameters updated by deterministic and Bayesian procedure are different, in particular the value of E_D. Also the corresponding frequencies exhibit marked differences, while MAC values are similar for every mode. Fig.4.8 illustrates how solutions of Bayesian model updating represented in the objective space e_F-e_M, where

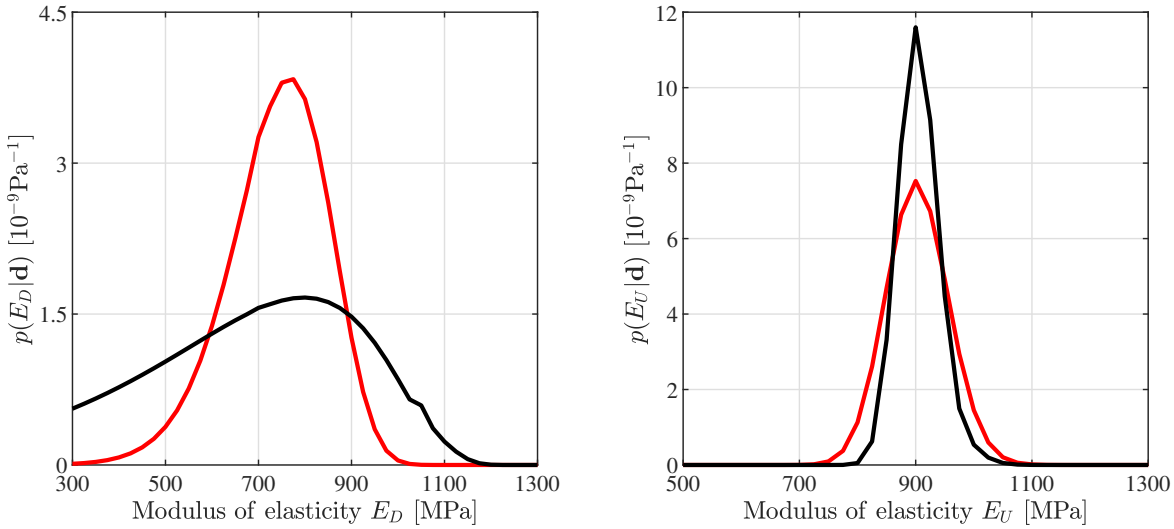

Figure 4.7: Fortress: comparison between posterior probability distributions of (a) parameter E_D and (b) parameter E_U. Red curves: distributions related to likelihood function of Eq.(4.8); black curves: distributions related to likelihood function of Eq.(4.9).

Table 4.9: Fortress: experimental and numerical modes - Bayesian approach (Eq.(4.9)).

Mode Shape	Exp. Freq. [Hz]	Num. Freq. [Hz]	ϵ [%]	MAC [%]
1st Bending E-W	1.72	1.79	3.95	94.53
1st Bending N-S	1.75	1.63	−7.28	90.12
1st Torsional	3.55	3.63	2.36	93.56

objectives are defined by Eq.(2.1) and Eq.(2.2) with γ=0.5, are not optimal solution in the sense of Eq.(3.3). This outcome is not surprising because different discrepancy functions have been used for the Bayesian and deterministic approaches. Solution of Bayesian model updating are located close to the part of the front generated using small values of α, highlighting how in this case the contribution of mode shape error is predominant in the calibration process.

4.5 Concluding remarks

In this chapter, the framework of Bayesian model updating has been presented and the benefits of handling a model updating problem in probabilistic manner highlighted. Moreover, a comparison with a deterministic approach for model updating has been performed

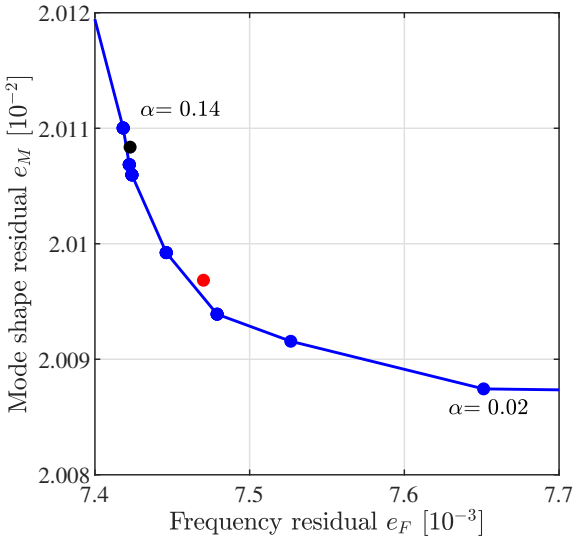

Figure 4.8: Fortress: solutions of Bayesian model updating in the objective space e_F-e_M. Blue dots: solutions of the Pareto front. Red dot: solution obtained using likelihood function of Eq.(4.8). Black dot: solution obtained using likelihood function of Eq.(4.9)

through the calibration of a simple numerical model and the FE model of the San Felice sul Panaro fortress, already described and employed in chapter 3. The deterministic approach is based on the resolution of a bi-objective optimization problem using the DE-S algorithm and on the subsequent choice of the preferred solution as the one characterized by the minimum distance from the equilibrium point of the Pareto front.

For the simple frame model, Bayesian model updating has been carried out considering three different prior distributions and two different likelihood functions with reference to the coefficients of variation. In the first case, the values of ϵ_f and ϵ_ϕ have been set to 1 % and 10 %, respectively. In the second, 5 % have been used for $\bar{\epsilon}$. The influence of the likelihood function turned out to be greater than that of the prior distribution. Moreover, standard deviations of the updated parameter distribution obtained in the first case of likelihood function are about one half of those obtained in the second.

For the fortress, a uniform prior and the two previously defined likelihood functions are considered. The posterior distribution less dispersed is obtained with the first definition of the likelihood function. Anyway, the parameters of the structure updated through the Bayesian framework have large uncertainty, especially E_D. The author believes that a greater number of accelerometers is needed to improve the mode shape accuracy and to increase the number of experimental modes that can be used in the model updating, thus reducing the uncertainty of the updated parameters.

Representation of solutions of Bayesian model updating in the objective space e_F-e_M revealed that in most of the situation analyzed, both for the two-floor frame and the fortress, unbalanced solution in terms of the objective e_F and e_M have been computed. Conversely, the solutions of the deterministic approach, represent, by definition, the best compromise between objectives. According to what has been shown, there is the need to introduce a criterion for choosing the appropriate weight to frequency and mode shape errors in the

Bayesian updating framework.

Chapter 5

Bayesian selection of residual weights

When dealing with the construction of the likelihood function, incorrect assumptions regarding the characteristic of the prediction error may unfairly influence the Bayesian updating results. An example has been provided by the calibration of the two case studies showed in section 4.3 and 4.4. In both cases, the solutions of the updating are affected by the predominant contribution of a residual, the frequency residual for tests N.1, N.2 and N.3 of the two-story frame and the mode shape residual for the fortress.

With reference to section 4.2.2, the incorrect assumptions may be related to fixed coefficient of variation of the prediction error, unknown a priori, or to uncorrelated or zero-mean probabilistic model. In this regard, the Bayesian inference framework enables to make use of the available data and to include the error parameters in the updating process in order to identify the characteristics of the prediction error [152]. The problem of unknown coefficients of variation has been addressed by Christodoulou and Papadimitriou [43], Papadimitriou [129], Zhang et al. [182] and Goller et al. [69] through their selection performed at the Bayesian model class selection level. In the cases, the uncorrelated and zero-mean model assumption for the prediction error is maintained. However, when errors are correlated or characterized by systematic components, the adoption of the previous probabilistic model is obviously not well suited. More refined studies have been realized by Kennedy and O'Hagan [98], who tried to estimate the parameters of a systematic error, and Simoen et al. [153], who focused on correlation parameters.

In this chapter, the author focuses on the determination of the optimal coefficients of variation of the prediction error, that are not supposed to be fixed a priori. Their relationship with the weights in bi-objective optimization is treated and, with reference to two real case studies, a comparison between methodologies is realized. Moreover, a surrogate-assisted procedure, aimed at reducing the computational cost of Bayesian model updating, is applied for calibration of the case studies.

The chapter is organized in this way: section 5.1 presents the theoretical framework of Bayesian Model Class Selection and the relationship between coefficients of variation and weights in bi-objective optimization; in section 5.2 the surrogate-assisted procedure is described. Finally, the results and the comparison between Bayesian and deterministic approaches are discussed with reference to the case studies of the San Felice sul Panaro fortress (section 5.3) and of the Ficarolo bell tower (section 5.4).

5.1 Bayesian model class selection

Bayesian model class selection (BMCS) is an additional level of model updating where the focus is addressed to the selection of the most plausible model class from a set of alternatives according to the measured data $\mathbf{d}$. Considering a discrete set of model classes $\boldsymbol{\mathcal{M}} = \{\mathcal{M}_k : k = 1, 2, ..., N_{MC}\}$, the Bayes' Theorem expressed at model class level updates the prior probability $P(\mathcal{M}_k|\boldsymbol{\mathcal{M}})$ into the posterior $P(\mathcal{M}_k|\mathbf{d}, \boldsymbol{\mathcal{M}})$ through the information contained in $\mathbf{d}$:

$$P(\mathcal{M}_k|\mathbf{d}, \boldsymbol{\mathcal{M}}) = \frac{p(\mathbf{d}|\mathcal{M}_k)P(\mathcal{M}_k|\boldsymbol{\mathcal{M}})}{p(\mathbf{d}|\boldsymbol{\mathcal{M}})} \tag{5.1}$$

If all the model classes are considered equally plausible a priori, the posterior probability depends exclusively on the factor $p(\mathbf{d}|\mathcal{M}_k)$, which is the Bayesian evidence for the model class $\mathcal{M}_k$, previously defined in the Eq.(4.2) for a generic model class $\mathcal{M}$. The denominator of Eq.(5.1) is a constant ensuring that the sum of the posterior probabilities related the all model classes gives 1. It is computed as:

$$p(\mathbf{d}|\boldsymbol{\mathcal{M}}) = \sum_{k=1}^{N_{MC}} p(\mathbf{d}|\mathcal{M}_k)P(\mathcal{M}_k|\boldsymbol{\mathcal{M}}) \tag{5.2}$$

where N_{MC} is the number of model classes composing the set $\boldsymbol{\mathcal{M}}$.

In [15] it was proven how the logarithm of the Bayesian evidence is obtained by the difference between two terms:

$$\ln\left[p(\mathbf{d}|\mathcal{M}_k)\right] = \int_{\mathbf{I}} \ln\left[p(\mathbf{d}|\mathbf{x}, \mathcal{M}_k)\right] p(\mathbf{x}|\mathbf{D}, \mathcal{M}_k)\, d\mathbf{x} - \int_{\mathbf{I}} \ln\left[\frac{p(\mathbf{x}|\mathbf{D}, \mathcal{M}_k)}{p(\mathbf{x}|\mathcal{M}_k)}\right] p(\mathbf{x}|\mathbf{D}, \mathcal{M}_k)\, d\mathbf{x} \tag{5.3}$$

The first term on the right hand side (RHS) of Eq. (5.3) quantifies the ability of the model to fit the data (average data-fit in the following), while the second is the relative entropy of the posterior $p(\mathbf{x}|\mathbf{D}, \mathcal{M}_k)$ with respect to the prior $p(\mathbf{x}|\mathcal{M}_k)$. The latter is a penalty term based on the model complexity. It penalizes more complicated models, that extract more information from the data. We refer to this term with the denomination information gain. In a general case, the number of model parameters affects the model complexity, hence the information gain increases with the number of model parameters [19].

Bayesian model class selection has been applied for different purposes. A first option is to use BMCS to select between different mechanical prediction models with the aim to reduce model error. Muto and Beck [120] performed the selection among a set of hysteretic structural models which give realistic responses to seismic loading. Mthembu et al. [118] used the Bayesian evidence to analyse competing FE models for two real case studies. In both cases, the updating procedure is carried out on the basis of measured natural frequencies.

The other approach relies on the determination of the optimal probabilistic model in order to represent the prediction error as well as possible. Some works in this field have been cited in the introduction of this chapter. With reference to the selection of the optimal coefficients of variation of the prediction error, model classes that compose the set $\boldsymbol{\mathcal{M}}$ are

characterized by different values of parameters ϵ_f and ϵ_{ϕ}. The number of parameters of all the model classes is always the same, so the penalty term of Eq.(5.3) depends exclusively on the amount of information extracted from the data. It is associated, in turn, to the relative weigh attributed to frequency and mode shape errors through the parameters ϵ_f and ϵ_{ϕ}.

Comparing the Eq. (4.8) with the Eqs.(2.1),(2.3) and (2.5), it is clear that the weights in the bi-objective optimization are inversely proportional to the frequency and mode shape coefficients of variations when no prior information about updating parameter is available, as widely reported in literature [43, 152]. Therefore, the relationship between the weighting factor α in bi-objective optimization and the quantity $\beta = \epsilon_{\phi}^2/\epsilon_f^2$ can be easily obtained as:

$$\alpha = \frac{\beta}{\beta + 1} \tag{5.4}$$

Once the optimal coefficients of variation are determined thanks to BMCS, a comparison with the weighted sum method can be performed computing the equivalent α with Eq. (5.4).

5.2 Surrogate for the estimation of the Bayesian evidence

Drawbacks that arise in the direct application of Eq. (4.2) have been discussed in section 4.2.3, as well as different methods for the computation of the posterior distribution have been cited. In this work, the author proposes the use of a Gaussian surrogate for the computation of the Bayesian evidence. The surrogate approximates the implicit-defined integrand function, namely the product between prior distribution and likelihood function. The computational cost of the integration operation on the surrogate model is significantly smaller than that of the original function, especially for large complex structures as historical masonry structures. The surrogate must be as accurate as possible using as few simulation evaluations as possible. The process to define a surrogate comprises three major steps which will be repeated iteratively:

1. Sample selection;
2. Construction of the surrogate model and calibration of model parameters;
3. Model validation and evaluation of the surrogate accuracy.

The accuracy of the surrogate depends on (i) the number and location of samples and (ii) a proper choice of the function that approximates the original implicit-defined function.

The complete procedure used in this work to define the surrogate can be summarized as follows:

1. Select a training dataset containing N samples. Each sample is a D-dimensional point with D equal to the number of unknown structural parameters to be calibrated. The

samples are selected by means of the Latin hypercube sampling (LHS) method. The Latin hypercube sampling method produces well-distributed set of sample points and avoids regions in the research space without samples or datasets with close points [83].

2. Compute the likelihood function of Eq. (4.7) by solving the Finite Element model for all samples of the selected dataset.

3. Identify a subset of data composed of samples for which the logarithm of the integrand has a value larger than the 30 % of the maximum value computed at point 2.

4. In the case an inadequate number of samples are selected in the step 3, reduce the research domain in a region close to the sample with the maximum values of the integrand function and select a new dataset. Compute the value of the integrand function for the new dataset.

5. Generate the surrogate by calibrating its parameters on the basis of the samples evaluated at points 1 and 3. In this paper a D-dimensional Gaussian function is used.

6. Compute the evidence from Eq. (4.2).

7. Validate the model. To do that, select a number N_2 of new samples, calculate the prediction error (i.e. the difference among the likelihood function predicted by the surrogate and those calculate solving the FE model) and verify if the quality of the fitting operation is satisfying. In this work, this occurs on the basis of two conditions. The first is related to the residuals of the fitting operation: if the mean value of the residuals is lower than a certain threshold it is not necessary to compute further points on the domain. However, it may happen that the surrogate is not able to accurately represent the distribution to be fitted. In this case the first condition cannot be satisfied and the operation stops when the relative change in the parameter values of the surrogate is lower than a fixed threshold.

8. Stop the procedure if the convergence is reached. Otherwise, repeat steps 3-7 adding points in a search space in the neighbouring of the points with the maximum value of the function predicted by the surrogate. The calibration of the surrogate has to be carried out taking into account also the samples evaluated in the previous iterations.

Based on the above listed procedure, the Bayesian model updating framework allows to determine the updating parameters and their uncertainties with a limited computational cost. The model parameters can be identified by selecting the maximum of the posteriori distribution (MAP) after the Bayesian evidence is numerically calculated with the surrogate.

5.3 The San Felice sul Panaro fortress

In this section, the comparison between results of the different approaches proposed and the assessment of the computational cost of the different procedures are performed for

the FE model of the San Felice sul Panaro fortress. The description of the structure, the ambient vibration test and the FE model can be found in section 3.5.

5.3.1 Bi-objective optimization and selection of the preferred solution

The bi-objective optimization has been performed with the weighted sum method (see section 3.2) adopting the objectives e_F and e_M defined by Eqs. (2.1) and (2.3). The definition of e_M is different from that employed in section 3.5.3, so different results are obtained. In this way, frequency and mode shape residuals are equal to those involved in Eq. (4.8) for Bayesian model updating and a direct comparison can be conducted. The weighting factor varies in the range [0.01; 1] with step size of 0.01. The associated Pareto front is shown in Fig. 5.1(a), while Fig. 5.1(b) illustrates the variation of the updated parameters with the weighting factor α. When α is between 0.01 and 0.7, the variation of the parameters E_U and E_D is very limited. Indeed, the solutions obtained varying the weighting factor in that range are all overlapped in few points located at the extreme right region of the front (Fig. 5.1(a)). This means that the modification of α in the range [0.01, 0.70] does not produce a wide variety of solutions for the optimization problem.

Considering the remaining values of α, a significant variation of the updated parameters is found, especially for E_D. At the same time, in the objective space there is a gap among the first points of the front placed on the right and the others. This is a drawback of the weighted sum method, namely that a uniform distribution of the weighting factors does not allow to generate a uniform distribution of the non-dominated solutions.

Fig. 5.2(a) compares the solutions estimated at the subsequent iterations of the direct procedure (Eq. 3.26) with those forming the Pareto front. The optimal solutions estimated from the two procedures are highlighted in Fig. 5.2(b). It can be observed from Fig. 5.2(a) that all the solutions obtained from the subsequent iterations of the direct procedure allow to identify the particular non convex shape of the front. The same consideration could have been drawn if all the solutions evaluated from the classical procedure were represented, rather than only the optimal ones.

As concerns the preferred solution of the classical procedure, the point corresponding to the range [0.48, 0.70] for the weighting factor has been selected using the criterion of the minimum distance from the equilibrium point. The value of the updated parameters E_U and E_D is 912 MPa and 585 MPa, respectively. The comparison between the experimental modal properties and those related to the preferred solution is reported in Table 5.1. The preferred solution identified by the direct procedure, shown in Fig. 5.2(b), is slightly different from the one found through the classical procedure because the direct one evaluates a subset of solutions that is not computed by the classical one and that has smaller distances from the equilibrium point.

5.3.2 Bayesian model updating and model class selection

Bayesian model updating and model class selection (see section 5.1) have been carried out in order to determine the optimal coefficients of variation ϵ_ϕ and ϵ_f and the posterior

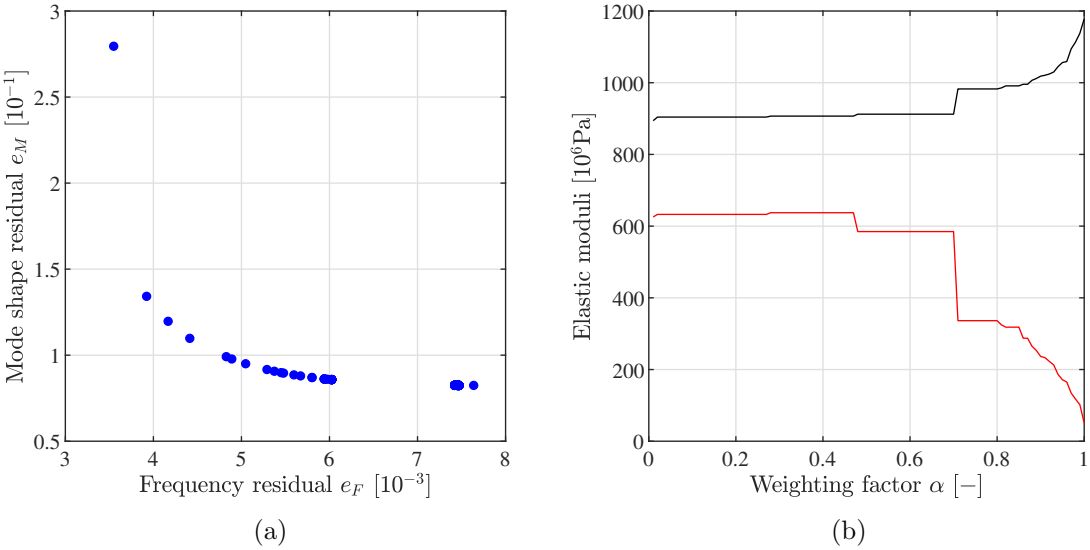

Figure 5.1: Model updating of the fortress FE model with bi-objective optimization: (a) Pareto front and (b) variation of E_U (black) and E_D (red) with the weighting factor.

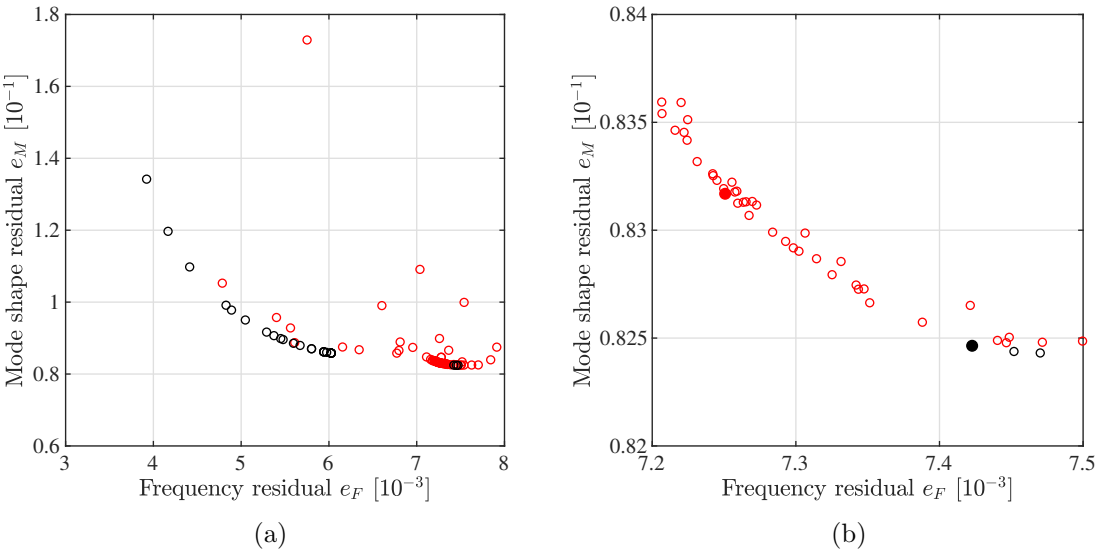

Figure 5.2: Fortress: (a) comparison between points evaluated from different procedures and (b) detail about the preferred solutions. Black circles: Pareto front computed with the classical procedure; red circles: points evaluated from the direct procedure; black dot: preferred solution for the classical procedure; red dot: preferred solution for the direct procedure.

Table 5.1: Fortress: comparison between the preferred solution of bi-objective optimization and the experimental modes.

Mode Shape	Exp. Freq. [Hz]	Num. Freq. [Hz]	ϵ [%]	MAC [%]
1st Bending E-W	1.72	1.79	3.95	94.53
1st Bending N-S	1.75	1.63	−7.28	90.12
1st Torsional	3.55	3.63	2.36	93.56

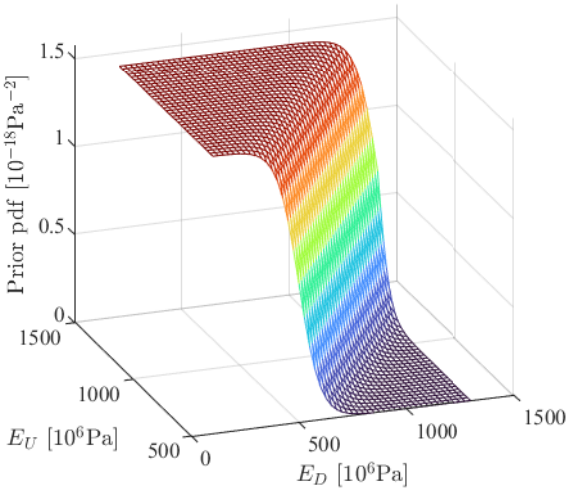

Figure 5.3: Fortress: second prior distribution employed in Bayesian model updating.

distribution of the parameter vector $\mathbf{x}$.

Two different prior distributions have been chosen for the updating. The first is a non-informative uniform distribution, while the second accounts for the damaged condition of the structure. Indeed, it is unlikely that the damaged areas have an equivalent elastic modulus larger than the one of the undamaged regions. This restriction is performed using the prior distribution:

$$p(\mathbf{x}|\mathcal{M}) = k^{-1}\frac{1}{1+\exp\left[-q(E_U - E_D)\right]} \tag{5.5}$$

where q is a parameter that controls the slope of the descending part and k is a constant ensuring that the distribution integrates to one. The 3D plot of the distribution of Eq. (5.5), obtained using a value of 0.2 for the parameter q, is shown in Fig. 5.3. The analysis carried out with the two different prior distributions are referred to as case 1 (non-informative uniform distribution) and case 2 (distribution that accounts for the damaged condition, Eq. (5.5)). The likelihood function is defined by Eqs. (4.7) and (4.8). The same parameter grid introduced in section 4.4.2 has been used for the computation of the Bayesian evidence.

First, the optimal coefficients of variation ϵ_ϕ and ϵ_f are selected on the basis of the Bayesian evidence. Fig.5.4 shows the contour plot of the posterior probability for case 1 and for

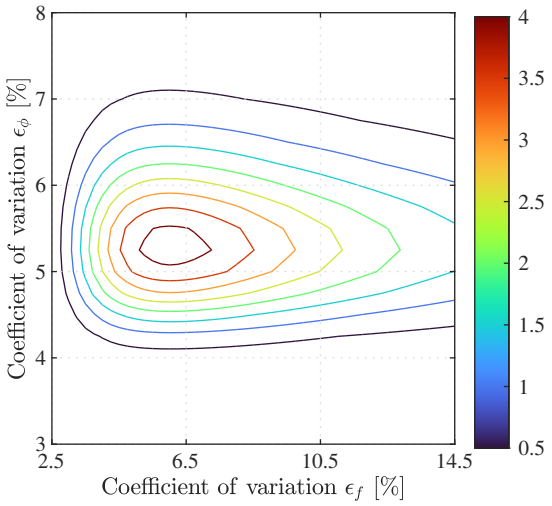

Figure 5.4: Fortress: contour plot of the posterior probability, scaled by a factor of 10^3, for different values of the coefficients of variation ϵ_f and $\epsilon_{\boldsymbol{\phi}}$.

different values of the variance coefficients. ϵ_f and $\epsilon_{\boldsymbol{\phi}}$ ranges, respectively, from 1 % to 15 % and from 1 % and 20 % with step size of 0.25 %. The optimal pair of coefficients, that corresponds to the pair with the maximum posterior probability, is ϵ_f=6 % and $\epsilon_{\boldsymbol{\phi}}$=5.75 %. Moving away from the maximum it can be observed that the slope of the distribution is steeper in the $\epsilon_{\boldsymbol{\phi}}$ direction, highlighting the more sensitivity of the posterior probability towards the mode shape coefficient. Results of case 2 are not represented since the optimal pair of variance coefficients are the same of case 1 and the posterior probability distribution is very similar.

For the optimal pair of variance coefficients, the posterior marginal distributions of updating parameters are reported in Fig. 5.5. The distributions of E_U for the two cases are very similar, while some differences are observed for E_D. In particular, the distribution of case 1 is characterized by an almost constant value of probability density for a large part of the domain. In the second case, the variability of the parameter is still remarkable, but reduced if compared to the first case. Mean values and standard deviations are listed in Table 5.2.

It is interesting to analyze the uncertainty related to updated parameters by varying the pair of the coefficients of variation. For the case 2, that involves the prior distribution of Eq. (5.5), the trend of the standard deviation for parameters E_D and E_U is reported in Fig. 5.6. For both parameters, the minimum values of standard deviations are obtained at the left boundary of the plot, for very small values of ϵ_f. Moving in the ϵ_f direction there is an abrupt increase of σ until the value of about 3%, then the slope slightly decreases for E_U while for E_D there is an almost flat development. The optimal pair of coefficients, identified on the basis of the Bayesian evidence, is not associated with the minimum standard deviation. The solutions characterized by low values of the standard deviation are examined in section 5.3.4 through the comparison with bi-objective optimization results.

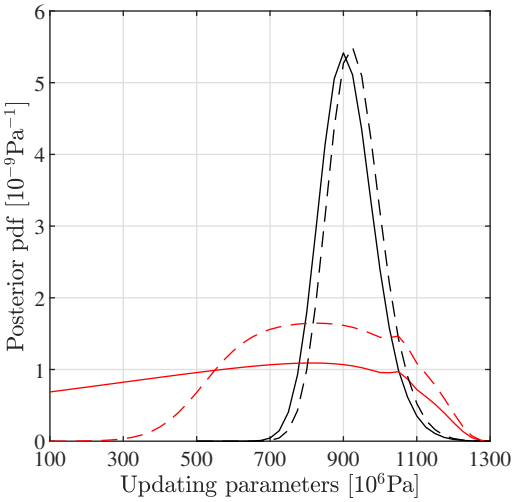

Figure 5.5: Fortress: marginal posterior distribution of the updating parameters. Black continuous line: distribution of the parameter E_U for the case 1; red continuous line: distribution of the parameter E_D for the case 1; black dashed line: distribution of the parameter E_U for the case 2; red dashed line: distribution of the parameter E_D for the case 2.

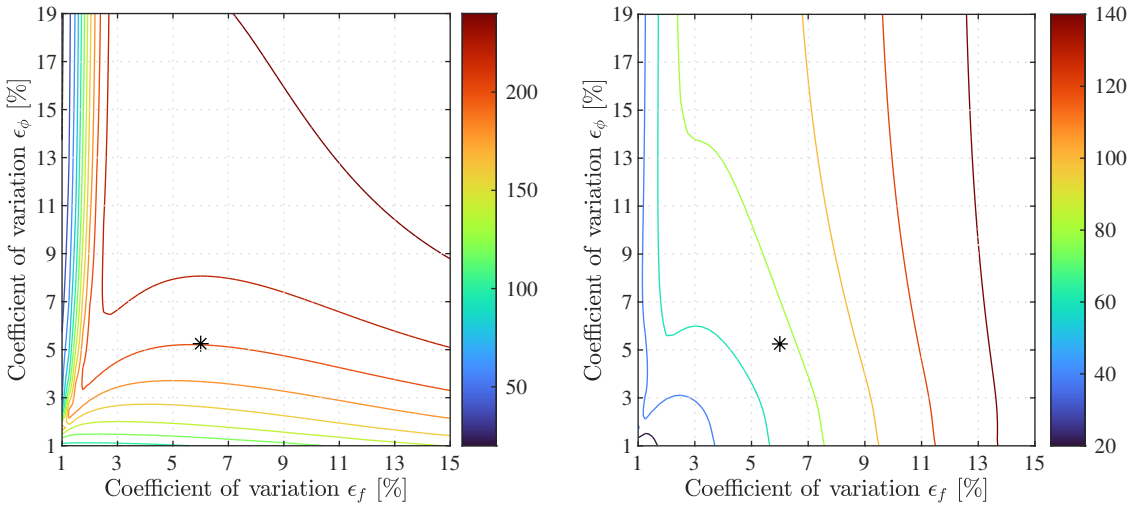

(a) (b)

Figure 5.6: Fortress: contour plot of the standard deviation expressed in 10^6 Pa for the parameters (a) E_D and (b) E_U in function of different values of the variance coefficients. Black asterisk: optimal solution identified on the basis of the Bayesian evidence.

Table 5.2: Fortress: mean values (μ) and standard deviations (σ) of the updated parameters.

Case	μ_{E_U} [10^6Pa]	σ_{E_U} [10^6Pa]	μ_{E_D} [10^6Pa]	σ_{E_D} [10^6Pa]
1	913	76	743	296
2	933	75	576	200

Table 5.3: Fortress: mean values (m) and coefficients of variation (CV) over the 100 repetitions of the logarithm of the evidence ($\log p(\mathbf{d}|\mathcal{M})$) and of the posterior distribution parameters (μ_{E_U},σ_{E_U},μ_{E_D},σ_{E_D}) estimated thanks to the Gaussian surrogate.

Case	$\log p(\mathbf{d}\|\mathcal{M})$		μ_{E_U}		σ_{E_U}		μ_{E_D}		σ_{E_D}	
	m [-]	CV [%]	m [10^6Pa]	CV [%]	m [10^6Pa]	CV [%]	m [10^6Pa]	CV [%]	m [10^6Pa]	CV [%]
1	31.96	0.1	905	0.4	75	44.0	754	4.3	429	14.8
2	32.00	0.2	921	0.4	74	23.7	585	3.3	243	9.9

5.3.3 Use of the surrogate for the computation of the evidence

Bayesian model updating and model class selection is performed adopting the approximated procedure that involves the use of a surrogate, as described in section 5.2. The variability of the procedure is assessed by repeating 100 times the updating considering both prior distributions (non-informative uniform distribution and that of Eq. (5.5)) and fixed values of the likelihood function coefficients of variation ϵ_f and ϵ_{ϕ}, taken equal to the optimal ones determined in subsection 5.3.2. Statistics about the natural logarithm of the evidence and the posterior distribution parameters is summed up in Table 5.3.

Results reveal how the evidence is well estimated for both cases with a low variability since the exact values of the natural logarithm of the evidence are 31.96 and 31.95 for case 1 and 2, respectively. Instead, focusing on the posterior distribution parameters, we note important differences between the two cases. Mean values of case 1 are very similar to the exact values and characterized by a low coefficient of variation but the standard deviation of E_D is significantly over-estimated. This occurs because the product between prior distribution and likelihood function, shown in the contour plot of Fig. 5.7(a), is different from a Gaussian distribution. Consequently, the fitting function is not suitable for the approximation and, in order to match the right tail of the distribution, that is more elongated than the left one, σ_{E_D} is over-estimated. Furthermore, both standard deviation σ_{E_U} and σ_{E_D} are highly variable.

As concerns the case 2, all parameters are calibrated with sufficient accuracy, with a maximum relative error of 21.5 % for σ_{E_D}, that is significantly lower compared to case 1. In this case the extension of the distribution tails in the E_D direction are comparable (Fig. 5.7(b)).

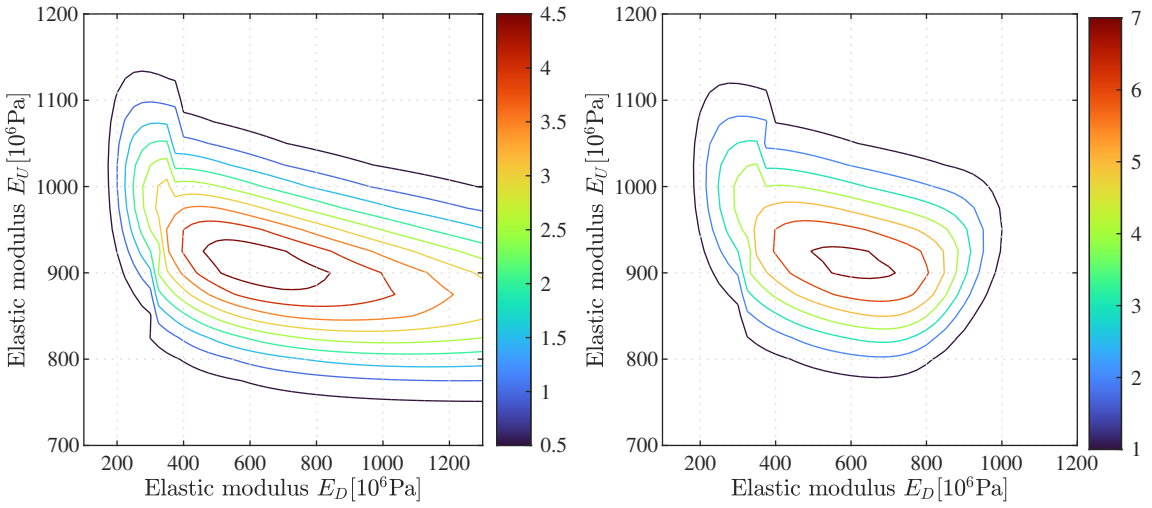

Figure 5.7: Fortress: contour plot of the product between prior distribution and likelihood function scaled by a factor 10^4. (a) case 1, (b) case 2.

5.3.4 Comparison between updating methods

MAP solutions of Bayesian model updating, obtained changing the coefficients of variation ϵ_f and ϵ_ϕ of the likelihood function as described in paragraph 5.3.2, are represented in the objective space e_F-e_M. The plot is illustrated in Fig. 5.8. Bayesian solutions are Pareto-optimal solutions that are not associated to a uniform distribution of weights. The only difference with the bi-objective optimization results involves the point corresponding to α=1.00, that has not been computed because it corresponds to a solution with $\epsilon_\phi \to +\infty$.

In section 5.1 it has been demonstrated how, considering the objectives e_F-e_M defined by Eqs.(2.1)-(2.3) and the likelihood function defined by Eqs.(4.7)-(4.8), there is an equivalence between the weighting factor α of bi-objective optimization and the coefficient β for Bayesian model updating (see Eq.(5.4)).

As concerns the selection of the optimal coefficients of variation, the equivalent weighting factor α for the Bayesian procedure computed with Eq.(5.4) is 0.43, while the range of preferred weighting factors selected with the criterion of the minimum distance from the equilibrium point, that in this specific case corresponds to the same updated parameters, is [0.48, 0.70]. These two solutions are not the same but they are close in the objective space. Considering only the term of the evidence related to the average data-fit (namely the first term on RHS of Eq. (5.3)), so neglecting the penalty term based on the information gain, the equivalent weighting factor associated to the optimal variance parameter is 0.52. Therefore, the latter is equal to the preferred solution of deterministic bi-objective optimization in terms of updated parameters.

Focusing on those Bayesian solutions characterized by low values of uncertainty (see Fig.5.6), although their standard deviations are the minimum found, they are not well balanced solutions in terms of frequency and mode shape residuals. The equivalent weighting factor is equal to 0.99, so they are in an extreme region of the front and are related to a high

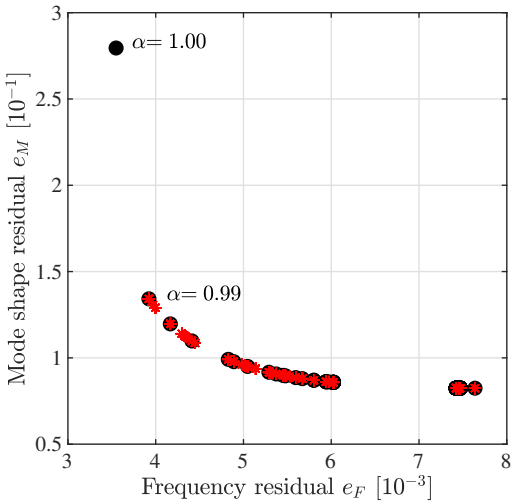

Figure 5.8: Fortress: Bayesian solutions in the objective space (red asterisks) together with the Pareto front (black dots) obtained with the bi-objective optimization.

value of mode shape residuals, as illustrated in Fig. 5.8. Computing the MAC value between experimental and numerical mode shapes, we obtain 90.19 %, 81.43 % ad 93.06 % for the first three the experimental modes. If we compare them with the MAC values of the preferred solution, listed in Table 5.1, we can remark how the correlation of the first and the second mode decreases of about 4 % and 9%, respectively. Moreover, the updated parameters of the solution corresponding to α=0.99 are very different from those of the preferred solution, as we can see in Fig. 5.1(b).

Finally, the computational burden of all the methods employed is analyzed. The classical Bayesian approach, that is performed through a parameter grid, needs 1617 evaluations of the likelihood function. At each evaluation a modal analysis of the FE model is realized. The efficiency is significantly improved with the surrogate-based procedure that requires only 90 evaluations. As regards the deterministic methods, the whole Pareto front has been built with a total amount of 3772 evaluations, on average 38 evaluations per point of the front. The direct procedure of section 3.4 takes 120 repetitions of a modal analysis, about 3 times the number needed for one point of the front, but allows to immediately select the preferred solution.

5.4 The Ficarolo bell tower

In this section, the subject of the comparison is the calibration of the FE model of the Ficarolo bell tower.

5.4.1 Description of the structure

The structure, showed in Fig. 5.9, is a masonry bell tower located in the city of Ficarolo (Veneto, Italy). Its construction started in 1777, after the realization of the neighbouring

Figure 5.9: The Ficarolo bell tower and the Saint Antonio Martire Church.

Saint Antonio Martire Church. The peculiarity of the tower is its impressive vertical inclination with a mean tilt angle of about 3° for the central portion. For this reason, it is known in Italy as "Pisa of Veneto", recalling the more famous tower of Pisa, whose maximum inclination reaches 4°.

The bell tower is composed of a double-barreled masonry structure with a spiral staircase connecting the two shaft from the ground level up to 45 meters where the belfry starts. The tower is about 68 m high and has a variable cross section whose dimension is variable, from about 8.50 m at the base up to 5.30 m at the cusp level. Two intermediate masonry cross-vaulted floors are located at the level of 45.0 m and 53.0 m, the first of those support the belfry. The outer shaft is a multi-leaf masonry wall with deceasing thickness (from 230cm at the base up to 40 cm at the belfry level), while the inner shaft has a single-leaf masonry wall of constant thickness equal to 15 cm.

Due to the Emilia earthquake occurred in 2012, the structure has suffered serious damage, thus retrofitting interventions where planned and performed in 2014. The main operations concerned: (i) the positioning of different types of external steel rings at the level of belfry and cusp structures, (ii) the insertion of two rigid floor timber floors at the height of 51.0 m and 59.0 m, (iii) local injection of mortar, rebuilding and repointing of the mortar joints, (iv) the rebuilding of cracked zones (especially in the area of the masonry cusp) and (v) the strengthening of masonry walls with carbon bars embedded in the masonry with epoxy resin.

5.4.2 Ambient vibration testing and modal identification

The dynamic behaviour of the Ficarolo bell tower has been characterized thanks to two ambient vibration tests performed before and after the aforementioned strengthening inter-

vention. The experimental campaign and the modal parameter identification are presented in the present section. Since the model calibration is performed with reference to the actual condition of the tower (namely after the strengthening), the identification of modal parameters presented in the following refers to that condition.

The dynamic tests were performed by means of the SHM602 system, namely a MEMS-based system developed by the University of Bologna and the University of Modena and Reggio Emila and engineered by Teleco SpA [73]. The system relies on an advanced architecture composed of digital buses and MEMS sensors presenting a noise floor of about 0.3-0.5 mg. The SHM602 system components consist in a controller and storage unit and several bus-connected sensing units. The main advantages of the bus connection are the prevention against electromagnetic interferences and a high degree of reliability. Each sensing unit can measure the temperature and the accelerations along two orthogonal axes, with a sampling frequency between 20 Hz and 80 Hz. The main peculiarities of this system are the digital data transmission and the possibility of performing some system analyses directly on-board of the sensors, which allows transferring only the processed synthetic data to the main computer.

To identify as many natural modes as possible, 11 biaxial MEMS-based accelerometers were arranged in six levels, namely the ground, 13.2 m, 18.4 m, 31.4 m, 45.1 m and 51.0 m. Except for the ground, two units are placed at each instrumented level at the opposite corners to better identify both translational and torsional mode shapes. Each sensing unit can measure accelerations along two orthogonal axes so that four time histories are attained for each section. One sensor is located at the ground level to acquire potential seismic events that could occur during the experimental campaign, which lasted three days. The instrumented levels and the layout of the accelerometers (R0-R5, N1-N5) are shown in Fig.5.10. The sensors were installed on the inner walls by means of metal plates and screws, as shown in Fig.5.11.

Fig.5.12(a) presents an example of the structural acceleration measured at the upper instrumented level, which ranges between -2 mg and 2 mg. The corresponding PSD function is shown in Fig.5.12(b), where three peaks can be recognized. The modal parameters are identified by applying the Enhanced Frequency Domain Decomposition method to the acquired accelerations [27]. The first five identified modes are represented in Fig.5.13, where the corresponding natural frequencies are indicated. The first four modes involve bending in the two directions, while the fifth mode is a torsional mode. Bending modes in X and Y direction are characterized by very close spaced frequency, due to the square plan and the stiffness symmetry in the two directions.

5.4.3 FE model of the bell tower

A FE model of a three-dimensional cantilever beam discretized in 32 elements with flexural and shear deformability has been developed for the bell tower. The variation of the shaft stiffness along its height may be affected by several factors. On the basis of the available mechanical and geometrical information, the most relevant uncertain parameters to be calibrated are the deformability of the soil-foundation system, the increment of stiffness due to the presence of a rock basement and the presence of a masonry vault at the height of 45 m. The calibration of the shaft stiffness distribution is thus necessary in order to match

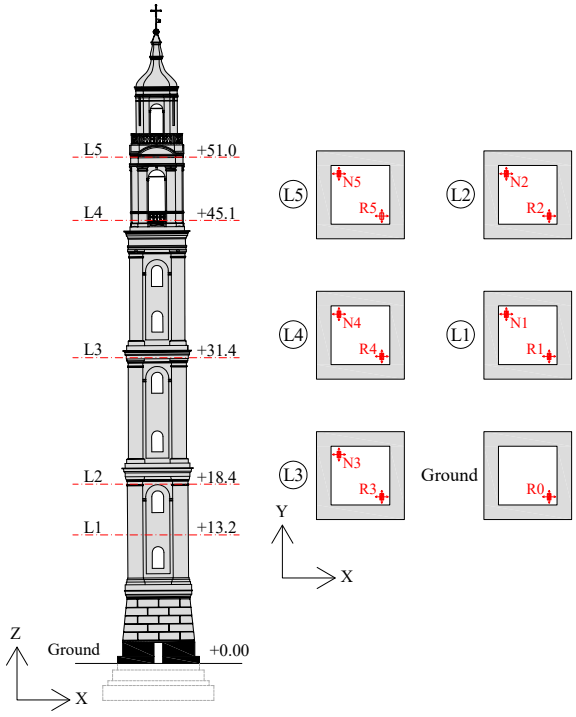

Figure 5.10: Bell tower: instrumented levels (ground, L1-L5) and MEMS-based accelerometer positioning.

(a) (b)

Figure 5.11: Bell tower: typical installation on MEMS-based accelerometers.

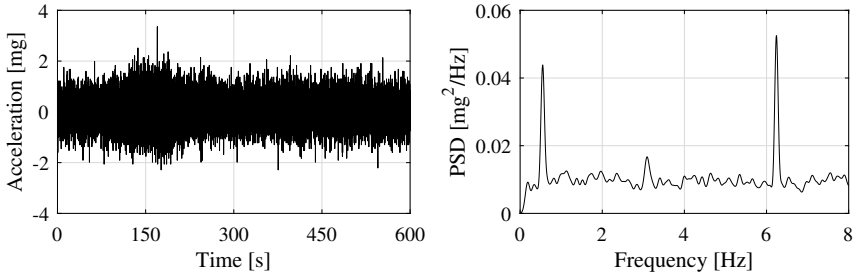

(a) (b)

Figure 5.12: Bell tower: (a) typical acceleration time history recorded at the upper instrumented level and (b) corresponding power spectral density (PSD) function.

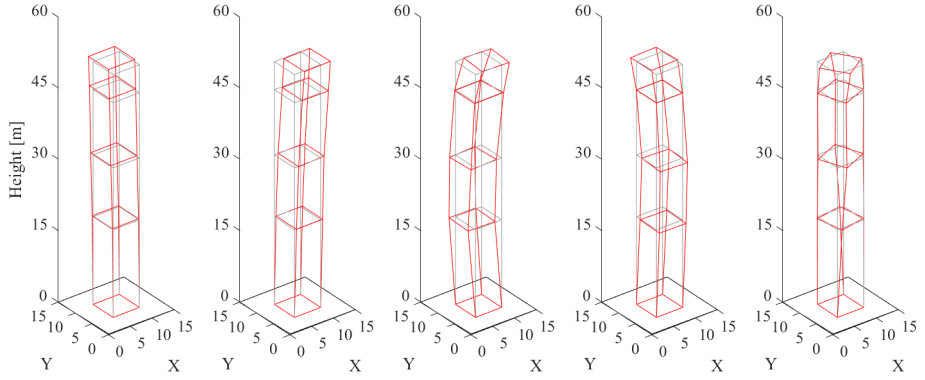

(a) $f = 0.547$ Hz (b) $f = 0.573$ Hz (c) $f = 2.158$ Hz (d) $f = 2.181$ Hz (e) $f = 3.103$ Hz

Figure 5.13: Bell tower: experimental mode shapes.

the experimental modal properties as well as possible. The variation of stiffness along the tower height is performed by implementing the so called damage function approach as proposed in [163]. The damage functions, proposed for the specific application of damage detection, describe the variation of a stiffness parameter inside a substructure, called damage element by the proposers, composed of a certain number of finite elements. Unlike the classical substructure approach, the value of the parameter inside a substructure may not be constant. The number of functions N_i employed is commonly lower than the number of finite elements of the model, in such a way that the number of variables to update is reduced. To this purpose, the external side of the square cross section, that affects both flexural and shear stiffness, is described by a piece-wise linear function, while the internal side of the cross section is supposed to have a constant value equal to 3.9 meters. A reference value B_0 of 7 meters has been considered and for each element e of the FE model the updated side B^e is computed through the parameter a^e, that represents the relative variation with respect to the reference value:

$$B^e = B_0 \left(1 - a^e\right) \tag{5.6}$$

Table 5.4: Bell tower: comparison between the preferred solution of bi-objective optimization and the experimental modes.

Mode Shape	Exp. Freq. [Hz]	Num. Freq. [Hz]	ϵ [%]	MAC [%]
1st Bending Y	0.547	0.563	2.83	96.48
1st Bending X	0.573	0.563	−1.83	96.80
2nd Bending Y	2.158	2.110	−2.24	96.05
2nd Bending X	2.181	2.110	−3.27	96.17
1nd Torsional	3.103	3.055	−1.53	94.71

The correction parameter a^e is computed by the linear combination of linear and step-wise functions N_i:

$$a^e = \sum_{i=1}^{N_F} p_i N_i \left(\mathbf{y}^e\right) \tag{5.7}$$

where N_F is the number of functions N_i used in the discretization, p_i are their multiplication factors and $\mathbf{y}^e$ is the vector containing the centroid coordinate of the element e. N_i are the damage functions and they describe the variation of the parameter a^e inside the structure. For this case study, three substructures, each one characterized by a linear stiffness variation, are defined. When the number of substructures is limited, the location of the boundaries significantly affects the parameter distribution. According to the structural information and after some preliminary analysis, the boundaries of each substructure are selected as the finite elements no.1, 3, 18 and 22, with the element numeration starting from the base. These elements are located at the base, to take into account the soil-foundation system deformability, at the end of the rock basement, at the base of the masonry vault and, finally, at the beginning of the belfry. The upper part of the bell tower does not significantly affect the modal behaviour of the tower and it is modeled accurately in term of masses and stiffeners. The updating parameters are the four multiplication factors p_i that appear in Eq. (5.7).

5.4.4 Bi-objective optimization and selection of the preferred solution

The bi-objective optimization has been performed with the weighted sum method (see section 3.2) adopting the definitions of Eqs. (2.1) and (2.3) for the objectives e_F and e_M, respectively. The weighting factor varies between 0.01 and 1 with step size of 0.01. Fig. 5.14 shows the Pareto front for the FE model of the bell tower together with a point representing a particular solution in the objective space. This solution has been computed with the same FE model where each element is characterized by given values properties of the cross section, computed according to the geometrical survey. Masses are also estimated from the geometrical survey, considering a constant value of the material density. Thus,

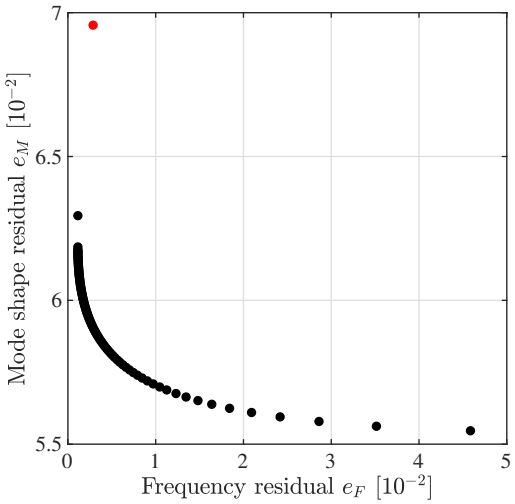

Figure 5.14: Bell tower: Pareto front (black dots) obtained with the weighted sum method and solution related to the updating of the only elastic modulus (red dot).

the elastic modulus of the elements is the only parameter to be tuned, whose updated value is 2141 MPa. It is possible to see that this particular solution is dominated by the Pareto front since there is a solution of the front with about the same value of the objective e_F but with a value of e_M smaller than about 0.01. This confirms that the parametrization of the FE model with piece-wise linear functions allows to obtain better results compared to the parametrization based on survey results.

The preferred solution of the optimization problem, selected with the criterion of the minimum distance from the equilibrium point, corresponds to a weighting factor of 0.36. The updated parameters of this solution are p_1=0.073, p_2=-0.125, p_3=0.262 and p_4=0.004. The associated distribution of the element bending stiffness EI, where E denotes the elastic modulus and I the moment of inertia of the cross section with respect to centroidal axis, is illustrated in Fig. 5.15. The distribution of shear stiffness $GA_{e,s}$, where G denotes the shear modulus and $A_{e,s}$ the equivalent shear area, is not represented, but it has a very similar trend. Both distributions are consistent with the physical consideration expressed in section 5.4.3. Due to the deformability of the soil-foundation system, the stiffness at the base of the tower is relatively low compared to its value at upper heights, since at that location the geometrical dimension of the cross section, obtained by the survey, are the largest of the tower. Moving upward, there is a rapid increase of stiffness for the presence of a stiffer rock basement. Finally, the linear decrement of stiffness with height, in compliance with the reduction of the cross section dimension, is interrupted by a significant positive variation to be ascribed to the masonry vault located at 45 m from the base.

The preferred solution identified with the direct procedure is very close to the one of the classical procedure. The updated parameters are p_1=0.072, p_2=-0.124, p_3=0.262 and p_4=0.004, while the estimated value of the weighting factor (Eq. (3.26)) is 0.37.

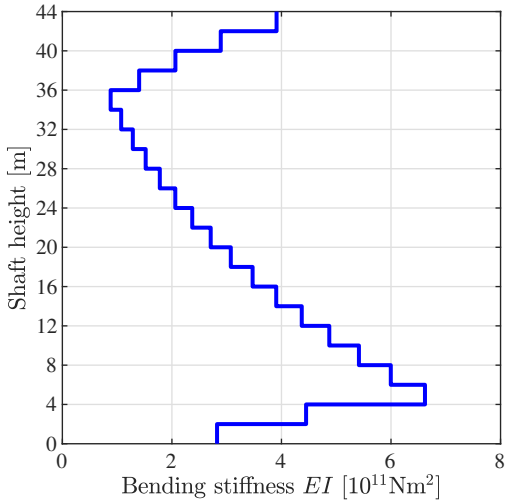

Figure 5.15: Bell tower: bending stiffness distribution along the shaft height.

5.4.5 Bayesian model updating and model class selection

Bayesian model updating and model class selection (see section 5.1) have been carried out in order to determine the optimal coefficients of variation ϵ_ϕ and ϵ_f for the likelihood function and the posterior distribution of parameter vector $\mathbf{x}$. The likelihood function is defined by Eqs. (4.7) and (4.8), while the prior distribution considered is a non-informative uniform distribution defined in a four dimensional hyper-cubic domain where each updating parameter p_i, introduced in 5.4.3, belongs to the interval [-0.5, 0.4]. The parameter domain was discretized into a regular grid employing a step size of 0.025 for each parameter.

As concerns the selection of the optimal coefficients of variation, several models has been considered varying ϵ_f in the range [1 %, 10 %] and ϵ_ϕ in the range [1 %, 15 %] both with step size 0.5 %. Fig. 5.16 shows the contour plot of the posterior probability for different values of the coefficients. The optimal pair of coefficients, that corresponds to the pair with the maximum posterior probability, is ϵ_f=2.5 % and ϵ_ϕ=3 %. Moving away from the maximum it can be highlighted as the slope of the distribution is steeper in the ϵ_ϕ direction, highlighting the more sensitivity of the posterior probability towards the mode shape coefficient.

The posterior marginal distributions of updating parameters are reported in Fig. 5.17, while mean values and standard deviations are listed in Table 5.5. It shows a considerable variability of results, especially for parameters p_1 and p_2. Consequently, the updated stiffness distribution of the tower base is characterized by large uncertainty, as illustrated in Fig. 5.18. Indeed, the maximum variation obtained between the extremities of the range $[\mu_{EI} - \sigma_{EI}; \mu_{EI} + \sigma_{EI}]$ is about $2.5 \cdot 10^{11} Nm^2$.

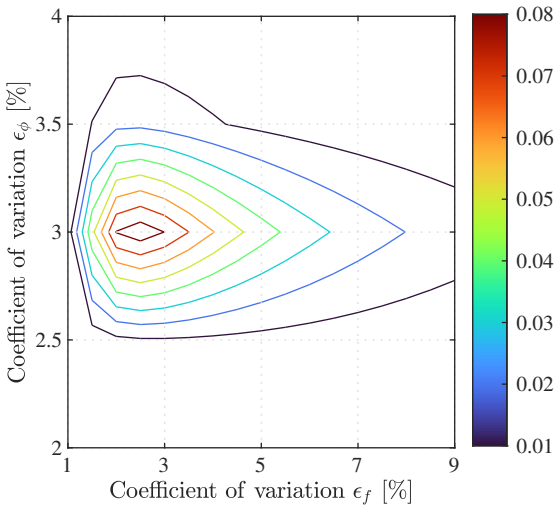

Figure 5.16: Bell tower: contour plot of the posterior probability for different values of the coefficients of variation ϵ_f and ϵ_{ϕ}.

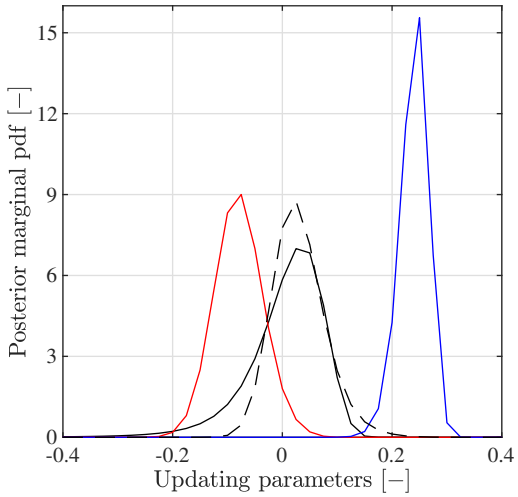

Figure 5.17: Bell tower: marginal posterior distribution of updating parameters. Black continuous line: distribution of the parameter p_1; red continuous line: distribution of the parameter p_2 ; blue continuous line: distribution of the parameter p_3; black dashed line: distribution of the parameter p_4.

Table 5.5: Bell tower: mean (μ) and standard deviation (σ) of the updated parameters.

p_1		p_2		p_3		p_4	
μ [−]	σ [−]	μ [−]	σ [−]	μ [−]	σ [−]	μ [−]	σ [−]
0.006	0.071	-0.079	0.044	0.240	0.026	0.031	0.049

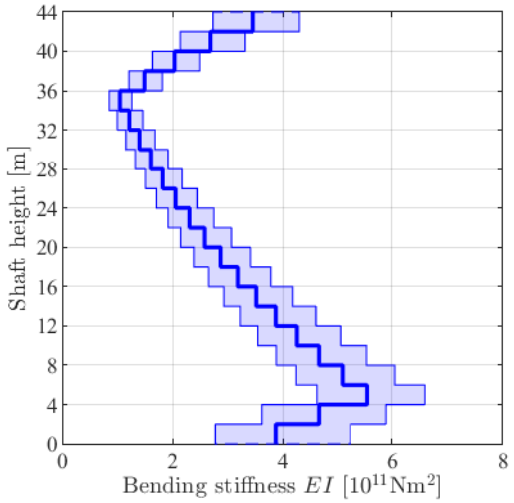

Figure 5.18: Bell tower: updated distribution of the tower stiffness along the shaft height. Blue line: mean value; light blue area: stiffness distribution in the range $[\mu_{EI} - \sigma_{EI}; \mu_{EI} + \sigma_{EI}]$.

5.4.6 Use of the surrogate for Bayesian model updating

Bayesian model updating and model class selection is performed adopting the approximated procedure that involves the use of a surrogate, as described in subsection 5.2. The variability of the procedure is assessed by repeating 100 times the computation of the Bayesian evidence for fixed values of the likelihood function coefficients of variation, taken equal to the optimal ones determined in subsection 5.4.5.

Since the updating parameters of the problem are 4, the complete characterization of a Gaussian function in 4 dimensions needs the definition of 15 parameters: a scale parameter, the mean vector of dimension 1×4 and the covariance matrix of dimension 4×4 that is composed by 9 independent parameters due to its symmetry. The procedure is performed in two cases, denoted as case A and B. In case A, the 4 random variables describing the updating parameters are considered as uncorrelated, reducing the number of parameters to determine to 9. In case B, the correlation between variables is maintained, leading to the 15 parameters previously described.

In case A, the mean value of the natural logarithm of the evidence is 112 and its coefficient of variation is less than 4 %. The exact value is 105.8, hence the relative error committed is about 6.3 %. The updated parameters substantially differ from the exact ones: it can be

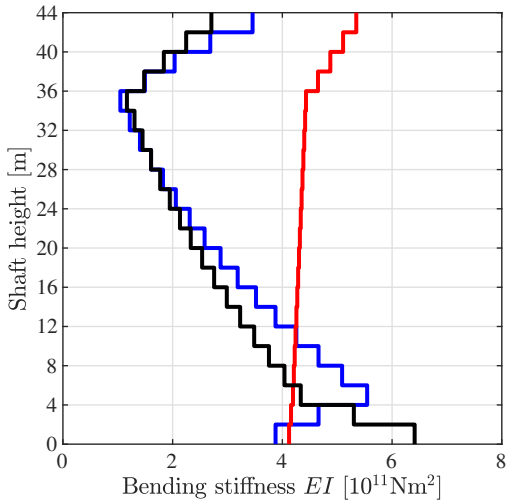

Figure 5.19: Bell tower: comparison of the updated stiffness distributions. Blue line: exact distribution; red line: updated distribution through Gaussian surrogate in case A; black line: updated distribution through Gaussian surrogate in case B.

clearly noticed in Fig. 5.19 by comparing the exact stiffness distribution (blue line) with the one related to the mean vector of the Gaussian surrogate (red line).

The optimization problem of case B is particularly complex due to the high number of parameters, i.e. 15, and due to the fact that the covariance matrix needs to be positive definite. The latter implies further constraints on the parameters describing covariance between variables: the problem is solved by assigning a penalty term to those parameter combinations that do not respect that condition.

The mean value of the natural logarithm of the evidence is 117 and its coefficient of variation is equal to 15 %. The updated stiffness distribution, represented with the black line in Fig. 5.19, is similar to the exact one except for the values at the base of the tower, where the initial stiffness reduction is not identified.

Results of the analysis reveal how in a 25 % of the repetitions the optimization algorithm does not converge and the procedure is stopped when the maximum number of iterations is reached. In these instances, the natural logarithm of the evidence is very far from its exact value and the same applies for the updated stiffness distribution.

5.4.7 Comparison between updating methods

Fig. 5.20 represents the MAP solution of Bayesian model updating, obtained changing the coefficients of variations ϵ_f and ϵ_ϕ of the likelihood function as described in section 5.3.2, in the objective space e_F-e_M. Similarly to what showed for the fortress, the solutions denote the same Pareto front obtained with the bi-objective optimization. In the case of Bayesian model updating, however, the optimal solutions are found by varying in a uniform way not the weights, but the coefficients of variation ϵ_f and ϵ_ϕ. Consequently, the equivalent weights are not uniformly distributed.

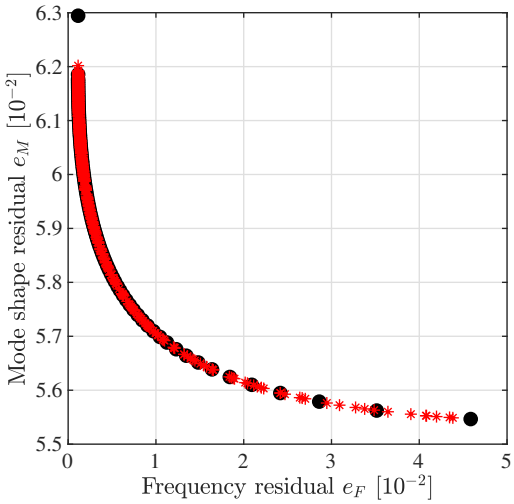

Figure 5.20: Bell tower: Bayesian solutions in the objective space (red asterisks) together with the Pareto front (black dots) obtained with the bi-objective optimization.

As concerns the selection of the optimal coefficients of variation, the equivalent weighting factor computed from Eq.(5.4) is 0.59, while the preferred weighting factor selected with the criterion of the minimum distance from the equilibrium point is 0.36. Considering only the term of the Bayesian evidence related to the average data-fit (namely the first term on RHS of Eq. (5.3)), so neglecting the penalty term based on the information gain, the equivalent weighting factor associated to the optimal variance parameter is 0.31. The latter is appreciably closer to the preferred weighting factor of bi-objective optimization.

Finally, the computational burden of all the methods employed is analyzed. The classical Bayesian approach performed through a parameter grid has a cost that grows exponentially with the number of parameters, requiring for this problem about $1.8 \cdot 10^6$ evaluations of the likelihood function, and consequently the realization of a modal analysis. The use of the Gaussian surrogate enables to hugely reduce the number of evaluations to 250. Also the deterministic methods are more expensive in terms of number of evaluations compared to the case of the San Felice sul Panaro fortress. The computation of the whole Pareto front needs about 35000 evaluations, on average 354 evaluations per point of the front. The direct procedure of section 3.4, takes 1815 repetitions of a modal analysis, about 5 times the number needed for one point of the front, but it is able to identify the preferred solution with a single optimization.

5.5 Concluding remarks

In this chapter, the Bayesian approach has been extended to the selection of the optimal coefficients of variation of the likelihood function, that are related to the weights attributed to frequency and mode shape residuals in the optimization. Moreover, a surrogate-assisted approach has been proposed to alleviate the computational burden of the method. The selection of the optimal coefficients of variation has been carried out for two real case

studies, the San Felice sul Panaro fortress and the Ficarolo Bell tower. Results, in terms of weights and computational effort, have been compared to the weights determined with the deterministic bi-objective approach and the proposed direct procedure both presented in chapter 3.

As expected, the direct procedure enables a sharp reduction of the computational cost (namely 97% for the fortress and 95% for the bell tower) while guaranteeing basically the same results of the classical bi-objective optimization. Results of the Bayesian model updating match pretty well those of the deterministic approach especially when the penalty term based on the information gain is neglected. A good agreement between results is observed mainly for the fortress, while no negligible differences are noted in the updated section stiffness EI at the base of the bell tower. Moreover, the introduction of a surrogate model to compute the Bayesian evidence strongly reduces the computational cost of the process. In particular, the number of simulations required decreases from 1617 to 90 for the fortress and from about $1.8 \cdot 10^6$ to 250 for the bell tower.

Let us analyze results of the San Felice sul Panaro fortress in more detail. The main key issue regarding the Bayesian model updating concerns the choice of the prior distribution. Indeed, if the relation $E_U > E_D$ between the undamaged E_U and damaged E_D masonry elastic modulus (case 2 in section 5.3.2) is accounted for in the definition of the prior distribution, mean values of the updating parameters are very close to those obtained from the deterministic approach. On the contrary, if a non-informative prior distribution is considered (case 1 in section 5.3.2), the mean value of the elastic modulus E_D is overestimated by about 25%. It is worth of note that in this specific case it is possible to fix a relation between parameters because (i) there are only two calibration parameters and (ii) their physical relation is clear and unequivocal. There is a good chance that in many other cases it would not be possible to fix a relation among parameters. To reduce the computational cost of the process, a Gaussian function is assumed to compute the Bayesian evidence. It is observed that the Gaussian model is well-suited for case 2, i.e. when the relation between the calibration parameters is accounted for in the definition of the prior distribution. Accordingly, in this case results are almost the same as those obtained without introducing the surrogate model. On the contrary, the chosen fitting function is not suitable for case 1 (non-informative prior distribution), causing the overestimation of the standard deviation of E_D.

Unlike the fortress, the Ficarolo bell tower is characterized by a simpler numerical model and four calibration parameters. In this case, a non-informative prior distribution is considered, as no relation among the updating parameters can be easily defined. Bayesian model calibration with four updating parameters results hard to handle because of the high number of simulations required in the parameter grid. To overcome this limit, a surrogate model is introduced, represented by a four-dimensional Gaussian function. Two different solutions are obtained depending on whether the correlation among the four random variables describing the updating parameters is considered or not. Better results can be obtained only if this correlation is considered, although even in this case the variability of the updating parameters is high. Inaccuracies in the surrogate-based Bayesian model updating are related to the calibration of the surrogate model, that can be complicated by the high number of function parameters involved.

Chapter 6

Damage detection with Artificial Neural Networks

Model updating methods for damage detection have been successfully applied in different contexts [85, 162, 133, 87]. However, they are usually time-consuming and do not enable the real-time identification of a damaged condition. On the contrary, machine learning (ML) techniques, if properly calibrated, ensure a quick identification, and a good efficiency in working with noise-corrupted data. Numerical models can be used for their calibration: they simulate ordinary conditions and damage scenarios. Among the several ML methods, artificial neural networks (ANNs) represent tools widely diffused in the field of damage detection. The goal of this activity is to define a procedure using ANNs, in particular a multi-layer perceptron (MLP), for the detection of damage in a railway bridge. Different kinds of dynamic data, such as modal properties and features extracted from acceleration and displacement response of the bridge recorded during the passage of a train are provided as damage features to networks with different architectures.

The chapter is organized in this way: section 6.1 presents a literature review about data-driven damage detection techniques; section 6.2 describes the specific type of ANN employed in this application from a mathematical point of view. In section 6.3 the proposed damage identification procedure is delineated with details about all the aspects that characterizes it: numerical models, simulation of the structural response, measurements and model uncertainties, data elaboration and damage scenarios. Two models have been employed for the development of the procedure due to the impossibility to have data related to a possible damage condition of the bridge and with the aim to taking into account the unavoidable discrepancy between model and reality. Performances of the analyzed networks are investigated with respect to a dataset generated through the first model in section 6.4.1, while in section 6.4.2 the network test is performed with data obtained by a more detailed model simulating the "real" structural behavior. Finally, conclusions are drawn in section 6.5.

6.1 Literature review

Data-driven methods are based on the extraction of damage-sensitive features from the measured experimental response, and they do not directly rely on the calibration of a physical model for damage detection. For this reason, the computational effort required by these methods is clearly limited compared to model-based techniques and a real-time identification of the structure condition can be carried out. The performance of these methods depends on the damage sensitivity of the features selected. Some of the main approaches to damage detection without ML techniques has been described in chapter 1 referring to the review work of Doebling et al. [54].

An extended version of that review was realized by Sohn et al. [156]. In this work, attention began to be placed on the development of statistical models for feature discrimination, a field ML techniques are part of. ML techniques employment for damage detection showed a significant increment in the last decades thanks to an impressive computational development that allowed the collection, the handling and the elaboration of a huge amount of data. Moreover, ML approaches are capable of working with uncertain and noise-corrupted data [99], typical characteristics of dynamic data employed in vibration-based damage detection. As a consequence of these developments, the damage detection process can be addressed as a pattern recognition problem, whose main phases are data acquisition, feature extraction and classification. The last task is usually accomplished by ML classifiers, among which ANN are the most diffused.

A proper distinction among ML damage detection methods relies on the feature extraction technique, as proposed in a recent review article by Avci et al. [6]. Parametric methods utilize dynamic parameters of the structure to determine the presence, location and severity of damage. These parameters are simply physical parameters like modal frequencies, masses, dampings and mode shapes. In this case, feature extraction is performed by modal identification techniques. On the other hand, non-parametric methods detect damage directly from the acquired accelerations by means of statistical tools. Time series modelling and signal processing techniques are employed to extract damage sensitive features that are then provided to a classifier. In the following, the principal works about ML-based damage detection are investigated according to the previous distinction.

6.1.1 Parametric ML methods

Numerous applications have been proposed in this context and most of them are based on the use of natural frequencies and mode shapes to construct the feature vector. Pawar el al. [131] presented an integrated method of spatial Fourier analysis and ANNs to localize damage in a fixed-fixed beam. Spatial Fourier analysis was performed to identify the mode shapes, that are the extracted features, from the free response of the beam. Mehrjoo et al. [114] carried out damage detection and localization of a simple truss bridge and the Louisville Bridge with a MLP which takes in input modal properties extracted from the acceleration response. These techniques were applied with successful results only to numerical exercises. Gonzalez and Zapico [70] proposed a multiple MLP-based method for seismic damage identification of a steel moment frame. The network was not used for classification purposes but, on the basis of modal properties provided, it was able to

compute modal mass and stiffness of the structure members, that are the features used to identify, locate and quantify damage. The method, however, showed a high sensitivity to input feature error. Bakhary et al. [8] developed another multiple ANN procedure associated to the substructure approach. The structure under examination, a two-span reinforced concrete slab, is divided into substructures and their local frequencies are the output of the first network. This output represents the input of a second network that is able to quantify and localize damage. The procedure is validated both numerically and experimentally. Betti et al. [23] proposed the combined use of MLP and genetic algorithms to improve damage detection considering the experimental SHM benchmark of the IASC-ASCE Task Group [93]. The genetic algorithm was used to update a FE model of the benchmark structure, which generates the training dataset of the ANN.

Some authors combined modal identification with other techniques for feature extraction. For example, Lam and Ng [105] employed simultaneously modal properties and Ritz vectors as extracted features for the same IASC-ASCE benchmark problem. A single MLP was optimized according to a Bayesian approach and a parametric study was conducted in order to determine the best activation function for damage identification purposes finding the hyperbolic tangent function as the preferred one. The study also demonstrates that modal properties, when are individually employed, allow to obtain better performances compared to Ritz vectors.

Along with MLPs, few different types of ANN have been employed as classifiers of the extracted features. Jiang et al. [90] combined probabilistic neural networks, rough set processing and data fusion for damage detection considering two analytical case studies. This procedure resulted in noise-resistant capabilities but it was not tested on real structures. The data fusion approach was proposed again by Jiang et al. [91] in a two stage method based on fuzzy neural network. It is shown that the fusion model plays an important role in increasing the accuracy level of the procedure. However, the latter needs to be validated on real structures as before.

Cury and Cremona [46] compared the accuracy of MLPs, support vector machines (SVMs) and Bayesian decision trees (BDTs) for SHM purposes using symbolic data analysis to manipulate monitoring data on a steel railway bridge in France. Interesting works about the influence of noise level and model error were carried out by Yeung and Smith [174] and Lee et al. [106]. Yeung and Smith dealt with the detection of girder connection damage of a suspension bridge. The feature vector is composed by mode shape peaks and it is given in input to two different unsupervised networks. Lee et al. used an analytical beam model, a FE model and experimental data registered by the monitoring of a bridge in order to study the effects of errors in baseline FE model. The mode shape variation with respect to a pre-damage condition represents the input vector for a MLP.

6.1.2 Non-parametric ML methods

A variety of combinations between features and classifiers have been investigated in the non-parametric ML method literature. Chun et al. [44] quantified damage severity caused by the corrosion of bridge girders through a MLP. The input features have been obtained by computing the mean and the variance of the measured acceleration signals. The methodology has been validated only with numerical simulations. This feature extraction process

is quite simple and it is highly affected by operational and environmental conditions in addition to damage.

A large part of more complex techniques employs auto-regressive (AR) time series modelling. Figuereido et al. [59] compared the performances of four classification approaches, auto-associative neural network (AANN), singular value decomposition (SVD), squared Mahalanobis distance (SMD) and feature analysis (FA). Damage features are the identified coefficients of AR models that reproduce the response of a small frame structure subjected to a random shaker excitation. AANN resulted the best performance with respect to the other classifiers. Gui et al. [72] applied SVM for the classification of two kinds of features extracted with AR modelling, namely the AR coefficients and the Residual Error (RE). Hyper-parameters of the SVM have been calibrated with three optimization techniques, particle swarm optimization (PSO), grid search (GS) and genetic algorithms (GA). Combinations GS + RE, GA + RE, PSO + AR and PSO + RE all showed excellent results.

De Lautour and Omenzetter [48] employed AR modelling in conjunction with principal component analysis (PCA) for dimensionality reduction. A large number of features was extracted with AR modelling of the vibration response of a laboratory frame and a benchmark structure. These features were then condensed with PCA and given in input to a MLP with a single hidden layer. The test phase with experimental data revealed that an accuracy of 97 % for stiffness reductions ranging from 7 % to 10 %.

Dackermann et al. [47] applied PCA directly on the acceleration signals in time domain without AR modelling. The damage features compressed by PCA were fed into an ensemble of ANNs for damage localization. The good accuracy obtained by numerical and experimental test conducted confirms the ability of PCA to filter noise. Bandara et al. proposed to apply PCA to FRFs in the case of a numerical model [9] and a laboratory structure [10]. Two distinct methodologies were studied: in the first a MLP with two hidden layers was trained with damage features extracted from individual FRFs only, while in the second the features for the same network are obtained considering the summation of FRFs. In the last case, a higher accuracy is reached.

The last part of literature review is dedicated to feature extraction techniques different from AR modelling and PCA. Liu et al. [111] combines wavelet decomposition of acceleration signals and multi-sensor feature fusion in order to detect and localize damage of the IASC-ASCE benchmark [93] considering only numerical simulations. The same case study was the focus of Ghiasi et al. [67], that used wavelet decomposition and SVM classifier, and Zhu et al. [185], which adopted interval modelling technique for feature extraction and the adaptive neuro fuzzy inferencesystem (ANFIS) for damage identification. Finally, the potentiality of self organizing maps (SOMs), a typical unsupervised learning tool, has been exploited by Abdeljaber and Avci [125] for the computation of damage sensitive features, which subsequently were processed by a MLP.

6.1.3 Drawbacks of damage detection methods

Several drawbacks and limitations emerge from the analysis of the main works about damage detection. The damage detection process is without doubt case sensitive. There is

no guarantee that a specific feature, and in parallel a specific classifier, will be the optimal, or almost a good, choice for all the damage detection exercises. Furthermore, the optimality of a combination feature/classifier may not depend only on the structure type but also on the damage type. These limitations are valid for ML-based methods and, for the major part, also for non ML-based methods. Finally, few works were focused on the experimental validation on real and extended structures of methods developed starting from numerical case studies.

6.2 Multi-layer perceptron for classification

Multi-layer perceptron (MLP) is surely the most popular kind of ANN that applies supervised training. It is composed of neurons arranged into layers. Each neuron in a given layer is connected to all the neurons in the following layer. The connections between neurons do not form cycles, therefore the information elaborated by the system moves only in the forward direction, from the input layer to the output one [77]. For this reason, the MLP is also denotes as feed-forward neural network.

In general terms, the connection between the output $a_{i,j}$ of i-th neuron belonging to the j-th layer and the output $a_{i,j+1}$ of the i-th neuron belonging to the $j+1$-th layer is expressed by:

$$a_{i,j+1} = f(x_{i,j+1}) \tag{6.1}$$

$$x_{i,j+1} = b_{i,j+1} + \sum_{i=1}^{N_j} w_{i,j+1} a_{i,j} \tag{6.2}$$

where $b_{i,j+1}$ and $w_{i,j+1}$ are the bias (or threshold) coefficient and the weight coefficient, respectively, that characterize the connection. The function $f(x_{i,j+1})$ is the so-called transfer function that introduces non-linearity in the process.

Since we employ the network for classification, a common choice for the transfer function of the output layer is the soft-max function, suggested for example by Bishop [24]. Considering a vector $\mathbf{x}$ that has a number of components N_c equal to the number of classes, the value of the soft-max function for the component x_i is:

$$f(x_i) = s_i = \frac{\exp(x_i)}{\sum_{j=1}^{N_c} \exp(x_j)} \tag{6.3}$$

This value represents the probability that the sample represented by $\mathbf{x}$ belongs to the i-th class. The transfer function of the hidden layers is generally chosen among:

- Sigmoid logistic function

$$f(x) = \frac{1}{1 + \exp(-x)} \tag{6.4}$$

- Hyperbolic tangent function

$$f(x) = \frac{\exp(x) - \exp(-x)}{\exp(x) + \exp(-x)} \tag{6.5}$$

- Rectified linear unit (ReLU) function

$$f(x) = \max\{0, x\} \tag{6.6}$$

Network training is the process where the network coefficients are tuned in order to increase the ability of the network to make correct predictions on the basis of the data available and to prevent their over-fitting. The ability of a network in classification problems is quantified by the average cross-entropy loss function E, that measures the discrepancy between the prediction vectors $\mathbf{s}_n$ and the corresponding targets $\mathbf{t}_n$ related to the training set. This function is expressed as:

$$E = -\frac{1}{N_t} \sum_{n=1}^{N_t} \sum_{j=1}^{N_c} t_{j,n} \log s_{j,n} \tag{6.7}$$

where N_t is the number of samples that constitute the training set.

The optimization of the network coefficients can be performed with several algorithms using gradient-based methods. In this work, the author has chosen the scaled conjugate gradient back-propagation algorithm [116], known for its efficiency in problems with a large number of neurons. The problem of data over-fitting has been addressed by providing a sufficient number of data that allows the generalization of the network [176]. More details about the number of data will be given in the next section.

6.3 The proposed damage identification procedure

The proposed procedure involves the use of different ANNs for the identification of a possible damaged state of a railway bridge. The localization and the quantification of a damaged state are not investigated. It is in the interest of the author to assess the performances of different networks, that share the typology (MLP) and the finality (classification), but differ for the dynamic data assumed as input features and for the architecture (in terms of number of neurons per layer and transfer function). Network performances are assessed with the accuracy of the predictions and with the number of uncertain predictions, whose meaning will be explained in the next sections. The role played by data in this procedure is without doubt fundamental for its success. In particular, the collection of data related to any damaged condition of the structure has to be deepened. A possible strategy is to realize different damage scenarios over the real structure or a prototype and to measure their experimental response. The execution of damage tests over a bridge in operational condition is not possible and the realization of a bridge prototype deals with feasibility problems and economical drawbacks. Indeed, in order to obtain reliable results from an experimental test, namely results that are not affected by the scale effect, a bridge prototype needs to have dimensions that are not comparable with the dimensions of a common

laboratory. For the previous reasons, the damage scenarios of the bridge will be simulated through two FE models different for the detail level. They simulate the "real" structural behavior and that of "the model", defined starting from the identified modal properties. In this way, the procedure is characterized also by the presence of a model error, namely the unavoidable discrepancy between a measured feature and the same predicted by a model. In this work, it is represented by the discrepancy between the same feature predicted by two different models of the same structure. The crucial aspects of the procedure are briefly listed:

- use of two FE models for the impossibility to have data about a damaged state of the real bridge and in order to account for model error;
- simulation of the structural response of the bridge due to the passage of a train;
- calibration of the simple model according to the response of the more detailed model simulating the "real" structural behaviour;
- inclusion of uncertainties regarding the measurements and some parameters of the models (train loads and velocity);
- creation of different damage scenarios;
- feature extraction from the structural responses;
- training and optimization of the networks;
- test of the trained networks.

They will be described in detail in the following.

6.3.1 Description of the structure and of the numerical models

The case study is a steel railway girder bridge approximately 40 meters long and 4.3 meters wide. Two simple supported steel girders support a concrete slab of thickness equal to 34 centimeters. The slab is connected with the top flanges of the girders through pegs that prevent the slip between the adjacent surfaces. The two steel girders are connected to each other by a complex bracing system. It is a three-dimensional system composed of a basic 3D truss, whose dimensions are 3.5 m $\times$ 2.4 m $\times$ 2.4 m, that recurs for the whole length of the bridge. A 3D view of the girders and of the bracing system is reported in Fig. 6.1. The cross section types and dimensions of the steel elements that compose the bridge are listed in Table 6.1. The value of the elastic modulus assumed for concrete and steel is 31475 MPa and 210000 MPa, respectively.

A detailed FE model, which simulate the "real" structural behaviour and will be employed for the test of the networks in the last phase of the procedure, is developed using the FE software MIDAS CIVIL. An image of the model is shown in Fig. 6.2. The walls of the steel girders and the concrete slab are modeled with plate elements, while truss elements are employed for the bracing system. Thicknesses of the plate elements are chosen according to the dimensions of the modeled member. Cross section areas of the truss elements are

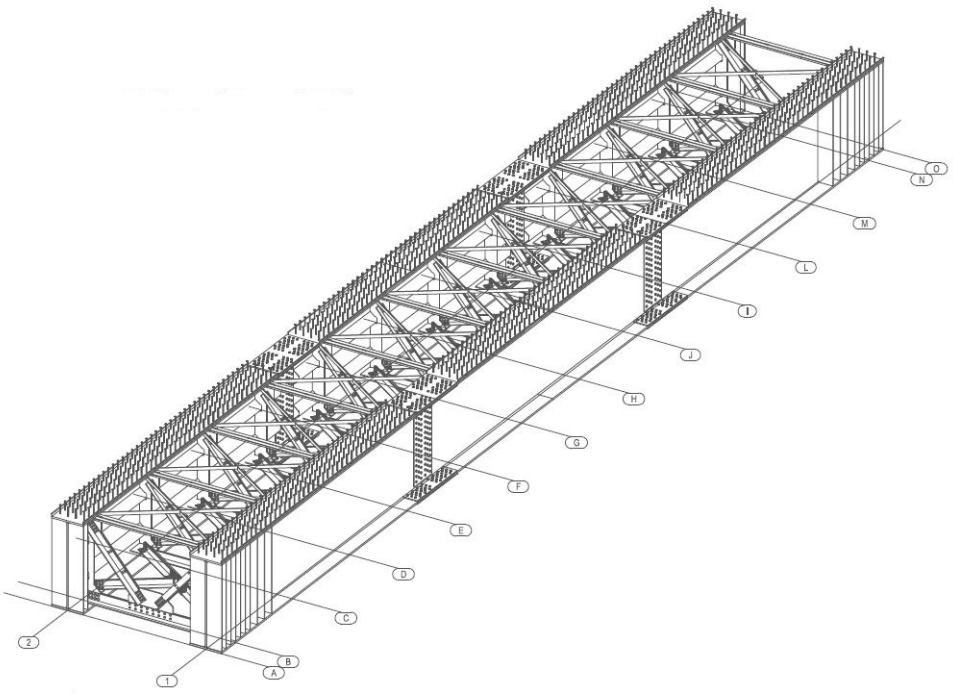

Figure 6.1: 3D view of the girders and of the bracing system.

Table 6.1: Cross section dimensions of the steel elements of the bridge. The abbreviations IF, SF and TF stand for inferior face, superior face and transversal face, respectively, of the basic 3D truss.

Element	Section Type	H [mm]	B [mm]	t_w [mm]	t_f [mm]
Girder	Welded I	2150	800	25	40
Diag. brac. - IF	Coupled L	150	150	14	14
Transv. brac. - IF (support)	Coupled L	200	200	16	16
Transv. brac. - IF (interior)	Coupled L	150	150	12	12
Diag. brac. - SF	Single L	80	80	8	8
Transv. brac. - SF	Coupled L	100	100	10	10
Diag. brac. - TF	Coupled L	100	150	12	12

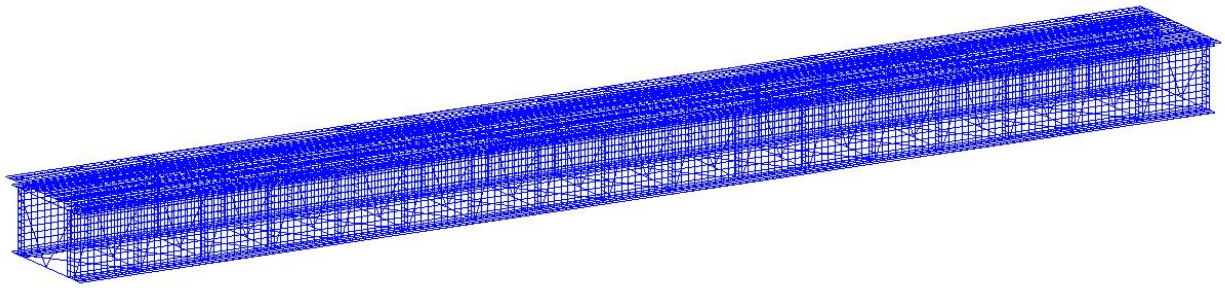

Figure 6.2: Isometric view of the bridge FE model realized with MIDAS CIVIL (model D).

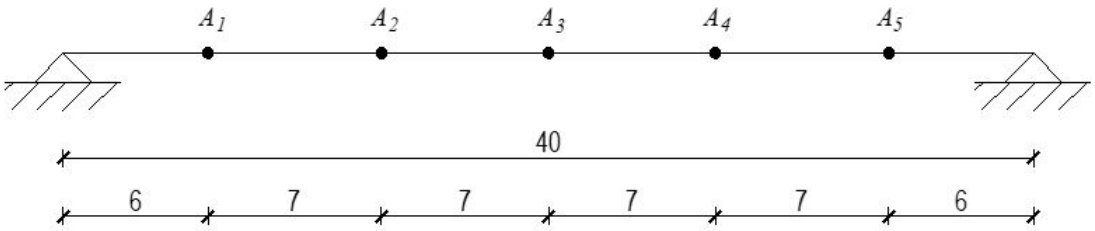

Figure 6.3: Disposition of the five sensors along the bridge length. Dimensions in meters.

computed on the basis of the dimensions provided in Table 6.1. The top flanges of the girders are connected to the concrete slab through rigid links. The middle plane of the flanges and of the slab are located at different heights in the model. We denote this detailed model as model D.

A simpler model has been developed for the generation of the network training dataset. The simplicity of the model is necessary due to the high number of analysis required to generate the data that will be included in the dataset. It is a simply supported beam with 100 finite elements whose equivalent rectangular cross section is characterized by both flexural and shear deformability. We denote this model as model S. The values of elastic modulus, shear modulus and mass density are calibrated in such a way that the response of this model matches as close as possible the response of the detailed model. More details about the calibration can be found in section 6.3.3.

6.3.2 Simulation of the structural response

A dynamic monitoring system is assumed to be installed on the bridge. The measurement equipment is composed of five accelerometers connected to the structure and placed at the locations illustrated in Figure 6.3. Therefore, the dynamic response of the structure is available only for the points corresponding to the sensor locations.

The same typology of data is simulated by both the FE models. Natural frequencies and mode shapes of both FE model are obtained performing modal analysis and modifying the exact values by adding noise with the aim to reproduce measurement errors and uncertainties characterizing the modal identification procedure. Details about the uncertainty modelling are described in the next section. Only the first four bending modes in the vertical plane are considered in the detection process.

On the other hand, several train passages are simulated to obtain displacement and acceleration responses. Due to the assumption that the structure is equipped with accelerometers, corresponding displacements are obtained from a double integration of the accelerations as described in [168]. For the simpler model (S), the train load has been modeled as a series of concentrated forces, representing the whole axle load, moving along the beam with a constant speed. In particular, the train is composed of 2 carriages 26 meter long with 4 axles per carriage. Values of axial load are defined according to the carriage weight of an Italian high speed train [110]. The acceleration response is numerically integrated in the modal space through a MATLAB routine considering the bridge as a single degree of freedom system. The contribution of different modes is taken into account via modal superposition.

For the detailed model (D), the difference in load modelling is the use of two concentrated forces, representing the load of each train wheel, instead of a single force for the whole axle. The two forces are symmetrically disposed with respect to the longitudinal axis of the bridge, in correspondence of the rail location. The acceleration and displacement response is computed with the specific algorithm of the software.

For both models, signals 3.5 seconds length and sampled with a time step of 10^{-3} seconds are considered.

6.3.3 Calibration of the model S

The simpler model is calibrated with the aim to reduce as much as possible the discrepancy between the responses of model S and D considering their undamaged state. The calibration is performed with respect to the natural frequencies of the first four bending modes in the vertical plane and the displacement response due to the passage of a specific train. It has a speed of 106 km/h, while the axle loads of model S and D are highlighted in Table 6.2. The loads in model S are the sum of the left and right loads in model D.

To achieve this goal, three properties of the beam, namely the elastic and the shear modulus and the mass density, are adjusted. These properties remain constant along the bridge length. In particular, in the first stage of the calibration a fixed value of the mass density is set and the values of the elastic and shear modulus are tuned in order to minimize the relative difference between the natural frequencies of model S and D, namely the function e_F defined in Eq. (2.1). Once the first stage is completed, a second constrained optimization is performed by modifying all the three parameters with the aim to reduce the discrepancies between the displacement responses of the five sensors A1, A2, A3, A4

Table 6.2: Axle loads of the specific train used in the calibration of model S. P_l: load of the left wheel in model D; P_r: load of the right wheel in model D; P: overall load in model S.

Position	Model D		Model S
	P_l [kN]	P_r [kN]	P [kN]
0	46	53	99
4	45	51	96
14	53	52	105
18	51	52	103
28	50	53	103
32	54	53	107
42	53	46	99
46	50	52	102

Table 6.3: Mechanical and geometrical parameters of the beam cross section of model S.

Area [m^2]	1
Moment of inertia [m^4]	0.225
Mass density [kg/m^3]	15800
Elastic modulus [MPa]	221250
Shear modulus [MPa]	6050

and A5 (see Fig.6.3). The discrepancy is expressed as:

$$e_D = \sum_{i=1}^{5} \|\mathbf{s}_{i,S} - \mathbf{s}_{i,D}\|_1 \tag{6.8}$$

where $\mathbf{s}_{i,S}$ and $\mathbf{s}_{i,D}$ are the displacement responses related to the i-th sensor computed by model S and D, respectively. The symbol $\|\cdot\|_1$ represents the generalized 1-norm. The constraint imposes that the natural frequency of model S during this second stage does not change with respect to the values computed in the first stage. The geometrical and mechanical properties of the beam cross section, included the values of the updated parameters, are listed in Table 6.3.

The comparison between the natural frequencies of the model S and D is showed in Table 6.4. It is easy to note that it is not reached a perfect correspondence between frequencies, so a residual discrepancy remains also after the calibration. The displacement and the acceleration response of sensor A3 computed by model S and D due to the train of Table 6.2 are represented in Fig. 6.4. The correspondence between displacement responses (Fig. 6.4(c)) is very good, while there are remarkable differences for accelerations, as it is possible to see in Fig. 6.4(a). Despite the mean trend is similar, differences both in terms of amplitude and frequency content for the acceleration responses of model S and D can be noted (Fig. 6.4(b)). It is worth underlying that accelerations have not been taken into

Table 6.4: Comparison between natural frequencies of model S and D after calibration.

	1st fr. [Hz]	2nd fr. [Hz]	3rd fr. [Hz]	4th fr. [Hz]
Model S	1.680	6.102	12.079	18.713
Model D	1.697	5.859	12.958	18.193
Discrepancy	0.017	-0.243	0.879	-0.519

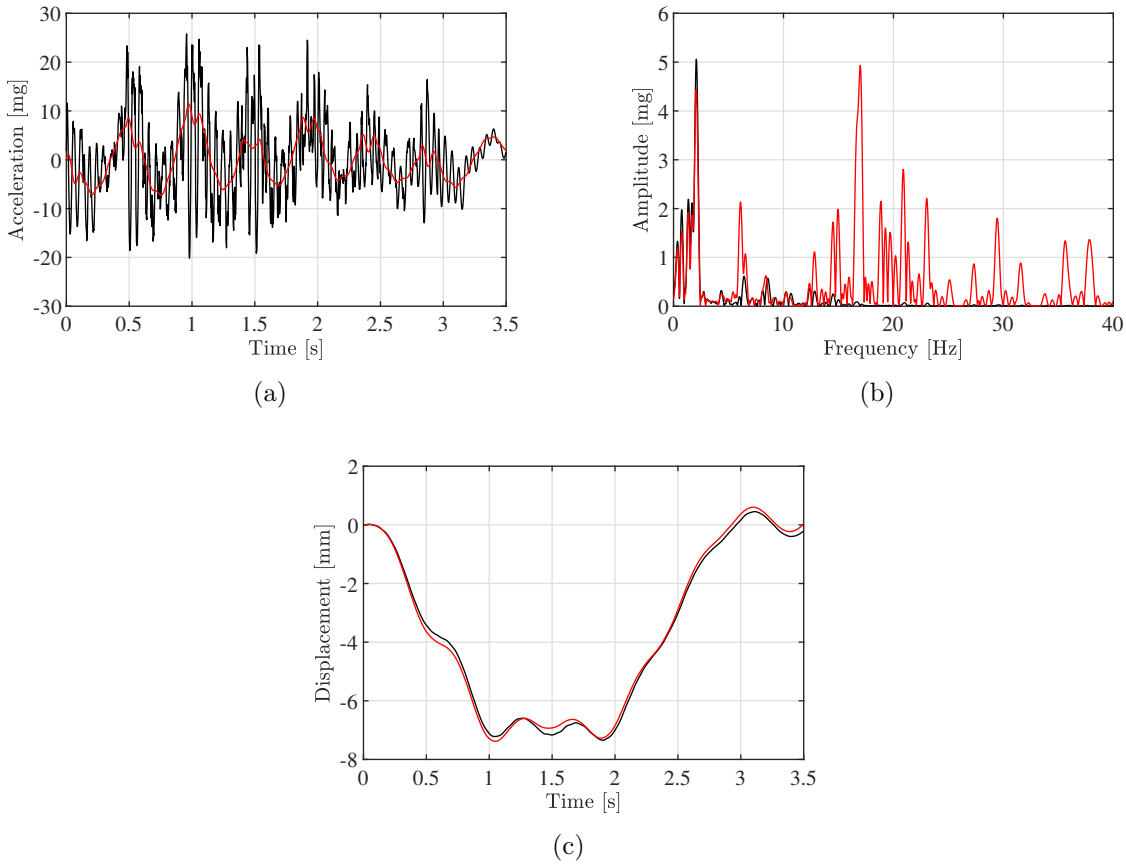

Figure 6.4: Comparison between responses of the sensor A3 computed by model S (black lines) and D (red lines):(a) acceleration response in time domain, (b) acceleration response in frequency domain and (c) displacement response in time domain.

account in the definition of the discrepancy function, but the differences showed in Fig. 6.4(a) do not depends on this fact. Indeed, a calibration of the beam parameters in order to minimize discrepancy between acceleration responses has been performed but results very similar to those of Fig. 6.4(a) have been obtained.

Mode shapes have not been included in the calibration since they are not sensitive to the modification of parameters that are constant along the bridge length. Anyway, mode shapes computed by the two models are not exactly the same. As an example, Fig. 6.5 highlights the comparison for mode 2 and 4. With reference to both modes, differences

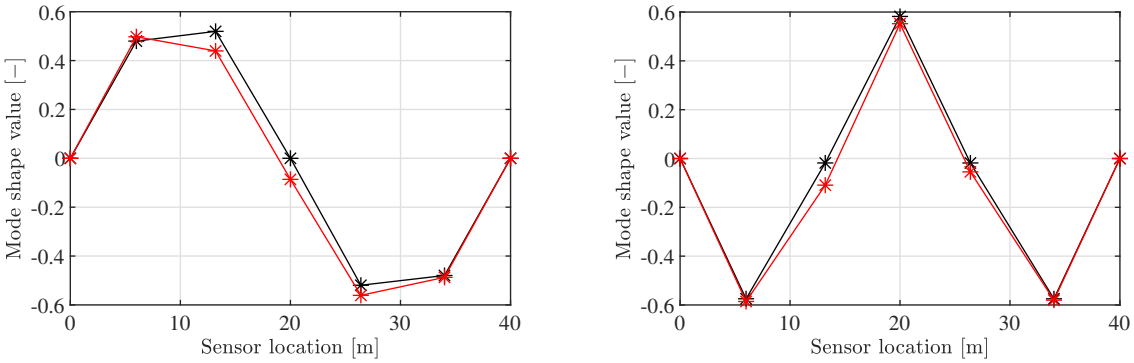

Figure 6.5: Comparison between unit norm mode shape components computed by model S and D for mode (a) 2 and (b) 4. Black asterisks: mode shape components of model S; red asterisks: mode shape components of model D.

can be noted especially for sensors A2, A3 and A4. Another aspect to underline regards the component related to sensor A3 for mode 2 and 4. The value computed by model S is practically zero, since it has a order of magnitude of 10^{-15}. It is unlikely to obtain a similar value for experimental mode shapes since near zero-components have normally a low accuracy. They have the second or the third decimal digits different from zero for the classical normalization methods used. For this reason, a specific source of error for pseudo-experimental data will be introduced in the next section.

6.3.4 Measurement and modelling uncertainties

In order to account for different sources of uncertainty that may influence the results, measurement and modelling uncertainties are introduced in the simulated data. The latter are related to limitations of the adopted numerical model to represent the actual structural behavior while the former take into account the presence of uncertainties in experimental measurements.

Moreover, model errors can be further classified in two groups: parametric uncertainties and model form uncertainties [38]. Parametric uncertainties characterize the differences between some parameter values of the actual physical system and the input parameters in the numerical model. Model form uncertainties are related to inaccuracies in the modelling of the physical system.

To account for measurement errors, a Gaussian noise with a coefficient of variation of 5% is added to the simulated acceleration response. The displacement response is obtained integrating twice the noised acceleration time series and thus it is affected by a magnification of the uncertainty added to accelerations. Furthermore, errors introduced by the numerical modal extraction technique and the fluctuation of the modal properties caused by the environmental conditions are taken into account by corrupting the exact response

z_{ex} and obtaining the corresponding pseudo-experimental value z_{ps} as:

$$z_{\text{ps}} = z_{\text{ex}} \left(1 + a_N \, N_r\right) \tag{6.9}$$

where N_r is a random number extracted from a standard normal distribution and a_N is the noise amplitude. a_N is set to 0.01 for frequencies and 0.05 for mode shapes. In case of mode shapes, and specifically for the component related to sensor A3 of mode 2 and 4, whose value is close to zero, another term to be added to z_{ps} is considered in Eq. (6.9). It is a sample extracted from a uniform distribution defined in the interval $[2;\ 4]{\cdot}10^{-3}$, which has the same sign of the component. In this way, the low accuracy of experimentally determined near-zero component is accounted for.

Parametric uncertainties regarding the train loading are considered on both load values and train speed. To consider the presence of unknown number of passengers on carriages, each train load is considered as a uniform random variable defined in the interval [90; 110] kN. Similarly, the speed of each train is considered as a random variable extracted from a uniform distribution in the interval [100; 120] km/h.

The response of the structure for a given damage scenario (see section 6.3.5) is computed several times (i.e., 200) extracting each time a different sample for the random variables.

6.3.5 Damage scenario

Bridge damage is simulated through the reduction of the elastic modulus of a single element of the structure. Considering the elastic modulus E_u of an undamaged element and the reduced elastic modulus E_d of a damaged element, it is possible to define the damage severity r as:

$$d_s = \frac{E_u - E_d}{E_u} \cdot 100 \tag{6.10}$$

A large dataset has been generated for the network training and validation. It is composed of the dynamic data described in section 6.3.2, namely modal properties, acceleration and displacement responses, related to the undamaged condition of the bridge and to different damage scenarios. Each scenario is characterized by a specific damage severity and location, that may assume different values. In detail, damage location varies with a step-size of 5 % of the bridge length over the whole structure, while its severity varies from 0 to 40 % with a step-size of 2.5 %. As previously mentioned in section 6.3.4, the response of the model S for a specific scenario is computed 200 times sampling each time the random variables defined in order to model different uncertainty sources. Instead, the response of the model for the undamaged scenario is computed 27000 times, since the dataset for the undamaged class is composed only by the response computed in this scenario. In this manner, the dimensions of the datasets related to the three classes are comparable.

6.3.6 Feature extraction, data compression and noise filtering

Different techniques, according to the data in exam, are employed for feature extraction. The first technique is modal analysis, that allows to obtain concise dynamic features like

frequencies and mode shapes. In this case, for simplicity modal analysis has been performed in a direct way starting from mass and stiffness matrix. The addition of noise (Eq. (6.9)) allows to simulate a real situation, where modal extraction is performed in an inverse way, starting from the structure response.

For the acceleration responses caused by train passages, the signal is represented in frequency domain using the Fast Fourier Transform (FFT) implemented in MATLAB. The frequency resolution of the signal is set to 0.02 Hz. For feature extraction from displacement responses, two techniques are used: the above mentioned FFT and a distance-based resampling. The second expresses displacements in function of the location of the concentrated forces simulating the axle load. This resampling can be summed as follows:

1. For a given train passage, consider the displacement time series $\mathbf{s}_1$,$\mathbf{s}_2$,...,$\mathbf{s}_5$ associated to each sensor;
2. Define a vector $\mathbf{z}_f$ containing the force location of interest. In this case, the author has chosen locations every 0.5 m starting from the left support and moving along the bridge.
3. On the basis of the train speed v_t, define the vector $\mathbf{t}_1$ containing the time instants t_i when the first force passes over the locations defined in $\mathbf{z}_f$.
4. When the first force reaches the end support, determine the position $\hat{z}_f$ of the second force. Repeat point 3) considering a reduced location vector $\mathbf{z}_{f,r}$ that goes from $\hat{z}_f$ to the position of the end support with step size equal to 0.5 m.
5. Define the vector $\mathbf{t}_2$ containing the time instants t_i when the second force passes over the locations defined in $\mathbf{z}_{f,r}$.
6. Repeat point 4) and 5) for the subsequent forces creating the vectors $\mathbf{t}_3$,...,$\mathbf{t}_{NF}$ where NF is the number of concentrated forces.
7. Concatenate all the vectors $\mathbf{t}_i$ with $i = 1, ..., NF$ in a vector $\mathbf{t}$ following the increasing order of subscripts.
8. Compute the reduced time series $\mathbf{s}_{r,j}$ $(j = 1, ..., 5)$ by selecting only the components of $\mathbf{s}_j$ corresponding to the time instants of $\mathbf{t}$.

Although features extracted from acceleration and displacement responses caused by train passages are reduced in dimension compared to the original signals in time domain, they still result difficult to handle for a MLP. This is especially true in the case of FFT that operates with an high frequency resolution. For this reason, principal component analysis (PCA) is applied to the extracted features for data compression. PCA is a known method used to reduce the dimensionality of large datasets. A large set of variables is transformed into a smaller one that contains most of the information stored in the large set. The loss of information is accepted in order to visualize and analyze data in a simpler manner. Principal components are linear combinations of the original variables, realized in such a way that the new variables are uncorrelated and most of the information contained in the original variables is compressed into the first new variables. The fundamental steps of PCA are briefly described in the following.

- Normalization of data in order to avoid that variables characterized by larger standard deviations dominate the process. For a given variable x with mean μ and standard deviation σ, the normalized variable z is obtained as:

$$z = \frac{x - \mu}{\sigma} \tag{6.11}$$

  Normalized data can be organized in columns forming the matrix $\mathbf{Z}$.

- Identification of the correlations between variables through the computation of the covariance matrix $\mathbf{\Sigma}$;

- Computation of the eigenvalues s_i and the eigenvectors $\boldsymbol{l}_i$ of the covariance matrix $\mathbf{\Sigma}$. The eigenvectors represent the principal components, while the corresponding eigenvalues give the amount of variance in each principal component.

- Discarding the components of lower significance on the basis of the relative amount of variance rv_i:

$$rv_i = \frac{s_i}{\sum_{i=1}^{n_v} s_i} \tag{6.12}$$

  In particular, the eigenvectors are ordered based on the descending value of the corresponding eigenvalue. The matrix that stores the eigenvectors as columns is denoted by $\mathbf{L}$. There is no a fixed rule for discarding the components of lower significance, since the operation highly depends on the available data. A common practice is to keep the first p principal components that allow to retain almost the 95 % of total amount of variance, namely

$$rv_1 + rv_2 + ... + rv_p \geq 0.95 \tag{6.13}$$

  The selected component organized by columns will form the loading matrix $\boldsymbol{L}_P$.

- Transformation of the data along the principal component axes

$$\boldsymbol{T} = \boldsymbol{L}_P^T \, \boldsymbol{Z} \tag{6.14}$$

  After the transformation, most of the information contained in the original data is described with a lower number of variables. Matrix $\boldsymbol{T}$ is denoted as score matrix and its elements as principal components scores.

- Reconstruction of the original variables through the loading matrix $\boldsymbol{L}_P$, discarding the last principal components whose variability is associated to noise:

$$\hat{\mathbf{Z}} = \left(\boldsymbol{L}_P \, \boldsymbol{L}_P^T\right) \, \boldsymbol{Z} \tag{6.15}$$

If the aim is the compression of data, the procedure ends with Eq. (6.14). Conversely, if it necessary to have noise-filtered data in the original coordinate system, then also Eq. (6.15) is needed.

Table 6.5: Network identifiers and corresponding input data.

Network identifier	Damage features
N1	Frequencies and mode shapes
N2	Frequencies and mode shapes filtered with PCA (14 comp.)
N3	Frequencies and mode shapes filtered with PCA (15 comp.)
N4	Acceleration features using FFT and PCA
N5	Displacement features using FFT and PCA
N6	Displacement features using resampling and PCA
N7	Displacement features using resampling

6.3.7 Input and output data of the networks

In this section the networks employed in this procedure are described, with reference to the construction of the input vector of the MLP. The networks and their corresponding identifiers are listed in Table 6.5 together with a brief description of the input features.

As concerns modal properties, three different networks are developed: they are network N1, N2 and N3. All these networks have an input vector composed of the natural frequencies followed by the mode shapes with only the components corresponding to the five sensor of the monitoring system (A1-A5 in Fig. 6.3). Network N1 takes in input the modal properties corrupted by noise according to Eq. (6.9). For network N2 and N3 a noise filtering operation is performed through PCA. A baseline set of frequencies and mode shapes is created considering only data referred to the undamaged state. Then PCA is applied separately to the frequency and mode shape sets in order to compute the loading matrices $\boldsymbol{L}_{P,f}$ and $\boldsymbol{L}_{P,\phi}$. At the end, data are reconstructed in the original coordinate system using Eq. (6.15).

The core of the problem lies in the choice of the number of principal components to retain. In this instance, frequency set is analyzed: each principal component describes about 25 % of the total variance. Consequently, all the four principal components are retained and the original data are conserved. As concerns mode shapes, the cumulative percentage of variance described by the principal components is represented in Fig. 6.6. Considering the values ranging from 14 to 16 of the principal components, the corresponding explained variance assumes the values of 91.5 %, 96.0 % and 99.9 %. Since the value of 99.9 % is high and it includes variability depending on noise, the implications of considering 14 or 15 principal components are studied. In the first case (14 components) the reconstructed data form the input vector of network N2, while in the second (15 components) we have network N3. It is worth noticing that baseline sets are composed of only data related to the undamaged scenario, but this operation is applied to data associated to any scenario.

Acceleration features given in input to network N4 are obtained applying the FFT to the signals in time domain and, subsequently, condensing the information of the 5 sensors in one vector by means of PCA. After FFT, the resulting signals in frequency domain are arranged in columns forming a matrix that is the subject of PCA. The input vector is the first column, corresponding to the first principal component, of the transformed matrix

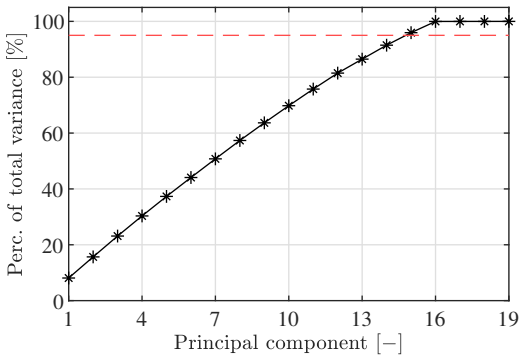

Figure 6.6: Cumulative percentage of total variance explained by the principal components of the mode shape baseline. Red dashed line: threshold value of 95 %.

(matrix $\boldsymbol{T}$ in Eq. (6.14)). The same operations are performed over the displacement response obtaining the input vector for network N5. The input features of network N7 are the resampled displacement time series of each sensor arranged in a vector, while for network N6 the resampled displacements are compressed with PCA in the same manner described for network N4 and N5.

The finality of each network is the classification, realized on the basis of the input features, of the state of the structure in one of the following conditions:

- undamaged condition;
- light damaged condition. Scenarios with a damage severity between 0 % and 15 % are part of this class;
- severe damaged condition. Scenarios with a damage severity greater than 15 % are part of this class.

The output is a 3×1 vector containing the probability associated to each class in the order kept in the previous list.

6.3.8 Training process, network performances and their optimization

The description of the training process is not dependent on the type of network listed in Table 6.5, hence in the following we refer to a generic dataset, not specifying the kind of data. A large dataset, created in the way delineated in section 6.3.5, is partitioned into a training and a test set.

The training set is used for the calibration of the network coefficients. An optimization problem is carried out where the average cross-entropy loss function defined with Eq. (6.7) has to be minimized. The test set is used to assess the network behavior with respect to data not included in the network training. In this case, the generalization capacity of the network is checked. The initial dataset is randomly shuffled before the partitioning in order

to increase the data variability inside the training and the test sets. Network creation and training are performed with the MATLAB functions "patternnet" and "train", respectively.

A third set is usually defined in the partitioning, called validation set. It can be used for regularization by means of the early stopping strategy: the training is stopped when the error on the validation data set increases, as this is a sign of over-fitting of the training set [136]. For this application, this strategy is unnecessary since the high number of data composing the training set is supposed to ensure network generalization.

Network performances can be assessed in terms of accuracy and number of uncertain predictions. Accuracy is a measure of the errors that a network commits, deriving from the comparison between network prediction and the relative target class. The accuracy of each network is calculated with reference to two different criteria. With the first criterion, the exact correspondence between predicted output and target is considered for the identification of errors. In the second case, a margin value δ, that has to be added to the damage severity boundaries previously introduced for the three classes, is assigned for the assessment of significant errors. If the classification output is not correct, but the damage severity belongs to the neighborhood defined by δ, the error committed is not considered as significant. A value of 5 % is assumed for δ. This leads to the distinction between:

- Strict accuracy, obtained accounting for all the errors committed;
- Soft accuracy, obtained accounting for only significant errors.

As concerns uncertain predictions, they can be computed considering the probability expressed by the soft-max function of Eq.(6.3). In particular, a threshold value ε is defined equal to 0.33, which discriminates the certainty of the prediction. Let $y_{ord} = [p_1, p_2, p_3]$ be the output vector of the network with probabilities ordered in descending order, where $p_1 > p_2 > p_3$, then if $p_1 - p_2 < \varepsilon$ the result is considered uncertain.

The optimization of the network architecture is performed with the aim to tune a series of hyper-parameters so that the performance of a network is the best possible. The hyper-parameters considered are the number of hidden layers, their size and the type of transfer function used. The possible values of the hyper-parameters are chosen according to common rules adopted in the ML community and in order to avoid an excessive requirement of analysis. The hidden layers can be one or two, their size may vary between the dimension of the output vector (i.e, 3) and the dimension of the input vector, which depends on the associated network. The possible choices for the transfer function are represented by the functions of Eqs. (6.4), (6.5) and (6.6). If two hidden layers are employed, they have the same transfer function.

First, the situation where a single hidden layer composes the network is studied. In the following, only the analysis related to network N2 and N5 are presented, as their results are representative and for the sake of simplicity. The evolution of the training and test accuracy in function of the number of neurons is showed in Fig. 6.7. At the same time, fixed the number of neurons, the activation function is changed between the alternatives provided by Eqs. (6.4), (6.5) and (6.6). For both networks N2 and N5 the accuracy obtained using a ReLU activation function (Eq. (6.6)) is lowest regardless of the number of neurons. The performance of the hyperbolic tangent function (Eq. (6.5)) and the Sigmoid

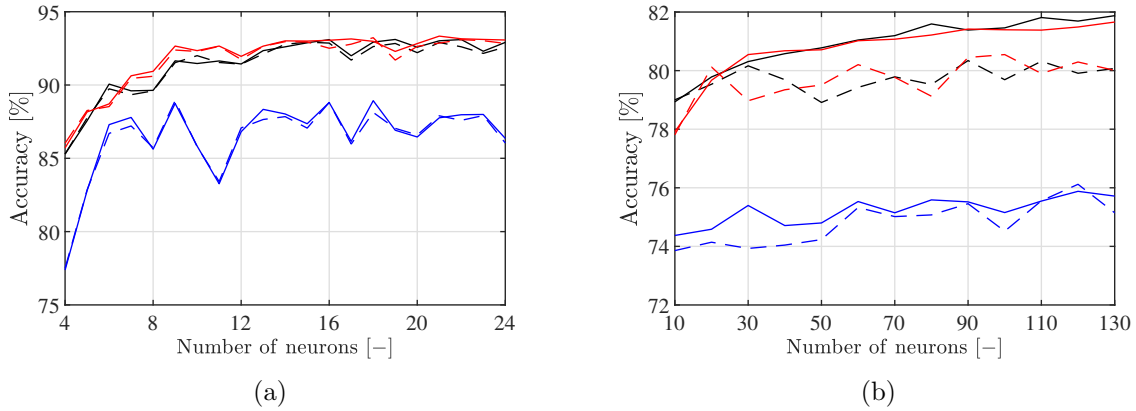

Figure 6.7: Accuracy of networks (a) N2 and (b) N5 for different numbers of neurons in the single hidden layer and for different activation functions. Black lines: hyperbolic tangent function; red lines: Sigmoid function; blue lines: ReLU function. Solid lines: accuracy related to the training set; dashed lines: accuracy related to the test set.

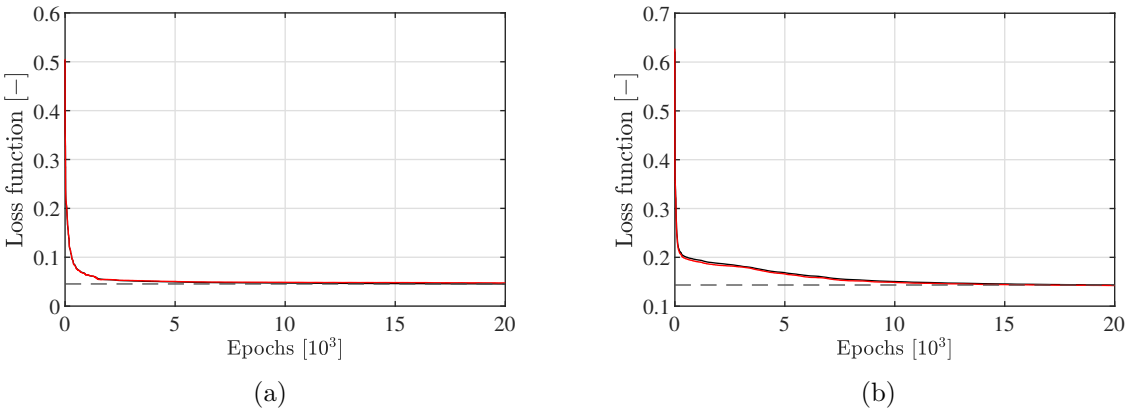

Figure 6.8: Loss function evolution with the number of training epochs for networks (a) N2 and (b) N5. Black line: loss function for training set; red line: loss function for test set; black dashed line: best value of the loss function.

logistic function (Eq. (6.4)) are substantially comparable. Focusing on the difference between training and test set, performances for N2 are very similar, denoting a high level of generalization, while for N5 the test accuracy is always lower than the train accuracy, except when few neurons are adopted. The number of epochs needed to train the networks are different and depends on the size of the input vector. N3 reach the best value of the loss function after approximately 5000 epochs (Fig. 6.8(a)) and during the remaining epochs the performance does not significantly improve. The same consideration is valid for networks N1 and N2. N5 needs about 10000 epochs, as highlighted in Fig. 6.8(b), and a similar behaviour is observed for N4, N6 and N7, even if the number varies between 10000 and 15000.

The introduction of a second layer improves the accuracy of all the networks. It has not

Table 6.6: Optimal architectures of the studied network. The layer size is expressed inside square brackets where the number of the hidden layer follows an ascending order.

Network	Transfer function	Layer sizes
N1	Hyperbolic tangent	[24; 20]
N2	Hyperbolic tangent	[10; 10]
N3	Hyperbolic tangent	[10; 10]
N4	Hyperbolic tangent	[200; 175]
N5	Sigmoid	[100; 50]
N6	Hyperbolic tangent	[50; 30]
N7	Hyperbolic tangent	[100; 50]

been adopted a grid strategy, namely modifying in an orderly way the number of neurons of the first and of the second hidden layer, because it would have implied a considerable loss of time. The optimization has been conducted with a trial-and-error strategy saving the architectures that resulted in better performances than those of the single hidden layer architecture. With this strategy the global optimum may not be obtained, even if the analysis performed have underlined a low variability of the performance with the number of neurons of the two hidden layers. It can be supposed that the resulting architectures represent near-optimal solutions. According to the findings of Fig. 6.7, the ReLU activation function has been discarded in the search, since it is characterized by the worst performances. The optimal architectures found with the previously explained strategy are summed up in Table 6.6.

6.4 Results of damage detection procedure

In this section, the results of the damage detection procedure are presented and analyzed. The discussion presents results of the training and test phase for data computed by model S (section 6.4.1) and results of the test phase for data computed by model D (section 6.4.2).

6.4.1 Training and test with model S

The performance indices of the network listed in Table 6.5 are shown in Fig. 6.9. The first consideration is about the very small difference between the same quantity (strict accuracy, soft accuracy or percentage of uncertain predictions) related to the training and test dataset for the same network. This excludes over-fitting of data for all the networks despite a validation dataset has not be used, since the high number of data ensure network generalization. Another general consideration regards the qualitative relationship between strict accuracy and number of uncertain predictions. The latter decreases when there is an increment of accuracy.

Performances of network N1, that takes in input noise-corrupted modal properties, are the

worst, both in terms of accuracy and reliability. This proves how the MLP has difficulties in finding patterns between data because the effect of noise covers the changes of modal properties caused by damage.

The application of PCA in order to filter noise is successful for both network N2 and N3: strict and soft accuracy are larger than 90 % and the percentage of uncertain predictions is lower than 10 %. There are not significant differences between N2 and N3, except for few percentage points in favour of N2. The choice between 14 or 15 principal components for the construction of the loading matrix ($\boldsymbol{L}_P$ in Eq. (6.15)) does not produce substantial differences in this phase.

The best performances have been obtained by networks N4, taking in input acceleration features. As concerns soft accuracy, the values of 100 % denotes the absence of significant errors. In addition, the percentage of uncertain predictions (4 %) is the lowest. Very good soft accuracy values, equal or larger than 90 %, have been obtained also for networks N5, N6 and N7, which employ displacement features. Strict accuracy values of these networks are lower and range between 72 % and 81 %. At the same time, an appreciable percentage of network predictions is uncertain, especially for N6. It is worth reminding that displacement response are obtained for double integration of noise-corrupted accelerations. In this way, errors are surely magnified and this may be a reason for the worse performances of networks N5, N6 and N7 compared to that of N4.

In Fig. 6.10 an analysis of errors committed by the networks is illustrated. Errors corresponding to uncertain predictions are an important part of total errors. The same is even more valid for significant errors. The highest percentage is obtained by network N1, where more than the 80 % of erroneous predictions are at the same time uncertain. This means that about the 27 % of the total predictions (with reference to the training set) are at the same time erroneous and uncertain. For example, a very lower number is obtained for network N4, where the errors are the 4 % of the total predictions (training set), and the 38 % of them are also uncertain. Repeating the same consideration, about the 2 % of the total predictions are at the same time erroneous and uncertain.

Finally, an additional test is carried out for networks using modal properties, i.e. networks N1, N2 and N3. The difference from a numerical point of view between a near-zero component computed by model S and D (the latter simulating "real" experimental data) has been highlighted in section 6.3.3. This may surely facilitate the distinction between damaged or undamaged state of the model, but it would remain a pure numerical exercise, without possibility of extension to an experimental case. The consequent adoption of a specific source of error for these components is described in section 6.3.4.

With the aim to verify if this source of error actually prevents the problem, the test under consideration involves the exclusion of the component associated to sensor A3 for all the modes from the data provided to the MLP. The operations regarding the detection procedure remain the same, the only difference lies in the number of mode shape components that is decreased. Due to the latter fact, the number of principal components selected is different. In particular, N2 and N3 have 10 and 11 components, corresponding to a percentage of total explained variance of 89.7 % and 95.4 %, respectively. The performances of these networks are shown in Fig. 6.11, while the percentage of errors that corresponds to uncertain predictions can be found in Fig. 6.12. Comparing these values with those

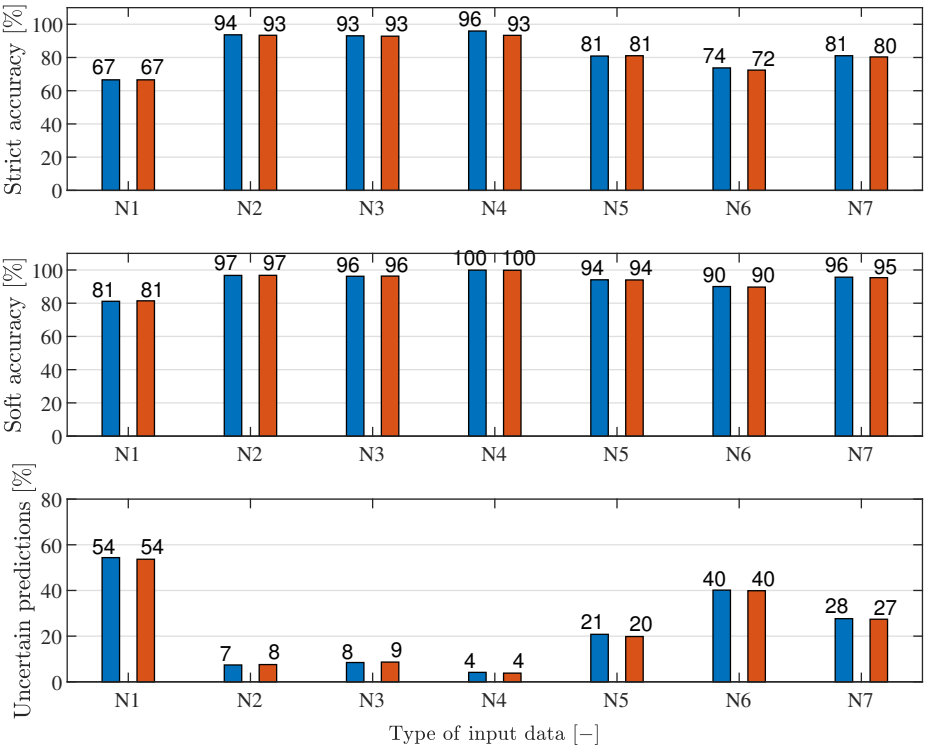

Figure 6.9: Network performances for the dataset generated by model S. Blue bars: performances related to the training dataset; red bars: performances related to the test dataset.

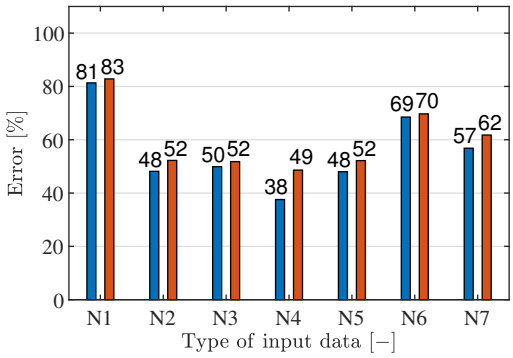

Figure 6.10: Percentage of errors (blue bars) and significant errors (red bars) corresponding to uncertain predictions for different networks.

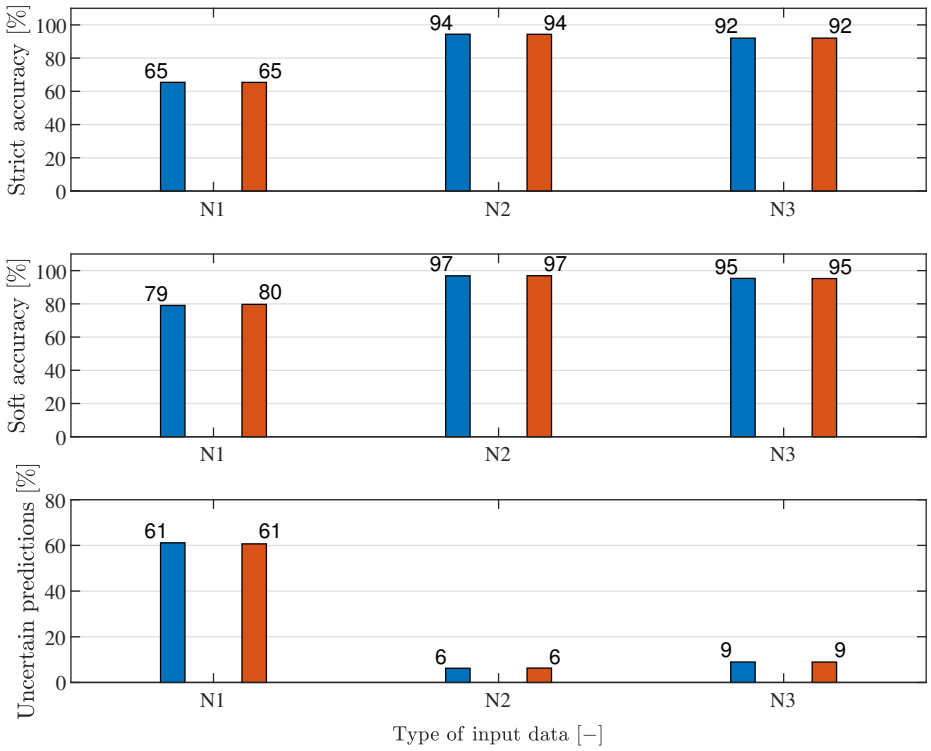

Figure 6.11: Performances of network N1, N2 and N3 using the dataset generated by model S discarding the sensor A3. Blue bars: performances related to the training dataset; red bars: performances related to the test dataset.

obtained in Fig. 6.9 and 6.10 for networks N1, N2 and N3, we may note that differences are very limited. Hence, the source of error for near-zero components is able to reduce their accuracy because the performances of network N1 are very similar in the two cases, namely the case with 5 sensors and a specific error for near-zero components and the case with 4 sensors. On the other hand, the application of PCA greatly reduces the influence of this error in the detection process, as we can see from the results of networks N2 and N3.

6.4.2 Test with model D

For the test with the more detailed model (model D), 7 scenarios have been taken into account: the first represents the undamaged state of the model, while the remaining six are damage scenarios, listed in Table 6.7 together with the previous one. Damage in the steel beam (with reference to scenarios S2, S3 and S4) is introduced by decreasing the elastic modulus of an element row of the bottom flange. The elastic modulus of these elements is set to a very low value, namely 1 MPa, aiming at simulating material discontinuity. The model corresponding to the scenario S3 is illustrated, as an example, in Fig. 6.13, where the damaged elements are represented in red. For scenarios involving damage of the concrete slab, i.e. S5, S6 and S7, the elastic modulus of concrete is reduced by 50 % simulating the openings of cracks. In S5 and S6 a whole element row along the slab width

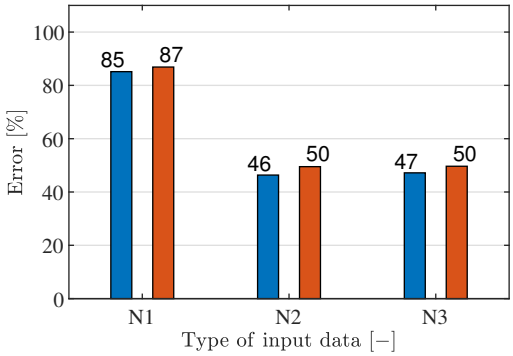

Figure 6.12: Percentage of errors (blue bars) and significant errors (red bars) corresponding to uncertain predictions for networks N1, N2 and N3 using the dataset generated by model S discarding the sensor A3.

Table 6.7: Scenarios created with model D.

Code	Damaged part	Location along the bridge length	Extension
S1	Undamaged condition	-	-
S2	Steel flange	One fourth	Element strip
S3	Steel flange	Middle	Element strip
S4	Steel flange	Three fourth	Element strip
S5	Concrete slab	One fourth	Element strip
S6	Concrete slab	Middle	Element strip
S7	Concrete slab	One third	Nearly semi-circular area

is damaged, while in S7 a nearly semi-circular area is considered, as shown in Fig. 6.14.

Dynamic data (modal properties, acceleration and displacement time series) are generated for each scenario. The natural frequencies of the seven scenarios are reported in table 6.8 together with the MAC values of the mode shapes. The MAC values are computed with reference to the undamaged scenario and by considering only the five components

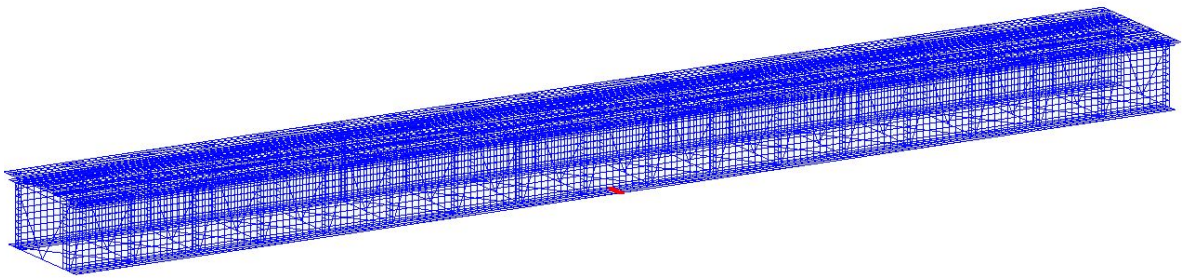

Figure 6.13: Damage scenario S3 for model D. The damaged elements are represented in red.

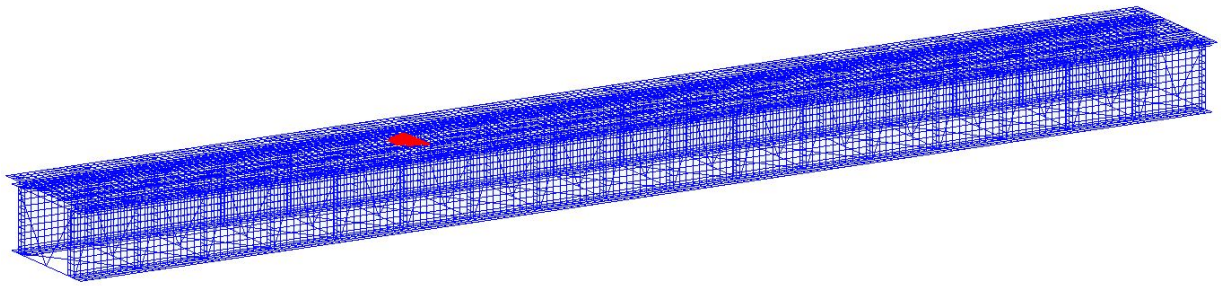

Figure 6.14: Damage scenario S7 for model D. The damaged elements are represented in red.

Table 6.8: Natural frequencies and MAC values, referred to the comparison with the undamaged condition, for the seven scenarios created with model D.

Frequency	Scenario						
	S1	S2	S3	S4	S5	S6	S7
1^{st} [Hz]	1.697	1.683	1.671	1.684	1.696	1.695	1.696
2^{nd} [Hz]	5.859	5.773	5.859	5.801	5.855	5.858	5.857
3^{rd} [Hz]	12.958	12.927	12.769	12.932	12.939	12.952	12.953
4^{rt} [Hz]	18.194	18.190	18.189	18.192	18.190	18.190	18.172
MAC value	Scenario						
	S1	S2	S3	S4	S5	S6	S7
1^{st} mode [%]	100	100	100	100	100	100	100
2^{nd} mode [%]	100	99.99	100	99.99	100	100	100
3^{rd} mode [%]	100	98.22	90.43	99.02	100	100	100
4^{rt} mode [%]	100	100	99.99	100	100	100	99.99

corresponding to the sensor location of the monitoring system. As expected, the frequencies of the damaged scenarios are all lower than the corresponding frequencies of the undamaged scenario. However, in few cases the reduction is remarkable. In the remaining, the reduction magnitude is surely comparable to the effect of noise or external factors. The effect of damage is even less clear observing the MAC values. Only for the third mode of scenario S3 there is a significant change. The discussion is divided in two sections referred to the network based on modal properties (section 6.4.2.1) and the networks based on acceleration and displacement features (section 6.4.2.2).

6.4.2.1 Network N1, N2 and N3

The focus is first addressed to the network predictions using the exact values of modal properties computed by the FE software. They are provided as they have been computed to network N1, while they are filtered using the PCA model constructed with 14 or 15 principal components for network N2 and N3, respectively. Table 6.9 contains the prediction results.

Table 6.9: Predictions of network N1, N2 and N3 based on exact modal properties. P_U: probability associated to the undamaged condition; P_{LD}: probability associated to the light damage condition; P_{SD}: probability associated to the severe damage condition.

Network	Probability	Scenario						
		S1	S2	S3	S4	S5	S6	S7
N1	P_U [-]	0.00	0.10	0.08	0.00	0.00	0.00	0.00
	P_{LD} [-]	0.00	0.03	0.80	0.00	0.00	0.00	0.00
	P_{SD} [-]	1.00	0.87	0.12	1.00	1.00	1.00	1.00
N2	P_U [-]	0.00	0.00	0.00	0.00	0.00	0.00	0.00
	P_{LD} [-]	0.00	0.00	0.00	0.00	0.00	0.00	0.00
	P_{SD} [-]	1.00	1.00	1.00	1.00	1.00	1.00	1.00
N3	P_U [-]	0.00	0.00	0.00	0.00	0.00	0.00	0.00
	P_{LD} [-]	0.00	0.00	0.00	0.00	0.00	0.00	0.00
	P_{SD} [-]	1.00	1.00	1.00	1.00	1.00	1.00	1.00

They are very similar for all the networks: all the scenarios are identified as severely damaged except for scenario S3 of network N1 that results in a light damage condition. Even scenario S1, corresponding to the undamaged state of the detailed FE model, is recognized as severely damaged with unit probability by all the networks.

The situation basically remains the same if exact modal properties are corrupted with Gaussian noise on the basis of Eq. (6.9) using 1 % and 5 % as coefficients of variation for frequencies and mode shapes, respectively, and 100 samples are extracted. In Table 6.10 the number of samples identified in the different classes for each scenario is indicated.

In the author's opinion, the reason of these bad results has to be attributed to the discrepancy between the modal properties computed by model D and model S. Although model S has been calibrated based on the response of the model D, residual errors still remains both for natural frequencies (Table 6.4) and mode shapes, as highlighted in Fig. 6.5 for mode 2 and 4.

The proposed solution is to correct modal properties computed by model D by adding the residual error obtained at the end of the calibration. The generic m-th corrected frequency $f_{m,cor}$ and mode shape $\boldsymbol{\phi}_{m,cor}$ can be computed starting from the exact values f_m and $\boldsymbol{\phi}_m$ as:

$$\begin{aligned} f_{m,cor} &= f_m + \eta_{f_m} \\ \boldsymbol{\phi}_{m,cor} &= \boldsymbol{\phi}_m + \boldsymbol{\eta}_{\boldsymbol{\phi}_m} \end{aligned} \tag{6.16}$$

where η_{f_m} and $\boldsymbol{\eta}_{\boldsymbol{\phi}_m}$ represent the residual error for the m-th frequency and the vector of residual errors for the m-th mode shape, respectively. This operation can be performed in a real case if a long-term monitoring of these properties is previously realized. In this way, the several sources of uncertainty affecting modal properties can be partially or mostly removed and their mean values identified. It is worth underlying that the residual error is applied in the same manner for all the structure conditions, both undamaged and damaged, despite

Table 6.10: Predictions of network N1,N2 and N3 based on pseudo-experimental modal properties. N_U: number of samples classified in the undamaged condition; N_{LD}: number of samples classified in the light damage condition; N_{SD}: number of samples classified in the severe damage condition.

Network	Prediction	Scenario						
		S1	S2	S3	S4	S5	S6	S7
N1	N_U [-]	0	0	0	0	0	0	0
	N_{LD} [-]	0	0	100	0	0	0	0
	N_{SD} [-]	100	100	0	100	100	100	100
N2	N_U [-]	0	0	0	2	2	1	0
	N_{LD} [-]	0	0	0	0	0	0	0
	N_{SD} [-]	100	100	100	98	98	99	100
N3	N_U [-]	0	0	0	0	0	0	0
	N_{LD} [-]	0	0	0	0	0	0	0
	N_{SD} [-]	100	100	100	100	100	100	100

it was computed referring to the first one. There is no guarantee that it does not change when the structure is damaged, but its computation for different damage scenarios was not performed because it is unrealistic to expect that experimental data about a damage scenario of a specific bridge can be available. Moreover, this solution is expected to enable the correct identification of the undamaged conditions of the structure since this is the problem revealed by results of Tables 6.9 and 6.10.

Predictions results are shown in Table 6.11. In this context, networks N1, N2 and N3 behave in different manners. As concerns N1 and N2, the first four scenarios are correctly identified with certain probabilities. The only questionable aspect is the classification of scenario 2 in high damage level and of scenarios 3 and 4 in light damage level despite the severity of damage is the same for all. Scenarios 5,6 and 7 are mistakenly recognized as undamaged: predictions for S5 and S7 are certain, while probabilities P_U and P_{LD} are very close for S6. On the other hand, network N3 identifies S1 in the light damage class, even if the result is highly uncertain with respect the severe damage class. S2 and S3 are recognized as severely damaged with P_{SD}=1, but it is not the same for S4 (P_U=1). N3 is the only network able to recognize scenarios S5, S6 and S7 in a damaged condition. S5 and S7 are classified in the light damage condition, while S6 in the severe condition.

The behaviour of the networks is analyzed also when exact values computed by model D are corrupted with Gaussian noise. The coefficient of variation is fixed to 1 %, while different cases are considered by varying the mode shape coefficient of variation in the range [1%, 10 %]. Once the coefficients of variation are fixed, 100 samples of pseudo-experimental data are extracted and the predictions of networks N1, N2 and N3 are computed. Fig. 6.15(a) shows the trend of the accuracy with the mode shape coefficient of variation (CV) for the three networks. Network N3, that does not identify the undamaged condition when exact data are employed, has a very bad accuracy regardless of the value of the mode shape

Table 6.11: Predictions of network N1, N2 and N3 with previous application of residual error. P_U: probability associated to the undamaged condition; P_{LD}: probability associated to the light damage condition; P_{SD}: probability associated to the severe damage condition.

Network	Probability	Scenario						
		S1	S2	S3	S4	S5	S6	S7
N1	P_U [-]	0.69	0.00	0.08	0.08	0.76	0.55	0.86
	P_{LD} [-]	0.28	0.00	0.80	0.92	0.22	0.40	0.13
	P_{SD} [-]	0.03	1.00	0.12	0.00	0.02	0.05	0.01
N2	P_U [-]	1.00	0.00	0.00	0.00	1.00	0.99	1.00
	P_{LD} [-]	0.00	0.00	0.00	1.00	0.00	0.00	0.00
	P_{SD} [-]	0.00	1.00	1.00	0.00	0.00	0.01	0.00
N3	P_U [-]	0.00	0.00	0.00	1.00	0.00	0.00	0.00
	P_{LD} [-]	0.54	0.00	0.00	0.00	0.96	0.26	0.94
	P_{SD} [-]	0.46	1.00	1.00	0.00	0.04	0.74	0.06

CV. Networks N1 and N2 present a comparable behaviour for a value of 1% of the CV, but, increasing its value, N1 has a rapid decrease of the accuracy, while N2 keeps a good value, larger than 60 %, also for a CV equal to 10 %. The behaviour for scenarios S2 and S3 is not shown since all the networks remain coherent in the identification of the severe damage condition.

In Fig. 6.15(b) the coherence of the networks with regard to the identification of the class predicted for exact values of the modal properties is investigated for scenario S4. The predictions for the exact values are different: severe damage for N1, light damage for N2 and no damage for N3. N2 has proven to be less sensitive to the magnitude of noise. Moreover, it classifies data in a damaged condition most of the times, unlike N3. Finally, results for scenarios S5, S6 and S7 are highly variable depending on the considered network. However, for all the network it can be seen an increment of cases identified as severely damaged when the mode shape CV ranges from 1 % to 10 %.

6.4.2.2 Network N4, N5, N6 and N7

Ten trains differing in axle loads and speed have been considered: their characteristics are listed in Table 6.12 (speed) and Tables 6.13 and 6.14 (axle loads). For each train, a dynamic analysis with moving loads has been performed obtaining acceleration and displacement responses in time domain. An example of these responses, related to sensor A3 and computed with reference to the characteristics of train nr.8 has been represented in Fig. 6.4 of section 6.3.3. The responses computed by model D are represented by red lines: the maximum displacement is about 7 mm, while the maximum acceleration is in the order of 25 mg. The corresponding responses computed by model S are represented with black lines in the same figures.

Response time series calculated for all the ten trains are then elaborated as described in

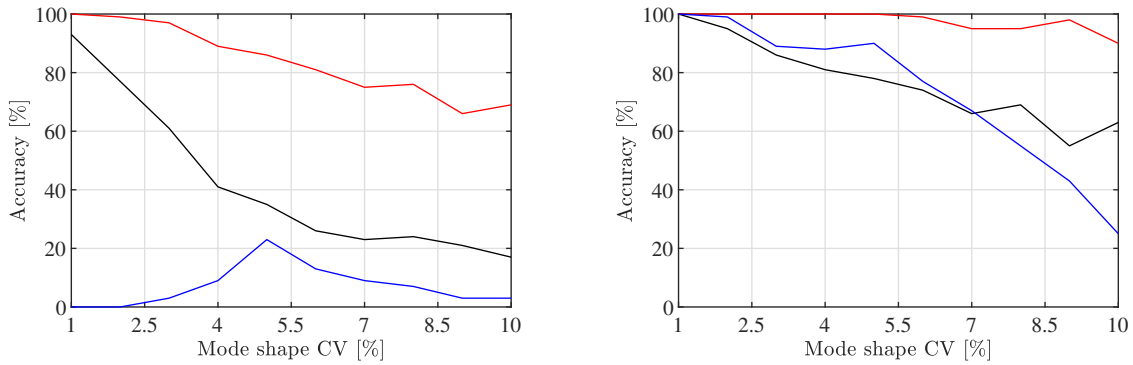

Figure 6.15: Accuracy trend of networks N1, N2 and N3 with mode shape CV for noise-corrupted data with the application of residual errors. Trend for (a) scenario S1 and (b) scenario S4.

Table 6.12: Speeds of the 10 trains considered in the test phase with model D.

Train number	Speed [km/h]
1	111
2	108
3	100
4	105
5	103
6	105
7	109
8	106
9	118
10	114

section 6.3.7 and the extracted features are given in input to networks N4, N5, N6 and N7. Prediction results are summed up in Table 6.15. Networks N4 (acceleration features extracted using FFT and PCA) and N6 (displacement features extracted using resampling and PCA) give the same results for all the scenarios, classifying almost the totality of the train data in a severe damage condition. For networks N5 (displacement features extracted using FFT and PCA) and N7 (displacement features extracted using resampling) the predictions are more variables but the undamaged scenario S1 is not recognized in most cases.

In order to analyze the causes of this behaviour, a comparison between the input features of the networks extracted from the responses computed by model D and S, for the same value of train speed and axle load, is performed. The characteristics of train nr. 8 are taken into account, as the undamaged scenario S1 for this train is never recognized and all the

Table 6.13: Axle load of the trains 1-5 considered in the test phase with model D. P_l: load of the left wheel; P_r: load of the right wheel.

Position	Train nr.1		Train nr.2		Train nr.3		Train nr.4		Train nr.5	
	P_l	P_r	P_l	P_r	P_l	P_r	P_l	P_r	P_l	P_r
[m]	[kN]	[kN]	[kN]	[kN]	[kN]	[kN]	[kN]	[kN]	[kN]	[kN]
0	42	46	52	67	57	55	48	47	51	50
4	46	42	59	63	57	53	51	54	47	46
14	44	42	38	43	57	48	52	55	50	48
18	61	52	54	65	53	51	47	49	55	53
28	46	49	51	53	43	46	46	46	50	45
32	53	49	43	49	53	54	48	48	50	54
42	49	57	47	53	58	44	48	49	47	52
46	54	51	51	48	52	44	49	51	50	50

Table 6.14: Axle load of the trains 6-10 considered in the test phase with model D. P_l: load of the left wheel; P_r: load of the right wheel.

Position	Train nr.6		Train nr.7		Train nr.8		Train nr.9		Train nr.10	
	P_l	P_r	P_l	P_r	P_l	P_r	P_l	P_r	P_l	P_r
[m]	[kN]	[kN]	[kN]	[kN]	[kN]	[kN]	[kN]	[kN]	[kN]	[kN]
0	53	51	47	52	46	53	47	54	50	46
4	46	52	45	50	45	51	55	53	55	50
14	48	49	52	53	53	52	52	51	51	46
18	48	49	50	52	51	52	50	47	53	53
28	51	55	50	54	50	53	50	47	50	53
32	46	45	54	54	54	53	46	54	49	52
42	52	54	51	48	53	46	52	45	53	46
46	46	54	51	52	50	52	45	50	46	52

Table 6.15: Predictions of network N4, N5, N6 and N7.N_U: number of samples classified in the undamaged condition; N_{LD}: number of samples classified in the light damage condition; N_{SD}: number of samples classified in the severe damage condition.

Network	Prediction	Scenario						
		S1	S2	S3	S4	S5	S6	S7
N4	N_U [-]	1	1	1	1	1	1	1
	N_{LD} [-]	0	0	0	0	0	0	0
	N_{SD} [-]	9	9	9	9	9	9	9
N5	N_U [-]	3	4	4	3	4	3	4
	N_{LD} [-]	2	1	0	1	1	2	1
	N_{SD} [-]	5	5	6	6	5	5	5
N6	N_U [-]	0	0	0	0	0	0	0
	N_{LD} [-]	0	0	0	0	0	0	0
	N_{SD} [-]	10	10	10	10	10	10	10
N7	N_U [-]	0	0	0	0	0	0	0
	N_{LD} [-]	5	8	8	7	5	6	5
	N_{SD} [-]	5	2	2	3	5	4	5

networks studied identify a severe damage condition. Fig. 6.16(a) shows the comparison for the first component scores (see section 6.3.6 for their definition) of the acceleration amplitude in frequency domain: there are significant discrepancies which derive from the differences between responses in frequency domain computed by model D and S, as we have noticed in Fig. 6.4(b).

For displacement features differences are surely less marked, as illustrated in Fig. 6.16(b) and Fig. 6.16(c) with reference to network N5 and N6, respectively. The comparison between input features of network N7 is not presented, but the same observations can be made. The differences found for all the networks, that are more pronounced for N4 compared to networks N5, N6 and N7, compromise their predictions.

Following the same approach delineated for network N1, N2 and N3 (section 6.4.2.1), residual errors between the extracted features of models D and S are computed. The focus is addressed only on displacement features because there are at least similarities in the comparison between responses of model D and S. On the other hand, it makes no sense to talk about residual errors when the discrepancies between the two models are so extended, like for accelerations.

With the aim to compute residual errors, the parameters influencing a generic displacement response, supposing that the stiffness and mass matrices remain unchanged, are analyzed. Displacements surely depend on the characteristics of the train, namely axle load and train speed. Even the axle load distribution, and not only the whole train load, is significant. In order to prove its influence, a specific distribution of forces, corresponding to the sum of left and right axle loads of Train nr.5, listed in Table 6.13, is considered and all the possible

permutations of that force vector are computed. Focusing only on 1000 permutations chosen in a random way among all the 40320 combinations, the displacement response of the structure is computed for a given speed value, the one of the train nr. 5. Fig. 6.17(a) shows the maximum and minimum values of the corresponding displacement time histories with reference to sensor A3: the maximum difference between the two responses is about 1 mm, that corresponds to an increment of the 16 % of the minor peak value. On the other hand, the first component scores are not affected by the force distribution, as proven in Fig. 6.17(b). Indeed, with reference to the frequency domain, the force distribution modifies only the amplitude of the harmonics composing the signal but not its frequency content. This is proven by the representation of all the 1000 responses of sensor A3 in the frequency domain, realized in Fig. 6.17(c). The latter depends only on the train speed. The first step of PCA involves the normalization of data, making the difference among the amplitudes of the harmonics irrelevant. Hence, when the frequency content of signals is the same, regardless of the amplitudes, the first component scores are the same.

Conversely, train speed influences both responses in time and frequency domain and their first component scores. The initial force distribution of the previous analysis, related to the train nr. 5 (Table 6.13), is considered again for the present analysis. In this case, the variable parameter is the train speed, ranging from 100 to 120 km/h with step size of 1 km/h. The responses in time domain of the sensor A3, calculated for each value of train speed, are represented in Fig. 6.18(a). It is easy to note even without calculating their FFT that the frequency contents of the signals are different. For this reason, the first component scores of the displacement responses vary significantly on the basis of the train speed (see Fig. 6.18(b)).

The previous considerations have been formulated for displacement responses and corresponding scores computed through PCA, which are the input features of network N5. Similar considerations can be made for the input features of N6 and N7. In particular, when PCA is applied to resampled displacements (input of N6) only train speed affects the feature, due to the normalization performed at the beginning of the procedure. The input features of N7, that are simply the resampled displacements, depend on both train speed and loads.

For the previous reason, residual errors are computed and applied only in the cases of networks N5 and N6. Results of the predictions are summed up in Table 6.16. Both networks identify with large accuracy scenarios S1-S4, with only one train that is not well recognized in the worst case. As concerns scenarios S5-S7, network N5 always predicts a damage class, that is the light one for S5-S6 and the severe one for S7. Instead, predictions of N6 are more uncertain for scenario S6 and S7 since there is not a class that is unequivocally identified.

The accuracy of networks N5 and N6 is surely improved with the application of residual errors, but in this perspective and thinking to a real situation, it is necessary to known a priori the relationship between frequency and errors in order to employ a early warning strategy. In this specific case, we are not able to determine a clear relationship, analytical or numerical, on the basis of the few cases of train speed examined.

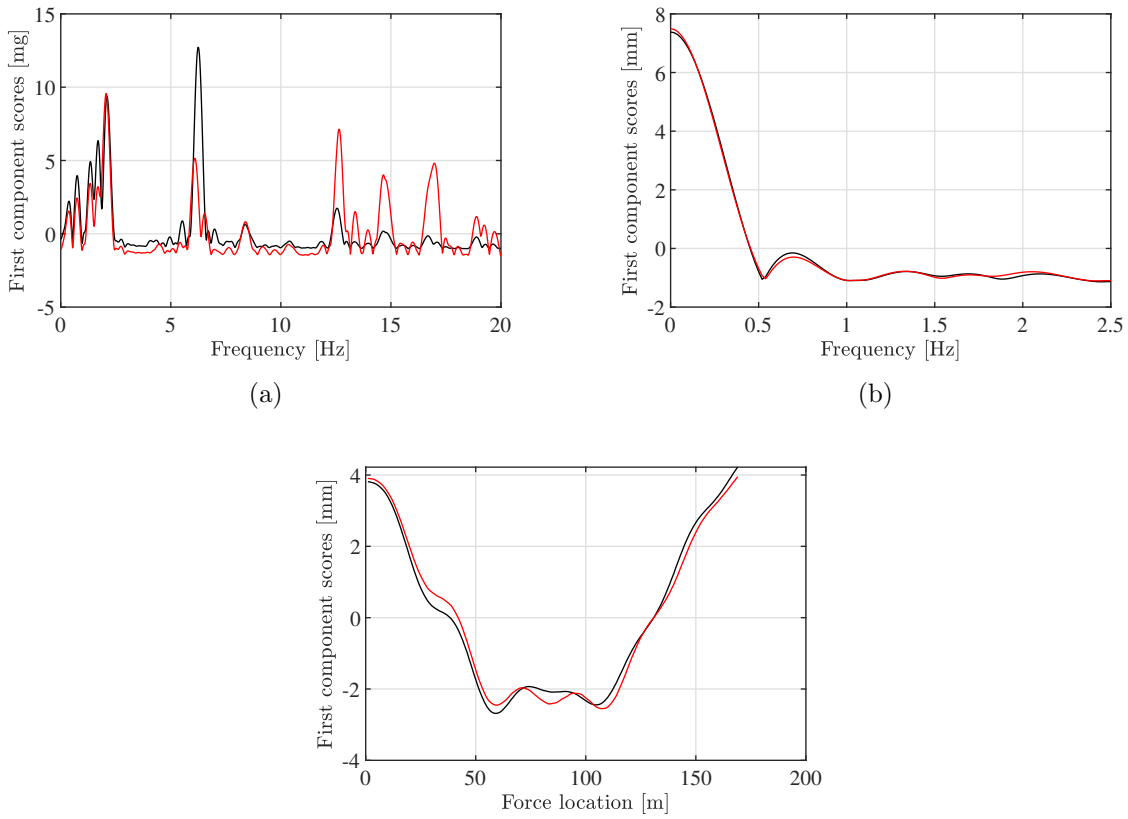

Figure 6.16: Features extracted from the responses related to sensor A3 computed by model S (black lines) and D (red lines) for the train nr.8. (a) PCA applied to the accelerations in frequency domain, input of N4; (b) PCA applied to the displacements in frequency domain, input of N5; (c) PCA applied to the resampled displacements, input of N6.

Table 6.16: Predictions of network N5 and N6 with previous application of residual errors. N_U: number of samples classified in the undamaged condition; N_{LD}: number of samples classified in the light damage condition; N_{SD}: number of samples classified in the severe damage condition.

Network	Prediction	Scenario						
		S1	S2	S3	S4	S5	S6	S7
N5	N_U [-]	10	0	0	0	1	0	0
	N_{LD} [-]	0	0	0	0	8	10	4
	N_{SD} [-]	0	10	10	10	1	0	6
N6	N_U [-]	9	0	0	0	0	4	3
	N_{LD} [-]	0	1	0	0	5	4	4
	N_{SD} [-]	1	9	10	10	5	2	3

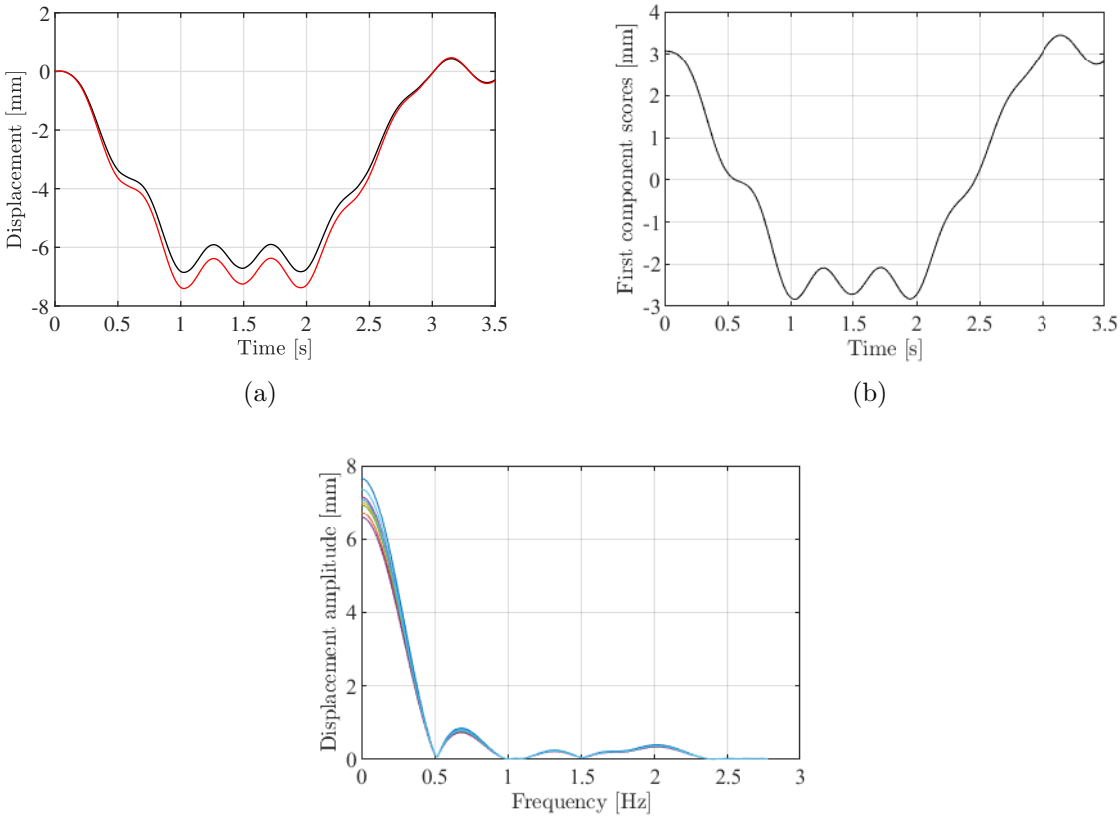

Figure 6.17: Displacement responses computed by model S and caused by a set of 1000 permutations of a specific force vector for a given value of train speed. (a) minimum and maximum values of the response of sensor A3 in time domain; (b) first component scores of the responses of sensors A1-A5 associated to the 1000 permutations and (c) responses in frequency domain of sensor A3 associated to the 1000 permutations.

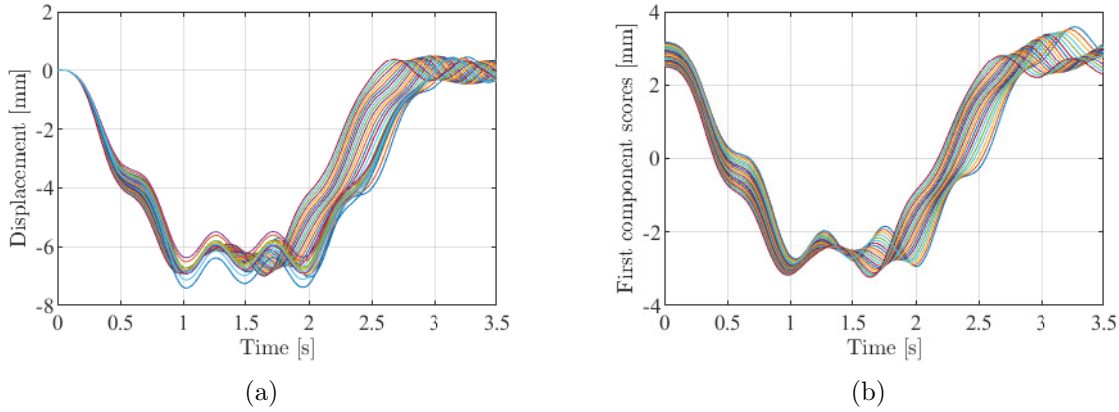

Figure 6.18: Displacement responses computed by model S and caused by a fixed load distribution but by a speed ranging in the interval [100; 120] km/h. (a) responses in time domain of sensor A3 and (b) first principal component scores of the responses of sensors A1-A5.

6.5 Concluding remarks

A damage detection procedure for railway bridges using artificial neural network has been presented in this chapter. The bridge studied is a mixed steel-concrete structure with a single railway line. Several kinds of dynamic data have been employed in the procedure and their efficiency in damage identification assessed. They are modal properties, displacement and acceleration responses caused by the passage of a train on the bridge. Regardless of the data kind, the detection process is a pattern recognition problem where damage features are provided to a multi-layer perceptron which works as classifier. The operations of feature extraction and compression are performed with different techniques: Fourier transform, PCA and a resampling operation proposed for displacements. The procedure includes the modeling of some parameters as random variables in order to account for model and measurement uncertainties, and the use of two numerical models describing the structural behaviour. A simpler model (model S) carries out the classical function of a model, while a more detailed one (model D) simulate the "real" structural behaviour in absence of experimental data. The training of the networks is realized with a dataset generated by model S, while the test phase involves both data from model S and D.

As concerns the training and test phase with model S, predictions of the calibrated networks highlight how the best performances are obtained using acceleration features extracted by FFT and PCA. Very good results are obtained by the two networks taking modal properties filtered by PCA. These networks differ from each other on the basis of the number of principal components adopted in the construction of the mode shape loading matrix. 14 and 15 principal components have been used, respectively. Lower accuracies are obtained for the network of unfiltered modal properties, that is the worst case analyzed, and for the networks using displacement responses. The computation of displacements for double integration of noised accelerations surely represents an additional source of errors that reduces the accuracy of those networks.

The test phase with model D showed the necessity to account for residual errors remained at the end of the calibration between models. In doing so, the undamaged condition and the damage scenarios of the steel beam are recognized in most cases. Otherwise, no network is able to correctly identify the scenarios created. The computation of residual errors show drawbacks for all the networks except for those taking modal properties in input. Indeed, from a pure theoretical point of view modal properties, and consequently their residual errors, are affected only by the characteristics of the structure. Experimental modal properties are actually affected by external factors, like environmental factors or the excitation amplitude, but this dependency can be removed observing these variations with a long-term monitoring. On the other hand, displacement or acceleration responses depends also on the train load and speed. The dependency is only limited to the train speed when the responses are normalized (first step conducted using PCA). In this case, however, from the available data regarding model D and S, a clear relationship between residual errors and train speed cannot be determined. The last analysis is about the influence of the noise added to the exact modal properties computed by model D. Only the network using PCA with 14 components showed a very limited reduction of the accuracy with an increasing level of noise, while the behaviour of the other networks using modal properties is considerably affected by noise.

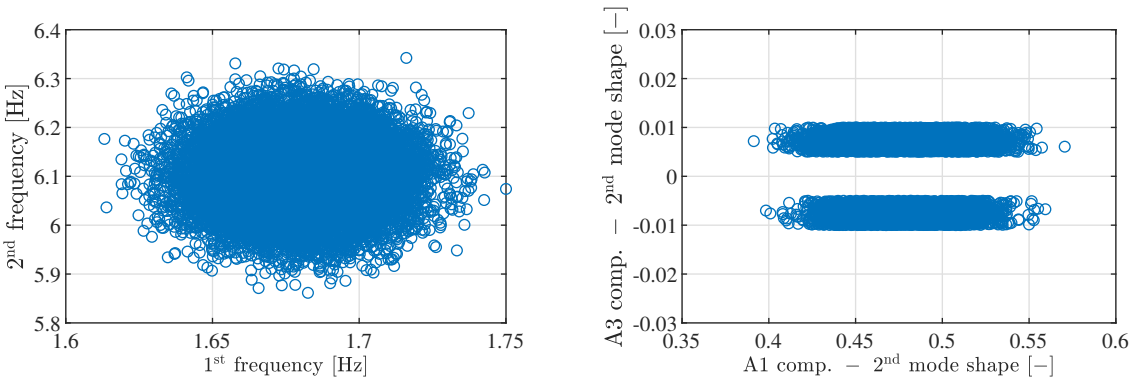

Figure 6.19: Scatter plot of some modal properties forming the baseline for PCA. (a) Fist and second natural frequencies and (b) components A1 and A3 of the second mode shape.

According to the previous results, the choice of the optimal number of principal components must be calibrated in order to obtain accurate results. Even in this case, light damage that does not produce a significant modification of the modal properties cannot be identified. In the author's opinion, an interesting analysis may regard the influence of the size of the baseline dataset on the cumulative explained variance associated to each principal component. This aspect affects the choice of the number of principal components and could improve the detection results. Remaining in this context, it is worth noting that noise filtering performed by PCA is very efficient because the errors introduced in the modal properties are modeled with a Gaussian variable, or in the most complex case (component of sensor A3 for mode 2 and 4) with the sum of a Gaussian and a uniform distribution. Fig. 6.19(a) shows the scatter plot of first and second frequency as an example, while Fig. 6.19(b) represents the variation of the components A1 and A3 of the second mode shape. In this last case, we can observe the elongated shape of the distribution in the A1 component direction due to the proportionality of the standard deviation with the mean value, that for A1 is two order of magnitude greater. Moreover, the addition of a uniform error accounting for the low accuracy of a near-zero component causes the absence of points with ordinate in the interval $[2; -2]\cdot 10^{-3}$. In a real situation, environmental or operational factor may influence different features in different way determining a nonlinear relationship between them [145]. PCA performs linear combination of the original variables, hence it is not the appropriate techniques in this case. Nonlinear techniques like kernel PCA [149, 122] or auto-encoders [31] may be employed in order to learn nonlinear relationship at the price of an increment of the procedure complexity.

For displacement responses, the discrepancy between model and reality (between model D and S in this application) is affected by a higher number of parameters, making its prediction a complex task. Data of model S and D at hand are limited, hence it would be advisable to collect a wide number of responses associated to different values of train load and speed. Further developments involve the extension of the procedure to the localization and the quantification of damage and its application to a real case study for the experimental validation.

Chapter 7

Conclusions

The present chapter summarizes the main conclusions of this work and provides recommendations for future researches in this field. Some damage detection techniques directly or indirectly employing numerical models of a structure have been analyzed, most of them taking advantage of soft computing techniques like evolutionary algorithms or artificial neural networks. First, the focus is addressed to model-based methods and the principal deterministic approaches for the updating of structural models have been cited. Among these, the multi-objective approach has been described in detail. It allows to evaluate all the multiple optimal solutions of the problem at the expense of a significant computational effort and to select the preferred solution according to additional criteria. The robustness of four selection criteria found in literature has been tested through the calibration of three numerical case studies, showing how the criterion of the minimum distance from the equilibrium point ensures the best performances. On the basis of this criterion, a direct procedure for the computation of the preferred solution has been developed. It additionally enables the a posteriori estimation of the weighting factor associated to this solution, maintaining a connection with the classical approach. The validation of the procedure carried out with the updating of a complex 3D FE model, describing a masonry fortress located in San Felice sul Panaro (Modena, Italy), basically confirmed the same results of the classical procedure allowing for a reduction of the computational time.

The focus has then been moved to Bayesian model updating, which enables the uncertainty quantification of the updated parameters as a measure of the reliability of results. Inside this framework, the selection of the optimal likelihood coefficients, namely the coefficient of variation of frequency and mode shape prediction errors, is performed at an additional level of updating, the Bayesian Model Class Selection. The author proposed the use of a Gaussian surrogate to approximate the posterior distribution, considerably simplifying its computation. Considering the San Felice sul Panaro fortress, updated parameters and optimal likelihood coefficients have been determined and compared with results of the deterministic approach. Indeed, there is a relationship between the weights in the multi-objective optimization and the likelihood coefficients. The equivalent weights in Bayesian model updating are the same of those determined with the criterion of the minimum distance from the equilibrium point for the fortress if only the term related to the average data-fit is taken into account in the Bayesian framework. As concerns the Bayesian results, two prior distributions have been considered, a uniform distribution and a particular

distribution taking into account the damaged condition of the fortress. The equivalence between weights is valid in both cases. However, results of the surrogate-based procedure are comparable to the exact ones only in the last case, where the posterior distribution is approximately symmetric. The comparison has been performed also for another case study, the Ficarolo bell tower. The FE model is simpler than that of the fortress, but the updating parameter are more numerous (4 instead of 2). Results of the two approaches are similar, with stiffness distributions of the tower that are in accordance with the physical consideration about the structural behaviour. The surrogate-based procedure showed good results only if the correlations between parameters are considered. The calibration of a 4D Gaussian variable is a complex task and the convergence of the algorithm has not been always reached.

For both deterministic and Bayesian approaches it will be interesting to develop in a future research a complete damage detection procedure employing measures of different epochs as long as to choose the more adequate parametrization of the model among several alternatives. This will aim to ensure a proper damage detection and the minimal complexity of the problem. Another aspect that could be investigated is the assessment of when it is strictly necessary to rely on stochastic approaches, since the very large number of computations required. Adopting proper simulations, this necessity can be related to the magnitude of the errors affecting the measures. As concerns the surrogate-based procedure for Bayesian model updating, results obtained for the San Felice sul Panaro fortress highlighted how sometimes the Gaussian distribution does not accurately approximate the posterior distribution because of its asymmetry. Hence, a Gaussian mixture model will be tested in its substitution.

The last part of this work involved the development of a data-driven damage detection procedure for railway bridges using artificial neural networks. The complete description of the procedure phases has been realized, including the use of two numerical models to simulate the unavoidable discrepancy between model and reality, the modelling of different sources of uncertainty affecting measurements, the feature extraction and classification tools used, the creation of the network datasets composed by different damage scenarios and the optimization of the network architecture. The simpler model, which perform the classical function of a model, has been denoted as model S, while the detailed model simulating the reality has been denoted as model D. Different data are employed, such as modal properties, displacement and acceleration responses caused by the passage of a train over the bridge, and their applicability as damage feature is tested. Prediction results related to the dataset generated by model S, used also for the network training, showed how the best performances have been obtained by network N4, using acceleration features extracted with FFT and PCA, and networks N2 and N3, which take in input modal properties filtered with PCA. The difference between N2 and N3 is represented by the number of principal components adopted for constructing the mode shape loading matrix. The other networks (N1, N5, N6 and N7) are more sensitive to errors affecting data, especially N1 (not filtered modal properties) that has an accuracy around 65 %. For networks N5, N6 and N7 a further error source is present, namely the magnification of errors due to double integration of accelerations. Despite this, their accuracy is close to 80 %. The test phase with model D highlighted the need to consider the residual errors obtained at the end of the calibration of the model. Otherwise, all the trained networks are not able to recognize the damage scenarios created with model D. If the residual errors are added

to the exact data, network N1 and N2 predict the target condition with good accuracy, while N3 is not able to recognize the undamaged scenario. Corrupting the exact values with noise the performance of N1 decreases with the increment of the noise amplitude. The filtering operation conducted with PCA for N2 makes the network not sensitive to noise, even if there are errors in the predictions regarding the scenarios of damage in the concrete slab, that are classified as undamaged. The computation of residual errors for the other networks allows to obtain good results, even better than those obtained by network N1 and N2, but it has limitations due to the type of data. Indeed, displacement or acceleration responses, and consequently their residual errors, depends on the train load and velocity. The dependency is only limited to the train velocity when the responses are normalized (first step conducted using PCA). In this case, however, from the available data regarding model D and S, a clear relationship between residual errors and train velocity cannot be determined.

According to the previous results, the choice of the optimal number of principal components for the noise-filtering operation must be calibrated in order to obtain accurate results. Even in this case, light damage that does not produce a significant modification of the modal properties cannot be identified. In the author's opinion, an interesting analysis may regard the influence of the size of the baseline dataset on the cumulative explained variance associated to each principal component. This aspect affects the choice of the number of principal components and could improve the detection results. Works presented in literature underline how a nonlinear correlation may exist between different modal features. In this case, nonlinear techniques like kernel PCA or auto-encoders could be applied in order to learn nonlinear relationship at the cost of an increment of the procedure complexity. The introduction of these techniques in the procedure should be examined and investigated. For displacement responses, the discrepancy between model and reality (between models in this application) is affected by a larger number of parameters, making its prediction a complex task. Data of model S and D at hand are limited, hence it would be advisable to collect a wide number of responses associated to different values of train load and velocity. Finally, further developments involve the extension of the procedure to the localization and the quantification of damage and its application to a real case study for the experimental validation.

Bibliography

[1] *Circolare 2019. Circolare n. 7 del 21/01/2019. Istruzioni per l'applicazione dell'aggiornamento delle Norme Tecniche per le Costruzioni di cui al D.M. del 17/01/2018 [in italian].*

[2] Ahmadian, H., Mottershead, J., and Friswell, M. Damage detection from substructure modes. *The 21th International Seminar on Modal Analysis (ISMA 21)* (01 1996), 983–991.

[3] Ahmadian, H., Mottershead, J. E., and Friswell, M. I. Regularisation methods for finite element model updating. *Mechanical Systems and Signal Processing 12*, 1 (1998), 47–64.

[4] Alkayem, N. F., Cao, M., Zhang, Y., Bayat, M., and Su, Z. Structural damage detection using finite element model updating with evolutionary algorithms: a survey. *Neural Computing and Applications 30*, 2 (July 2018), 389–411.

[5] Allemang, R., and Brown, D. A correlation coefficient for modal vector analysis. In *Proceedings of the 1st International Modal Analysis Conference* (Orlando, Florida, USA, 1982), pp. 110–116.

[6] Avci, O., Abdeljaber, O., Kiranyaz, S., Hussein, M., Gabbouj, M., and Inman, D. J. A review of vibration-based damage detection in civil structures: From traditional methods to machine learning and deep learning applications. *Mechanical Systems and Signal Processing 147* (2021), 107077.

[7] Baghernejad, A., Yaghoubi, M., and Jafarpur, K. Exergoeconomic optimization and environmental analysis of a novel solar-trigeneration system for heating, cooling and power production purpose. *Solar Energy 134* (2016), 165 – 179.

[8] Bakhary, N., Hao, H., and Deeks, A. J. Substructuring technique for damage detection using statistical multi-stage artificial neural network. *Advances in Structural Engineering 13*, 4 (Aug. 2010), 619–639.

[9] Bandara, R., Chan, T., and Thambiratnam, D. The three-stage artificial neural network method for damage assessment of building structures. *Australian Journal of Structural Engineering 14* (Jan. 2013).

[10] Bandara, R. P., Chan, T. H. T., and Thambiratnam, D. P. Structural damage detection method using frequency response functions. *Structural Health Monitoring 13*, 4 (Feb. 2014), 418–429.

[11] Bao, Y., Xia, Y., Li, H., Xu, Y.-l., and Zhang, P. Data fusion-based structural damage detection under varying temperature conditions. *International Journal of Structural Stability and Dynamics 12* (02 2013).

[12] Bassoli, E., Vincenzi, L., Bovo, M., and Mazzotti, C. Dynamic identification of an ancient masonry bell tower using a MEMS-based acquisition system. In *Proceedings of the 2015 IEEE Workshop on Environmental, Energy and Structural Monitoring Systems* (Trento, Italy, 2015).

[13] Bassoli, E., Vincenzi, L., D'Altri, A. M., de Miranda, S., Forghieri, M., and Castellazzi, G. Ambient vibration-based finite element model updating of an earthquake-damaged masonry tower. *Structural Control and Health Monitoring 25*, 5 (2018), e2150.

[14] Beck, J., and Arnold, K. *Parameter Estimation in Engineering and Science*. Probability and Statistics Series. Wiley, 1977.

[15] Beck, J. L. Bayesian system identification based on probability logic. *Structural Control and Health Monitoring 17* (11 2010).

[16] Beck, J. L., and Au, S.-K. Bayesian updating of structural models and reliability using markov chain monte carlo simulation. *Journal of Engineering Mechanics 128* (04 2002), 380–391.

[17] Beck, J. L., Au, S.-K., and Vanik, M. A bayesian probabilistic approach to structural health monitoring. In *Proceedings of 1999 American Control Conference* (San Diego, USA, 2–4 June 1999), vol. 126, pp. 1119 – 1123 vol.2.

[18] Beck, J. L., and Katafygiotis, L. S. Updating models and their uncertainties. i: Bayesian statistical framework. *Journal of Engineering Mechanics 124* (1998), 455–461.

[19] Beck, J. L., and Yuen, K.-V. Model selection using response measurements: Bayesian probabilistic approach. *Journal of Engineering Mechanics 130*, 2 (2004), 192–203.

[20] Behmanesh, I., and Moaveni, B. Probabilistic identification of simulated damage on the dowling hall footbridge through bayesian finite element model updating. *Structural Control and Health Monitoring 22* (08 2014).

[21] Behmanesh, I., Moaveni, B., and Papadimitriou, C. Probabilistic damage identification of a designed 9-story building using modal data in the presence of modeling errors. *Engineering Structures 131* (11 2016).

[22] Bernagozzi, G., Mukhopadhyay, S., Betti, R., Landi, L., and Diotallevi, P. P. Output-only damage detection in buildings using proportional modal flexibility-based deflections in unknown mass scenarios. *Engineering Structures 167* (2018), 549–566.

[23] Betti, M., Facchini, L., and Biagini, P. Damage detection on a three-storey steel frame using artificial neural networks and genetic algorithms. *Meccanica 50*, 3 (2015), 875–886.

[24] Bishop, C. M. *Pattern Recognition and Machine Learning*. Springer, 2006.

[25] Bishop, C. M. *Pattern Recognition and Machine Learning (Information Science and Statistics)*. Springer-Verlag, Berlin, Heidelberg, 2006.

[26] Braak, C. J. F. T. A Markov Chain Monte Carlo version of the genetic algorithm Differential Evolution: easy Bayesian computing for real parameter spaces. *Statistics and Computing 16*, 3 (2006), 239–249.

[27] Brincker, R., Zhang, L., and Andersen, P. Modal identification of output-only systems using frequency domain decomposition. *Smart Materials and Structures 10*, 3 (2001), 441.

[28] Brinker, R., Zhang, L., and Andersen, P. Modal identification from ambient responses using frequency domain decomposition. In *Proceedings of the 18th International Modal Analysis Conference* (Kissimmee, Florida, USA, 2000).

[29] Buche, D., Schraudolph, N. N., and Koumoutsakos, P. Accelerating evolutionary algorithms with Gaussian process fitness function models. *IEEE Transactions on Systems, Man, and Cybernetics, Part C (Applications and Reviews) 35*, 2 (May 2005), 183–194.

[30] Bursi, O. S., Zonta, D., Debiasi, E., and Trapani, D. *Structural health monitoring for seismic protection of structure and infrastructure systems*. Springer International Publishing, Cham, 2018, pp. 339–358.

[31] Cadini, F., Lomazzi, L., Ferrater Roca, M., Sbarufatti, C., and Giglio, M. Neutralization of temperature effects in damage diagnosis of mdof systems by combinations of autoencoders and particle filters. *Mechanical Systems and Signal Processing 162* (2022), 108048.

[32] Caicedo, J. M., and Yun, G. A novel evolutionary algorithm for identifying multiple alternative solutions in model updating. *Structural Health Monitoring 10*, 5 (2011), 491–501.

[33] Carden, E. P., and Fanning, P. Vibration based condition monitoring: A review. *Structural Health Monitoring 3*, 4 (Dec. 2004), 355–377.

[34] Casalegno, C., and Russo, S. Dynamic characterization of an All-FRP bridge. *Mechanics of Composite Materials 53*, 1 (2017), 17–30.

[35] Castagnetti, C., Bassoli, E., Vincenzi, L., and Mancini, F. Dynamic assessment of masonry towers based on terrestrial radar interferometer and accelerometers. *Sensors 19*, 6 (2019).

[36] Castellazzi, G., D'Altri, A. M., Bitelli, G., Selvaggi, I., and Lambertini, A. From laser scanning to finite element analysis of complex buildings by using a semi-automatic procedure. *Sensors 15*, 8 (2015), 18360–18380.

[37] Castellazzi, G., D'Altri, A. M., de Miranda, S., and Ubertini, F. An innovative numerical modeling strategy for the structural analysis of historical monumental buildings. *Engineering Structures 132* (2017), 229–248.

[38] Castro-Triguero, R., M, S. M., Gallego, R., and Friswell, M. Robustness of optimal sensor placement under parametric uncertainty. *Mechanical Systems and Signal Processing 41* (12 2013), 268–287.

[39] Cattari, S., Degli Abbati, S., Ferretti, D., Lagomarsino, S., Ottonelli, D., and Tralli, A. Damage assessment of fortresses after the 2012 Emilia earthquake (Italy). *Bulletin of Earthquake Engineering 12*, 5 (2014), 2333–2365.

[40] Ching, J., and Beck, J. L. Bayesian Analysis of the Phase II IASC-ASCE Structural Health Monitoring Experimental Benchmark Data. *Journal of Engineering Mechanics 130*, 10 (2004), 1233–1244.

[41] Ching, J., and Chen, Y.-C. Transitional Markov Chain Monte Carlo Method for Bayesian Model Updating, Model Class Selection, and Model Averaging. *Journal of Engineering Mechanics 133* (07 2007).

[42] Christodoulou, K., Ntotsios, E., Papadimitriou, C., and Panetsos, P. Structural model updating and prediction variability using pareto optimal models. *Computer Methods in Applied Mechanics and Engineering 198*, 1 (2008), 138 – 149.

[43] Christodoulou, K., and Papadimitriou, C. Structural identification based on optimally weighted modal residuals. *Mechanical Systems and Signal Processing 21*, 1 (2007), 4 – 23.

[44] Chun, P.-j., Yamashita, H., and Furukawa, S. Bridge damage severity quantification using multipoint acceleration measurement and artificial neural networks. *Shock and Vibration 2015* (09 2015), 1–11.

[45] Cornwell, P., Farrar, C., and Doebling, S. Environmental variability of modal properties. *Experimental Techniques 23* (01 2008), 45 – 48.

[46] Cury, A., and Crémona, C. Pattern recognition of structural behaviors based on learning algorithms and symbolic data concepts. *Struct. Control Health Monit. 19*, 2 (Mar. 2012), 161–186.

[47] Dackermann, U., Li, J., and Samali, B. Dynamic-based damage identification using neural network ensembles and damage index method. *Advances in Structural Engineering 13*, 6 (Dec. 2010), 1001–1016.

[48] de Lautour, O. R., and Omenzetter, P. Damage classification and estimation in experimental structures using time series analysis and pattern recognition. *Mechanical Systems and Signal Processing 24*, 5 (2010), 1556–1569. Special Issue: Operational Modal Analysis.

[49] Deb, K., and Gupta, S. Understanding knee points in bicriteria problems and their implications as preferred solution principles. Tech. rep., Indian Institute of Technology Kanpur, 2010.

[50] Diaconis, P., and Ylvisaker, D. Conjugate Priors for Exponential Families. *The Annals of Statistics 7*, 2 (1979), 269 – 281.

[51] Dilena, M., Limongelli, M., and Morassi, A. Damage localization in bridges via the FRF interpolation method. *Mechanical Systems and Signal Processing 52-53* (2015), 162–180.

[52] Dincer, I., Rosen, M., and Ahamadi, P. *Optimization of Energy Systems*. Wiley, 2017.

[53] Doebling, S. W., Farrar, C. R., and Prime, M. B. A summary review of vibration-based damage identification methods. *The Shock and Vibration Digest 30* (1998), 91–105.

[54] Doebling, S. W., Farrar, C. R., Prime, M. B., and Schevitz, D. W. Damage identification and health monitoring of structural and mechanical systems from changes in their vibration characteristics: a literature review. Technical report la-13070-ms, Los Alamos National Laboratory, 1996.

[55] Dyke, S., Bernal, D., Beck, J., and Ventura, C. Experimental Phase II of the Structural Health Monitoring Benchmark Problem. In *Proceedings of the 16th ASCE Engineering Mechanics Conference* (2003).

[56] Dyke, S., Bernal, J., Beck, C., and Ventura, C. An experimental benchmark problem in structural health monitoring. In *Proceedings of the 3rd International Workshop on Structural Health Monitoring* (2001).

[57] Emmerich, M. T. M., Giannakoglou, K. C., and Naujoks, B. Single- and multiobjective evolutionary optimization assisted by Gaussian random field metamodels. *IEEE Transactions on Evolutionary Computation 10*, 4 (Aug 2006), 421–439.

[58] Feng, D., and Feng, M. Q. Output-only damage detection using vehicle-induced displacement response and mode shape curvature index. *Structural Control and Health Monitoring 23*, 8 (2016), 1088–1107.

[59] Figueiredo, E., Park, G., Farrar, C. R., Worden, K., and Figueiras, J. Machine learning algorithms for damage detection under operational and environmental variability. *Structural Health Monitoring 10*, 6 (Nov. 2010), 559–572.

[60] Fiore, A., and Marano, G. C. Serviceability performance analysis of concrete box girder bridges under traffic-induced vibrations by structural health monitoring: A case study. *International Journal of Civil Engineering 16*, 5 (May 2018), 553–565.

[61] Fontul, M., Ribeiro, A. M. R., Silva, J. M. M., and Maia, N. M. M. Transmissibility matrix in harmonic and random processes. *Shock and Vibration 11* (2004), 438986.

[62] Forghieri, M., Bassoli, E., and Vincenzi, L. Dynamic behaviour of the San Felice sul Panaro fortress: Experimental tests and model updating. In *Proceedings of the 6th ECCOMAS Thematic Conference on Computational Methods in Structural Dynamics and Earthquake Engineering* (Rhodes Island, Greece, 2017).

[63] Forrester, A. I. J., Sóbester, A., and Keane, A. J. *Engineering design via surrogate modelling: a practical guide.* John Wiley & Sons, Ltd, 2008.

[64] FOX, R. L., and KAPOOR, M. P. Rates of change of eigenvalues and eigenvectors. *AIAA Journal 6*, 12 (1968), 2426–2429.

[65] Friswell, M. I. *Damage Identification using Inverse Methods.* Springer Vienna, Vienna, 2008, pp. 13–66.

[66] Friswell, M. I., and Mottershead, J. E. *Finite element model updating in structural dynamics.* Kluwer Academic Publishers, Dordrecht, 1995.

[67] Ghiasi, R., Torkzadeh, P., and Noori, M. A machine-learning approach for structural damage detection using least square support vector machine based on a new combinational kernel function. *Structural Health Monitoring 15*, 3 (Apr. 2016), 302–316.

[68] Godat, A., Labossière, P., Neale, K. W., and Chaallal, O. Behavior of RC members strengthened in shear with EB FRP: Assessment of models and FE simulation approaches. *Computers & Structures 92-93* (2012), 269 – 282.

[69] Goller, B., Beck, J., and Schuëller, G. Evidence-based identification of weighting factors in bayesian model updating using modal data. *Journal of Engineering Mechanics 138* (05 2012), 430–440.

[70] González, M. P., and Zapico, J. L. Seismic damage identification in buildings using neural networks and modal data. *Computers & Structures 86*, 3 (2008), 416–426. Smart Structures.

[71] Green, P. J., and Mira, A. Delayed rejection in reversible jump metropolis-hastings. *Biometrika 88*, 4 (Dec. 2001), 1035–1053.

[72] Gui, G., Pan, H., Lin, Z., Li, Y., and Yuan, Z. Data-driven support vector machine with optimization techniques for structural health monitoring and damage detection. *KSCE Journal of Civil Engineering 21*, 2 (2017), 523–534.

[73] Guidorzi, R., Diversi, R., Vincenzi, L., Mazzotti, C., and Simioli, V. Structural monitoring of a tower by means of MEMS-based sensing and enhanced autoregressive models. *European Journal of Control 20*, 1 (2014), 4–13.

[74] Haario, H., Saksman, E., and Tamminen, J. An adaptive metropolis algorithm. *Bernoulli 7*, 2 (2001), 223–242.

[75] Hansen, P. C. *Rank-deficient and discrete ill-posed problems: numerical aspects of linear inversion.* SIAM, 1998.

[76] Hastings, W. D. Monte Carlo Sampling Methods Using Markov Chains and Their Applications. *Biometrica 57* (1970), 97 – 109.

[77] Haykin, S. *Neural Networks: A Comprehensive Foundation.* International edition. Prentice Hall, 1999.

[78] Hou, R., and Xia, Y. Review on the new development of vibration-based damage identification for civil engineering structures: 2010–2019. *Journal of Sound and Vibration 491* (2021), 115741.

[79] Hu, H., Wang, B.-T., Lee, C.-H., and Su, J.-S. Damage detection of surface cracks in composite laminates using modal analysis and strain energy method. *Composite Structures 74*, 4 (2006), 399–405.

[80] Huang, Y., Shao, C., Wu, B., Beck, J., and Li, H. State-of-the-art review on bayesian inference in structural system identification and damage assessment. *Advances in Structural Engineering 22* (11 2018), 136943321881154.

[81] Ibrahim, S. R. *Correlation of Analysis and Test in Modeling of Structures: Assessment and Review*. Vieweg+Teubner Verlag, Wiesbaden, 1988, pp. 195–211.

[82] Ierimonti, L., Venanzi, I., Cavalagli, N., Comodini, F., and Ubertini, F. An innovative continuous bayesian model updating method for base-isolated rc buildings using vibration monitoring data. *Mechanical Systems and Signal Processing 139* (2020), 106600.

[83] Iman, R. L., and Conover, W. Small sample sensitivity analysis techniques for computer models with an application to risk assessment. *Communications in statistics-theory and methods 9*, 17 (1980), 1749–1842.

[84] Imregun, M., and Visser, W. P. J. A review of model updating techniques. *The Shock and Vibration Digest 23* (1991), 9–20.

[85] Jaishi, B., and Ren, W. X. Damage detection by finite element model updating using modal flexibility residual. *J. of Sound and Vibration 290*, 1–2 (1996), 369–387.

[86] Jaishi, B., and Ren, W. X. Structural finite element model updating using ambient vibration test results. *J. of Structural Engineering ASCE 131*, 4 (2005), 617–628.

[87] Jaishi, B., and Ren, W. X. Finite element model updating based on eigenvalue and strain energy residuals using multiobjective optimisation technique. *Mechanical Systems and Signal Processing 21* (2007), 2295–2317.

[88] Jaynes, E., Jaynes, E., Bretthorst, G., and Press, C. U. *Probability Theory: The Logic of Science*. Cambridge University Press, 2003.

[89] Jaynes, E. T. Information theory and statistical mechanics. *Physical Review 106* (1957), 620–630.

[90] Jiang, S.-F., Zhang, C.-M., and Yao, J. Eigen-level data fusion model by integrating rough set and probabilistic neural network for structural damage detection. *Advances in Structural Engineering 14*, 2 (Apr. 2011), 333–349.

[91] Jiang, S.-F., Zhang, C.-M., and Zhang, S. Two-stage structural damage detection using fuzzy neural networks and data fusion techniques. *Expert Systems with Applications 38*, 1 (2011), 511–519.

[92] Jin, S. S., Cho, S., Jung, H. J., Lee, J. J., and Yun, C. B. A new multi-objective approach to finite element model updating. *Journal of Sound and Vibration 333*, 11 (2014), 2323 – 2338.

[93] Johnson E., A., Lam H., F., Katafygiotis L., S., and Beck J., L. Phase i iasc-asce structural health monitoring benchmark problem using simulated data. *Journal of Engineering Mechanics 130*, 1 (Jan. 2004), 3–15.

[94] Karami, K., Manie, S., Ghafouri, K., and Nagarajaiah, S. Nonlinear structural control using integrated dda/ismp and semi-active tuned mass damper. *Engineering Structures 181* (2019), 589–604.

[95] Katafygiotis, L., Papadimitriou, C., and Lam, H.-F. A probabilistic approach to structural model updating. *Soil Dynamics and Earthquake Engineering 17*, 7-8 (Oct. 1998), 495–507.

[96] Katafygiotis, L. S., and Beck, J. L. Updating models and their uncertainties. ii:&x2002;model identifiability. *Journal of Engineering Mechanics 124*, 4 (1998), 463–467.

[97] Katafygiotis, L. S., and Lam, H.-F. Tangential-projection algorithm for manifold representation in unidentifiable model updating problems. *Earthquake Engineering & Structural Dynamics 31*, 4 (2002), 791–812.

[98] Kennedy, M., and O'Hagan, A. Bayesian calibration of computer models. *Journal of the Royal Statistical Society Series B 63* (02 2001), 425–464.

[99] Khan, S., and Yairi, T. A review on the application of deep learning in system health management. *Mechanical Systems and Signal Processing 107* (2018), 241–265.

[100] Khuri, A., and Cornell, J. A. *Response surfaces. Designs and analyses*. Marcel Dekker Inc., New York, 1996.

[101] Kim., I. Y., and de Weck, O. L. Adaptive weighted-sum method for bi-objective optimization: Pareto front generation. *Structural and Multidisciplinary Optimization 29*, 2 (2005), 149–158.

[102] Ko, J., Wong, C., and Lam, H. The location of defects in structures: a comparison of the use of natural frequency and mode shape data,. In *Proceedings of the 10th International Modal Analysis Conference* (1994), pp. 522–528.

[103] Konak, A., Coit, D. W., and Smith, A. E. Multi-objective optimization using genetic algorithms: A tutorial. *Reliability Engineering and System Safety 91*, 9 (2006), 992 – 1007.

[104] Kong, X., Cai, C., and Kong, B. Damage detection based on transmissibility of a vehicle and bridge coupled system. *Journal of Engineering Mechanics 141*, 1 (2015). cited By 44.

[105] Lam, H. F., and Ng, C. T. The selection of pattern features for structural damage detection using an extended Bayesian ANN algorithm. *Engineering Structures 30*, 10 (2008), 2762–2770.

[106] Lee, J. J., Lee, J. W., Yi, J. H., Yun, C. B., and Jung, H. Y. Neural networks-based damage detection for bridges considering errors in baseline finite element models. *Journal of Sound and Vibration 280*, 3 (2005), 555–578.

[107] Limongelli, M. Frequency response function interpolation for damage detection under changing environment. *Mechanical Systems and Signal Processing 24*, 8 (2010), 2898–2913.

[108] Limongelli, M. The interpolation damage detection method for frames under seismic excitation. *Journal of Sound and Vibration 330*, 22 (2011), 5474–5489.

[109] Lin, T. W., and Wang, C. H. A hybrid genetic algorithm to minimize the periodic preventive maintenance cost in a series-parallel system. *J. of Intelligent Manufacturing 23*, 4 (2012), 1225–1236.

[110] Liu, K., De Roeck, G., and Lombaert, G. The effect of dynamic train–bridge interaction on the bridge response during a train passage. *Journal of Sound and Vibration 325*, 1 (2009), 240–251.

[111] Liu, Y.-Y., Ju, Y.-F., Duan, C.-D., and Zhao, X.-F. Structure damage diagnosis using neural network and feature fusion. *Engineering Applications of Artificial Intelligence 24*, 1 (2011), 87–92.

[112] Maia, N. M., Almeida, R. A., Urgueira, A. P., and Sampaio, R. P. Damage detection and quantification using transmissibility. *Mechanical Systems and Signal Processing 25*, 7 (2011), 2475–2483.

[113] Majidi, M., Nojavan, S., Esfetanaj, N. N., Najafi-Ghalelou, A., and Zare, K. A multi-objective model for optimal operation of a battery/PV/fuel cell/grid hybrid energy system using weighted sum technique and fuzzy satisfying approach considering responsible load management. *Solar Energy 144* (2017), 79 – 89.

[114] Mehrjoo, M., Khaji, N., Moharrami, H., and Bahreininejad, A. Damage detection of truss bridge joints using artificial neural networks. *Expert Systems with Applications 35*, 3 (2008), 1122–1131.

[115] Metropolis, N., Rosenbluth, A., Rosenbluth, M., Teller, A., and Teller, E. Equation of state calculations by fast computing machines. *J. Chem. Phys. 21* (11 1952), 1087–1092.

[116] Møller, M. A scaled conjugate gradient algorithm for fast supervised learning. *Neural Networks 6* (12 1993), 525–533.

[117] Mottershead, J., and Friswell, M. Model updating in structural dynamics: A survey. *Journal of Sound and Vibration 167*, 2 (1993), 347 – 375.

[118] Mthembu, L., Marwala, T., Friswell, M. I., and Adhikari, S. Model selection in finite element model updating using the bayesian evidence statistic. *Mechanical Systems and Signal Processing 25*, 7 (2011), 2399 – 2412.

[119] Müller, J., Shoemaker, C. A., and Piché, R. SO-MI: A surrogate model algorithm for computationally expensive nonlinear mixed-integer black-box global optimization problems. *Computers & Operations Research 40*, 5 (2013), 1383 – 1400.

[120] Muto, M., and Beck, J. L. Bayesian updating and model class selection for hysteretic structural models using stochastic simulation. *Journal of Vibration and Control 14*, 1-2 (2008), 7–34.

[121] Nelson, R. B. Simplified calculation of eigenvector derivatives. *AIAA Journal 14*, 9 (1976), 1201–1205.

[122] Nguyen, H., Mahowald, J., Golinval, J.-C., and Maas, S. Damage detection in civil engineering structure considering temperature effect. In *International Modal Analysis Conference IMAC XXXII Dynamics of Coupled Structures* (2014), vol. 4.

[123] Nocedal, J., and Wright, S. J. *Numerical Optimization*, second ed. Springer, New York, NY, USA, 2006.

[124] Nzabonimpa, J., Hong, W.-K., and Kim, J. Nonlinear finite element model for the novel mechanical beam-column joints of precast concrete-based frames. *Computers & Structures 189* (2017), 31 – 48.

[125] Osama, A., and Onur, A. Nonparametric structural damage detection algorithm for ambient vibration response: Utilizing artificial neural networks and self-organizing maps. *Journal of Architectural Engineering 22*, 2 (June 2016), 04016004.

[126] Palmonella, M., Friswell, M. I., Mottershead, J. E., and Lees, A. W. Finite element models of spot welds in structural dynamics: review and updating. *Computers & Structures 83*, 8 (2005), 648–661.

[127] Pandey, A., and Biswas, M. Damage detection in structures using changes in flexibility. *Journal of Sound and Vibration 169*, 1 (1994), 3–17.

[128] Pandey, A., Biswas, M., and Samman, M. Damage detection from changes in curvature mode shapes. *Journal of Sound and Vibration 145*, 2 (1991), 321–332.

[129] Papadimitriou, C. Bayesian updating of weight values uncertainties in weighted residuals methods for model updating and response predictions. In *Proceedings of the XXIV International Conference On Sound and Vibration in Engineering and III International Conference on Uncertainty in Structural Dynamics* (Leuven, Belgium, 2010), pp. 5207–5222.

[130] Park, G., Muntges, D., and Inman, D. Self-monitoring and self-healing jointed structures. pp. 75–84.

[131] Pawar, P. M., Venkatesulu Reddy, K., and Ganguli, R. Damage detection in beams using spatial fourier analysis and neural networks. *Journal of Intelligent Material Systems and Structures 18*, 4 (Dec. 2006), 347–359.

[132] Peeters, B., and De Roeck, G. One year monitoring of the z24-bridge: Environmental influences versus damage events. *Proceedings of SPIE - The International Society for Optical Engineering 2* (05 2000).

[133] Perera, R., and Ruiz, A. A multistage FE updating procedure for damage identification in large-scale structures based on multiobjective evolutionary optimization. *Mechanical Systems and Signal Processing 22*, 4 (2008), 970 – 991.

[134] Plevris, V., and Papadrakakis, M. A hybrid particle swarm – gradient algorithm for global structural optimization. *Compter-aided civil and infrastructure engineering 26*, 1 (2011), 48–68.

[135] Pourfalah, S., Cotsovos, D., and Suryanto, B. Modelling the out-of-plane behaviour of masonry walls retrofitted with engineered cementitious composites. *Computers & Structures 201* (2018), 58 – 79.

[136] Prechelt, L. *Neural Networks: Tricks of the Trade*. Springer, 2012, ch. Early Stopping — But When?

[137] Radzieński, M., Krawczuk, M., and Palacz, M. Improvement of damage detection methods based on experimental modal parameters. *Mechanical Systems and Signal Processing 25*, 6 (2011), 2169–2190. Interdisciplinary Aspects of Vehicle Dynamics.

[138] Rainieri, C., and Fabbrocino, G. Automated output-only dynamic identification of civil engineering structures. *Mechanical Systems and Signal Processing 24*, 3 (2010), 678 – 695.

[139] Rainieri, C., Fabbrocino, G., and Verderame, G. Non-destructive characterization and dynamic identification of a modern heritage building for serviceability seismic analyses. *NDT & E International 60* (12 2013), 17–31.

[140] Regni, M., Arezzo, D., Carbonari, S., Gara, F., and Zonta, D. Effect of environmental conditions on the modal response of a 10-story reinforced concrete tower. *Shock and Vibration 2018* (2018).

[141] Ren, W.-X., and De Roeck, G. Structural Damage Identification using Modal Data. I: Simulation Verification. *Journal of Structural Engineering 128* (01 2002).

[142] Ren, W. X., Fang, S. E., and Deng, M. Y. Response surface–based finite-element-model updating using structural static responses. *J. Eng. Mech. 137*, 4 (2011).

[143] Reynders, E. System identification methods for (operational) modal analysis: Review and comparison. *Archives of Computational Methods in Engineering 19* (03 2012), 51–124.

[144] Reynders, E., Pintelon, R., and De Roeck, G. Uncertainty bounds on modal parameters obtained stochastic subspace identification. *Mechanical Systems and Signal Processing 22* (3 2008), 948–969.

[145] Reynders, E., Wursten, G., and De Roeck, G. Output-only structural health monitoring in changing environmental conditions by means of nonlinear system identification. *Structural Health Monitoring 13*, 1 (2014), 82–93.

[146] RIBEIRO, A., SILVA, J., and MAIA, N. On the generalisation of the transmissibility concept. *Mechanical Systems and Signal Processing 14*, 1 (2000), 29–35.

[147] Rytter, A. *Vibrational Based Inspection of Civil Engineering Structures*. PhD thesis, Denmark, 1993. Ph.D.-Thesis defended publicly at the University of Aalborg, April 20, 1993 PDF for print: 206 pp.

[148] Salawu, O. Detection of structural damage through changes in frequency: a review. *Engineering Structures 19*, 9 (1997), 718–723.

[149] Schölkopf, B., Smola, A., and Müller, K.-R. Nonlinear component analysis as a kernel eigenvalue problem. *Neural Computation 10* (07 1998), 1299–1319.

[150] Schwarz, B. J., and Richardson, M. H. Introduction to operating deflection shapes. *CSI Reliability Week 10*, 538 (1999), 121–126.

[151] Seyedpoor, S. A two stage method for structural damage detection using a modal strain energy based index and particle swarm optimization. *International Journal of Non-Linear Mechanics 47*, 1 (2012), 1–8.

[152] Simoen, E., De Roeck, G., and Lombaert, G. Dealing with uncertainty in model updating for damage assessment: A review. *Mechanical Systems and Signal Processing 56–57*, 0 (2015), 123–149.

[153] Simoen, E., Papadimitriou, C., and Lombaert, G. On prediction error correlation in bayesian model updating. *Journal of Sound and Vibration 332*, 18 (2013), 4136 – 4152.

[154] Snyman, J. A., and Wilke, D. N. *Practical mathematical optimization: basic optimization theory and gradient-based algorithms; 2nd ed.* Springer optimization and its applications. Springer, Cham, 2018.

[155] Sohn, H. Effects of environmental and operational variability on structural health monitoring. *Philosophical Transactions of the Royal Society A: Mathematical, Physical and Engineering Sciences 365*, 1851 (2007), 539.

[156] Sohn, H., Farrar, C. R., Hemez, F. M., and Czarnecki, J. J. A review of structural health review of structural health monitoring literature 1996-2001.

[157] Sohn, H., and Law, K. H. A bayesian probabilistic approach for structure damage detection. *Earthquake Engineering & Structural Dynamics 26*, 12 (1997), 1259–1281.

[158] Soize, C. Maximum entropy approach for modeling random uncertainties in transient elastodynamics. *The Journal of the Acoustical Society of America 109*, 5 (2001), 1979–1996.

[159] Storn, R., and Price, K. Differential evolution - a simple and efficient heuristic for global optimization over continuous spaces. *Journal of Global Optimization 11* (1997), 341–359.

[160] Stubbs, N., Kim, J.-T., and Topole, K. An efficient and robust algorithm for damage localization in offshore platforms. *Proc. ASCE Tenth Structures Congress* (03 1992).

[161] Teughels, A. *Inverse modelling of civil engineering structures based on operational modal data*. PhD thesis, 2003.

[162] Teughels, A., and De Roeck, G. Structural damage identification of the highway bridge Z24 by FE model updating. *Journal of Sound and Vibration 278*, 3 (2004), 589 – 610.

[163] Teughels, A., Maeck, J., and De Roeck, G. Damage assessment by FE model updating using damage functions. *Computers & Structures 80*, 25 (2002), 1869 – 1879.

[164] Tikhonov, A. N. *Numerical methods for the solution of ill-posed problems*. Kluwer Academic Publishers, Boston, 1995.

[165] Titurus, B., and Friswell, M. I. Regularization in model updating. *International Journal for Numerical Methods in Engineering 75*, 4 (2008), 440–478.

[166] Vanik, M. W., Beck, J. L., and Au, S. K. Bayesian probabilistic approach to structural health monitoring. *Journal of Engineering Mechanics 126*, 7 (2000), 738–745.

[167] Vincenzi, L. *Identificazione dinamica delle caratteristiche modali e delle proprietá meccaniche di strutture mediante algoritmi di ottimizzazione*. PhD thesis, University of Bologna, Italy, 2007.

[168] Vincenzi, L., Bassoli, E., Ponsi, F., Castagnetti, C., and Mancini, F. Dynamic monitoring and evaluation of bell ringing effects for the structural assessment of a masonry bell tower. *Journal of Civil Structural Health Monitoring 9*, 4 (2019), 439–458.

[169] Vincenzi, L., and Gambarelli, P. A proper infill sampling strategy for improving the speed performance of a Surrogate-Assisted Evolutionary Algorithm. *Computers and Structures 178* (2017), 58–70.

[170] Vincenzi, L., and Savoia, M. Coupling response surface and differential evolution for parameter identification problems. *Computer-Aided Civil and Infrastructure Engineering 30*, 5 (2015), 376–393.

[171] Vrugt, J., ter Braak, C., Diks, C., Robinson, B., Hyman, J., and Higdon, D. Accelerating markov chain monte carlo simulation by differential evolution with self-adaptive randomized subspce sampling. *International Journal of Nonlinear Sciences and Numerical Simulation 10 (2009) 3 10* (11 2008).

[172] Walker, W., Harremoës, P., Rotmans, J., Sluijs, J., Asselt, M., Janssen, P., and Kraus, M. Defining uncertainty: A conceptual basis for uncertainty management in model-based decision support. *Integrated Assessment 4* (03 2003).

[173] Worden, K., Farrar, C. R., Manson, G., and Park, G. The fundamental axioms of structural health monitoring. *Proceedings of the Royal Society A: Mathematical, Physical and Engineering Sciences 463*, 2082 (June 2007), 1639–1664.

[174] Yeung, W., and Smith, J. Damage detection in bridges using neural networks for pattern recognition of vibration signatures. *Engineering Structures 27*, 5 (2005), 685–698.

[175] Yin, T., Jiang, Q.-H., and Yuen, K.-V. Vibration-based damage detection for structural connections using incomplete modal data by bayesian approach and model reduction technique. *Engineering Structures 132* (02 2017), 260–277.

[176] Ying, X. An overview of overfitting and its solutions. *Journal of Physics: Conference Series 1168* (feb 2019), 022022.

[177] Yuen, K.-V. *Bayesian Methods for Structural Dynamics and Civil Engineering*. 04 2010.

[178] Yuen, K.-V., Beck, J. L., and Katafygiotis, L. S. Efficient model updating and health monitoring methodology using incomplete modal data without mode matching. *Structural Control and Health Monitoring 13*, 1 (2006), 91–107.

[179] Yuen, K.-V., and Lam, H. F. On the complexity of artificial neural networks for smart structures monitoring. *Engineering Structures 28* (06 2006), 977–984.

[180] Żak, A. J., Krawczuk, M., and Ostachowicz, W. M. Vibration of a laminated composite plate with closing delamination. In *Damage Assessment of Structures* (6 1999), vol. 167 of *Key Engineering Materials*, Trans Tech Publications Ltd, pp. 17–26.

[181] Zare Hosseinzadeh, A., Ghodrati Amiri, G., Seyed Razzaghi, S., Koo, K., and Sung, S. Structural damage detection using sparse sensors installation by optimization procedure based on the modal flexibility matrix. *Journal of Sound and Vibration 381* (2016), 65–82.

[182] Zhang, E., Feissel, P., and Antoni, J. A comprehensive bayesian approach for model updating and quantification of modeling errors. *Probabilistic Engineering Mechanics 26*, 4 (2011), 550 – 560.

[183] Zhang, Y., Lie, S. T., and Xiang, Z. Damage detection method based on operating deflection shape curvature extracted from dynamic response of a passing vehicle. *Mechanical Systems and Signal Processing 35*, 1 (2013), 238–254.

[184] Zhang, Y., Wang, L., and Xiang, Z. Damage detection by mode shape squares extracted from a passing vehicle. *Journal of Sound and Vibration 331*, 2 (2012), 291–307.

[185] Zhu, F., and Wu, Y. A rapid structural damage detection method using integrated anfis and interval modeling technique. *Applied Soft Computing 25* (2014), 473–484.